Helmholtz-Zentrum Berlin für Materialien und Energie | Universität Potsdam

Spin Polarization, Circular Dichroism, and Robustness of Topological Surface States: A Photoemission Study

Dissertation
zur Erlangung des akademischen Grades
"doctor rerum naturalium" (Dr. rer. nat.)
in der Wissenschaftsdisziplin Experimentalphysik

eingereicht an der
Mathematisch-Naturwissenschaftlichen Fakultät
der Universität Potsdam

vorgelegt von
Markus Reiner Scholz

Universität Potsdam, 29. Oktober 2012

Published online at the
Institutional Repository of the University of Potsdam:
URN urn:nbn:de:kobv:517-opus4- 96686
http://nbn-resolving.de/urn:nbn:de:kobv:517-opus4- 96686

Contents

Chapter 1

Motivation

A topological insulator is a strange kind of system. You can describe it within one sentence: It is insulating in its interior and conducting on its boarders. But you can also write a full thesis about a system *called* a topological insulator that does not even fulfill both of these two basic properties: Bi_2Se_3 and Bi_2Te_3, the systems under investigation in this thesis, suffer from the drawback of a strong intrinsic electron doping that makes these systems conducting in their interior. Nevertheless, they are the systems that are, up to now, most intensely studied under the label of topological insulators.

Significantly, these systems are described by a topological invariant that is *odd* in their case and *even* in the case of a trivial insulator. From this *oddness*, one can derive what makes these systems so special, or distinct from their trivial counterparts. To do so it is instructive to first describe what a topological invariant is. A topological invariant is an integer that classifies topologically distinct objects or groups of objects. A glass, a cup, a donut and an orange can be ordered into two classes according to their genus, the topological invariant that counts holes in surfaces. Thus the cup goes with the donut and the glass goes with the orange. In other words: there exists a continuous transformation from the cup to the donut and from the glass to the orange. But in order to transform a donut into an orange one has to tear a hole into the orange's surface. Tearing a hole is, however, a discontinuity: a hole is a full hole, something like half a hole does not exist.

Insulators can be classified topologically according to the kind of gap they show at the Fermi level. The trivial insulator has a gap according to its definition in band theory. In topological insulators, however, the gap is inverted. This is not unusual by itself as Shockley noticed in 1939 that inverted band gaps give rise to surface states. However, in the up to date known topological insulators it is strong spin-orbit coupling that causes the band inversion. One can calculate the band structure of a system with and without spin-orbit coupling. If, by switching the spin-orbit coupling on, the conduction band takes the role of the valence band and *vice versa* then the gap is called inverted and the system might[1] be a topological insulator and the invariant becomes *odd*. If one smoothly increases the spin-orbit coupling then at some point the gap of the trivial insulator will close and this is the discontinuity where the invariant changes.

The interesting physics starts to happen when the topological insulator is not considered to be infinite but shares an interface to a trivial insulator, e.g., vacuum. Obviously, at the interface the topological invariant changes from *odd* to *even* but this may not happen

[1] One has to investigate the effects of spin-orbit coupling on the band order at all time reversal invariant momenta of the Brillouin zone. Details will be discussed in Chapter 3

continuously. The gap will have to close at the interface and this is the reason why there is always a metallic state at the surface.

Such kind of *topological surface states* are known from the quantum Hall effect. The difference is that the latter requires a magnetic field, which breaks time reversal symmetry, while in the topological insulator, time reversal symmetry explicitly holds. They have in common, that they are extremely robust against perturbations. However, in the case of topological insulators, the metallicity of the surface state is guaranteed by time reversal symmetry. In turn, breaking time reversal symmetry will open a gap in the surface state and the surface may become insulating.

An aspect closely related and of particular importance is that it is an odd number of surface states that provides the metallicity which in turn implies that the surface state is spin polarized. Chapter 3 of this thesis gives a more detailed description of the concept of the topological insulator and how topology applies to solid state physics.

A lot of prospects are placed onto these new materials. First and foremost, there are the potential applications in spintronic devices. The idea behind spintronics is that instead of the charge the spin degree of freedom is the quantity that is controlled and manipulated within a device. While this idea promises nonvolatility, an increased dataprocessing speed, a further increase of the integration densities and a decrease in electric power consumption, the issues connected to spintronics turn out to be rather challenging. Up to date, the attempts for an efficient spin injection, efficient spin current generation and spin conserving transport are still unsatisfying. Great hope lies in the topological insulator especially in terms of spin current generation and injection of this current into a spin conserving medium. While the generation of spin currents can also be achieved very well in ferromagnetic metals, the injection into a spin conserving medium like, for example, a magnetic semiconductor is very inefficient due to the great mismatch between the conductivities of a metal and a semiconductor. This mismatch could get significantly reduced with an ideal topological insulator with very low bulk conductivity.

At present stage the residual bulk conductivity, however, turns out to be the biggest drawback of the known topological insulators to overcome in order to be able to use them as efficient spin current generators that allow for an efficient injection. There is a long path ahead to go and great need for understanding the fundamentals of the materials that fulfill the preconditions for being *real* topological insulators.

In this sense, this thesis tries to deliver a contribution to understand the fundamentals of the materials. That is, first of all, a reliable measurement of the spin polarization of the topological surface states. This is the topic of Chapter 4 in which, after a basic description of the electronic structure measured with angle resolved photoemission, the spin polarization of the surface states in Bi_2Se_3 and Bi_2Te_3 is determined by means of spin resolved photoemission.

Still fundamental, but aiming already on possible applications, is the topic of Chapter 5. Therein, the effect of impurities deposited on the surface of Bi_2Te_3 and Bi_2Se_3 is investigated. From a fundamental point of view it is the robustness, that is tested in such kind of experiments. From an applied point of view it is also important to generate knowledge about the impact of an interface on the electronic structure. Integration of a topological insulator into electronic devices will undoubtedly necessitate a contact with metallic circuits.

As pointed out above, time reversal symmetry is the ultimate precondition to observe the topological insulator phase. Thus, the effect of a time reversal symmetry breaking

perturbation such as magnetic impurities on the surface is of great fundamental interest. Is there a difference to non-magnetic impurities, and can we open an energy gap in the surface state by breaking time reversal symmetry? A gap in the surface state could lead to a system that hosts an anomalous quantum Hall state and would also be of interest for device applications since the surface state system would be a two dimensional equivalent of a magnetic semiconductor with oppositely spin polarized electron and hole states.

Chapter 6 is focused on the decay mechanisms for photoholes. From an analysis of the linewidth of angle resolved photoemission spectra the lifetime of photohole states is gained and related to the scattering properties of the topological surface states. It is thus again a fundamental property of the topological insulator that is probed. Time reversal symmetry forbids a backscattering of electrons and promises dissipationless currents or at least currents with reduced dissipation.

Together with the number of ideas for spintronic devices or the number of materials suggested to host interesting physics for spintronic applications, the demand for experimental techniques that are capable of investigating such effects, materials, and ideas grows. One of the most powerful tools in this aspect is spin resolved photoemission. However, it is a very demanding technique due to the low efficiency of spin detectors. Thus, the beginning of the age of spintronics is intimately related to the development of new techniques dedicated for the investigation of "spintronics". Chapter 7 discusses a promising candidate for an efficient alternative to conventional spin resolved photoemission.

To help those readers not familiar with photoemission to understand the results presented in the experimental part of this thesis the following chapter is dedicated to an introduction to the basic knowledge of this powerful technique.

Chapter 2

Photoelectron Spectroscopy for the Investigation of Topological Insulators

The distinction of topological insulators from their trivial counterparts is found –as the name already indicates– in the topology of the electronic band structure. Since the most direct probe of the band structure of solids is photoelectron spectroscopy, it has become the method of choice to experimentally find and characterize new topological insulators [1, 2, 3] and to investigate their unique properties.

To guide those readers not familiar with photoelectron spectroscopy through the results of this thesis I will give in this chapter a short introduction to the basics of spin and angle resolved photoemission (SARPES). Specific aspects, like the lifetime broadening of photoemission peaks due to manybody interactions (Chapter 6), or the dependence of photoemission spectra on the polarization of light (Chapter 7) will be discussed in the respective chapters.

Additionally, the experimental setups used for spin and angle resolved photoemission will be sketched at the end of this chapter.

2.1 Basic Knowledge

Photoemission is a very established technique. Developed to study the electronic structure of solids already in 1957 by Kai Siegbahn [4], it is based on the process of photoemission discovered already in 1887 by Heinrich Hertz [5]. Later it has been explained by Albert Einstein [6, 7, 8] as a manifestation of the quantum nature of light which is expressed in the fundamental photoelectric equation:

$$E_{kin}^{max} = h\nu - \Phi_f. \tag{2.1}$$

Here E_{kin} denotes the kinetic energy of the photoelectron and $h\nu$ is the energy of the exciting photon with frequency ν. The quantity Φ_f is a characteristic material and surface dependent constant of the solid and is called *work function*. If a monochromatic source of photons is used and Φ_f is known, then measuring the kinetic energy of a photoelectron is in a first approximation equivalent to the determination of its binding energy E_B in the solid making use of the following equation:

$$E_B = h\nu - E_{kin} - \Phi_f. \tag{2.2}$$

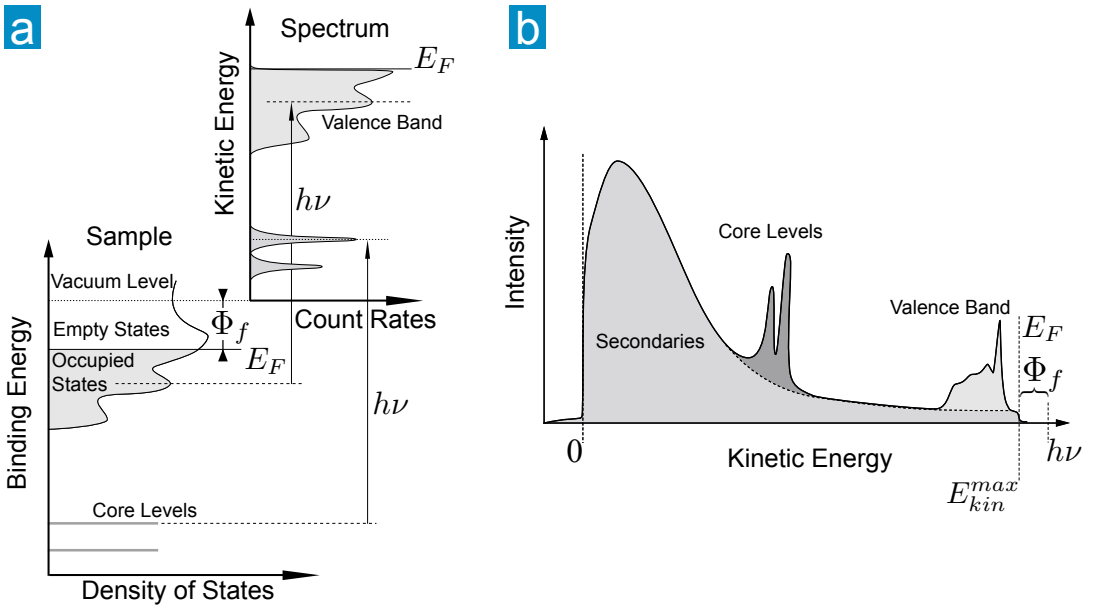

Figure 2.1: The photoemission process. a) Energy diagram illustrating the photoexcitations with monochromatized light. b) The photoemission spectrum is entailed by secondary electron background that increases drastically towards low kinetic energies. Redrawn from Ref. [9].

Here we use the common convention that the binding energy is a positive quantity for bound electrons, with the Fermi level E_F, i.e., the chemical potential μ[1] being the zero of energy by definition. Eq. 2.2 can be visualized in the well known sketch of Fig.2.1 a), which shows the density of occupied states of a solid as a function of binding energy and the number of detected electrons as a function of kinetic energy.

While photoemission has to be viewed as a quantum mechanical measuring process in order to treat all possible forms of interactions between the incoming photon and the excitations that may occur within a specimen, it is much more instructive to start with a simplified picture. In this, so called *three-step model of photoemission* one divides the photoemission process into three *independent* steps [9]: i) optical excitation, ii) transport to the surface, and iii) escape from the crystal.

2.1.1 Optical Excitation Process

The first step is further simplyfied in terms of a single-particle approximation [9] and is the optical excitation of an electron from an initial eigenstate $|\Psi_i(E_i, \mathbf{k_i}, \mathbf{s_i})\rangle$ into an unoccupied final eigenstate $|\Psi_f(E_f, \mathbf{k_f}, \mathbf{s_f})\rangle$ by a *single* photon of an incoming monochromatic light beam of energy $h\nu$. Here, the indices i and f mark the initial and final state properties, respectively. The important quantities are the electron energy $E_{i,f}$, the electron momentum $\mathbf{k_{i,f}}$, and the electron spin $\mathbf{s_{i,f}}$. The probability for the transition between the the two states

[1] By definition, the Fermi level is defined only at T=0 K and at finite temperature the term chemical potential is used instead. Following general usage, I will use the term Fermi level throughout this thesis being aware of the inconsistency.

(w_{if}) is given by Fermi's golden rule:

$$w_{if} \propto \frac{2\pi}{\hbar} \left| \langle \Psi_f \left(E_f, \mathbf{k_f}, \mathbf{s_f} \right) | \, H' \, | \Psi_i \left(E_i, \mathbf{k_i}, \mathbf{s_i} \right) \rangle \right|^2 \delta \left(E_f - E_i - h\nu \right). \tag{2.3}$$

The δ-function is responsible for the energy conservation and the operator H' denotes the Hamiltonian of the interaction between the electron and the electromagnetic field of the incoming beam with vector potential $\mathbf{A}$. By neglecting two photon processes and setting the gauge of the electromagnetic field such that the scalar potential $\phi = 0$ the Hamiltonian may be written as [9]:

$$H' = \frac{e}{2mc} \left(\mathbf{A} \cdot \mathbf{p} + \mathbf{p} \cdot \mathbf{A} \right), \tag{2.4}$$

where e and m denote electron charge and mass as usual and $\mathbf{p} = i\hbar\nabla$ is the momentum operator. Making use of the commutation relation $[\mathbf{p}, \mathbf{A}] = 2\mathbf{A} \cdot \mathbf{p} + i\hbar\nabla \cdot \mathbf{A}$ together with the dipole approximation, i.e, $\nabla \cdot \mathbf{A} = 0$[2] one finds:

$$H' = \frac{e}{2mc} \mathbf{A} \cdot \mathbf{p}. \tag{2.5}$$

Thus, to describe the excitation process we simply have to replace the momentum operator in the Hamiltonian of the Schrödinger equation by Eq. 2.5. However, since we will deal with spin-polarized electrons and perform spin resolved photoemission, the Schrödinger approach is not adequate and should be replaced by the Dirac equation, since in the former the electron is treated as spinless [10]. The Dirac Hamiltonian is written

$$\begin{aligned} H_{Dirac} = & \frac{1}{2m} \left(\mathbf{p} - \frac{e}{c} \mathbf{A} \right)^2 + eV(\mathbf{r}) \\ & - \frac{e\hbar}{2mc} \sigma \nabla \times \mathbf{A} + \frac{ie\hbar}{4m^2c^2} \mathbf{E} \cdot \mathbf{p} - \frac{e\hbar}{4m^2c^2} \sigma (\mathbf{E} \times \mathbf{p}), \end{aligned} \tag{2.6}$$

where the first two terms, i.e., the first line, is equivalent to the Schrödinger approach. The electron spin is denoted as σ and we identify three spin dependent terms in the second line. The first spin dependent term represents the interaction of the spin with a magnetic field $\sigma\nabla \times \mathbf{A} = \sigma \cdot \mathbf{B}$. The second spin dependent term is called Darwin term and can be understood as a relativistic energy correction to the electron energy. The last spin dependent term reflects the spin-orbit coupling.

For high photon energies the $\sigma \cdot \mathbf{B}$ term may lead to spin flip transitions. Thus, the initial state spin $\mathbf{s_i}$ is not *a priori* conserved during the excitation process and may thus differ in the final state. However, for the photon energies used for the investigations presented within this thesis, typically several tens eV, spin flip transitions are about two orders of magnitude less probable than spin conserving transitions [11, 10]. For convention, we can therefore assume the optical excitation process as a spin conserving transition and thus $\mathbf{s_i} = \mathbf{s_f}$.

It goes without saying that the spin-orbit interaction may lead to a spin polarization in the initial state. But also electrons from an unpolarized initial state may appear polarized

[2] It is assumed that the vector potential $\mathbf{A}$ is constant within the crystal, because the wavelength of the incoming light is typically much larger than atomic distances inside a solid [9]. However, this is valid only for translational symmetry which is always broken at the surface. In a finite area close to the surface $\mathbf{A}$ changes to the vector potential of the vacuum. Since photoemission is a very surface sensitive technique the change of $\mathbf{A}$ may become important. An example of this will be discussed in Chapter 7.

in the final final state, due to the relativistic selection rules [12]. The initial state spin may couple to wavefunctions of different spatial symmetry. If the incoming photon couples to one of the wavefunctions selectively, then only photoelectrons of a specific spin orientation will get excited. This process, called *optical orientation*, will be discussed again with respect to the circular dichroism in Chapter. 7. Explicitly, the relativistic selection rules are written $\Delta j = 0, \pm 1$ and $\Delta m_j = \pm 1$ with j and m_j referring to the total, spin-orbit coupled momentum [10].

Concerning the final state, one typically assumes that it can be approximated by a free electron state for high enough excitation energies. However, this largely depends on the system under investigation and it will be shown in Chapter 7 for Bi_2Te_3 that this approximation fails for final state energies ten times higher than those considered free electron like for other systems. Furthermore, the reader should note that the photoemission process can explicitly not take place for a free electron. Making use of the relations $[\mathbf{p}, H_0] = -i\hbar\nabla \cdot V(\mathbf{r})$ and $[\mathbf{r}, H_0] = i\hbar\mathbf{p}/m$, whereas $H_0 = \frac{p^2}{2m} + V(\mathbf{r})$ with an arbitrary potential $V(\mathbf{r})$ the matrix elements of Eq. 2.3 with the Hamiltonian H' of Eq. 2.5 and with $\mathbf{A} = const.$ can be written as

$$\langle \Psi_f | \, \mathbf{p} \, | \Psi_i \rangle \propto \langle \Psi_f | \, \mathbf{r} \, | \Psi_i \rangle \propto \langle \Psi_f | \, \nabla \cdot V(\mathbf{r}) \, | \Psi_i \rangle \, . \tag{2.7}$$

Thus, the transition matrix element is zero if $\nabla \cdot V(\mathbf{r}) = 0$, which is the case for a free electron.

2.1.2 Transport to the Surface and Surface Sensitivity

The second stage in the three-step model is the transport of the photoelectron to the crystal surface. From this stage one can intuitively understand that photoemission is a very surface sensitive technique. While the radiation can be assumed to penetrate deep into the bulk without significant reduction of its intensity, the photo-excited electron has a rather high probability to get scattered inelastically. The inelastic scattering is encoded in the secondary electron background which is found to increase drastically at low kinetic energies, as sketched in Fig. 2.1 b). The most important scattering mechanism at commonly used excitation energies is the electron-electron interaction. Electron-phonon interaction becomes important at very low energies only and can be neglected for the moment. Essentially, the inverse inelastic mean free path λ_i^{-1} is determined by the dielectric function $\epsilon(\mathbf{q}, \omega)$, where $\mathbf{q}$ is the momentum and ω the energy transfer of an inelastic scattering event. The dielectric function is material specific and one should thus expect a strong variation of the inelastic mean free path of photoelectrons over various materials. Nevertheless, the dependence of λ_i on the electron energy (final state energy) is, for high enough energies, found to be roughly described through a universal curve given by the empirical formula [13]

$$\lambda_i = 0.41 a^{3/2} \sqrt{E_{kin}}. \tag{2.8}$$

Here, a denotes the lattice constant of the material through which the electrons have to pass and is expressed in nm, whereas the kinetic energy of the electrons is expressed in eV. The reason for this almost universal behavior of λ_i is that for high enough energies ($E_{kin} \gg 10\,\mathrm{eV}$) the electrons in a solid can again be approximated as a free electron gas. For this case the plasma frequency which is a function of only the electron density

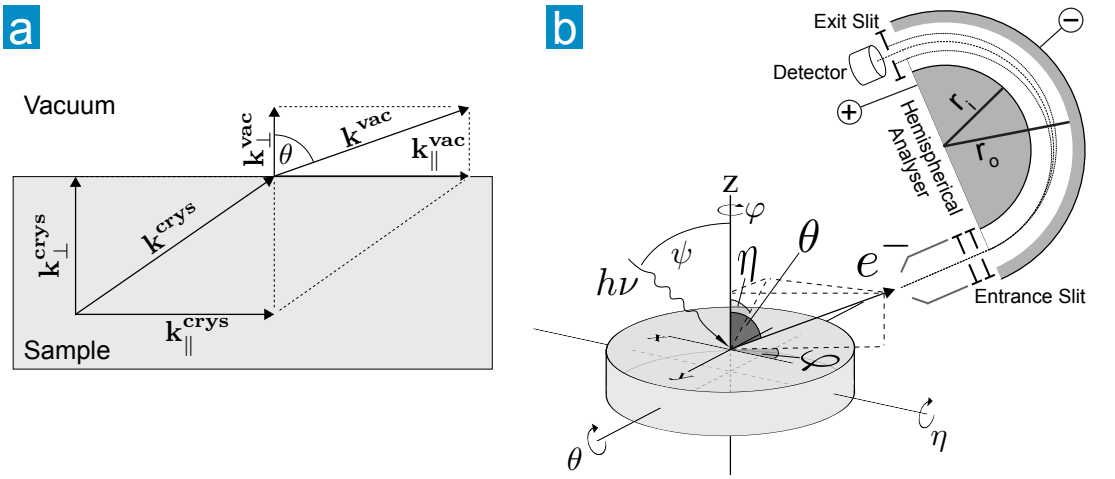

Figure 2.2: Angle resolved photoemission. a) The broken translational symmetry perpendicular to the surface causes a refraction of the electron of momentum $\mathbf{k}^{\mathbf{crys}}$ within the crystal and leads to a difference in the total momentum $\mathbf{k}^{\mathbf{vac}}$ outside of the crystal. The component parallel to the surface is conserved ($\mathbf{k}^{\mathbf{crys}}_{\parallel}$=$\mathbf{k}^{\mathbf{vac}}_{\parallel}$) while the component perpendicular to the surface gets reduced ($\mathbf{k}^{\mathbf{crys}}_{\perp}$>$\mathbf{k}^{\mathbf{vac}}_{\perp}$). b) By varying the emission angles θ, η, and φ and measuring the kinetic energy of the photoelectrons the in plane bandstructure is mapped.

determines the loss function. Hence, the dependence of the inelastic mean free path on the material is reduced as compared to a dependence of the loss function on the dielectric function [9].

The number of photoelectrons $N(d)$ excited at a depth d perpendicular to the surface which contribute to the photoemission signal at the detection angle θ relative to the surface normal depends exponentially on d:

$$N(d) = N_0 \exp -\frac{d}{\lambda \cos\theta}. \tag{2.9}$$

One defines further the escape depth d_e as the layer thickness from which $1/e$ of all detected electrons have been excited:

$$d_e = \lambda \cos\theta. \tag{2.10}$$

Two aspects should be noted: First, by evaluating Eq. 2.10 for θ=0°, i.e., normal emission, and Eq. 2.8 for moderate energies it becomes clear, that the major contribution to the photocurrent corresponds to the first few atomic layers. This holds up to several hundred eV in general and especially for the photon energies used for the investigations presented throughout this thesis (mostly between ∼20 and ∼50 eV). And second, the dependence on the detection angle allows for a depth profiling of the system under investigation. This is, however, only interesting if a substantial depth is reached that covers more than only a few atomic layers like for very high photon energies in the x-ray regime. Since such high energies are not available at the beamlines of BESSY II at which the data for this thesis have been collected (mostly UE112 and U125/2) such methods have not been applied and are mentioned to demonstrate their potential.

The last step in the three-step model is the escape of the photoelectron through the surface barrier. Naturally, only electrons that have a final state energy E_f higher than the

vacuum level, i.e., work function Φ_f can escape the crystal and would thus have the kinetic energy

$$E_{kin} = h\nu - E_B - \Phi_f. \tag{2.11}$$

Hence, to determine the binding energy of an electron the explicit knowledge of the work function of the sample is necessary. However, practically if one deals with a metallic sample only the work function of the spectrometer Φ_s needs to be known: sample and spectrometer are connected to the same potential and thus the chemical potential of sample and detector are equal. As a consequence, the kinetic energy of the photoelectrons that escape the crystal get retarded by the potential difference between the work functions of sample and detector and this retarded energy E'_{kin} is the one which is measured [14]. Explicitly,

$$E_{kin} + \Phi_f = E'_{kin} + \Phi_s \tag{2.12}$$

and the determination of E_B is straightforward if the Fermi edge is determined in experiment, as sketched in Fig. 2.1.

2.1.3 Escape from the Crystal and Angle Resolution

An aspect of particular importance is the refraction of the photoelectrons at the surface. Translational symmetry is given only for the directions parallel to the surface, while it is broken in the direction perpendicular to the surface. In Fig. 2.2 a) an electron with momentum $\mathbf{k^{crys}}$ inside the crystal gets excited by an incoming photon and travels to the surface without being scattered. Since the photon wave vector is negligible at typical energies used in angle resolved photoemission ($< 100\,\mathrm{eV}$) the transition from the initial to the final state is direct, i.e., the electron has practically the same momentum in the final as in the initial state ($\mathbf{k_i} = \mathbf{k_f} \equiv \mathbf{k^{crys}}$). We divide the total momentum up into its components parallel and perpendicular to the surface: $\mathbf{k^{crys}} = \mathbf{k_\parallel^{crys}} + \mathbf{k_\perp^{crys}}$. The surface barrier refracts the passing electron but only the component $\mathbf{k_\perp^{crys}}$ is changed, while the in-plane component is preserved ($\mathbf{k_\parallel^{crys}} = \mathbf{k_\parallel^{vac}}$). Outside the crystal the electron propagates with momentum $\mathbf{k^{vac}}$ in a new direction described by the angle θ relative to the surface normal. Combining the basic energy-momentum relation $E_{kin} = \frac{(\hbar \mathbf{k^{vac}})^2}{2m}$ and simple trigonometry one yields

$$|\mathbf{k_\parallel^{crys}}| = \frac{1}{\hbar}\sqrt{2E_{kin}m} \cdot \sin\theta. \tag{2.13}$$

An experimental setup as sketched in Fig. 2.2 b) allows the angle resolved detection of the emitted electrons of energy E_{kin} and the result translates into the band structure $E(\mathbf{k}_\parallel)$ making use of Eq. 2.13 and Eq. 2.11.

For a two dimensional dispersion such as the one of a surface state, this is already sufficient since $\mathbf{k_\perp^{crys}} \equiv 0$ due to the two dimensional confinement. For a three dimensional state, however, the situation is more complicated. The determination of $\mathbf{k_\perp^{crys}}$ is only approximately possible by making use of the following equation [15]:

$$\mathbf{k_\perp^{crys}} = \sqrt{(\mathbf{k_\perp^{vac}})^2 + \frac{2mV_0}{\hbar^2}}, \tag{2.14}$$

where the inner potential V_0 is an empirically adjustable parameter.

For completeness it should be mentioned that by varying the photon energy $h\nu$ of the excitation source and detecting the photoelectrons at normal emission it is possible to determine the perpendicular component of the wave vector quite easily. This is possible due to the different dispersions of initial and final state bands in $\mathbf{k}_\perp$ and due to energy conservation. Since energy conservation has to be obeyed, by changing $h\nu$ in reasonably small steps one reaches different points of the $\mathbf{k}_\perp$ dispersion. This method requires knowledge of the final state dispersion in order to trace back the dispersion of the initial state. Typically it is assumed to be a free electron parabola or one relies on band structure calculations where available. In turn, this method is applied for the identification of surface and other two dimensional states since they have vanishing $\mathbf{k}_\perp$ dispersion and thus their energetic position in the measured spectrum is not altered by a change of $h\nu$.

2.1.4 Many-Body Aspects

Up to now, the photoemission process has been viewed in a single-particle picture. To introduce many-body aspects we follow the excellent review article by Damascelli, Hussain and Shen [16].

In general, we are dealing with an N-electron system from which a single electron is removed by the excitation process and an $(N-1)$-electron system is left behind. The $(N-1)$ particle system is in an excited state and is about to relax during the photoemission process. To simplify one thus assumes, that the photoelectron is removed from the system instantaneously and does not "feel" the relaxation process of the system left behind. This is called *sudden approximation*. This is again justified for relatively high excitation energies. Under this assumption it is possible to factorize the final state into the wave functions of the photoelectron $\Psi_f^{\mathbf{k}}$ with momentum $\mathbf{k}$ and the one of the $(N-1)$-particle system Φ_f^{N-1} [16]:

$$\Psi_f^N = \mathcal{A} \cdot \Psi_f^{\mathbf{k}} \cdot \Phi_f^{N-1}. \tag{2.15}$$

The antisymmetric operator $\mathcal{A}$ satisfies the Pauli principle for the N-electron final state wave function Ψ_f^N. However, for the $(N-1)$-electron system a manifold of possible excited states Φ_m^{N-1} with energies E_m^{N-1} are possible and the total transition probability is then given by the sum over all possible excited states m. If one assumes that the initial state is given by a single Slater determinant [16] a similar factorization is possible where the state of the electron that is going to be excited, i.e., $\Psi_i^{\mathbf{k}}$ is a one electron-orbital:

$$\Psi_i^N = \mathcal{A} \cdot \Psi_i^{\mathbf{k}} \cdot \Phi_i^{N-1}. \tag{2.16}$$

Now the matrix element of Eq. 2.3 may be rewritten as:

$$\begin{aligned} \left\langle \Psi_f^N \right| H' \left| \Psi_f^N \right\rangle &= \left\langle \Psi_f^{\mathbf{k}} \right| H' \left| \Psi_i^{\mathbf{k}} \right\rangle \left\langle \Phi_m^{N-1} \right| H' \left| \Phi_i^{N-1} \right\rangle \\ &\equiv M_{f,i}^{\mathbf{k}} \cdot c_{m,i} \end{aligned} \tag{2.17}$$

The total photocurrent $I(\mathbf{k}, E_{kin})$ measured at a momentum $\mathbf{k}$, i.e, under the emission angle θ, as a function of E_{kin} is then proportional to

$$\sum_{f,i} \left| M_{f,i}^{\mathbf{k}} \right|^2 \sum_m |c_{m,i}|^2 \, \delta\left(E_{kin} + E_m^{N-1} - E_i^N - h\nu\right), \tag{2.18}$$

If only one final state is possible for the $(N-1)$ particle system then Eq. 2.18 resembles again Eq. 2.3. In general many of the $c_{m,i}$ contribute to the photoemission signal and this will become of particular importance in Chapter 6 where we analyze the lifetime broadening of the surface state in Bi_2X_3. Therein we will show that all kinds of possible final states can be approached by the one-particle spectral function.

We have now already introduced two powerful tools for the investigation of topological surface states. The surface location can be investigated by excluding a dispersion in $\mathbf{k}_\perp$ with photon energy dependent photoemission. In turn, by measuring the dispersion in $\mathbf{k}_\parallel$ (Chapter 4) the metallicity of the surface state can be confirmed by investigation of the dispersion close to the Fermi level. Also the Fermi surface can be mapped with the presented methods: all that one needs is a second rotational degree of freedom besides the angle θ in Fig. 2.2 a). One may either measure the full $E(\theta)$ dispersion at different angles about the surface normal (η) or at different polar angles (φ) as indicated in Fig. 2.2 b). The method allows to count the number of surface states that cross the Fermi level, and as will be discussed in Chapter 3 this number should be odd. However, we are not yet able to exclude a degeneracy of states with different spin. To do so, one has to resolve the spin of the photoelectrons and the method that has been applied in this thesis is based on Mott scattering.

2.1.5 Spin Resolution by Mott Scattering

Instead of a detector that, in principle, simply counts the number of electrons as a function of their emission angle and kinetic energy one may use a detector that is capable to distinguish the spin direction of the photoelectrons in terms of a spin polarization P defined as

$$P = \frac{n\uparrow - n\downarrow}{n\uparrow + n\downarrow}. \tag{2.19}$$

The most widely used detectors[3] in this sense are Mott-type spin detectors which make use of the spin dependent scattering of high energetic ($E_{acc} \geq 20\,\mathrm{keV}$) electrons from targets of high nuclear mass. This type of scattering mechanism was first discussed by N.F. Mott in 1929 [18]. The principle is based on the fact that due to the spin-orbit interaction *fast* electrons have a higher probability to be scattered to the left (right) by the target atoms if they have spin *up* (*down*)[4]. If the electrons are detected under their spin dependent deflection angles, one measures an intensity asymmetry $P_I = \frac{I_A - I_B}{I_A + I_B}$ in the two electron detectors A and B if the incoming electron beam is spin polarized. Ideally, the asymmetry P_I would be equivalent to the polarization P of the incoming beam. However, in reality it is largely reduced by the ability of the detector to distinguish the spin components which is encoded in the so called Sherman function S. If S is known, the spin polarization of the incoming beam is determined by

$$P = \frac{1}{S}\frac{I_A - I_B}{I_A + I_B}. \tag{2.20}$$

The intensity asymmetry is, hence, a measure for the initial state spin, if polarization effects in the final state can be excluded (see Chapter 7 for details). However, an additional

[3] For an introduction to other spin detection methods see for example the review articles by Johnson [10] and Dil [17] and references therein.

[4] Up, down, left, and right are chosen arbitrarily.

asymmetry arises if the two electron detectors have different efficiency which is typically the case. This will be discussed with respect to our spin-resolved measurements in Chapter 4. For magnetic systems, two different counters are already sufficient, since the quantization axis may in principle be aligned to the detection axis, such that the full polarization will show up in these two counters. However, for the investigation of spin-orbit split systems like the Rashba splitting or the topological surface states, the spin quantization axis is not defined in real space but only in k-space and is locked to the momentum of the electrons. In order to investigate the spin structure of such spin-orbit split bands, the detection of more than one spatial component of the spin is necessary [17]. This becomes particularly important if the spin is not anymore fully locked perpendicularly to the momentum and further rotates out of plane as it has been proposed for Bi_2X_3 [19, 20].

2.2 Experimental Setups

In this section a description of the experimental setups that have been used to obtain the data presented in this thesis shall be given. In favor for presenting as much results as possible in the experimental part, this section is kept as short as possible.

2.2.1 The ARPES 1^2 Setup

Depicted in Fig. 2.3 is the BESSYII user endstation ARPES 1^2. Most of the data presented within this thesis has been measured with this machine. It is equipped with a VG Scienta R8000 hemispherical electron analyzer that allows for an ultimate nominal energy resolution below 1 meV at low kinetic energies (<25 eV).

The setup is connected to the PGM2a branch of the UE112 beamline which is an undulator beamline designed for ultimate energy resolution in the VUV-XUV regime (∼20-200 eV). The APPLE II type undulator has a period length of 112 mm and a minimal gap of 22.2 mm. The difference of the APPLE II to a standard planar undulator is that the bottom and top magnet rows are separated horizontally into two parts that can be shifted relative to each other. In addition to linearly polarized light these undulators are capable of producing eliptically and circularly polarized light which has been used to obtain the data presented in Chapter 7. Details on the beamline and the APPLE II undulator can be found on the homepage of the Helmholtz Zentrum Berlin [21], which operates the BESSY II storage ring, and in the references given there.

The ARPES 1^2 setup is devided into two connected ultra high vacuum chambers, whereas the lower analytical chamber can be shut off from the upper preparation chamber by a gate valve, which allows to use preparational methods, such as adatom deposition by evaparation, without affecting the vacuum conditions of the analytical chamber. For this purpose the preparation chamber offers several ports which can be equipped with exchangeable evaporators in a standard setup as shown on the photography of Fig. 2.3. Typical pressures lie between $1{\cdot}10^{-10}$ and $1{\cdot}10^{-11}$ mbar with the gate valve between upper and lower chamber open. During evaporation the pressure is typically in the low 10^{-9} mbar range.

The load lock allows a relatively fast way of exchanging the samples, an important aspect for the Bi_2Se_3 and Bi_2Te_3 systems studied by us. Before the samples are placed into the vacuum system they are cleaved several times with common adhesive tape in air. The idea behind this procedure is that the crystal will tend to cleave first at the plane

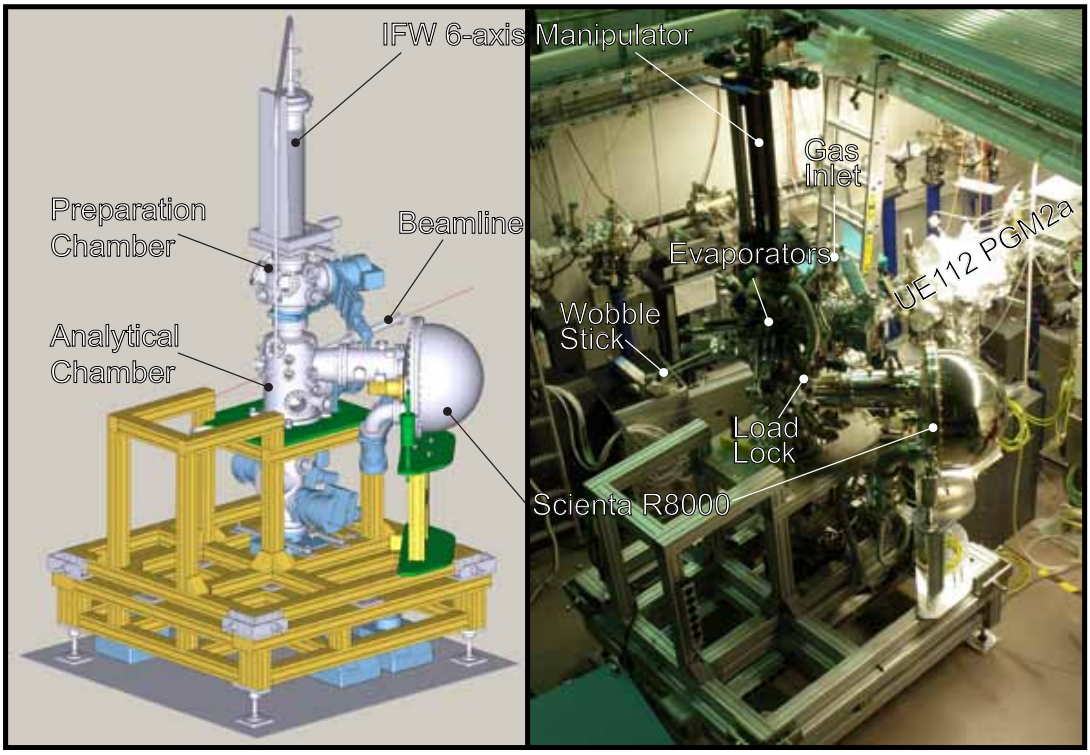

Figure 2.3: The ARPES 1^2 setup used for ultra high resolution angle resolved photoemission measurements. Left: CAD drawing of the chamber with only basic components attached (drawing courtesy of A. Varykhalov). Right: Photography of the chamber in working conditions at the UE112 PGM2a undulator beamline of BESSY II.

with the lowest surface quality and, hence, the surface quality gets iteratively improved over several cleavages. Afterwards copper adhesive tape is attached to the samples which is lifted in ultra high vacuum with the help of a wobble stick. Once the samples are contaminated they cannot be reprepared *in situ* but have to be taken out of the vacuum.

To allow for k-space mapping, the chamber is equipped with a 6-axis manipulator, which offers three translational and three rotational degrees of freedom. The three possible rotation angles (θ, η, φ) are shown in Fig. 2.2 b).

The light incidence ψ is rotated by 45° with respect to the detection plane of the analyzer, which is vertical in this setup. In addition, the incidence is tilted by ∼6° above the horizontal plane.

The entrance slit of the analyzer defines the angle dispersive axis, while its width defines the lateral angular resolution. A slit width of 0.2 μm has been used for most of the data presented within this thesis. The maximal acceptance angle on the angle dispersive axis is ±15° but for most of the measurements presented within this work the acceptance has been set to ±7°. This is enough to detect the topological surface state of Bi_2Se_3 and Bi_2Te_3 at $\pm k_y$ simultaneously for all used photon energies and up the Fermi level where the surface state shows its largest expansion in k-space.

The radius between the inner (r_i) and outer hemisphere (r_o), as sketched in Fig.2.2 b), is given by $r=(r_i+r_o)/2=200$ mm. The potential difference between inner and outer shell

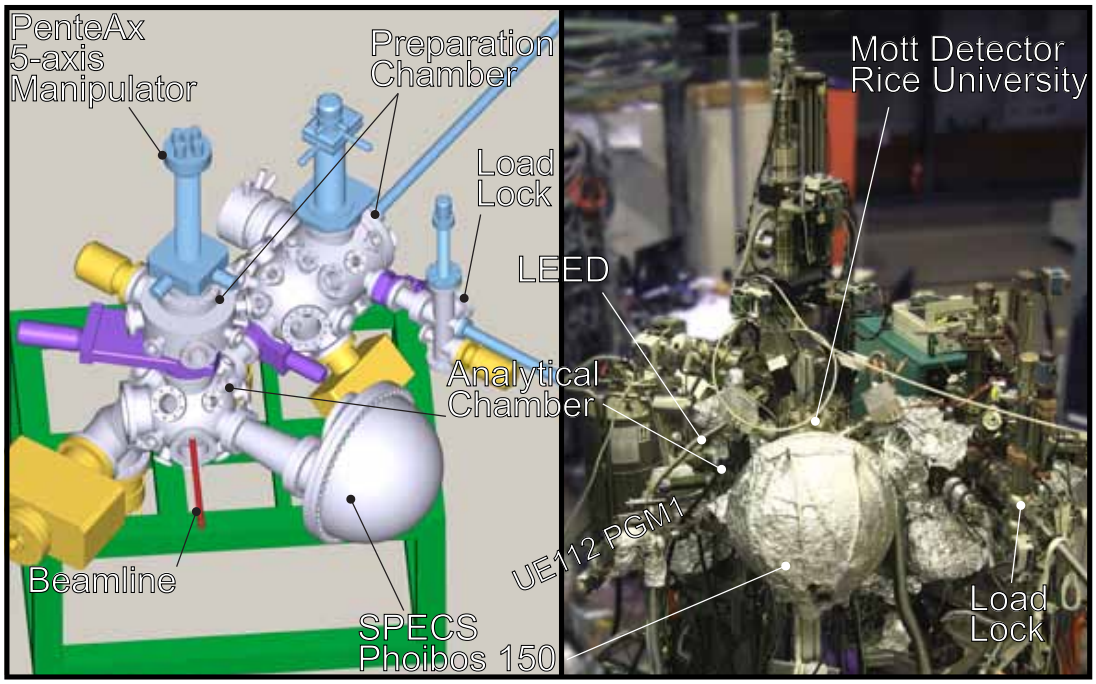

Figure 2.4: The PHOENEXS setup used for spin resolved measurements. Left: CAD drawing of the chamber with only basic components attached (drawing courtesy of A. Varykhalov). Right: Photography of the chamber in working conditions at the UE112 PGM1 undulator beamline of BESSY II.

(U_P) defines the pass energie E_P according to

$$E_P = \frac{eU_P}{r_2/r_1 - r_1/r_2}. \tag{2.21}$$

Electrons get deflected by the electric field between inner and outer hemisphere and only electrons in a finite energy window pass through the analyzer and get mapped on the detector. All data presented in this thesis is measured in a constant analyzer transmission, which means, that electrons get retarded to the pass energy. The retardation voltage is ramped according to the size of the predefined energy step to allow electrons of the predefined kinetic energy window to pass through the analyzer.

The passed electrons are detected by a multi-channel plate which is monitored by a CCD camera. The two dimensional detector image is seen in real time on the computer screen which allows for an easy adjustment of the sample in angle resolved photoemission. The detector system is capable to resolve 1060 energy channels and ∼750 angular channels simultaneously. The energy window covers about 12% of the pass energy and for angle resolved photoemission three different lens modes project ±15°, ±7°, or ±3° on the angular channels. The angular resolution is between 0.1° and 0.4° depending on the spot size of the excitation source.

2.2.2 The PHOENEXS Setup

Fig. 2.4 shows the PHOENEXS[5] setup which is equipped with a SPECS PHOIBOS 150 hemispherical energy analyzer.

The PenteAx 5-axis manipulator has 3 translational degrees of freedom and 2 rotational degrees of freedom, that are, rotation about the surface normal φ and about the manipulator axis η. The precission of rotation is about 0.5° for both directions.

Sample cleavage has been done in the preparation chamber similarly to what has been described above for the ARPES 1^2 setup. In addition, the PHOENEXS chamber offers a second preparation chamber above the analytical chamber.

The geometry of the photoemission setup is such that light incidence and electron detection direction are rotated by 45° to each other. The light incidence is horizontal. The analyzer entrance slit is oriented horizontally, i.e., within the plane of light incidence and normal emission. Dispersions can be measured by several energy distribution curves at different emission angles η.

For *in situ* sample characterization a low energy electron diffraction (LEED) facility is mounted in the analytical chamber. In principle this allows an exact orientation of the samples for angle resolved photoemission, however, this turns out to be complicated for the case of Bi_2Se_3 and Bi_2Te_3 since they show a tendency to surface facetting, meaning that the surface contains areas which are oriented differently with respect to each other, a fact which can be observed directly in LEED. A one to one matching of photoemission and LEED position is therefore hardly achieved. This leads to some uncertainties for the case of spin resolved measurements, presented and discussed in Chapter 4. All chambers are under ultra high vacuum of typically $\sim 10^{-10}$ mbar.

For electron detection, two sets of channeltrons are available. The *front-channeltrons* are optimized for a high transmission of electrons, to allow spin-integrated photoemission with high intensities and good statistics. They consist of 6 separate channeltrons that are added for a higher efficiency.

However, the special feature of this setup is the Rice University type Mott detector [23] which is visible on the photography on the right hand side of Fig. 2.4 and which allows to resolve the two in-plane components of the electron spin on the surface under investigation. After the electrons have passed the analyzer the beam is deflected into the Mott detector where the electrons are accelerated to high kinetic energies by the applied high voltage (between 23 and 26 kV). The electrons get scattered off spin dependently by a thorium target and are detected by two pairs of channeltrons, where the pairs are oriented perpendicular to each other and the two channeltrons of each pair are positioned symmetrically at ±120° with respect to the thorium target.

The energy resolution of the analyzer in a spin resolved measurement is only about 100 meV. Nevertheless, the setup is capable of resolving extremely small energy splittings below 10 meV between states of opposite spin at room temperature since the electrons are detected in separate channeltrons. The spin resolution is not affected by the energy resolution and this is practically used to increase the flux of photoelectrons by opening the exit slit of the beamline, to increase the light intensity which in turn increases the photocurrent.

More critical, especially when it comes to the determination of the absolute initial spin polarization in topological insulators turns out to be the increase of the acceptance angle of the analyzer by opening the built-in aperture. The relatively small diameter of the surface

[5] A more detailed description of the setup is given in Ref [22]

Fermi surface in Bi_2Se_3 and Bi_2Te_3 ($<0.2\text{Å}^{-1}$) may lead to an admixture of the states with opposite spin since the signal is integrated over the full acceptance angle. Assume that the electrons are 100% spin polarized in the initial state and a finite contribution of the other half of the Brillouin zone which is also 100% polarized but in the opposite direction is detected simultaneously. Then the measured spin polarization will appear reduced since the polarization is calculated by the intensity difference in the two separate counters, according to Eq. 2.20.

Another problem arises from the detection of the spin components with individual channeltrons. Since each channeltron shows a different sensitivity there is always an asymmetry in the intensity, even for an unpolarized electron beam. This has to be taken into account in the data procession and will be discussed in Chapter 4.

The use of Th as a target increases the efficiency of the Mott polarimeter in terms of the Sherman function (S) introduced above. In a simplified picture, the Sherman function is proportional to the atomic number Z. Commonly used as a target is Au, and compared to this we can estimate an increase of the Sherman function by about 14% [22]. If operated at a high voltage of 26 kV the Sherman function is about 0.16. The figure of merit of the Mott detector is defined as:

$$FOM = S^2 \cdot \frac{I}{I_0}, \tag{2.22}$$

where I_0 and I are the intensities of the incoming beam and Mott scattered electrons, respectively. This ratio is typically in the range of 5×10^{-3} [23] which gives a FOM of 1.4×10^{-4}.

From the low figure of merit of a *state of the art* Mott detector that is used in this thesis it becomes clear that the increasing demand for spin resolved studies in material research is hard to satisfy. For a spin resolved spectrum of good statistics a measurement time of several hours has to be taken into account. This is acceptable in many cases, but if, for example, the sample surface is very sensitive, or if a detailed knowledge of the spin texture is required, then such a setup reaches its limits quite soon. Thus, there is a high need for more efficient spin detectors or, alternatively, high efficient methods that allow an indirect probe of the spin. One such possibilty will be discussed in Chapter 7 and we will see that one has to be very careful with indirect probes.

Chapter 3

On the Distinction of Topological Phases

As the name topological insulator readily indicates, the key for understanding this new quantum phase of matter lies in a basic understanding of topology and how it applies to solid state physics. Even though the experimental results of this thesis may be understood without a deeper understanding of topology, the idea and motivation behind will stay buried under the unfamiliar language connected to it. Therefore, I will review some prominent effects and their explanation in a historical framework to give a comprehensive introduction into this new and fast growing field. For a more detailed introduction the reader may be referred to reviews by Hasan and Kane [24], Hasan and Moore [25] as well as Qi and Zhang [26].

3.1 The Integer Quantum Hall Effect

Basically, the mathematical discipline of topology deals with properties that are preserved under continuous deformation of objects. Thus, topologically distinct objects cannot be transformed into one another without going through some discontinuity. One has to tear a hole into a sphere in order to get a torus and the topological invariant which accounts for the distinction of the two is the genus which indeed counts the number of holes in their surfaces.

The gate for an application of topology to solid state physics was opened by the discovery of the integer quantum Hall effect by von Klitzing, Dorda, and Pepper in 1980 [27]. They found that in the two-dimensional electron gas of a MOSFET[1] device at low temperatures ($T << 10\,\mathrm{K}$) and in high magnetic fields ($B > 10\,\mathrm{T}$) the Hall conductance (σ_{xy}) is quantized to extremely high accuracy as

$$-\sigma_{xy} = n \cdot \frac{e^2}{h}, \tag{3.1}$$

where n is an integer, e the electron charge, and h is Planck's constant.

With increasing gate voltage the Hall voltage (U_H) is decreasing following a step like curve as can be seen in the original measurement shown in Fig. 3.1 a).

[1] Metal-Oxide-Semiconductor-Field-Effect-Transistor

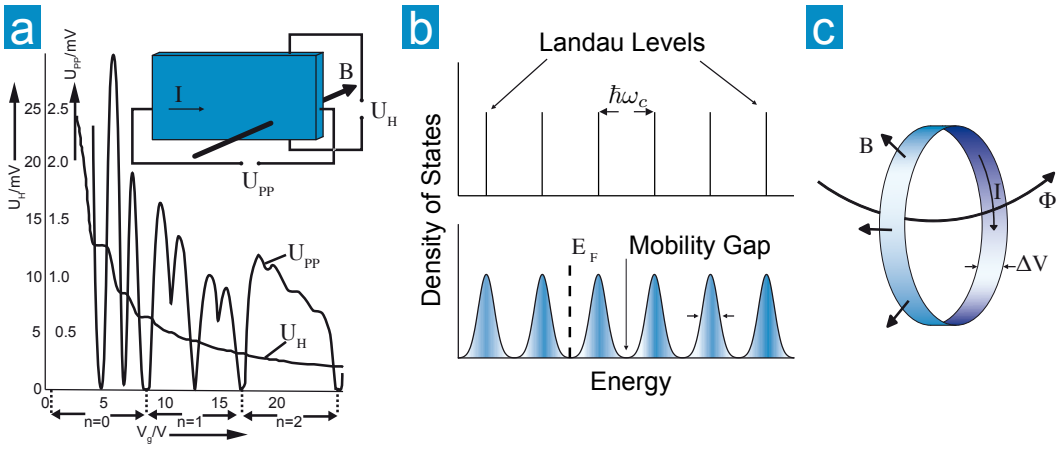

Figure 3.1: Quantum Hall effect. a) Original measurement reproduced from Ref. [27] and schematic of the measurement arrangement *(Copyright (1980) by the American Physical Society).* b) Landau quantization of the density of states (top) and broadening in real systems (bottom). c) Schematic of Laughlin's Gedankenexperiment.

On the one hand this effect can be readily explained with the condensation of electron orbits on Landau levels in a magnetic field [28]. The density of states of a perfect two dimensional system is then represented by a sequence of δ-functions which are energetically separated by $\Delta E = \hbar\omega_c$ (upper panel of Fig. 3.1 b). The cyclotron frequency ω_c is determined by the magnetic field B penetrating perpendicular through the plane of electron motion. Also the degree of degeneracy is determined by the magnitude of the magnetic field. At some critical values of B all states on the highest occupied Landau level are occupied and the Fermi level lies half the way between this level and the lowest unoccupied level. By applying a gate voltage one can move the Fermi energy to match the energy of the highest occupied Landau level, thus increasing the carrier concentration. The latter is quantized with the density of states. The next increase of carrier concentration will only appear as the gate voltage again drives the Fermi level to energetically match a Landau level. The Hall voltage is proportional to the inverse of the carrier concentration ν.

$$U_H = \frac{B}{\nu e} \cdot I \tag{3.2}$$

$$\nu = n \cdot \frac{eB}{h} \tag{3.3}$$

Since the carrier concentration increases stepwise, the Hall voltage decreases in steps.

On the other hand this explanation has two important shortcomings which cannot be explained within the framework described above. First, it was assumed that the system is perfect. In a real system there is always disorder present and the Landau levels get broadened, thus leading to partially filled Landau levels irrespective of the applied magnetic or electric field (lower panel of Fig. 3.1 b). But the quantization of the Hall voltage is observed in real systems and is independent of the sample purity. And second, a fully occupied band does not contribute to any ohmic current since the carriers transported in all directions average to a net conductance of zero.

It was Laughlin who pointed out that the exactness and the insensitivity of the Hall conductance must be due to a fundamental principle [29]. Even though his argumenta-

tion was not based on topological concepts, his famous *gedanken experiment* has inspired research in this field up to today.

Instead of the plane he considered a looped two dimensional metal, subjected by a uniform magnetic field B with the field vector perpendicularly pointing outward everywhere on the surface (Fig. 3.1 c). The interior of the loop is threadened by a fictitious flux Φ which can be varied adiabatically. The electron gas is kept at temperatures where quantum coherence holds and therefore states extending around the whole loop are present and can be described by wave functions [30]. Furthermore, there are Anderson localized states between the extended states. The latter are energetically within a finite width around the Landau levels of the unperturbed system described above. The Fermi energy is pinned to the localized states (mobility gap) and this can be understood as an explanation for the appearance of finite plateaus in the Hall conductance of a real system.

Laughlin related the total current around the loop induced by a change of the flux $\mathrm{d}\Phi$ to the potential drop ΔV between the two edges of the loop. Quantization is achieved by assuming gauge invariance as the fundamental principle behind the quantum Hall effect: According to Bloch's theorem the free energy of the equilibrium state of such a loop is a periodic function of the flux ϕ with a period h/e [31]. In addition to the classical condition that the potential may be altered in a way such that

$$-\nabla \delta U = \frac{\partial \delta \mathbf{A}}{\partial t}, \qquad \nabla \times \delta \mathbf{A} = 0, \tag{3.4}$$

where δU is the change in the electrical and $\delta \mathbf{A}$ in the vector potential, there are further restrictions for a quantum mechanical particle moving in a not simply connected space. Since the vector potentials enter the Schrödinger equation Aharonov and Bohm found that the system is only invariant if

$$\oint_{system} \delta \mathbf{A}(\mathbf{r}) d\mathbf{r} = n \frac{h}{e}, \tag{3.5}$$

where n is an integer [32].

If the flux through Laughlin's loop changes by one flux quantum, then the system is back to its initial state. Apart from trivial changes of the phase of the wave functions there may have been particles transported between the two edges of the loop. The number of electrons transported this way determines the change in the free energy as $\Delta F = neV$. The current through the ring is given by the partial derivative of the free energy with respect to the magnetic flux. Together one can derive the desired relation

$$I = \frac{\partial F}{\partial \Phi} = \frac{\Delta F}{\Delta \Phi} = n \frac{e^2}{h} V \tag{3.6}$$

The result shows that the quantization can be derived from gauge invariance. However, in quantum mechanical systems running a sequel of equivalent flux changes does not imply that the amount of transported charge is always the same [30]. Therefore one would not expect an exact quantization on average.

In addition it is still unclear how the fully occupied Landau levels can give a finite conductance especially since there is a lack of mobile states at the Fermi level. Halperin pointed out that there are quasi one-dimensional edge states that carry a conductance and do not become localized even in the presence of disorder [33].

For the special case of two dimensional electrons moving simultaneously in a magnetic field and in a periodic potential, Thouless, Kohmoto, Nightingale, and den Nijs (TKNN)

obtained topological invariants for the Hall conductance [34] as they calculated it with the Kubo formula [35]. The latter gives the linear response of the system to an applied electric field in standard perturbation theory [31]. They found that the Hall conductivity is then given by

$$\sigma_{xy} = \frac{-2e^2}{2\pi h} \sum_{\epsilon_\alpha < E_F} \int_{BZ} d^2k \left(\left\langle \frac{\partial u}{\partial k_1} \middle| \frac{\partial u}{\partial k_2} \right\rangle - \left\langle \frac{\partial u}{\partial k_2} \middle| \frac{\partial u}{\partial k_1} \right\rangle \right). \tag{3.7}$$

where the sum is over the occupied states with energies ϵ_α and $|u\rangle$ denotes an eigenfunction of the Hamiltonian which satisfies the periodic boundary condition. This way it was shown that the *subbands* of the Landau levels, which are introduced by the periodic potential, carry a current which is an *integer* multiple of e^2/h and not as one might expect a *fraction* of the total Hall conductance of the entire Landau level.

The point that the TKNN integers are a result of the underlying geometrical nature of the problem and therefore the first explicit connection to topology was made by Avron, Seiler, and Simon [36]. With this it became clear that the TKNN integers are equivalent to the first Chern number[2]. In another paper Simon showed that the geometrical phase factor which was discovered by – and therefore named after– Michael Berry (Berry's phase) [37] is closely related to the TKNN integers. One can show that the integrand of Eq. 3.7 fulfills the characteristics of a Berry curvature K in momentum space [38].

The integral of the Berry curvature over the whole Brillouin zone gives the Berry phase. By applying the Gauss-Bonnet-Chern theorem it directly follows that the value of this integral must be an integer. Since the two dimensional Brillouin zone can be viewed as a Torus (T^2) due its periodic boundary conditions this integer is identified as the first Chern number.

That the Hall conductivity reflects a topological invariant readily explains the plateaus in the measurement. A smooth change of any parameter of the Hamiltonian changes the curvature. But the integral of the curvature over the Brillouin zone, which is proportional to the Hall conductivity must be an integer and can therefore not change smoothly. The argumentation implies that the bands are not degenerated in the Brillouin zone which is provided by the assumed periodic potential. If the variation of the parameters is strong, states may become degenerate. For this case the Chern number is no longer well defined since the curvature diverges when the levels cross. A further increase of the perturbation will lift the degeneracy again. The Hall conductivity may have changed now but is again an integer multiple of e^2/h. Nevertheless, it is now assigned to a different topological phase since the Chern number must have changed as well.

There is a general statement, that at the interface between topologically different phases there must be boundary states with reduced dimensionality. This can be understood if one keeps in mind, that in order to change the topological invariant, states have to get degenerated, i.e., the energy gap must close. Consider the interface between a quantum Hall insulator and a trivial insulator. At the interface the Chern invariant changes abruptly. This fact necessitates the existence of gapless boundary states [39] since the gap must be closed to change the Chern number. It follows that these states are extremely robust against disorder and chiral in the sense that they move in one direction only along the edge of the sample [24]. The only way to remove the states is to have both materials in the same topological class. A typical boundary state is destroyed easily by contamination

[2] Topological invariant named after Shiing-Shen Chern. He generalized the Gauss-Bonnet formula, which counts the number of handles of a geometric object, to be applied to the geometry of eigenstates [30].

of the sample's boundary. This is indeed one way to identify trivial surface states in photoelectron spectroscopy, for example by a controlled oxygen deposition. Topologically protected surface states can neither get destroyed nor localized by disorder. This will be the main subject of Chapter 5.

That the Hall conductance is related to such edge states was already suggested by Halperin [33] but they have not been discussed in the framework of topology. Hatsugai was able to find the missing link in 1993 [40, 41] by pointing out that the Hall conductance of the edge states equals that of the bulk. Interestingly, the value of the Chern number and therefore the multiple of the Hall conductance equals the number of robust edge states. Each edge state contributes one *conductance quantum* to the total Hall conductance. Nevertheless, it should be noted that the Chern number is a characteristic of the bulk and the quantum Hall effect can therefore not be simply understood as an edge effect.

The integer quantum Hall effect is observed only in the presence of a strong magnetic field ($B \simeq 10T$). Therefore, *time reversal symmetry* is broken. In the absence of any magnetic field or any other time reversal symmetry breaking perturbation the total Chern number is trivial and equals zero, which implies of course a zero Hall conductivity. But in recent years several theoretical approaches have shown that a trivial Chern number is not tantamount to a trivial topology. Moreover, new topological invariants have been identified in two [42, 43, 44, 45] and three dimensions [46, 47]. This has led to the prediction of new, nontrivial phases which have subsequently been experimentally observed [48, 1].

3.2 Quantum Spin Hall Effect and Topological Insulators

Typically, these new phases are characterized as two or three dimensional band insulators which exhibit one or two dimensional *gapless* boundary states, respectively. But they are clearly distinct from the quantum Hall phase since time reversal symmetry is obeyed. Conservation of time reversal symmetry is the precondition for observing these phases.

3.2.1 Two Dimensional Systems

In two dimensions the quantum spin Hall effect was first proposed by Kane and Mele [43] taking the two dimensional carbon allotrope graphene as a model system. A sufficient spin-orbit interaction provided, they predicted a sizable spin-orbit gap in the two dimensional bulk at the two distinct time reversal invariant points K and K' [49]. In contrast to a gap due to the breaking of the AB-symmetry of graphene's sub-lattices, the spin-orbit gaps would have *opposite signs (sic)* for opposite spin $\sigma_z = \pm 1$ at K and K' [43]. An applied electric field would induce a current where spin *up* and spin *down* electrons counter-propagate along the edges (Fig. 3.2 a). Thus, the net charge current would be $\mathbf{J_c} = 0$ whereas the spin current would be given by $\mathbf{J_s} = (\hbar/(2e))\,(\mathbf{J}_\uparrow - \mathbf{J}_\downarrow)$. In absence of σ_z-non-conserving terms, the current would be characterized by a *quantized* spin Hall conductivity $\sigma^s_{xy} = e/(2\pi)$. However, in real systems such terms are always present and therefore the spin Hall conductivity is not expected to be quantized in general like the Hall conductivity in the quantum Hall effect is; the quantum spin Hall effect cannot be characterized by the spin Hall conductivity [50].

One can regard the quantum spin Hall effect as two copies of a quantum Hall effect for the two spin directions, where the spin-orbit interaction acts like a magnetic field penetrating the surface of the sample perpendicularly with the field vector pointing up

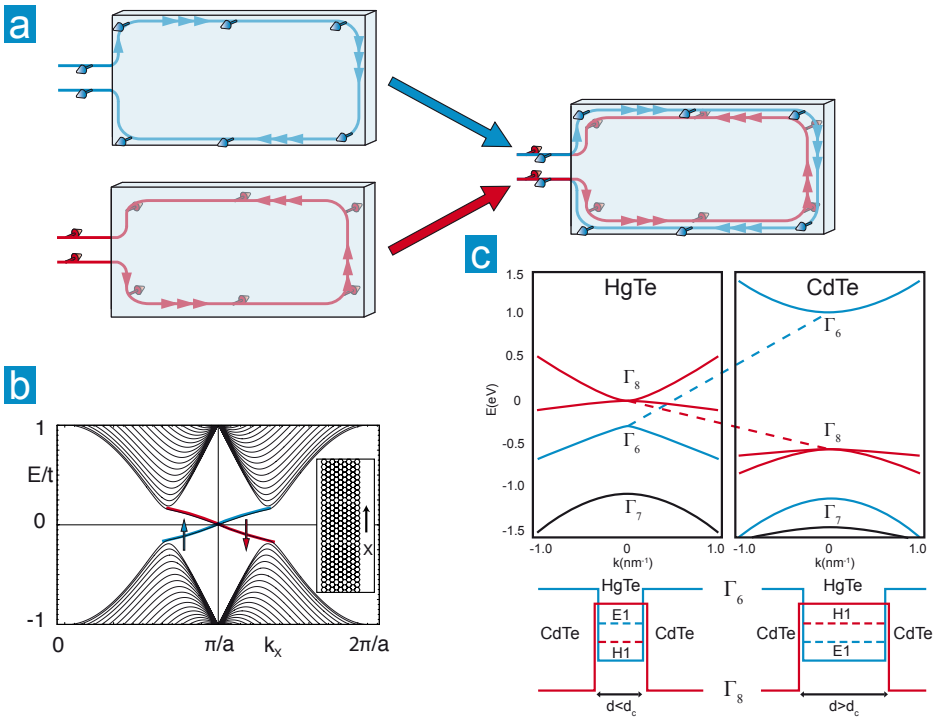

Figure 3.2: a) A quantum spin Hall system (right) can be thought as two copies of a quantum Hall system (left) where the magnetic field points out of (top) or into (bottom) the surface plane. Spin orbit coupling takes the role of the magnetic field in the quantum spin Hall effect. b) Original proposal of the quantum spin Hall phase in graphene (reprinted from Ref. [43]; *Copyright (2005) by the American Physical Society*). A finite spin orbit gap in the two dimensional electronic structure should lead to the formation of one dimensional spin polarized edge states in the considered stripe geometry (inset). c) Band structure of HgTe (left) and CdTe (right). If both systems get arranged in a heterostructure such that HgTe is sandwiched by CdTe then above a critical thickness d_c of the HgTe layer a band crossing of the Γ_6 and Γ_8 bands occurs leading to the quantum spin Hall phase (reprinted from Ref. [44]; *Copyright (2006) by the American Association for the Advancement of Science*).

for the one and down for the other copy (Fig. 3.2 a). From this consideration, one can intuitively understand that the spin current is carried by edge states, since an integer quantum Hall phase has always edge states as described in the previous section. Indeed, the tight binding model calculated for a strip geometry of graphene (inset of Fig. 3.2 b) by Kane and Mele [43] reveals a single pair of gapless and spin filtered edge states which form a Kramer's doublet. These states obey time reversal symmetry

$$E(k,\uparrow) = E(-k,\downarrow), \tag{3.8}$$

and are thus protected from elastic backscattering. Moreover, the degeneracy of the Kramer's doublet cannot be lifted by perturbations that do not break time reversal symmetry. It follows, that the edge states of the quantum spin Hall effect are robust and therefore distinct from usual boundary states. A common surface state of for example the Shockley type is easily localized by disorder.

In a subsequent paper Kane and Mele characterized the quantum spin Hall insulator with a newly introduced topological invariant ν, named $\mathbb{Z}_2$ invariant [42]. For a trivial

insulator the $\mathbb{Z}_2$ invariant takes an even value, for the quantum spin Hall insulator it is odd. In contrast to the quantum Hall effect, where every Chern number characterizes a different phase, all odd and all even $\mathbb{Z}_2$ numbers are in the same phase. Thus, ν being either 0 (even) or 1 (odd), two elements are enough to characterize the distinction and from this the name $\mathbb{Z}_2$ is derived.

There have been different approaches formulated to determine the $\mathbb{Z}_2$ invariant [42, 51, 45, 46, 52, 50]. Also, a very general description by a topological field theory for time reversal invariant insulators was given [53] which takes into account many-body interactions for which the $\mathbb{Z}_2$ invariant is not well defined. Nevertheless, the most commonly used approach is based on single particle Bloch wavefunctions $|u_{k,n}\rangle$ of the occupied states that are non-degenerate in the Brillouin zone except for special points $\mathbf{k_i}$ (in momentum- or k-space) where a double degeneracy may occur due to time reversal symmetry. The invariant ν is then determined over the zeros of a *Pfaffian*[3] (Pf[...]) as [42]

$$(-1)^{\nu} = \prod_{i=1}^{4} \delta_i, \tag{3.9}$$

where the factors δ_i are given by

$$\delta_i = \frac{\sqrt{\det[w(\mathbf{k_i})]}}{\mathrm{Pf}[w(\mathbf{k_i})]} = \pm 1. \tag{3.10}$$

The elements of the unitary matrix $w(\mathbf{k_i})$ are given by

$$w_{mn}(\mathbf{k}) = \langle u_{-\mathbf{k},m}| \, \Theta \, |u_{\mathbf{k},n}\rangle \,, \tag{3.11}$$

where the operator of time reversal is denoted with Θ and m, n are the indices of the occupied bands. In general the formalism implies the knowledge of the phase of the wavefunctions in the whole Brillouin zone. But in inversion symmetric systems the determination of the δ_i is greatly simplified to a product over the parity eigenvalues ξ_{2m} of the $2m$th occupied energy band at the four time reversal and parity invariant momenta Γ_i, which share the same eigenvalue $\xi_{2m} = \xi_{2m-1}$ with its Kramers degenerate partner $2m-1$ [52]:

$$\delta_i = \prod_{m=1}^{N_i} \xi_{2m}(\Gamma_i). \tag{3.12}$$

The product runs over all occupied bands N_i, where the index i accounts for a difference in the number of occupied bands at the indivdual Γ_i. The invariant ν is determined according to Eq. 3.9.

Carbon's low spin-orbit interaction requires very low temperatures to cause a finite band gap and the quantum spin Hall insulating state in graphene is experimentally inaccessible. Bernevig, Hughes, and Zhang have suggested CdTe/HgTe quantum wells as a system which undergoes the topological quantum phase transition above a critical thickness of the HgTe layer sandwiched between CdTe layers [44]. In resistivity measurements König *et al.* were able to show that above the critical thickness of 6.3 nm the system is indeed in the quantum spin Hall state [48]. The band structure then shows the predicted band inversion of s and p

[3] For any $2n \times 2n$ skew-symmetric matrix A the determinant may be written as the square of a polynomial of the matrix entries: $\mathrm{Pf}(A)^2 = \det(A)$. Source: http://en.wikipedia.org/wiki/Pfaffian

derived bands which occurs due to the strong spin-orbit coupling in this system (Fig. 3.2 c). Even though the method applied in Ref. [44] for identifying the quantum spin Hall state in HgTe quantum wells was a different one and furthermore, HgTe is of zincblende structure and therefore not inversion symmetric, one can apply the method of Fu and Kane [52] just by assuming a model Hamiltonian for HgTe which is inversion symmetric. The $\mathbb{Z}_2$ invariant is then found to be odd, which can be viewed as a proof of concept. The full power of this approach is revealed in three dimensional systems for which other methods to determine the topological class of the systems are even more tedious than in two dimensions.

3.2.2 Three Dimensional Systems

In three dimensions the $\mathbb{Z}_2$ characterization has to be extended to four invariants $(\nu_0; \nu_1\nu_2\nu_3)$ [46]. If, and only if ν_0 is odd the system is a *strong* topological insulator whereas ν_{1-3} characterize a *weak* topological insulator. Only the strong phase is robust: the gapless surface states in the weak phase get localized by weak disorder similar to an ordinary insulator.

To determine ν_0 the formulas given for inversion symmetric and asymmetric systems in two dimensions have to be modified only slightly. The product of equation (3.9) is now over the occupied Kramers pairs at the eight time reversal and parity invariant momenta (Γ_{1-8}) of the three dimensional Brillouin zone:

$$(-1)^{\nu_0} = \prod_{i=1}^{8} \delta_i. \tag{3.13}$$

Again, if the system is inversion symmetric, the problem is reduced to the determination of the parity eigenvalue of the occupied bands at these eight points. The δ_i are also called parity invariants [54]. They are indeed a topological invariant as well, but lose their meaning in the absence of inversion symmetry whereas the ν_i hold independently of inversion symmetry. With this method it was possible to predict the first three dimensional topological insulator to be observed experimentally: the alloy $Bi_{1-x}Sb_x$ [52, 1, 55]. Interestingly, the realization of a three dimensional topological insulator in an alloying compound readily approves the robustness of the topological phase since an alloy typically involves a non negligible amount of disorder. Another interesting aspect of $Bi_{1-x}Sb_x$ is that the phase transition can be tuned by the amount of Sb substituting Bi in the compound. Therefore, the phase transition can be examined not only theoretically like in the stoichiometric compounds Bi_2Se_3 and Bi_2Te_3, which are the subject of the experimental part of this thesis, but in principle also in experiment.

3.2.3 The First Realization: $Bi_{1-x}Sb_x$

Bi and Sb are both group-V semimetals and crystalize in the rhombohedral $A7$ structure where two layers are paired to bilayers (Fig. 3.3 a). Within a bilayer the trivalent atoms form strong covalent bonds to the three nearest neighbors. The inter-bilayer coupling is of a weak *van der Waals*-type. Both systems exhibit a finite direct bulk energy gap in the whole Brillouin zone (Fig. 3.3 b) but an indirect negative gap due an overlap of bands that are separated in k-space [56]. By calculating the product of Eq. 3.13, Bi is characterized to be in the $\mathbb{Z}_2$ class (0;000) and Sb in the $\mathbb{Z}_2$ class (1;111) [52]. Even though this means that the $\mathbb{Z}_2$ class of Sb is nontrivial, it is not a topological insulator: since the band gap is indirect it is semimetallic. The difference between Bi and Sb is found in the parity invariant

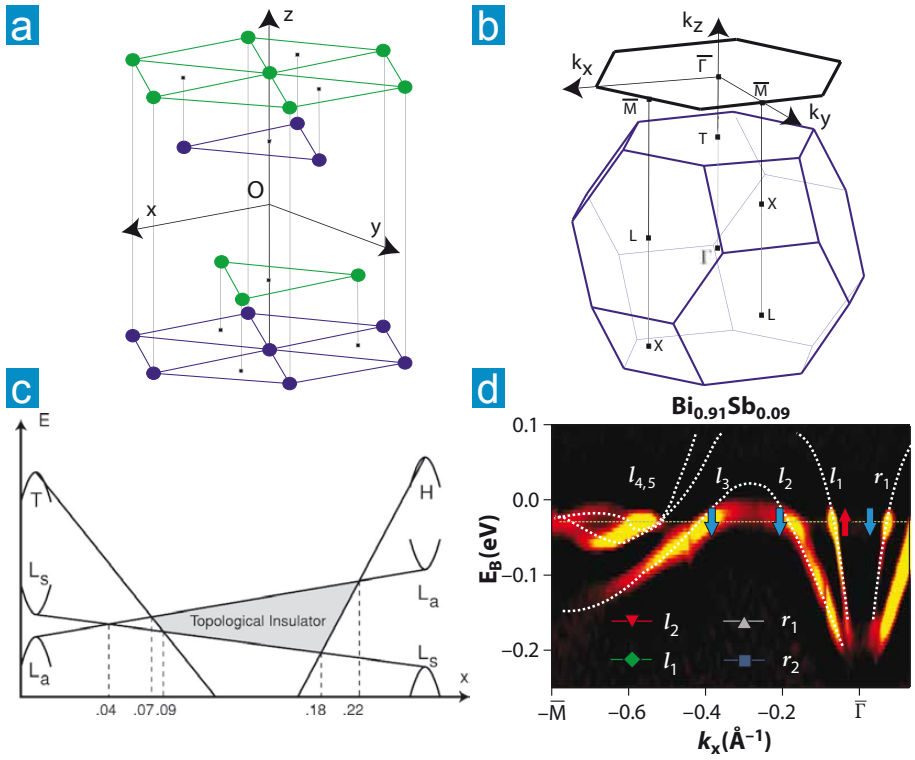

Figure 3.3: $Bi_{1-x}Sb_x$ a) Rhombohedral crystal structure and b) bulk and hexagonal surface Brillouin zone (reprinted from Ref. [54]; *Copyright (2008) by the American Physical Society*). Schematic of the band inversion as a function of Sb concentration x (reprinted from Ref. [52]; *Copyright (2007) by the American Physical Society*). Left hand side reflects the energetic order of the bands L_a, L_s and T in pure Bi, whereas the right hand side corresponds to pure Sb. The band inversion occurs at x=0.04 but the indirect bulk gap becomes positive between x=0.07 and x=0.09. d) Angle resolved photoemission result for x=0.09 (reprinted from Ref. [55]; *Copyright (2009) by the American Association for the Advancement of Science*). Arrows indicate the different spin polarization for the individual bands. White dashed lines correspond to band structure calculations.

at the three L-points of the Brillouin zone which give $\delta(L) = +1(-1)$ for Bi (Sb). The evolution of the band structure of Bi with an increasing amount of Sb substitution was already sketched in 1996 by Lenoir and co workers [57] and is adapted in Fig. 3.3 c). On the left hand side, the energetic order of the pure Bi bands of interest in valence (L_a) and conduction band (L_s) at the L point are sketched. Of further interest is the band labeled with T which, together with L_s, defines an indirect negative band gap between the T and L point of the three dimensional Brillouin zone. The right edge shows the same but for pure Sb, where L_s and L_a are inverted compared to pure Bi thus reflecting the different parity invariant. If Sb is added into the Bi matrix, the L_s conduction band of Bi is lowered whereas the L_a valence band is elevated until they resemble the situation in pure Sb, when all Bi is substituted with Sb. In between, the direct gap at the L point is closed at a relative Sb concentration of $x = 0.04$. At this band touching point the $\mathbb{Z}_2$ invariant ν_0 changes its value from even (0) to odd (1). With increasing x, the direct gap at L reopens with *inverted order* of L_s and L_a, but the system is not yet in an insulating state, since the indirect band gap between L and T is still negative. At $x = 0.07$ the indirect gap changes

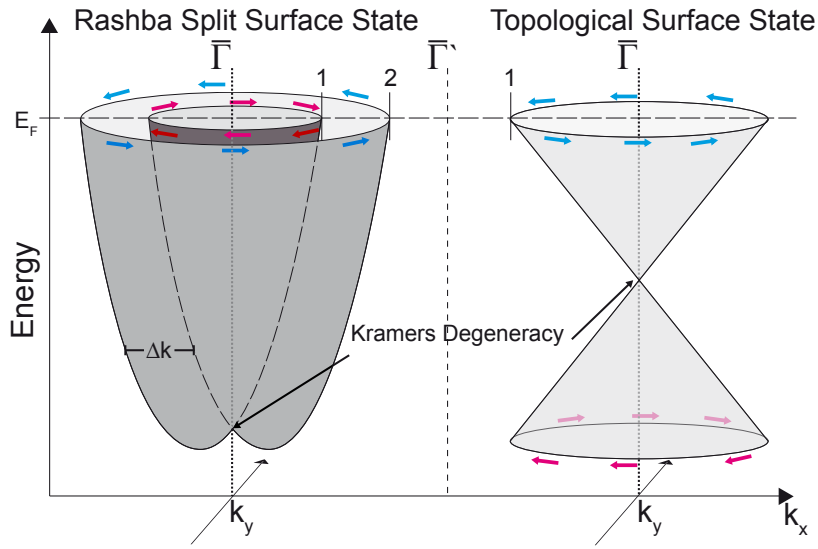

Figure 3.4: Schematics of a) a Rashba split and b) an ideal topological surface state (Dirac cone). In the Rashba case, there are two (an even number of) crossings with the Fermi level E_F between the time reversal symmetric momenta $\overline{\Gamma}$and $\overline{\Gamma}$‘, while in the case of a topological insulator there is only one (an odd number of) intersection(s).

its sign when the T band crosses the bottom of the L_a conduction band. The alloy is now a semiconductor with an indirect band gap unless x exceeds 0.09. At this concentration the T band energetically crosses the L_s valence band and the energy gap becomes a direct gap at L. The evolution from a semimetal to a direct band insulator is reversed at $x = 0.18$ where the gap becomes indirect again as the H band is lifted above the L_s band and finally becomes an indirect semimetal again when the maximum energy of the H band crosses the minimum energy of the L_a band at $x = 0.22$. Please note that at the crossings of the T and H bands with the L_a or L_s bands the $\mathbb{Z}_2$ invariant is not allowed to change its value since the bands are well separated from each other in k-space and the phase transition requires a band touching [58].

The surface state spectrum of $Bi_{1-x}Sb_x$ in the topological insulator phase is the most interesting part, since the interesting physics is placed at the surface. As theory predicts, the topological surface state must obey time reversal symmetry from which the two most important features can be derived: protection of the *gapless* surface states against perturbation that do *not* break time reversal symmetry and spin polarization of the surface state which is distinct from any other known spin polarized surface state. To justify this claim the topological surface state spectrum is compared to topologically trivial surface states which obtain a Rashba-type spin-orbit splitting due to the broken inversion symmetry at the surface. The splitting in the Rashba effect is proportional to the component of an external or intrinsic electric field perpendicular to the surface under investigation E_z [59]. Assuming a parabolic dispersion of the surface state like the surface state of the Au(111) surface [60, 61, 62] the splitting along an arbitrary direction k_x of the surface Brillouin zone

is characterized by

$$E_{\uparrow,\downarrow}(k_x) = \frac{\hbar k_x^2}{2m^*} \pm \alpha_R k_x, \tag{3.14}$$

$$\alpha_R \propto \langle E_z \rangle \,, \tag{3.15}$$

where α_R is the Rashba parameter, and m^* denotes the effective mass. A sketch of the effect is given on the left of Fig. 3.4 together with a sketch of an ideal topological surface state (right). Both show a crossing at the time reversal symmetric momentum Γ and the Fermi surface is circular with the spin locked perpendicular to the momentum. The obvious difference is that in the Rashba case there are two circles or two intersections of surface states with the Fermi level along a given direction of the two dimensional Brillouin zone, whereas in the case of the topological insulator there is only one. This difference has some important consequences.

First, if the system is two dimensional, meaning one dimensional topologically protected edge states instead of two dimensional surface states, backscattering is in general forbidden for the two dimensional topological insulator (or quantum spin Hall insulator) whereas the Rashba effect only suppresses *elastic* backscattering: a spin up electron cannot be scattered into a spin down state without flipping the spin[4]. In a three dimensional topological insulator with a circular Fermi surface only a scattering process with the angle π is forbidden whereas scattering in other angles is allowed but the probability is reduced as a function of the scattering angle.

Second, the fact that there is only one intersection of the surface state spectrum with the Fermi level in the nontrivial system implies that there is no smooth transition to a gapless state at the boundary. The surface states traverse the gap all the way from the bulk valence to the bulk conduction band. Thus, an absolute gap into which the Fermi level could be moved by doping or applying a gate voltage does not exist. In addition, time reversal symmetry guarantees that the boundary states remain gapless even in the presence of disorder or impurities. The contrary applies for example to the trivial surface state of Au(111) which lies in the so called L-gap and exhibit a Rashba type spin splitting [60, 61, 62]. There, it is possible to push the Fermi level below the band minimum of the surface state. All branches connect to the bulk conduction band and none to the valence band.

The protection of the topological surface states goes even beyond the absence of backscattering or the guaranty of being gapless. Topology dictates the existence of gapless boundary states whenever the $\mathbb{Z}_2$ invariant changes at an interface between two materials. Since the invariant is an integer there is no continuous way to change it. At the interface a phase transition takes place. Therefore, the band gap has to close at the interface what is provided by the boundary states. Thus, the only way to remove the boundary states is to have both systems building up the interface in the same $\mathbb{Z}_2$ class. In contrast, the trivial boundary states at an interface with another trivial system, most likely vacuum, can simply be removed by a small amount of disorder or impurities.

One can summarize the characteristics given above to the theorem that an odd number of surface states crossing the Fermi level between two time reversal symmetric momenta

[4] A spin flip may occur by scattering on a magnetic impurity *via* exchange interaction. Spin orbit interaction is also able to rotate the spin in a scattering process. But the probability for a clockwise and a counterclockwise rotation of the spin are equal and this leads to destructive interference of the electron wavefunctions. The phase difference between clockwise and counterclockwise rotation is 2π and thus the spin 1/2 particle wavefunctions are related as $\Psi_{\circlearrowleft} = -\Psi_{\circlearrowright}$ [26].

is *the* hallmark of a three dimensional topological insulator. Thus, angle resolved photoemission is perfectly suited for the identification of topological insulators. But since degenerated states cannot be distinguished, spin resolution is crucial to unambiguously identify a topological insulator.

As can be seen in Fig. 3.3 d) the surface state spectrum of $Bi_{0.9}Sb_{0.1}$ below E_F measured with angle resolved photoemission does not consist of a single surface state crossing but five [1] between the two time reversal invariant momenta of the two dimensional surface Brillouin zone $\overline{\Gamma}$ and $\overline{M}$. With the help of spin resolved photoemission Hsieh and co-workers were able to suggest which of the five states connects the valence and the conduction band [55], thus establishing the $\mathbb{Z}_2$ topological order in this material. However, due to the very low intensity of the bands labeled with 4 and 5 they were unable to conduct a successful spin resolved measurement close to the L point. In principle, the fifth branch could be doubly degenerated which would alter the number of crossings from odd to even and the $\mathbb{Z}_2$ invariant would equal zero. For a higher Sb concentration of $x = 0.12 - 0.13$ in a very detailed spin resolved study Nishide *et al.* where able to remove last doubts [63].

Today's research is focused on the so called second generation of topological insulators, the ternary compounds Bi_2X_3 where X=Te, Se. Over $Bi_{1-x}Sb_x$ these systems have the advantages of being stoichiometric, exhibiting a much larger bulk band gap, and they have a much simpler surface state structure with only one Dirac cone at the center of the surface Brillouin zone $\overline{\Gamma}$. Details for these systems will be given in the next chapter.

Their simple surface band structure make these systems ideal candidates to investigate a manifold of interesting proposals on the physics of topological insulators in general. These proposals reach from applied topics like the exploration of the electron spin for future electronic devices (*spintronics*) over unusual superconductivity and quantum computation to such exotic topics as Majorana fermions. To discuss all these effects is far beyond the scope of this thesis. The reader may thus be referred again to the reviews mentioned in the beginning of this chapter, which give at least an excellent starting point. Where appropriate, I will discuss interesting effects and proposals in the prefaces of the individual experimental chapters.

Chapter 4

Second Generation Topological Insulators: Bi_2X_3

Soon after the discovery of the three dimensional topological insulator phase in $Bi_{1-x}Sb_x$ the focus of research has moved over to the so called second generation of topological insulators: Bi_2Te_3, Bi_2Se_3 and also Sb_2Te_3 [64]. These systems share some peculiar advantages over $Bi_{1-x}Sb_x$: First, being stoichiometric compounds which have been studied extensively due to their thermoelectric properties [65, 66, 67], high quality single crystalline samples are available and easy to produce [68]. Moreover, the amount of disorder is reduced compared to the alloy compound $Bi_{1-x}Sb_x$. Second, the layered crystal structure allows for an easy *in situ* preparation of clean surfaces by cleavage through common adhesive tape; an advantage far from negligible for surface sensitive techniques such as angle resolved photoemission. Third, and most importantly, these systems exhibit a single Dirac cone-like surface state at the Fermi level which is centered at the high symmetry point $\overline{\Gamma}$ of the surface Brillouin zone. Due to their extraordinary simplicity these systems have been named the *hydrogen atom* of topological insulators [3].

4.1 Basic Properties of Bi_2X_3

While the surface electronic structure is rather simple in Bi_2Se_3 and Bi_2Te_3 as shall be seen later on in this chapter, the bulk electronic structure as well as the crystal structure carry some peculiarities and complexity which shall be discussed in the following as a starting point

4.1.1 Crystal Growth and Structure

As mentioned before Bi_2Se_3 and Bi_2Te_3 are well established materials. Their thermoelectric properties have been studied for years and can be tailored through alloying [69] or the fabrication of nanostructures [70, 71, 72, 73] with reduced dimensions or heterostructures [74]. But the lack of theoretical concepts and understanding has kept their topological properties secret until recently [64, 2, 3]. Nonetheless, today's research on the topological properties benefits from the progress in fabrication of high quality samples.

Large single crystals of Bi_2X_3 can be grown by the Bridgman method which is the method of choice for the samples used for the investigations presented within this thesis.

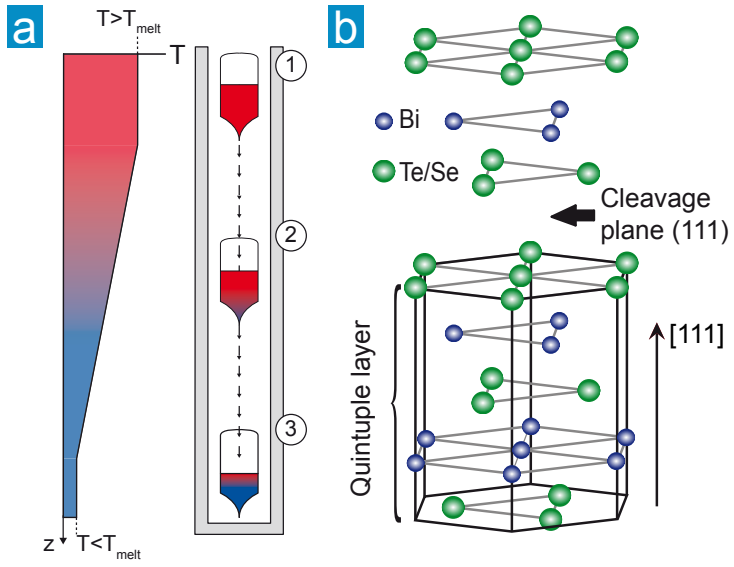

Figure 4.1: Crystal growth. a) Cartoon of the Bridgman method. 1) The ampoule is placed at a position where the temperature is constant and above the melting temperature (T_{melt}) of the high purity elements. 2) The ampoule is driven through a linear temperature gradient at a constant speed. In the tip of the ampoule solidification starts at temperatures below T_{melt}. 3) At the end the ampoule is kept at a constant temperature well below T_{melt} before it is cooled down slowly. The resulting crystal structure is sketched in b).

Since the growth was carried out by our collaborators from the Moscow State University only a short description of the method will be given in the following. Fig. 4.1 a) shows a drawing of the Bridgman setup. High purity (6N) powders of Bi and Te/Se are placed inside a sealed and evacuated ampoule. For Bi_2Te_3 the source materials are excessed with Te to avoid the trend of intrinsic p-doping. The shape of the ampoule is decisive for the growth of single crystalline samples as it exhibits a diminuition on its lower end. The driving force of the condensation is given by a nearly linear temperature gradient of 10 K/cm along the ampoule. First, the ampoule is driven at a speed of ∼5 mm/h up to the starting position where it is kept for about 0.5-2 h while it gets stirred periodically. Afterwards the ampoule is driven at a speed of ∼0.5 mm/h through the gradient from the hot (top) region to the cold (bottom) region. As it passes into the cold region the solidification begins. Outside the gradient region the ampoule is kept at a constant temperature well below the melting temperature. From this procedure large single crystalline ingots of a length of approximately 10 cm and a diameter of 2-3 cm have been obtained. From the ingot, samples of about 1 cm length, 0.5−1 cm widths and with a thickness of 0.1−0.3 mm are cut, as exemplified by a Bi_2Te_3 sample in Fig. 4.2 a).

The excellent crystal quality, as shown in Fig. 4.2, has been confirmed by transmission electron microscopy (TEM) (b,c), low energy electron diffraction (LEED, with the surface Brillouin zone overlaid) (d), as well as scanning tunneling microscopy (STM) at room temperature (e,f). The lattice spacing obtained from TEM is in rough agreement with the values from Ref [75] given in Tab. 4.1.

As already pointed out, the crystal structure allows for an easy cleavage for surface preparation. This can be understood from the crystal structure sketched in Fig. 4.1 b).

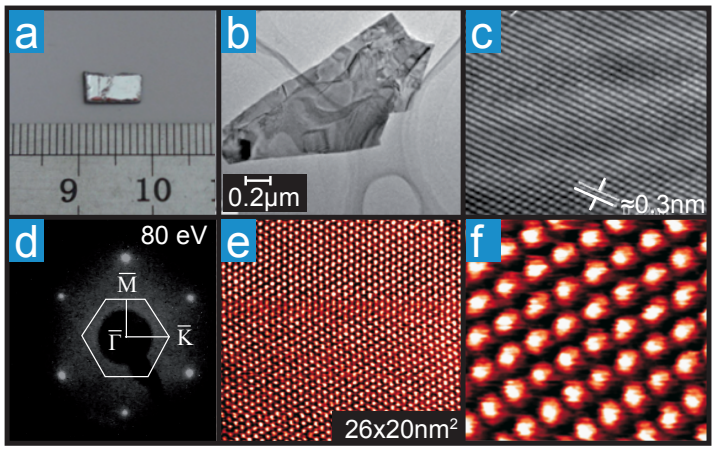

Figure 4.2: Characteristation of Bi_2Te_3 samples. a) Picture of a typical sample cut from the as grown ingot. b) Transmission electron microscopy of a sample before cleavage on a large scale and c) with high resolution. The lattice spacing is ∼0.22 nm. d) Low energy electron diffraction pattern measured with 80 eV. Overlaid is the surface Brillouin zone with the high symmetry directions $\overline{\Gamma M}$ and $\overline{\Gamma K}$. e) Scanning tunneling microscopy at room temperature and f) a zoom in. All characterization methods demonstrate the excellent crystal quality.

Both compounds crystallize in a rhombohedral structure with space group D^5_{3d} ($R\bar{3}m$). Along the [111] direction we find a sequence of atomic layers with only one species per layer. Each of this layers forms a triangle lattice with three possible positions A, B and C [76]. Along the [111] direction the layers stack in the sequence A-B-C-B-A—A. Five of these layers form a so called quintuple layer and the atomic elements alternate like X(1)-Bi-X(2)-Bi-X(1)—X(1). The total crystal is then build of stacked quintuple layers which are bound by relatively weak van der Waals forces between two layers of X(1) atoms. This weakness allows for the easy cleavage and the (111) cleavage plane is always terminated by X(1) atoms as indicated in Fig. 4.1 c). Within a quintuple layer bonds are covalent. The X(2) atoms have a distorted octahedral coordination with three Bi atoms from the layer above and three Bi atoms from the layer below as nearest neighbors. A similar coordination exists for the two equivalent Bi layers but the six nearest neighbors are three X(1) and three X(2) atoms. The bonding length between two X(1) layers is larger as compared to the covalent bonds such that the coordination lacks a clear symmetry for the X(1) atoms (Tab. 4.1). This crystal structure exhibits three discrete symmetries: A threefold

X	X(1)-X(1)	X(1)-Bi	Bi-X(2)	X(2)-Bi	Bi-X(1)	X(1)-X(1)
Te	3.72	3.04	3.24	3.24	3.04	3.72
Se	3.30	2.99	3.06	3.06	2.99	3.30

Table 4.1: Bonding lengths between different neighbors in Bi_2X_3 given in Å [75].

rotation about the z-axis, a twofold rotation about the x-axis and inversion symmetry with the X(2) atom as a center of inversion. The latter allows the application of the method introduced by Fu and Kane to determine the $\mathbb{Z}_2$ invariant [52, 64] like it has been described

in Chapter 3.2.1.

4.1.2 Electronic Structure

As pointed out in Chapter 3 the $\mathbb{Z}_2$ number is a characteristic of the bulk electronic structure. Even though an experimental proof of the topological insulator phase always has to probe its peculiar surface state structure, a reliable prediction for a specific compound always has to be based on the bulk electronic structure. For Bi_2X_3 and Sb_2Te_3 a very instructive theoretical investigation was given by Zhang *et al.* [64] and more detailed by Liu *et al.* [76]. The authors have at first compared the bulk electronic structure of Bi_2Se_3 without and with spin-orbit coupling. Despite some shifting of occupied and unoccupied bands they found at the Γ-Point a band gap opening together with an inversion of the band mass of the occupied band closest to the Fermi level.

Regarding the bond formation from atomic orbitals in Bi_2Se_3 this inversion can be understood even though the picture is simplified. One can divide the formation into four independent steps [76]. Taking the strong covalent bond within the quintuple layers into account it is reasonable to focus on the bonds between Bi and Se atoms and all atoms in the crystal matrix exhibit at least three such bonds.

The electron configurations are $6s^2p^3$ and $4s^2p^4$ for Bi and Se, respectively, and expecting the bonds to be build from p orbitals is reasonable since they are the outmost ones. In total there are 15 orbitals per unit cell since the five atoms in the unit cell contribute with three (p_x, p_y, p_z) orbitals each. In the first step the coupling between Bi and Se atoms leads to a level repulsion and hybridization into new orbitals which are elevated in energy for Bi and lowered in Se, accordingly. On the Se side there are two energy levels, where the one closer to the Fermi level has six degenerated orbitals. The three other orbitals can be neglected since they are split off in energy and do not contribute to first approximation. On the Bi side there is one energy level which also contains six orbitals. Due to inversion symmetry, the second step divides the hybridized states in bonding and anti-bonding states with a defined parity, either odd or even. Orbitals with odd parity gain energy while the ones with even parity get reduced in energy on both, Bi and Se sites. In Bi, orbitals with an even parity are now closest to the Fermi level while in Se odd parity is found near E_F, and these are thus considered only. Crystal field splitting lifts the degeneracy between p_z and $p_{x,y}$ such that the p_z orbital in Bi is reduced in energy while it is lifted in Se. The unequality of the p_z and $p_{x,y}$ orbitals is a direct consequence of the layered structure described above[1]. If the $\mathbb{Z}_2$ value was evaluated now, according to the method described in Ref. [52], it would be trivial. The $\mathbb{Z}_2$ number changes to be odd if the spin-orbit coupling is taken into account.

A level crossing between the Se and Bi derived p_z orbitals occurs and conduction and valence band change their roles compared to the system without or reduced spin-orbit coupling [64]. Since the two bands involved in the crossing have opposite parity the parity eigenvalue, defined in Chapter 3 changes from "−" to "+" at and only at the time reversal invariant point Γ of the three dimensional Brillouin zone (Fig. 4.4 b). It is now straightforward from the considerations of Chapter 3 to conclude that the $\mathbb{Z}_2$ number also changes from "0" to "1". Similar results can be obtained for Bi_2Te_3 and Sb_2Te_3.

The strength of the spin-orbit coupling is determined by the atomic number Z of the involved nuclei, which is $Z = 83$ for Bi, $Z = 52$ for Te, $Z = 51$ for Sb and $Z = 34$ for

[1] The coordinate system is chosen such that the z direction is along the [111] direction and the x and y direction lie inside the layers.

Se. Consequently, Sb_2Se_3 is found to be a trivial band insulator as the spin-orbit coupling strength is not strong enough to change the orbital order. On the other hand, a high Z-value does of course not guarantee the topological insulator phase to be realized, as can be seen in the example of Bi. Even though it has one of the highest Z-values of the stable elements, it has a trivial $\mathbb{Z}_2$ value[54]. In contrast, Sb carries a nontrivial $\mathbb{Z}_2$ number despite the reduced atomic number as compared to Bi [54]. However, both materials are semi metallic in the pristine crystal and only the alloy of the two materials shows the topological insulator phase as described in Chapter 3.2.3. It is the interplay of different degrees of freedom that controls the topological phase transition and consequently systems like $NaCoO_2$ where spin-orbit coupling is not expected to be extraordinarily strong are proposed to exhibit a nontrivial topology [77].

Bi_2Se_3

This interplay of different degrees of freedom is also reflected in the distribution of the resulting sizes of the bulk band gaps over the different compounds. While in Bi_2Te_3 one may expect the strongest spin-orbit interaction, due to the heaviest elements, the size of the gap is with $\sim 150\,\mathrm{meV}$ significantly smaller than in Sb_2Te_3 ($\sim 200\,\mathrm{meV}$) and Bi_2Se_3 ($\sim 200 - 300\,\mathrm{meV}$)(see references in [67] and [64]). Band structure calculations without considering the spin-orbit interaction result in a direct band gap at the Γ-point for Bi_2Te_3 [78] while the band gap is indirect if spin-orbit interaction is taken into account (see Fig. 4.4 a), reproduced from Ref. [79]). The same behavior has been found in calculations for Bi_2Se_3 [64] as shown in Fig. 4.3 a) and b) (reproduced from Ref. [79]). The band gap is indirect as soon as spin-orbit effects are introduced. Clearly visible is the band inversion as explained above. At the Γ point of the bulk Brillouin zone (see also Fig. 4.4 b) two parabolic bands with opposite effective masses are visible if the spin-orbit interaction is neglected (Fig. 4.3 b) and the transition from the valence band maximum to the conduction band minimum is direct. In contrast, the inverted band structure (Fig. 4.3 b) has a local minimum in the highest occupied band at Γ which is surrounded by local maxima in the different directions of k-space. The valence band maximum is now found between F and Z while the conduction band minimum is still at Γ, thus giving an indirect band gap. While the band inversion takes place at the Γ-point only, bands are influenced by the spin-orbit interaction everywhere in the Brillouin zone and this qualitatively explains why the position of lowest energy separation between valence and conduction band shifts in k-space and also why the size of the gap is not simply defined by the *strength* of spin-orbit coupling.

The results from first principle calculations can be compared to angle resolved photoemission results conducted with $h\nu$ =50 eV undulator radiation as excitation source (Fig. 4.3). The sample is oriented with the $\overline{\Gamma\mathrm{K}}$-direction along the angle dispersive direction of the analyzer. We find overall qualitative agreement in shape and energy position of the bands. Most of the discrepancies which are found can be traced back to the limitation of angle resolved photoemission that it probes the occupied bulk energy bands only at one specific k_z-point which is determined by the excitation energy. Throughout this thesis we are mainly interested in the surface electronic structure. Thus, methods to determine the full band structure have not been carried out.

The most obvious difference between calculations and measurement is the state close to the Fermi level. Clearly, a "V"-shaped band is crossing the Fermi level while the calculations predict the Fermi energy in a bulk energy gap. To emphasize this discrepancy,

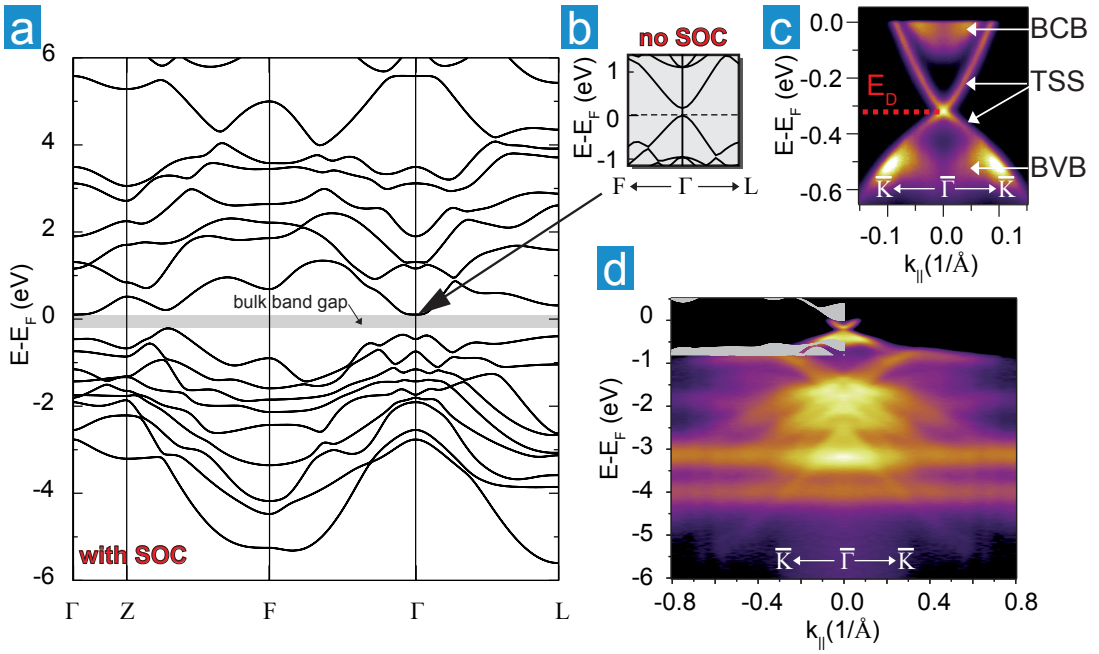

Figure 4.3: Bulk and surface electronic structure of Bi_2Se_3. First principles calculations with (a) and without (b) spin-orbit interaction effects (dobted from Ref. [79]). The gray shaded area has been added to mark the bulk energy gap. c) In gap surface state (TSS) together with bulk valence (BVB) and bulk conduction band (BCB) along the $\overline{\Gamma K}$-direction. The Dirac point is nicely visible and its energy position (E_D) is marked with a red dashed line. d) Angle resolved overview of the valence band along the $\overline{\Gamma K}$-direction. The superimposed semitransparent area corresponds to the bulk electronic structure projected on the (111) plane (calculation adopted from Ref. [80]).

a projection of a calculated bulk electronic structure on the (111) plane (semi-transparent area in the left half of Fig. 4.3 d), adopted from Ref. [80]) is overlaid with the angle resolved photoemission spectrum, measured by us. The state appears to be within the bulk energy gap, a typical characteristic of surface states. Indeed, it has been shown that this state exhibits no significant k_z-dispersion by exciting electrons with different photon energies [3] (see also Chapter 2), as it is expected for a two dimensional surface state.

A closer view on the surface state structure is shown in Fig. 4.3 c), where the photon energy is set to 18 eV and the sample temperature is T ~10 K. The dispersion of the surface state is close in shape to an ideal Dirac cone of linearly dispersing or massless Dirac fermions. At the Dirac point, however, the surface state deviates from the light-like dispersion and gains an effective mass. This fact is widely ignored in the literature, but by definition the band effective mass is proportional to the second derivative of E after k ($m^* \propto \nabla_k^2 E$), which is nonzero whenever the dispersion is not linear. Strictly, it is thus not correct to speak about Dirac fermions for the surface state of Bi_2Se_3 (and also Bi_2Te_3), since a Dirac fermion is massless by definition. Nevertheless, the surface states of topological insulators are typically addressed with this nomenclature in the community and for simplicity it will be used in this thesis, as well.

The energy of the Dirac point (E_D) is marked with a red dashed line and is found 320 meV below the Fermi energy. In addition to the surface state two pronounced features are visible below the Dirac point (labeled with BVB) and between the surface state branches

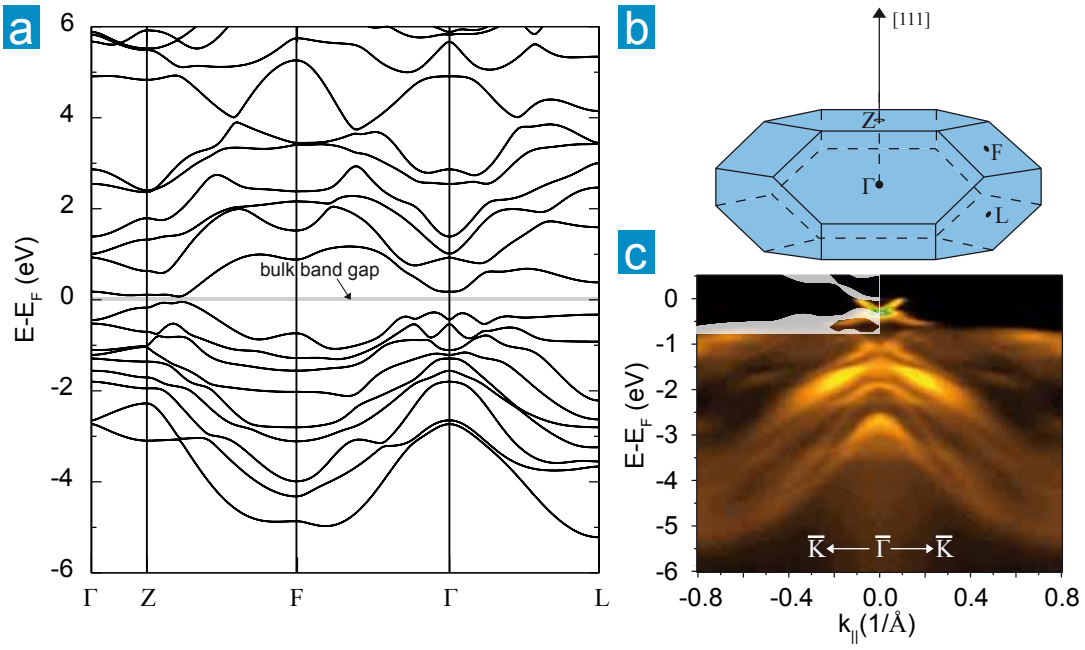

Figure 4.4: Bulk electronic structure of Bi_2Te_3. a) First principles calculations including spin-orbit interaction effects (adopted from Ref. [79]) The gray shaded area has been added to mark the bulk energy gap. b) Brillouin zone of the rhombohedral crystal structure. The [111]-direction is perpendicular to the plane of cleavage. c) Angle resolved photoemission spectrum of the valence band measured with a photon energy of 55 eV along the $\overline{\Gamma K}$ direction.

(BCB) at the Fermi level. BCB is not seen in the valence band overview of Fig. 4.3 d) which hints at its bulk origin: The state disperses in the k_z-direction which excludes a surface localization in agreement with Ref. [3]. In the same way, the second, M-shaped feature can be identified as a bulk valence band state. Its ostentatious dispersion can also be identified from the bulk band structure calculations. While the necessary condition for a topological surface state, an odd number of surface state crossings through the Fermi level, seems to be fulfilled the bulk electronic structure resembles a metal, and hence Bi_2Se_3 cannot be called a topological insulator. The bulk metallicity is caused by a stochastic electron doping which is caused by Se atoms which occupy Bi sites in the crystal matrix. Control over this intrinsic doping can be achieved by varying the initial Se weight during the crystal growth or by doping the crystals with Ca in the bulk [81]. This shortcoming appears to be technically vincible and speaking about an insulating phase is therefore well justified with respect to the relatively large band gap which allows for room temperature applications once the Fermi level is set into the gap.

Bi_2Te_3

Figure 4.4 c) shows results from angle resolved photoemission on Bi_2Te_3 over a wide energy- and $k_{||}$-range where electrons have been excited with 55 eV photons. The crystal is oriented with the $\overline{\Gamma K}$ direction of the surface Brillouin zone along the angle dispersive direction of the electron analyzer (details are described in Chapter 2). The temperature has been set

to $T = 50\,\mathrm{K}$. If we check the measured band structure against the band structure obtained from *ab initio*-calculations [79] (Fig. 4.4 a) we find overall a nice qualitative agreement in shape and position of the bands taking into account the insufficiencies of photoemission described above. An in-gap surface state is also present in Bi_2Te_3 with a pronounced degeneracy point at $\overline{\Gamma}$ and ∼310 meV below the Fermi level. That this state is indeed surface localized has been shown by Chen *et al.* in 2009 [2] using photon energy dependent angle resolved photoemission to exclude a k_z-dispersion. Even though our measurements do not show the full first Brillouin zone, the necessary condition for a topological surface state seems to be fulfilled, as there is only one state crossing the Fermi level between the two time reversal invariant points of the surface Brillouin zone $\overline{\Gamma}$ and $\overline{\mathrm{M}}$ as can be seen in Fig. 4.5 a) where a zoom-in into the region of the surface state dispersion is shown along both high symmetry directions ($\overline{\Gamma\mathrm{K}}$ and $\overline{\Gamma\mathrm{M}}$) measured with 21 eV photons. The equivalent condition, that the Fermi arc encloses only one (or an odd number of) time reversal symmetric momenta is nicely proven by the constant energy surface at 0 eV shown in Fig. 4.5 b).

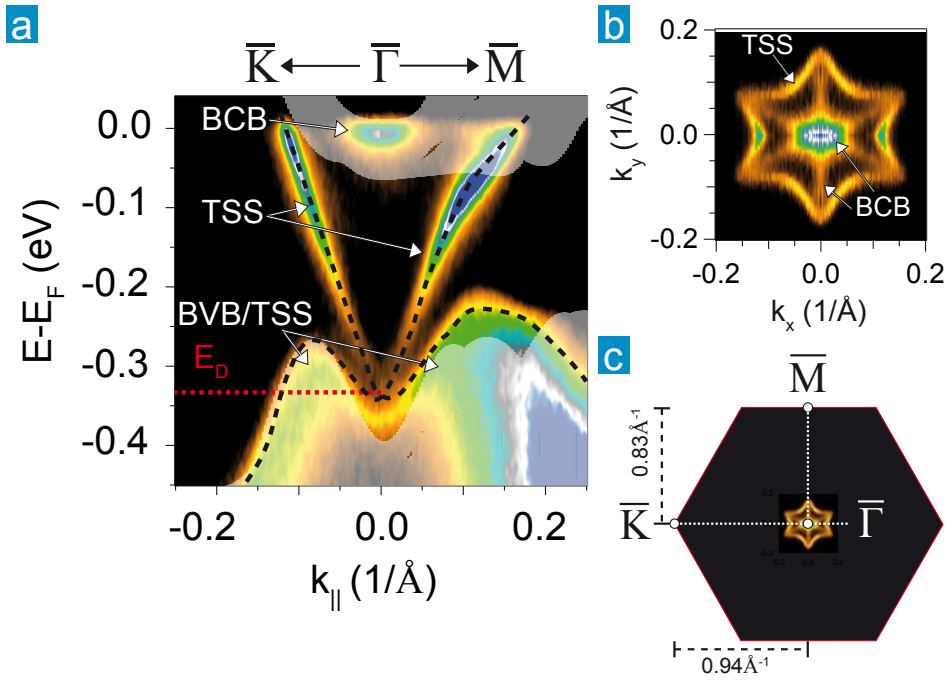

Figure 4.5: Bulk and surface electronic structure of the (111) plane. a) In-gap surface state (TSS) as well as bulk valence (BVB) and conduction band (BCB) along both high symmetry directions $\overline{\Gamma\mathrm{K}}$ and $\overline{\Gamma\mathrm{M}}$. The energy of the Dirac point (E_D) is marked with a red dashed line. The semi-transparent shaded area corresponds to the projected bulk electronic structure calculated in Ref. [80]. Black dashed lines are a guide to the eye to follow the surface state dispersion. b) Surface (TSS) and bulk Fermi surface (BCB). c) Hexagonal surface Brillouin zone of the (111)-plane and Fermi surface. The topological surface state crosses the Fermi level only once between two time reversal invariant momenta $\overline{\Gamma}$ and $\overline{\mathrm{M}}$ [2]. Both, bulk and surface state show a six-fold symmetry. The surface state experiences strong hexagonal warping while it approaches the bulk conduction band [19].

The topological surface state (TSS), however, deviates strongly from the ideal shape of a Dirac cone. Along the $\overline{\Gamma K}$-direction it disperses highly linearly down to the Dirac-point (E_D). Along $\overline{\Gamma M}$ the surface state is linear only in the vicinity of the Dirac-point. Around 150 meV above E_D the group velocity is reduced and the dispersion not anymore linear. This leads to a deformed surface Fermi-surface which exhibits concave parts around the $\overline{\Gamma K}$-direction and a convex shape in the vicinity of the $\overline{\Gamma M}$-direction. Overall, the surface Fermi surface resembles a snowflake-like shape with the three-fold symmetry of the crystal structure around the [111]-direction.

These, so called *hexagonal warping effects* have been explained as the rhombohedral counterpart of cubic Dresselhaus spin-orbit coupling [19] and are currently under strong investigation due to their implications on the spin texture of the surface state (see below). Even though the $k \cdot p$ Hamiltonian given by Fu was able to reproduce the right shape of the constant energy surfaces of the topological surface state [19], it failed with the correct dispersions. While the dispersion along $\overline{\Gamma M}$ comes out linear, the group velocity appeares *increased* along $\overline{\Gamma K}$, which is clearly not the case as can be seen in Fig. 4.5 a) and was first observed in Ref. [2]. On the basis of *ab initio* calculations Zhang *et al.* proposed the dispersion of the surface state more accurately along the high symmetry directions of the surface Brillouin zone [64]. The size of the bulk band gap is, however, underestimated; a typical shortcoming of *first principles* calculations.

Like for Bi_2Se_3 we find a difference between the calculated and measured position of the Fermi level. While the bulk band structure in calculations exhibits a clear absolute band gap, thus no bulk states at the Fermi level, photoemission reveals states enclosed in k-space by the Fermi surface of the topological surface states. These states exhibit a pronounced k_z-dispersion [2] and are therefore assigned to bulk states (see Chapter 2 for details). Since these states lie above and furthermore cross the Fermi level[2], Bi_2Te_3 is also not in an insulating state. However, we can apply the same argumentation as presented above for Bi_2Se_3 and thus Bi_2Te_3 can in principle be assumed to be in or easily converted to an insulating regime.

The extraordinary shape of the surface Fermi surface was proposed to have implications on important properties like the spin orientation and the scattering rates which are intimately connected to each other. For the spin orientation there are mainly two effects: the out of plane rotation of the spin [19] and the fact that the in plane component is not perpendicular to the momentum like it should be for an ideal Dirac cone [20]. These deviations follow the symmetry of the crystal structure discussed above. Mirror symmetry dictates the spin to be fully in plane in the $\overline{\Gamma M}$-direction independently of the warping. When cycling around the Fermi surface the z-component of the spin rotates alternately into the surface or out of the surface having its maxima along the six $\overline{\Gamma K}$-directions of the surface Brillouin-zone. The in plane component is always tangential on the curvature of the surface Fermi surface[20]. Thus, it is still always perpendicular to the momentum along the paths connecting the high symmetry points $\overline{\Gamma}$ with $\overline{K}$, or $\overline{\Gamma}$ with $\overline{M}$ and 180° backscattering is still strongly suppressed. Please note, that in order to backscatter an electron propagating along the $\overline{\Gamma K}$ direction, the spin polarization vector has to be fully reversed since the out of plane component is threefold symmetric and thus points in the opposite direction on the reversed side. The same holds away from the high symmetry directions

[2]Please note that the Fermi level defines the zero of energy and the occupied states have positive binding energies. Thus, the occupied states are *above the Fermi level*. In most of the angle resolved photoemission intensity plots of this thesis, the binding energy increases from top to bottom and one may intuitively think that *above the Fermi level* is devoted to unoccupied states, which is misleading

and thus 180° backscattering is still strongly suppressed. This is easy to understand if one keeps in mind that the warping does not violate time reversal symmetry.

Nevertheless, the warping is influencing the scattering away from the 180° backscattering angle [82, 83]. Since a non-magnetic impurity does not allow a spin flip, the probability ($\Psi(\mathbf{k},\mathbf{q})$) for elastic scattering is proportional to a spin dependent matrix element [84]:

$$\Psi(\mathbf{k},\mathbf{q}) \propto T(\mathbf{q},\mathbf{k}) = |\langle \mathbf{S}(\mathbf{k})|\, \mathbf{S}(\mathbf{k}+\mathbf{q})\rangle|^2 . \tag{4.1}$$

Here $\mathbf{k}$ is the electron momentum, $\mathbf{q}$ is an arbitrary scattering vector and $\mathbf{S}$ contains the spin orientation. Thus the probability is proportional to the spin overlap of initial ($\mathbf{k}$) and final state ($\mathbf{k}+\mathbf{q}$) and the matrix element equals zero if the spins are antiparallel. A more detailed discussion of the spin dependent scattering will be given with respect to our own experimental results in Chapter 6. For completeness it shall be mentioned that similar, but much weaker warping effects have also been reported for Bi_2Se_3 [85].

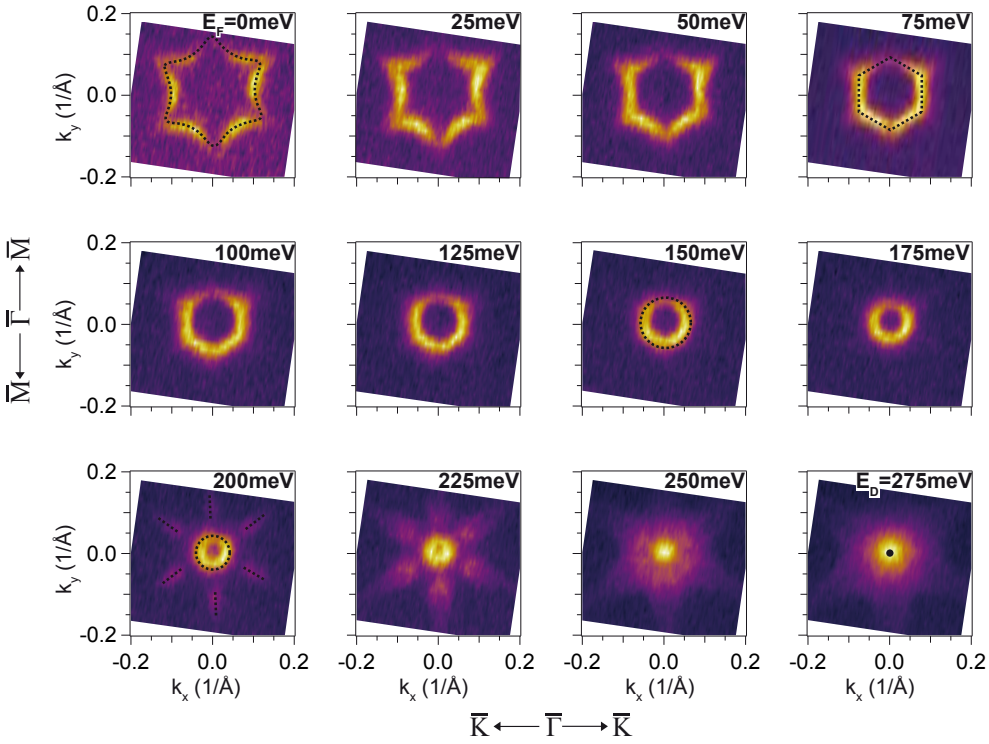

Figure 4.6: Constant energy cuts from the topological surface state of Bi_2Te_3 measured at 55 eV photon energy at 50 K. The shape of the constant energy surface alters from being snowflake-like (0-50 meV) over a hexagon (75-125 meV) and an ideal circle (150-250 meV) to merge into the Dirac point at 275 meV binding energy. Black dotted lines emphasize the actual shape.

In Figure 4.6 we present several constant energy cuts from the Fermi level to the Dirac point in 25 meV steps measured with 55 eV photons at a sample temperature of 50K. The evolution from the snowflake-like shape of the surface Fermi surface to the Dirac point can be followed and goes through three different shapes, which are retraced with black dotted lines in the cuts at 0, 75, 150, 200, and 275 meV. For the cuts at 0, 25 and 50 meV binding

energy we observe a snowflake before it smoothly deforms into a hexagon between 50 and 100 meV. Between 125 and 150 meV the shape becomes more and more circular and stays like this up to the Dirac point. While at the Dirac point the constant energy surface really appears as a point in Bi_2Se_3 [85] we again find a threefold symmetric pattern in the case of Bi_2Te_3. This is explained by the appearance of the bulk valence band, i.e. the topological surface state which disperses to lower binding energy after the Dirac crossing point and thus follows the behavior of the valence band (compare Fig. 4.5 a) and Fig. 4.4 a)+c)). They first appear along the $\overline{\Gamma M}$-direction between 175 and 200 meV binding energy making the constant energy surface look like a sun. Between 225 and 250 meV the valence band maxima along the $\overline{\Gamma K}$-direction become visible and the constant energy surface becomes star-like.

The Dirac point of the topological surface state is thus buried in a valley formed by itself and the valence band and the so called topological transport regime [81], where the bulk density of states vanishes and the Dirac-point is at the Fermi level can not be accessed without tayloring the dispersion. A way out of this inaccessibility will be presented in Chapter 5.1.1. It shall be noted that the bulk conduction band states seen in the constant energy cuts of Fig. 4.5 are not visible here because of the different k_z values that we probe at different photon energies. The difference in E_D is not caused by the change in photon energy since surface states have a vanishing k_z-dispersion due to their two-dimensionality. The reason is instead that the intrinsic doping varies from sample to sample since it is caused by defects hence following a stochastic behavior.

Band Inversion

According to band structure calculations the spin-orbit interaction causes a band inversion between the bonding and antibonding states of Bi and Se. This inversion is the key to the nontrivial topology. Hence we can draw a similar picture for Bi_2Te_3 if we replace Se atoms by Te atoms and the corresponding antibonding state is derived from Te5p instead of Se4p orbitals. Bonding and antibonding states have opposite parity and we can make use of the photoemission matrix element to show that the highest occupied band has even parity thus corresponding to the bonding state of Bi atoms as predicted [64]. As discussed in Chapter 2 the photoemission intensity is proportional to the dipole matrix element of the transition:

$$I_0 \propto |M^{\mathbf{k}}_{f,i}|^2 \propto |\left\langle \phi^{\mathbf{k}}_f \right| \epsilon \cdot \mathbf{r} \left| \phi^{\mathbf{k}}_i \right\rangle|^2. \tag{4.2}$$

A contribution is thus only found if the whole integrand of the overlap integral in Eq. 4.2 has even parity with respect to the mirror plane shown in Fig. 4.7. The final state $\phi^{\mathbf{k}}_f$ must be even, otherwise the mirror and the detection plane would lie in a nodal plane of the final state and the intensity would vanish. The scalar product $\epsilon \cdot \mathbf{r}$ is even if the polarization vector ϵ lies within the mirror plane, thus for p-polarized light. Odd parity is then found for s-polarized light, i.e., the polarization vector being perpendicular to the mirror plane. The parity of the initial state may have either parity, but $\epsilon \cdot \mathbf{r} \left| \phi^{\mathbf{k}}_i \right\rangle$ must be even to have the full integrand even. This means that we expect the highest occupied band of Bi_2Te_3 to give high intensity for p polarized light only, since it should have even parity if the band inversion has taken place.

The results of the described experiment are summarized in Fig. 4.7 b) for Bi_2Te_3 along the $\overline{\Gamma M}$-direction of the surface Brillouin zone measured with 50 eV photons and with the

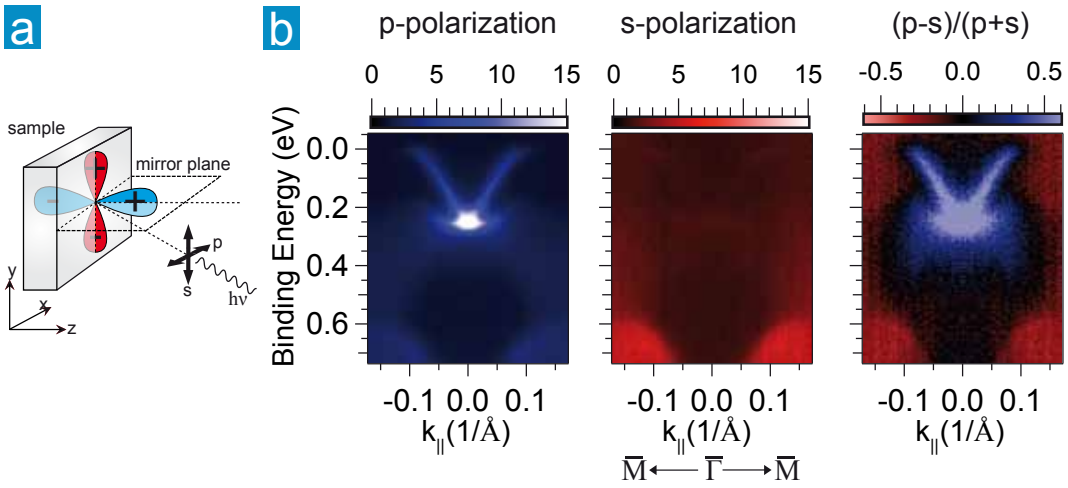

Figure 4.7: Angle resolved light polarization dependent photoemission of Bi_2Te_3. a) Sketch of the experimental setup. A real space representation of atomic p_y (red) and p_z (blue) orbitals is shown, having different parity with respect to the mirror plane defined by the incoming light and the direction of electron detection. b) Obtained intensity distribution of the photoelectrons for p- (left) and s-polarized (center) light. The right panel shows the normalized difference spectrum.

sample kept at T=50 K. When changing the light polarization from p (left panel) to s (center panel) the photoemission intensity around $\overline{\Gamma}$ gets strongly reduced between 0.6 and 0.0 eV binding energy. To emphasize this effect further the difference of the two spectra divided by their sum is shown in the right panel. In addition, we can conclude that surface state and highest occupied valence state share the same symmetry, since they show the same polarization dependence.

4.1.3 Temperature induced gating effects in Bi_2Te_3

In 1992 Thomas *et al.* reported an unexpected temperature dependence of the charge carrier density in Bi_2Te_3 observed in optical measurements [78]. In contrast to most metals, where the charge carrier density is constant with temperature and lightly doped semiconductors, where the charge carrier density decreases with decreasing temperature due to a carrier freeze-out Bi_2Te_3 shows an increase of the charge carrier density with decreasing temperature. It was argued that cooling causes a condensation of above gap states into the metallic states. As the samples under investigation were grown with an excess of Bi atoms they exhibited p-doping and a metallic hole band. For such samples Noh *et al.* reported a time dependent shifting of the band structure which they found to be independent of the sample temperature [86]. The authors also argued that the formation of the V-shaped surface state, which we have assigned to the topological surface state, appears only with time and they have ascribed this surface state to a band bending caused by a relaxation of the inter quintuplelayer distance with time. The authors were however not aware of the concept of the topological insulators and it is thus more likely that the surface state is always present and that it became visible with the time dependent shift of the Fermi level.

As stated above, the ARPES results from our samples show an n-type doping which is due to an excess of Te atoms during the growth. In these samples we did not observe a time dependent change of the band structure as described by Noh *et al.* which is an indication

that the given explanation might not be true. At least we would expect a similar relaxation of the inter quintuplelayer distance. In Ref. [78] it was already pointed out, that the excess of Bi during crystal growth should lead to a substitution of Te atoms by Bi atoms in the Te(2) layer of the quintuplelayer, i.e., the central layer. Thus we can assume the inter quintuplelayer bonds being unaffected by the doping.

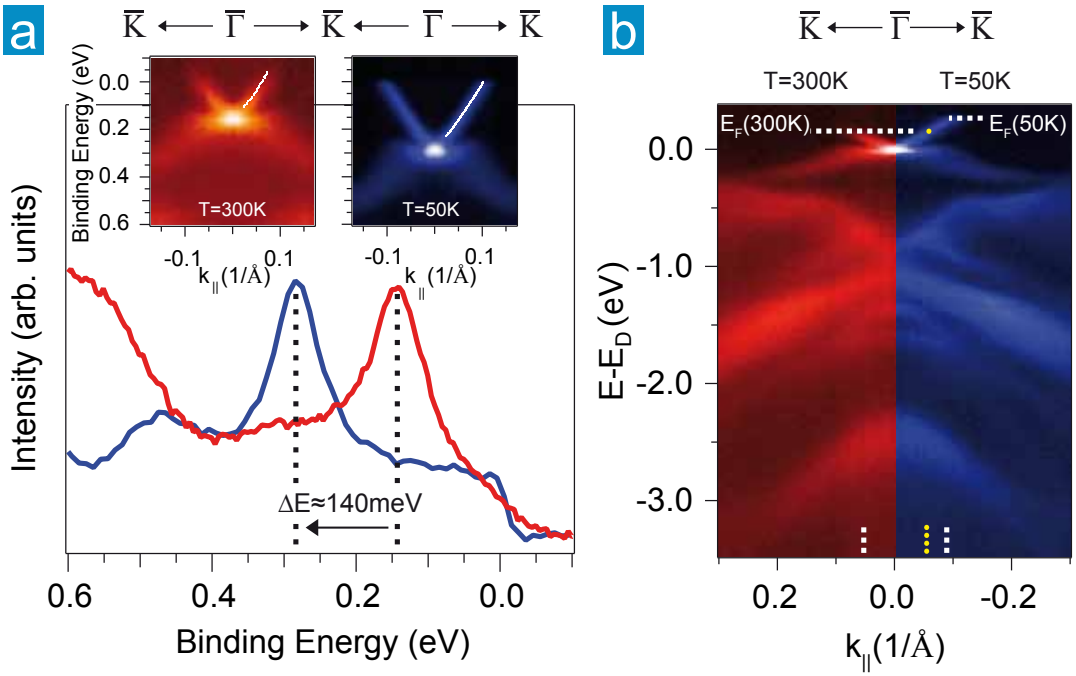

Figure 4.8: Temperature induced shift of the Fermi level (E_F) in Bi_2Te_3. a) Energy distribution curves at $\overline{\Gamma}$ for room temperature (red) and for low temperature (blue). The Dirac point appears shifted to higher binding energy after the sample is cooled to 50 K. The insets show the angle distribution along $\overline{\Gamma K}$ for T=300 K (left) and T=50 K (right). b) By comparison of the valence band structure along the $\overline{\Gamma K}$-direction a rigid shift of all bands to higher binding energy is observed. The energy scale is given relative to the Dirac point (E_D) to allow for a straightforward comparison. The horizontal white dashed lines mark the positions of E_F for each temperature, while the outer vertical dashed lines at the bottom mark the position of the Fermi wave vector k_F. The inner yellow dashed line marks the wave vector given by the intersection of the Fermi level at 300 K with the dispersion at 50 K

We, however, do observe a strong change in the band structure with temperature. Upon cooling the Fermi level shifts towards the unoccupied states which is in agreement with the observations in Ref. [78]. In Fig. 4.8 a) we show photoemission spectra integrated over $k_{||}$. The pronounced peaks gain their spectral weight mostly from the Dirac point as becomes clear by a comparison with the angle resolved intensity plots in the insets. The red curve and intensity plot represent the spectra obtained at room temperature while the blue curve and color scale represent the spectra obtained at T=50 K. We observe a strong shift of $\Delta E \sim 140$ meV between the red and the blue peak maximum of the angle integrated plot. The insets report a clear shift of the whole surface band structure.

In Fig. 4.8 b) we compare directly a valence band overview for room temperature (left half, red color scale) to a spectrum measured at T=50 K (right half, blue color scale). The

energy axis of each spectrum is scaled relative to the energy position of its Dirac point, such that $E_D = 0$ for both cases. This allows for a better comparison and one finds that the band structure has shifted rigidly in the whole energy and momentum range shown in the figure. The position of the Fermi level is marked with horizontal white dashed lines for each half to make the difference more clear. On the $k_{||}$-axis the white dashed line mark the position of the Fermi wave vector k_F. The yellow dotted line marks the position of k_F assuming that the Fermi levels would match for both temperatures. As can be seen in both cases we obtain a value of $|k_F| \sim 0.057\text{Å}^{-1}$. In addition, the results of a fit to momentum distribution curves (white dots in the insets of Fig. 4.8 a)) reveals that the group velocity for low and room temperature is approximately $|v_g| \sim 3.0\,\text{eV·Å}(\sim 4.5{\cdot}10^5\,\text{m/s})$, thus the bandstructure really appears to shift rigidly. As already visible with the naked eye, the topological surface state peak widths appear broader at room temperature and the fit reports an average reduction of the full width at half maximum of the momentum distribution curves at low temperature by a factor of 0.7. This qualitatively confirms the findings by Thomas *et al.*, who reported a reduced inelastic scattering upon cooling [78], as the peak width is proportional to the imaginary part of the electrons' self energy which in turn is proportional to the scattering rate. A more profound discussion of this topic will be given in Chapter 6.

A similar, but less pronounced effect was observed in Bi_2Se_3 [87] and it was shown that the effect is fully reversible and reproducible. It was therefore assumed that the effect is intrinsic and not caused by adsorption of residual gases in the chamber. That for example Shockley type surface bands show a strong temperature dependent shift is well known [88] and understood. Thermal expansion of the lattice is modifying the periodic potential experienced by the electrons and it is straightforward to expect an effect on the band structure [89]. Also the phonon distribution has a temperature dependence and the lattice vibrations affect the band structure as well. In semiconductors, an increase of the band gap with decreasing temperature is quite common and similar effects have been observed in metals. Since the Shockley-type surface states exist within $E(k)$ regions that are *forbidden* in the bulk band structure two statements are evident: first, the size of the gap will effect the energy position of the surface state. For the surface states of Ag(111), Cu(111) and Au(111) it was shown that they follow the behavior of the valence band and thus shift to higher binding energies with decreasing temperature [88]. And second, the topological surface states, like the Shockley ones, exist within a gap and similar temperature effects on their dispersion appear hence likely.

Further insight into the mechanisms behind the energy shifts can be gained from core level spectroscopy. On the one hand we do not observe any pronounced changes in the shape of the Bi5*d* and Te4*d* core levels of Bi_2Te_3 (Fig. 4.9) like the shoulders that appear besides the Bi5*d* peaks upon deposition of adatoms (compare Chapter 5.2.1). This may indicate that the shifts are intrinsic and not caused by adsorption of residual gases. On the other hand the core levels exhibit a shift which is in size and sign comparable to the one of the bulk valence band and the topological surface state (Fig. 4.9). Temperature dependence of core levels is known from other materials and a connection to the thermal expansion was drawn [90]. But the absence of shoulders does not rule out the possibility of a shift due to an enhanced adsorption of residual gases with decreasing temperature. Gas adatoms or molecules might be only physically adsorbed which will not have the effect of a chemical shift in the core level spectra but may alter the surface potential and give rise to the shift of the band structure (compare Chapter 5.1.1). Contrary to the argument

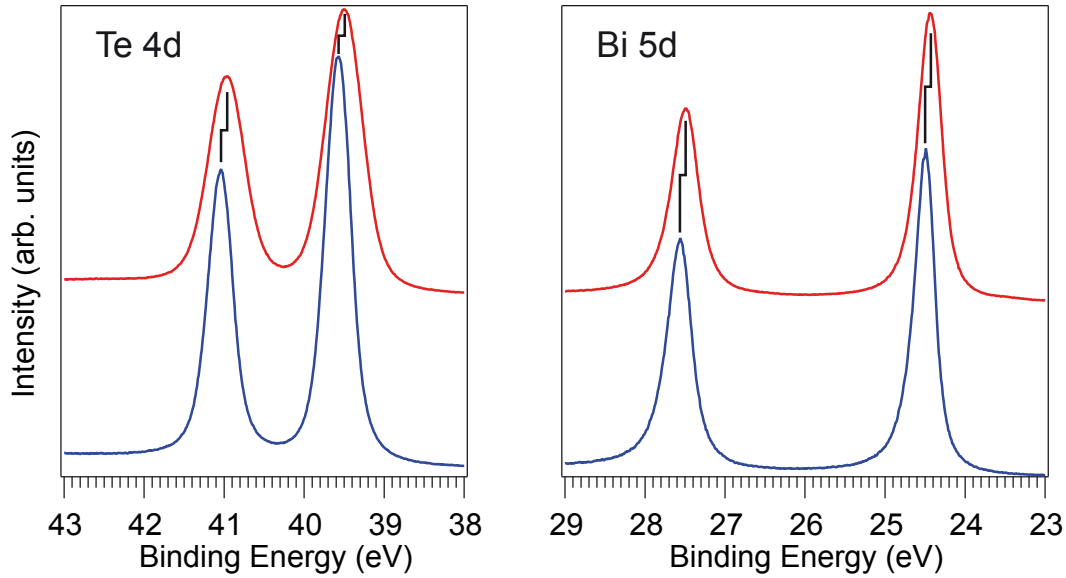

Figure 4.9: Te 4d (left) and Bi 5d (right) core levels excited with 150 eV photons at room temperature (red) and at 50 K (blue). The core levels exhibit a similar energy shift as the valence band and the topological surface state. The peak maxima are marked by black lines.

given in Ref. [87] this would also fit to the reversal and reproducibility of the effect upon warming up and re-cooling the sample, respectively. Physisorbed molecules will be released and re-adsorbed during warming up and cooling down again.

Sample	A	B	C	D	E
E_D/meV (T=300K)	155	150	270	150	190
E_D/meV (T=50K)	295	260	320	240	300
ΔE/meV	140	110	50	90	110

Table 4.2: Binding energies and energy shifts of E_D upon cooling Bi_2Te_3.

Remarkable appears also the non-reproducibility of the shift over different samples. Table 4.2 contrasts the energy shifts of different samples and cleavages. In the first two lines, the initial energetic position of the Dirac point at 300K and its position at 50K are given. Relative shifts between 50 meV (Sample C) and 140 meV (Sample A) have been obtained. The large difference may be explained by the large difference in the intrinsic doping. While the Dirac point in Sample A is found at 155 meV at 300K it resides at 270 meV in Sample C. Such large differences in the occupation of states should also affect the potentials and could therefore influence the effect of thermal expansion on the band structure. However, for comparable initial Dirac point energies in samples A, B and D (150 meV) we observe also a significant difference in the shift upon cooling. In Sample B it amounts to 110 meV and in Sample D to only 90 meV both significantly less than the 140 meV shift observed in Sample A. By comparing with Sample E we can additionally conclude that the impression of a less pronounced shift for higher intrinsic doping is not

confirmed. With 190 meV the Dirac point resides at significantly higher binding energy than in Sample D but the shift amounts to 110 meV thus larger than in Sample D. Of course, there is an uncertainty in the determination of the temperature as the sample temperature was not measured directly on the sample. But the experimental setup was identical for all samples and temperature should thus not vary too much among the samples. The position of the Dirac point is determined from spectra measured with 55 eV excitation energy in all cases and thus the error of the energy position is with $\sim \pm 3$ meV the same for all. If the temperature induced shift was purely intrinsic we would expect the shift being the same for all samples at least for similar intrinsic doping. On the other hand the differences can be explained easily in an extrinsic scenario, since we expect the partial pressure of the residual gases causing the effect in the chamber to differ over the span of time in which the samples were measured (two years).

Another noteworthy observation is that all occupied energy bands measured seem to shift by the same amount and rigidly while different temperature coefficients for different valence bands and for the surface state have been reported, e.g., for Cu(111) [91]. At the chosen photon energy of 55 eV we cannot trace the bulk conduction band in angle resolved photoemission since it has dispersed already above the Fermi level along the ΓZ direction of the bulk Brillouin zone (compare Fig. 4.4 a) and b)). Thus a different shift of the conduction band, i.e., all unoccupied bands of the ideal undoped system cannot be ruled out directly. However, the relative photoemission intensities for the bands at 300K and at 50K shown in Fig. 4.8 b) appear similar for both temperatures. Since the unoccupied bands take the role of a final state in photoemission we may expect changes in the relative intensities of the different bands if the unoccupied final state band would shift differently. This would be similar to a change of the photon energy which leads to a different final state with different matrix element of the transition. It is, however, not clear how the bands at ∼55 eV above the Fermi level behave as compared to the conduction and valence band, and the argument has to be viewed as speculative. An investigation of the photon energy dependence of the intensities for relatively low photon energies $h\nu < 10eV$ at high and low temperatures may deliver information needed to confirm this argument, but has not been carried out so far.

More important could be the effect of the lattice expansion on the dispersion of $\mathbf{k}_\perp$. A different shift of occupied and unoccupied bands with the temperature would be similar to a change of the photon energy to map different $\mathbf{k}_\perp$ values as shortly described in Chapter 2 and should thus show up in a difference of the energetic positions of bulk states at normal emission. But again, such effects are not observed in Fig. 4.8 which thus delivers a further indication, that all bands shift more or less rigidly.

All observations taken together suggest that at least in the case of Bi_2Te_3 the temperature induced shifts cannot be explained by thermal expansion and compression only. But since thermal expansion is a generic phenomenon and effects on the band structure are likely, we believe that both extrinsic and intrinsic effects may play a role here.

We can only speculate on the type of gas which could be the reason of the observed shift. Oxygen can be ruled out as it causes a non-rigid shift of the bands to *lower* binding energies as will be shown in Chapter 5.1.1. Other quite common residual gases are CO and CO_2. The former has been reported to cause shifts of the band structure to higher binding energies if adsorbed on Bi_2Se_3 [92]. It thus goes without saying that CO could cause similar effects if adsorbed on Bi_2Te_3.

4.2 Spin Polarization in Bi_2X_3

Probing the spin polarization of topological surface states is the most direct possibility to unambiguously distinguish them from trivial surface states in photoemission. One may for example think of a degenerated pair of surface states or a surface state with a spin splitting below the detectability of state of the art angle resolved photoemission setups. Such states would show no spin polarization. Concerning the hexagonal warping described above, interesting predictions about the orientation of the polarization vector were made [19, 20]. Yazyev, Moore and Louie used DFT calculations to show that the strong spin-orbit interaction in Bi_2X_3 reduces the spin polarization to values ∼50% [80]. This would of course have direct implications for any spintronic application. In addition the first spin resolved measurements for Bi_2Te_3 given in the literature where rather unsatisfying, showing a measured spin polarization of only 20% [81].

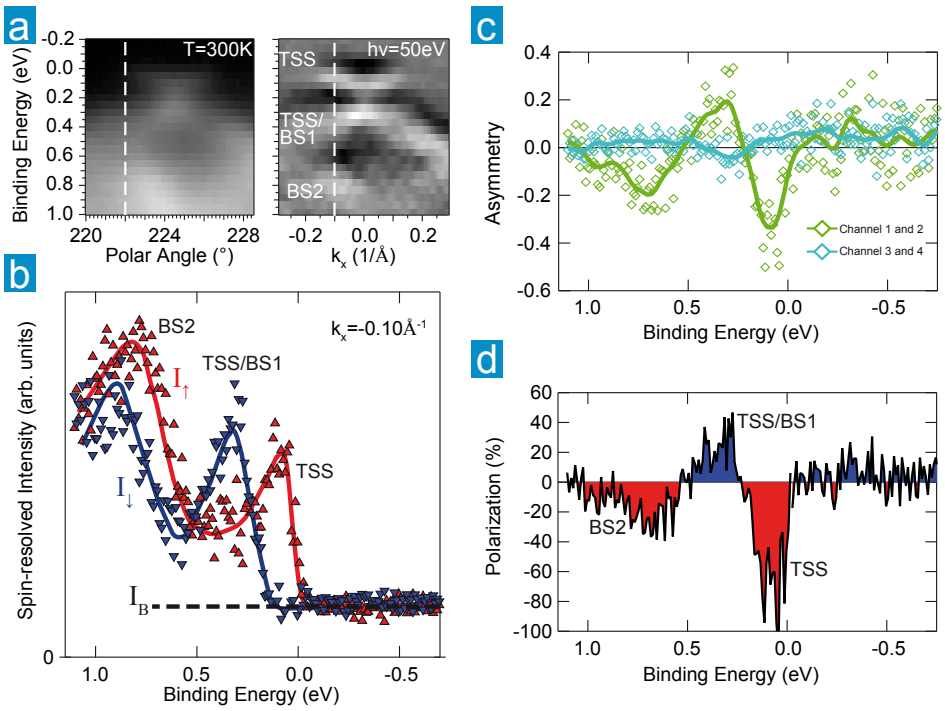

Figure 4.10: Spin- and angle-resolved photoemission from Bi_2Te_3. a) Dispersion measured with spin-channeltrons (left) without high voltage at the Mott detector and its second derivative plot (right). We can distinguish several energy regions: below ∼0.6 eV the topological surface state (TSS) is not present (BS2). Between ∼0.2 eV and ∼0.6 eV the TSS falls together with the bulk valence band (BS1). Above ∼0.2 eV only the TSS is present. b) Spin-resolved spectrum taken at the angle, i.e., k_x-value marked with white dashed lines in a). Spin up ($I_\uparrow$) and spin down ($I_\downarrow$) intensity are represented by red and blue triangles, respectively. Curves are guides to the eye. The black dashed line marks the background intensity (I_B) above E_F. c) Asymmetries of spin channels 1 and 2 (green diamonds), and 3 and 4 (turquoise diamonds). Channels 1 and 2 show a strong asymmetry and represent the S_y direction. d) The spin polarization of the TSS after background removal amounts to (70±10)%. In the TSS/BS1 and BS2 range we also observe a high polarization.

The spin texture of an ideal Dirac cone would be such that the spin is always perpen-

dicular to the momentum vector and it would lie within the surface plane. But as pointed out above, deviations from the ideal form do affect the spin such that it should show a finite out of plane rotation, which is momentum dependent and also the perpendicular locking of the in-plane component to the momentum parallel to the surface is not anymore guaranteed [20]. Thus for Bi_2Te_3 we expect a more or less complicated spin structure depending on the actual shape of the constant energy cuts of Fig 4.6. Which of these shapes can be accessed depends on the intrinsic doping and the sample temperature as discussed above.

4.2.1 Bi_2Te_3

In Fig. 4.10 a) an angle resolved spectrum of Bi_2Te_3 measured with 50 eV photons at room temperature is shown. Please note that the photoemission setup with spin-resolution is not equipped with a two-dimensional detector and also the spin averaged dispersions have to be assembled from energy distribution curves measured at different emission (polar) angles. In order to do this on a reasonable time scale, the number of angle steps is chosen such that it contains just enough information to decide on the angles to be measured with spin resolution. In addition we have used the spin channeltrons without an applied high voltage to the Mott-detector. This directs a large number of photoelectrons into the spin channeltrons, however without any spin sensitivity. The advantage lies solely in the identity of the electron trajectories and one avoids readjustment to the different focus positions between spin- and front-channeltrons. This advantage has to be paid for with a reduced resolving power and the overall quality of the obtained spectra is reduced. We are nevertheless able to identify the important features as described above and the second derivative of the intensity along the energy axis shown in the right panel of Fig. 4.10 a) enhances them even more.

The "V"-shaped topological surface state (TSS) is clearly seen dispersing up to the Fermi level and also the states at higher binding energy (TSS/BS1 and BS2) are resolved. The white dashed line marks the angle at which we have obtained the spin-resolved spectrum of panel b) where the surface state is close to the Fermi level. The red (blue) triangles mark the spin-resolved intensity of the arbitrarily defined spin up (down) components S_y perpendicular to the momentum component k_x. The topological surface state shows intensity mainly in the channel defined as spin up which is emphasized by the red line. Around the state at ∼0.4 eV binding energy we find intensity in both channels but a clear peak is seen only for the spin down component which reflects the behavior expected for an ideal Dirac cone where the upper and the lower half would have opposite spin helicity due to the crossing of the spin-polarized dispersions at the Dirac point. The third feature (BS2 in the Fig. 4.10) appears also with different intensity for the two components, but as emphasized with the red and blue line the peak maxima for the two components appear shifted against each other which indicates a pair of states that might be spin split. A similar pair of states was found in Sb_2Te_3 and identified as a Rashba split surface state by means of spin- and angle-resolved photoemission in combination with DFT calculations [93].

Panel c) shows the spin asymmetry as it is obtained from the raw data by calculating $((I_\downarrow - I_\uparrow)/(I_\downarrow + I_\uparrow) - A_{\uparrow\downarrow})/S)$, where $I_\downarrow$ is the intensity in spin channel 2 (i.e., spin channel 4 for the component S_x parallel to the momentum as explained in Chapter 2), $I_\uparrow$ the intensity in channel 1 (3), $A_{\uparrow\downarrow}$ is a constant offset between the channels[3] and S is the Sherman function of the detector as introduced in Chapter 2. Green (torquoise) diamonds

[3]This *apparative* offset is due to the different sensitivity of the different channeltrons and may change over a long time span.

reflect the asymmetry obtained for channels 1 and 2 (3 and 4 for S_x) and the line is obtained from a smoothing routine applied to the data.

Important is that we find for channel 1 and 2 the expected reversal of the sign between the upper and the lower half of the Dirac cone and also an asymmetry in the range of BS2 is seen. For channel 3 and 4 the asymmetry is negligible within the errors. The asymmetry values obtained for the topological surface state do not exceed 0.4 and 0.2 for the upper and lower half, respectively. But these do not represent the true spin polarization as they contain a background signal of an order of magnitude comparable to the signal itself, marked with I_B in panel b). To obtain the spin polarization, this background must be subtracted:

$$P_{\uparrow\downarrow} = \left(\frac{I_\downarrow - I_\uparrow}{I_\downarrow + I_\uparrow - 2I_B} - A_{\uparrow\downarrow} \right) / S \tag{4.3}$$

The result is shown in panel d) and the spin polarization amounts to (70±10)% for the upper and (40±10)% for the lower part of the Dirac cone. In the range of BS2 we find a similar polarization as in the lower half. Please note that above the Fermi level we still show the spin asymmetry of panel c) since the denominator in Eq. 4.3 gives hardly finite values above E_F and thus the spin polarization would fluctuate between values much higher or lower than +100% and -100% which is of course unphysical.

On the one hand the polarization values obtained constitute a substantial progress compared to the 20% polarization measured before [81] and with 70% polarization for the upper half the polarization is still significantly higher than the 50% predicted from first principles calculations [80]. On the other hand there is a *missing* polarization of 30% left compared to the expectation of 100% polarization for the ideal topological surface state. If we think about future applications in *spintronic* devices this lack of polarization does matter. But for our measurements there are a few shortcomings which have to be taken into account and which might explain the reduced polarization without excluding that the states are really 100% polarized. First, as can be seen in Fig. 4.10 a), especially in the second derivative plot, the dispersion exhibits a gap where the Dirac point should be. This gap is due to a small tilt of the sample surface which was impossible to correct since the available manipulator does not offer the required extra degree of rotation. As a consequence we cut in the k_y direction slightly off normal through the Dirac cone and miss the point (compare also Fig. 4.13 b)). Thus, we would expect a finite component in counters 3 and 4 as the spin would have a component in the x direction which, for the case of an ideal Dirac cone is not expected if we cut the cone exactly at $\overline{\Gamma}$, i.e., through the Dirac point. The warping in Bi_2Te_3 may enhance these effects further, on the one hand. But as can be seen in the spin asymmetries shown in panel c) of Fig. 4.10 chanels 3 and 4 do not deliver the missing polarization as it is below 10% even if we would subtract the background to obtain the polarization. But on the other hand the warping may also rotate the spin such that the in plane component is still fully aligned with the S_y direction even for a cut offset in the k_x direction as the spin vector is not anymore locked perpendicular to the momentum [20]. Unfortunately, due to the lack of resolution we are not able to specify how the sample is oriented and therefore where exactly we cut through the Dirac cone in k-space. Typically, one would use information from low energy electron diffraction (LEED) to assign the high symmetry directions of the crystal structure in the sample. But for the single crystalline Bi_2Te_3 samples it is not straightforward to reproduce the sample position observed in LEED for the photoemission measurements because of a strong faceting of our samples which results in differently rotated and tilted surface regions. The large scattering

of the data points of channel 3 and 4 does however not allow to conclude about any spin rotation, neither that it is fully aligned along the S_y direction nor that there is a finite polarization along the S_x direction. To decide this question much better statistics would be needed.

Second, the available setup does not allow the measurement of the component out of plane, S_z. For strong hexagonal warping, however, an out of plane rotation of the spin is predicted [19] and also observed in experiment [94]. This rotation is also k dependent and may, according to theory, amount up to 30% along the $\overline{\Gamma K}$ direction while it is, due to mirror symmetry, zero along the $\overline{\Gamma M}$ direction [20]. In addition, the out of plane component is binding energy dependent in the sense that the shape of the constant energy surface alters as a function of the energetical distance to the Dirac point energy (E_D). In the present case E_D is estimated to be between 200 and 220 meV binding energy which corresponds to a shape of the Fermi surface comparable to the cuts at 50 meV or 75 meV in Fig. 4.6 and to a maximum out of plane spin polarization of approximately 20% calculated for this shape [20]. However, this is not enough since in order to obtain 100% polarization an out of plane polarization similar to 70% has to be added to the 70% along the y direction, assuming a vanishing polarization along the x direction, as is indeed measured.

As a third point the limited resolution of the experimental setup has to be taken into account. Especially the angle acceptance of the analyzer may lead to a reduced spin polarization the more closer to normal emission we measure. As soon as the opposite spin of the other half of the surface Brillouin zone contributes to the signal this will show up in the spin polarization. For the present case, i.e., a photon energy of 50 eV and an angle acceptance similar to $\pm 0.5°$ we average over a momentum range of $\sim \pm 0.03 Å^{-1}$ along the k_x axis. Keeping in mind that the topological surface state at the Fermi level of the present intrinsic doping is completely within a range of $\sim \pm 0.1 Å^{-1}$, it becomes clear that the angle acceptance is crucial for the measured spin polarization.

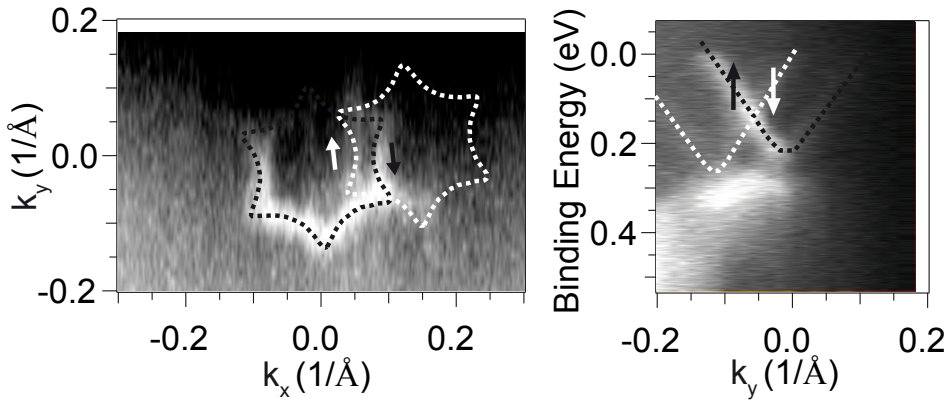

Figure 4.11: Twinning of the band structure. Slightly differently oriented surface regions may lead to a doubling of the band structure in photoemission if probed simultaneously. This can be seen in the constant energy cut (left) as well as in the dispersion (right). The black and white dashed lines are guides to the eye and mark the two warped Fermi surfaces (left), i.e., the topological surface state above the Dirac point (right). The arrows qualitatively mark the spin orientation of the two superimposed states.

This becomes even more important if we take into account the abovementioned issues

of the sample quality. In Fig. 4.11 we present high resolution angle resolved photoemission data from the same sample but with a fresh cleaved surface. The data is obtained from a surface region where two domains with slightly different local surface normal border one another. Besides the expected warped surface Fermi surface (black dashed line) we find faint traces of a second domain (white dashed line) which appears shifted in k_x and k_y and also slightly rotated against the main signal (right panel). The left panel shows a cut along the k_y direction and we find two shifted surface states originating from the two different sample regions. The arrows mark in both panels the qualitative orientation of the spin. For such a configuration the spins are almost opposite to each other and thus, depending on the relative intensities from the two adjacent sample regions the spin-polarization can be significantly reduced or even vanish in a spin resolved measurement. If the two regions are rotated even stronger against each other as in the given example of Fig. 4.11 it is also possible to see a strong polarization in all channels of the Mott detector if for example two Fermi surfaces intersect each other such that the intersecting branches are perpendicular to each other. Then one branch would give high polarization in S_x, while the other would give high polarization in S_y. Taken together the measured polarization could thus appear higher than it is in reality.

It is also possible that the two energetically shifted Dirac-points, i.e., the two minima of the parabolas mapped in Fig. 4.11 do not originate merely from two different off normal cuts through the Dirac cone but from different intrinsic dopings. This makes the interpretation even more complicated; a different intrinsic doping would lead to different warping and different spin rotation and disentangling the obtained data may become impossible.

Even though the data of Fig. 4.11 stems from the same sample as that shown in Fig. 4.10, the fact that it was cleaved again and measured in a different photoemission setup means that the data has to be viewed as obtained from two different samples. It is thus clear that we cannot directly compare the data sets. Nevertheless, it is not unlikely that the spin-resolved data is obtained from a sample region suffering from similar quality defects as we typically integrate over macroscopic sample areas of $\sim 0.25\,\mathrm{mm}^2$. But it is also worthwhile mentioning in this context again that the obtained polarization of $\sim$70% for the topological surface state in a *macroscopic* area is a great progress. It also shows that the so far unsatisfying results from transport measurements are not explained from an intrinsic limitation of the spin polarization over a macroscopic area. One may draw such a conclusion when comparing macroscopic with microscopic probes under the assumption that the spin polarization guarantees high mobilities due to the forbidden backscattering. On the macroscopic scale the investigation of Shubnikov-de Haas oscillations in Bi_2Se_3 revealed a high bulk mobility whereas a surface contribution was found to be absent [95], indicating high scattering rates for the surface electrons. On the microscopic scale, however, the observation of Landau quantization of the topological surface state in Bi_2Se_3 by means of STM indicates a high mobility of the surface electrons [96, 97]. A more conceiving explanation to this discrepancy seems to be the fact, that STM is highly surface sensitive and that it is more challenging to reveal the surface state characteristics in a bulk sensitive probe such as the Shubnikov-de Haas efefct [98]. The scattering properties of the surface state electrons in topological insulators are the topic of Chapter 6 and we postpone this discussion.

From the same sample and cleavage as in Fig. 4.10 we have measured spin-resolved energy distribution curves at positive and negative emission angles with respect to the surface normal. The results are condensed in Fig. 4.12. In panel a) and b) we show

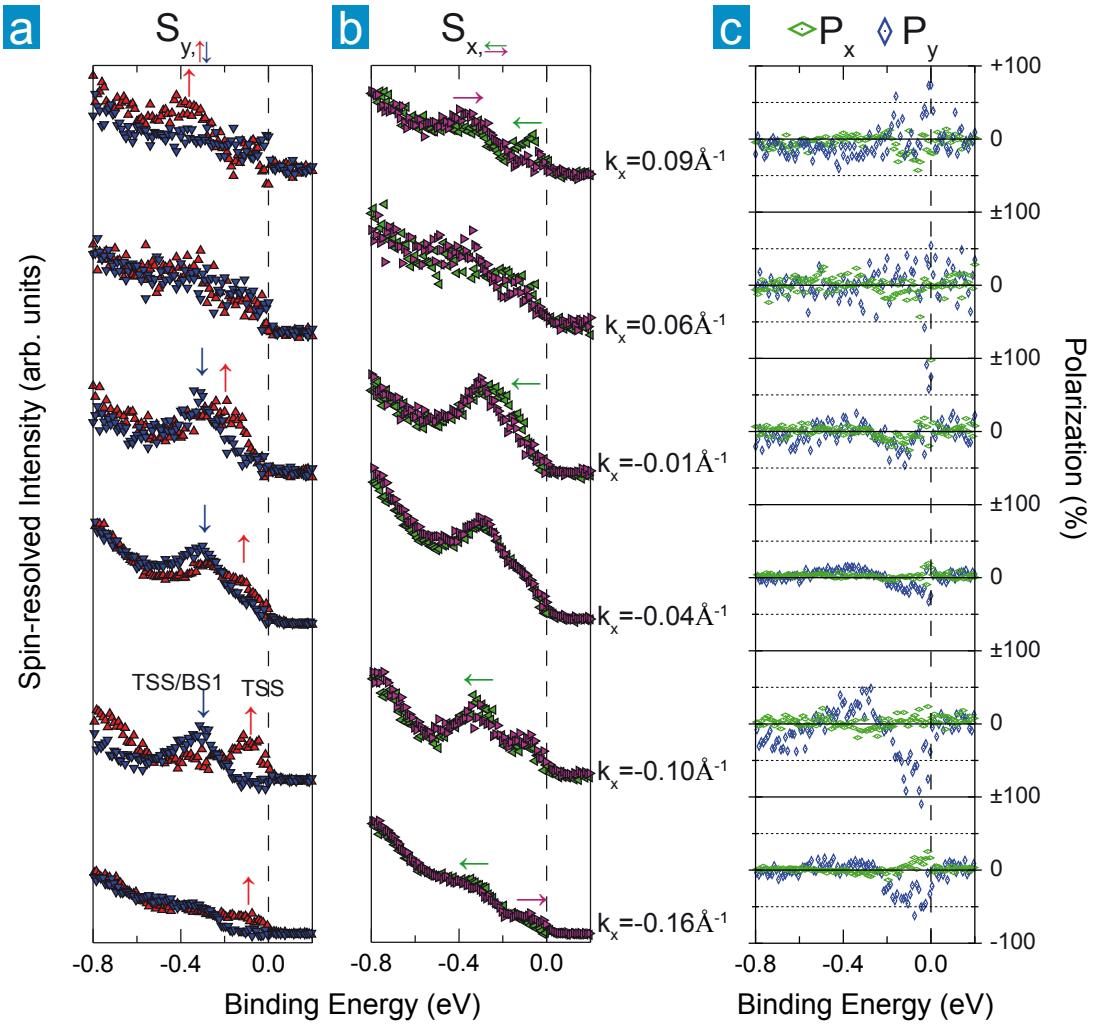

Figure 4.12: Spin-resolved photoemission from Bi_2Te_3 at various emission angles. a) Spin-resolved energy distribution curves perpendicular and b) parallel to the momentum. At high negative k_x-values the intensity stemming from the pure topological surface state (TSS) shows a rather high polarization in c) perpendicular to k_x (blue diamonds) as expected for a simple Dirac cone. The components parallel to k_x (green diamonds) show almost no polarization. While approaching normal emission (k_x ~0) the total polarization gets reduced due to an enhanced admixture of the state that has opposite polarization at -k_x. The S_x component is comparable to the S_y component closest to normal emission. For positive k_x the TSS shows no polarization perpendicular to the momentum but a polarization of ~20% parallel to k_x. The state at higher binding energies shows a lower but opposite polarization compared to the TSS. The sign of the polarization gets reversed by reversing the sign of k_x.

the spin-resolved intensity of the two pairs of spin channeltrons 1 and 2, and 3 and 4, respectively, as obtained from the standard analysis routine explained above (Eq. 4.3). In c) we present the spin polarizations of channel 1 and 2 (blue diamonds), and 3 and 4 (green diamonds) after background removal. Between panel b) and c) we specify the k_x values of the appurtenant rows. The blue and red (green and magenta in b)) arrows mark the dominant spin component in the energy region of the topological surface state (TSS) and

in the valence band, i.e., lower half of the surface state (TSS/BS1).

For negative k_x-values up to approximately normal emission the obtained picture in a) is rather conclusive. The spin up component is always dominant for the topological surface state but with varying polarization. The latter can be explained within the framework of an increasing admixture from the state of the adjacent half of the surface Brillouin zone as described above. The closer to normal emission we measure the higher is the admixture and the polarization will be reduced as seen in panel c). That the polarization with ∼50% is reduced for k_x =-0.16Å^{-1} compared to the 70% maximum at k_x=-0.1Å^{-1} can be understood in terms of the very low intensity as the state is already about to cross the Fermi level. For this k_x value we find an almost vanishing but still finite polarization for the TSS/BS1 energy range which has the opposite sign as the TSS energy range. Almost up to normal emission the sign of the polarization is preserved. The amount of polarization again reflects an increasing admixture from the opposite side. In channeltrons 3 and 4 the measured polarization is low for all emission angles. On the negative k_x side, the only k_x value where we have observed a polarization which is worth mentioning is -0.01Å^{-1}. Here, the polarization is with ∼15% comparable to the one measured in channels 1 and 2. Since the k_x cut we probe is set off from zero in k_y it is reasonable to expect a significant polarization in all channeltrons close to k_x=0 even for the circular constant energy surface that should be present at the binding energy corresponding to the state close to zero momentum.

In contrast, for positive emission angles the quality of the data is pretty much reduced and not straightforward to interpret. For k_x=0.06Å^{-1} the scattering of the data in channels 1 and 2 is so strong that we cannot draw any conclusions. For the S_x component the statistics is a bit better and we find a very low polarization with opposite sign for the two energy ranges TSS and TSS/BS1. At 0.09Å^{-1} we find the most remarkable result for positive emission, namely that the polarization has the opposite sign in the TSS/BS1 range as compared to the opposite half of the surface Brillouin zone. This confirms the presence of the expected spin fingerprint even outside the bulk energy gap and is a strong indication that the electrons are spin polarized in the initial state and do not acquire a polarization in the final state as it was suggested recently for Bi_2Se_3 [99]. In that work no change of the sign was found outside the bulk gap for opposing k_x-values but a strong modulation of the polarization with the photon energy. We however can not exclude an additional polarization in the final state due to spin dependent matrix elements as we have measured with 50 eV photons only, since the intensity is reduced significantly for other photon energies.

In general, bulk states do not show any spin polarization due to inversion symmetry which is present in the case of Bi_2X_3. But there are two possible explanations besides the spin dependent matrix element effects which naturally explain the measured polarization. First, as band structure calculations reveal, the topological surface state is present also outside of the gap (see e.g. Ref. [64]). We can therefore expect that it will show up spin polarized in our measurements. If we simultaneously probe an unpolarized bulk state so that their photoemission intensities add up than the polarization obtained will be reduced. One would have to subtract the intensity originating from bulk states in order to obtain the true spin polarization. Second, in Section 4.1.2 we have revealed by the polarization dependence of the photoemission intensity that the topological surface state shares its orbital symmetries with the highest occupied valence states. This means that the states can and must hybridize if they become degenerated at $\overline{\Gamma}$. Through this hybridization the bulk

states may acquire an intrinsic spin polarization from the surface state without violating the bulk inversion symmetry. In fact, a strong hybridization of topological surface states with bulk states under transfer of the locking of spin and momentum has been postulated in connection with the observation of an unusual magnetofingerprint in Bi_2Se_3 [100]. With respect to our observations this appears a realistic scenario.

The S_x component at positive emission angles is at $k_x = 0.06\text{Å}^{-1}$ again of inferior quality and does not show any conclusive tendency. At 0.09Å^{-1} we find on the other hand a polarization of approximately 20% for the TSS range which appears reversed but with a very low magnitude in the TSS/BS1 range. Considering Fig. 4.11 again we can give two possible explanations why the positive emission angles do not reflect the clear behavior of the negative side. Apparently, a twinning of the surface state as we discussed above may only affect one side. Besides the fact that the spin loses its strict perpendicular locking to k_x due to the warping, the second surface domain might not only be tilted against the main part but also rotated and would give another possibility for finite polarization in the S_x component. The second explanation becomes evident when we consider a cut along the k_y direction of Fig. 4.11, like it is shown on the right side. On the positive emission angle side, the signal is so weak that it cannot be distinguished anymore from the background. Such a loss of intensity may for example happen at the edge of the sample or if a crystal flake is only partially lifted during the cleavage and produces a *shadow* in the signal. While we can still derive the dispersion of the surface state in spin-averaged angle resolved photoemission, the intensity of the signal is reduced by orders of magnitude in the Mott detector and may thus deliver no significant signal above the noise level. This argument is affirmed by the relative flatness of the spectra at positive emission angles and much lower count rates in the raw data. That this loss of intensity is not pronounced in Fig. 4.10 a) can be understood by the much larger exit slit of the beamline for the spin-resolved measurements. The slit has to be opened to gain intensity but this comes along with a much larger light spot and we thus probe a much larger sample area. Therefore, it may be that surface distortion plays a role for spin-resolved measurements only.

4.2.2 Bi_2Se_3

While single crystals of Bi_2Se_3 do suffer from the same quality problems after cleavage as Bi_2Te_3 samples, i.e., differently oriented domains which cannot easily be distinguished without the use of a two-dimensional detector, the warping is expected to be much weaker and can be neglected in the discussion of the spin-resolved measurements. In Fig. 4.13 we present spin- and angle-resolved data of Bi_2Se_3 measured with 50 eV excitation energy and at room temperature. Panel a) shows a dispersion measured with the spin channeltrons without a high voltage applied. Again, a gap in the surface state is seen which is due to a tilt of the surface normal with respect to the plane of electron detection. As described above, such a tilt leads to an offset in the k_y direction with respect to zero and the mapped cut through the Dirac cone exhibits a gap and the dispersion appears parabolic, as is sketched in panel b). Due to the high group velocity of the surface state electrons ($\sim 6 \cdot 10^5 \frac{m}{s}$ in agreement with Ref. [3]) a small tilt will appear as a relatively large gap but, assuming a circular Fermi surface, we expect only a small rotation of the spin towards the S_x direction. As the reduced warping makes the out of plane component also negligible, the polarization should be visible in channels one and two only. This expectation is indeed confirmed for the part of the topological surface state that is fully within the bulk energy gap (TSS) as

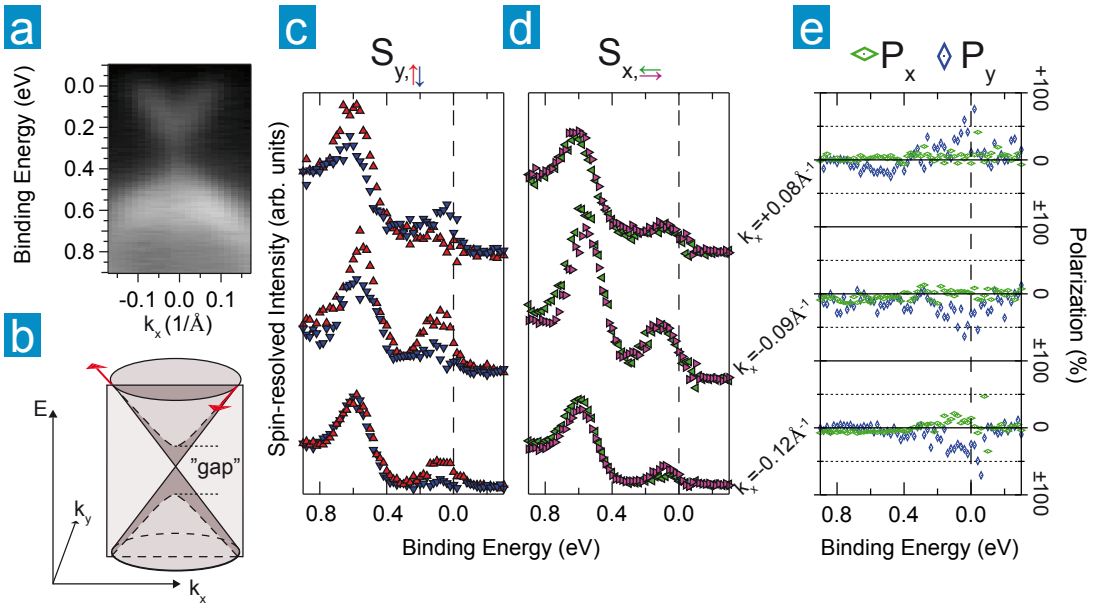

Figure 4.13: Spin- and angle-resolved photoemission from Bi_2Se_3 at various emission angles. a) Dispersion of the low energy states measured at 50 eV at room temperature. The gap in the surface state is due to a small tilt of the sample and normal emission cannot be reached as sketched in b). c) shows the spin component S_y perpendicular to and d) the component S_x parallel to k_x while e) shows the respective polarizations P_y (blue diamonds) and P_x (green diamonds). The topological surface state shows opposite polarization within and outside of the gap where it is degenerated with bulk states. Both signs are reversed by reversing the sign of k_x as expected for the ideal Dirac cone.

can be seen by comparing the spectra in Fig. 4.13, whereas the S_y component is shown in panel c) and the S_x component is shown in panel d). Also, for this part it is seen that the spin is reversed when moving from negative to positive k_x, i.e., from -0.09Å^{-1} to 0.08Å^{-1}. The polarization after removal of the background intensity above the Fermi level is shown in panel e) with the polarization components P_x and P_y being represented by green and blue diamonds, respectively.

In contrast to Bi_2Te_3 the magnitude of P_y is comparable for both, positive and negative k_x on the one hand, but on the other hand, it does not exceed ±50%. The P_x component is negligible with an upper limit of 5%. Yazyev *et al.* have argued that the spin polarization is reduced due to the strong spin-orbit interaction [80]. In brief, the Bloch states are not spin eigenstates but have a strong entanglement between their spin and orbital parts. The surface states should thus consist of a mixture of bulk states from a broad energy range [80]. Our finding of only 50% polarization for Bi_2Se_3 is in nice agreement with their suggested upper limit for the polarization.

Another source of intrinsically limited spin-polarization was found theoretically by a layer-resolved [101] or sublattice-resolved [102] investigation of the spin polarization. It was found that the spin is oriented differently in the adjacent layers of a quintuple layer in Bi_2Te_3 and Bi_2Se_3. Hence, the expectation value of the spin polarization is expected to be a function of the escape depth of the electrons which can be tuned by the photon energy. However, other groups report a polarization value of 75% [103] and 80% [99] in

the topological surface state of Bi_2Se_3, significantly more than the given entanglement limitation. Even though both groups [103, 99] conclude on a similar polarization there is a big disagreement between the two studies. While the latter study [99] reports a spin polarization in the range of the bulk valence band that is not reversed for the two opposed halves of the first surface Brillouin zone, the former study [103] claims that the bulk states do not show a spin polarization at all. As a loophole through this disagreement might appear the photon energy dependence [99] suggesting a spin dependent matrix element effect. In our case the bulk states also show a polarization which is not reversed when going from $+k_x$ to $-k_x$ and as we have used with 50 eV the same photon energy as Ref. [103], spin dependent matrix elements cannot explain the disagreement but makes the findings in Ref. [99] more reasonable.

One issue from which all the spin resolved measurements on topological insulators are suffering is the lack of an adequate method to compensate for the instrumental asymmetries of the detector. Having separate channeltrons for each spin direction the countrates differ among them sensitively as a function of the efficiency of the channeltrons and the alignment of the sample with respect to the detector focus and the alignment of the chamber to the photon beam. For the investigation of ferromagnets the adequate method is to simply reverse the magnetization and remeasure the sample [22]. In this way, the instrumental asymmetry is naturally removed. Another prominent subject which has been investigated intensely by spin-resolved photoemission are Rashba split surface states, like for example on Au(111) [62], on Bi(001) [104] or quantum well states of Au and Ag on W(110) [105]. In these systems one finds two energetically separated spin polarized states at each emission angle[4], i.e., momentum $k_{\|}$, which should carry the same amount of spin polarization. Thus, the instrumental asymmetry is determined in the middle between the two extrema in the polarization as a function of binding energy. The characteristics of the topological insulator, in the case of Bi_2X_3 a single Dirac cone, rules out the second possibilty as well. Using the upper and lower half of the Dirac cone to find the asymmetry level of the instrument would be possible only if no other states contributed to the signal which is clearly not the case for the lower half of the Dirac cone, where bulk states are present. Speaking of bulk states it shall be noted that a normalization to zero polarization of bulk states is a high source of error because we can not expect the photoelectrons to be unpolarized in the final state even for an unpolarized initial state [99]. Moreover, a Rashba polarization in the *initial* state is also possible for bulk continuum states close to the surface [106] and may thus be observed in photoemission, due to the high surface sensitivity [107].

In our case we have used the intensity above the Fermi level to correct the asymmetry. This however contains uncertainties as well, at least for synchrotron radiation, where higher order peaks may occur above the Fermi level, i.e. above the maximum kinetic energy according to the used photon energy. Even though we have measured a wide range above the Fermi level, where no significant signal beyond the noise is seen, the secondary electron background from states above the measured range may lead to a finite polarization in the background above E_F. Thus a small probability remains that the instrumental asymmetry is not determined correctly which would lead to wrong values of the polarization. Nevertheless, we believe that this is the most adequate method in these systems despite the use of a ferromagnetic reference system.

[4]Except at normal emission.

Sensitivity of Bi_2Se_3 to Photons

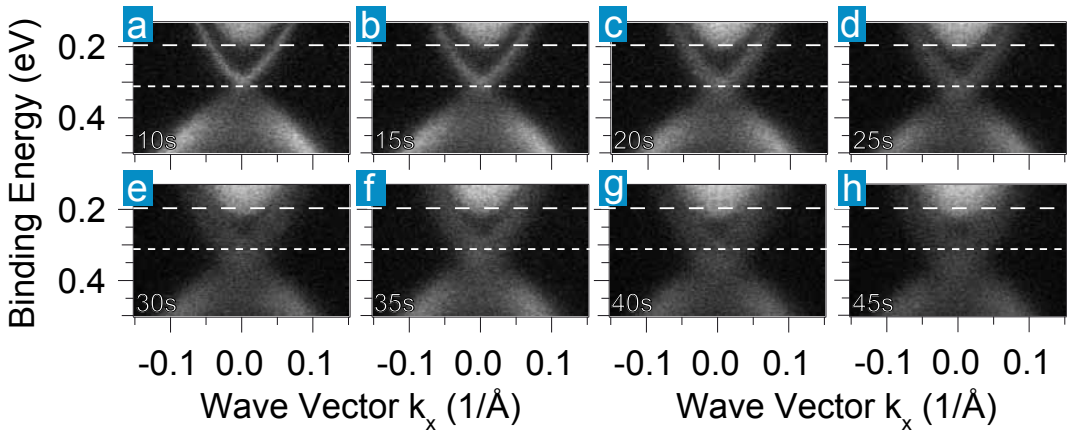

Figure 4.14: Effects of photon exposure at room temperature. The exposure time increases from 10s in a) in subsequent steps of 5s to 45s in h). The photon energy is set to 21 eV. The picture is getting more and more blurred out, indicating a sensitivity of the surface to photons.

A number of interesting studies report a time dependence [86, 108, 109, 92], i.e., a sensitivity of the topological surface state as well as the bulk conduction and valence band to residual gases in the vacuum system. This leads to a strong electron doping of the samples and a quantization in the conduction and valence band to two dimensional electron gases [108]. The quantized conduction band state becomes even Rashba split [109]. We, however, have not observed such strong doping and quantization effects in the samples investigated by us. Either our vacuum system "lacks" the residual gases responsible for the effects, which is unlikely since the CO is the most promising candidate to cause these effects [92] and is a typical residual gas in any vacuum system, or there is a connection to the growth of the samples, i.e., the intrinsic doping. There is plenty of room for speculation since we cannot directly compare to samples from the literature. Nevertheless, it shall be mentioned that such effects can strongly distort a spin resolved measurement because it lasts typically a couple of hours to gain a spectrum of substantial statistics.

Another interesting effect, which we have observed in our Bi_2Se_3 samples is a strong sensitivity of the photoemission signal when exposing the samples to the photon beam with the sample kept at room temperature. To verify this, we present in Fig. 4.14 a series of valence band spectra which have been measured subsequently under the continuous exposure to photons of $h\nu$=21 eV. We have used the snapshot mode of the Scienta R8000 analyzer which collects the photoelectrons of a fixed energy window the size of which is determined by the pass energy which was set to 5 eV. The time step between each measurements is 5s. In Fig. 4.14 a) we show the photoemission signal approximately 10s after the exposure to the beam. The band structure appears well defined and the surface state is sharp and well pronounced. All features become more and more blured as the exposure time increases which is nicely seen in panels b) through h). The dashed lines mark the initial position of the bottom of the conduction band and of the Dirac point. While especially the Dirac point appears shifted when comparing, e.g., panel a) and h) we attribute this effect to the blurring of the picture and not to doping. When moving the

sample relative to the beam the initial sharp picture can be reproduced and the blurring effect can be observed from the beginning. This demonstrates that the effect is caused by the photon beam and not simply by residual gases, since the latter would affect the whole sample right after cleavage. The photons are concentrated on a relatively small spot and it is likely that the high intensity locally distorts the surface. Interestingly, at low temperatures the photoemission signal is very stable and similar effects are not observed. As will be seen in the next chapter, impurities stabilize the photoemission signal also at room temperature. It is thus likely that surface defects play a role and destabilize the surface structure. As soon as the defects get occupied by impurities a stabilization occurs.

The sensitivity has an influence on the spin resolved photoemission as well. The decrease in quality and intensity reduces the count rates and aggravates the distinction of bulk and surface states. While the arguments given up to now on the reduced spin polarization have been mainly extrinsic, on an ill-defined surface the intrinsic spin polarization may also be reduced. The strong defect potentials will increase the scattering rates and thus reduce the spin polarization.

Summary of Conclusions

By conducting spin and angle resolved photoemission we have shown that the Bi_2Se_3 and Bi_2Te_3 samples grown by our collaborators L. Yashina and A. Volykhov from Moscow State University show the predicted characteristics of topological insulators in agreement with previous results [2, 3, 81]. We found a spin polarization of the topological surface state of Bi_2Te_3 of $\sim$70%, which is substantially more than reported recently [81] and more than the maximum value expected from DFT calculations [80]. The spin polarization in Bi_2Se_3 was found to be lower for the topological surface state, reaching values of $\sim$50%. However, several arguments have been presented that may explain the limited spin polarization as caused by extrinsic effects, mostly by the limited resolution. In this context a sensitivity of the measured band structure of Bi_2Se_3 to photons has been presented as well, which has not yet been reported. Nevertheless, it may still be doubted that the surface states of Bi_2Se_3 and Bi_2Te_3 are really 100% spin polarized.

Additionally, a high spin polarization was observed in both systems in an energy range where bulk and surface state cannot be distinguished anymore, which suggests a hybridization of bulk and surface states, which is supported by results from polarization dependent angle resolved photoemission.

A temperature dependent shift of the band structure of Bi_2Te_3 has been observed and discussed within the framework of electron doping caused by residual gas adsorption.

Now, that the basic properties of the topological insulator phase in Bi_2Se_3 and Bi_2Te_3 are discussed with respect to our photoemission results, in the following chapter we will present our systematic study of the influence of diverse adsorbates on the surface electronic structure. Our focus is set to magnetic impurities, i.e., Fe, since interfaces between topological insulators and ferromagnets are of special interest for electronic and spintronic devices due to the possibility of opening a band gap at the Dirac point by breaking time reversal symmetry.

Chapter 5

Robustness of Topological Surface States

The surface states of topological insulators are predicted to show a unique robustness [39]. From the viewpoint of topology the existence of the surface state is guaranteed simply by the fact, that across the interface between a topological and a trivial insulator the $\mathbb{Z}_2$ number, defined in Chapter 3 changes from non-trivial to trivial. From an electronic structure point of view, a topological insulator is characterized by a band inversion that occurs when spin-orbit interaction is *switched on* [64]. Further, if one would be able to smoothly increase the spin-orbit interaction and follow the evolution of the band structure then the change of the $\mathbb{Z}_2$ value would occur when the trivial band gap is closed and reopens as an inverted band gap [110]. Heuristically, one can conclude that if the $\mathbb{Z}_2$ value changes across the interface, then somewhere along the way the band gap must be closed. This is provided by the existence of a surface state. In turn, the only way to get rid of the surface state is to have both materials in the same topological class or to make the $\mathbb{Z}_2$ number ill-defined. The former naturally explains the expected robustness of the surface state, since the only way to change the $\mathbb{Z}_2$ value is to close the inverted *bulk* band gap of the topological insulator or to introduce a band inversion in the trivial insulator. The robustness will be demonstrated in the first part of this chapter taking oxygen and silver as an example.

How can we make the $\mathbb{Z}_2$ number ill-defined? The $\mathbb{Z}_2$ number is defined for *time reversal symmetric* systems, only [42]. Thus, if we break time reversal symmetry, the $\mathbb{Z}_2$ number loses its meaning and the surface state its protection against gaps. This *ill-definition* of the $\mathbb{Z}_2$ number has been used to demonstrate the two-dimensional topological insulator phase in HgTe/CdTe quantum wells [48]. Time reversal symmetry was broken by an external magnetic field applied perpendicular to the quantum well plane and this caused a breakdown of the topological insulator phase [48]. For three-dimensional topological insulators much more efficient than an external magnetic field would be the exchange field of a magnetic film deposited directly on the surface. We will follow this approach in the second part of this chapter, where we investigate the influence of Fe impurities on the surface state. We will, however, show that we can deposit a massive amount of Fe *without* opening a gap at the Dirac point which can be interpreted as a first step to functional devices made of topological insulators and ferromagnets.

5.1 Non-Magnetic Impurities

In the following sections we investigate the effect of non-magnetic impurities. We show a controlled oxidation of the surface of Bi_2Te_3 and the surface deposition of Ag on Bi_2Se_3.

5.1.1 *In Situ* Oxidation of Bi_2Te_3

The robustness of the topological surface state is one of its most interesting characteristics. A trivial surface state always contains of a pair of states with opposite spin at each point in k-space. Assume that a trivial insulator has surface states containing of two Dirac cones lying on top of each other or being shifted in momentum but not in energy against each other. Then any distortion is able to introduce a gap without violating time reversal symmetry as long as both states get gapped. The topological insulator with its single Dirac cone on the surface on the other hand can not get gapped without breaking time reversal symmetry. The existence of a gap necessitates that the state has the same spin in both halves of the surface Brillouin zone, otherwise there would be a discontinuity in the spin eigenfunction at zero momentum. Consequently, a perturbation that does not violate time reversal symmetry cannot introduce a gap.

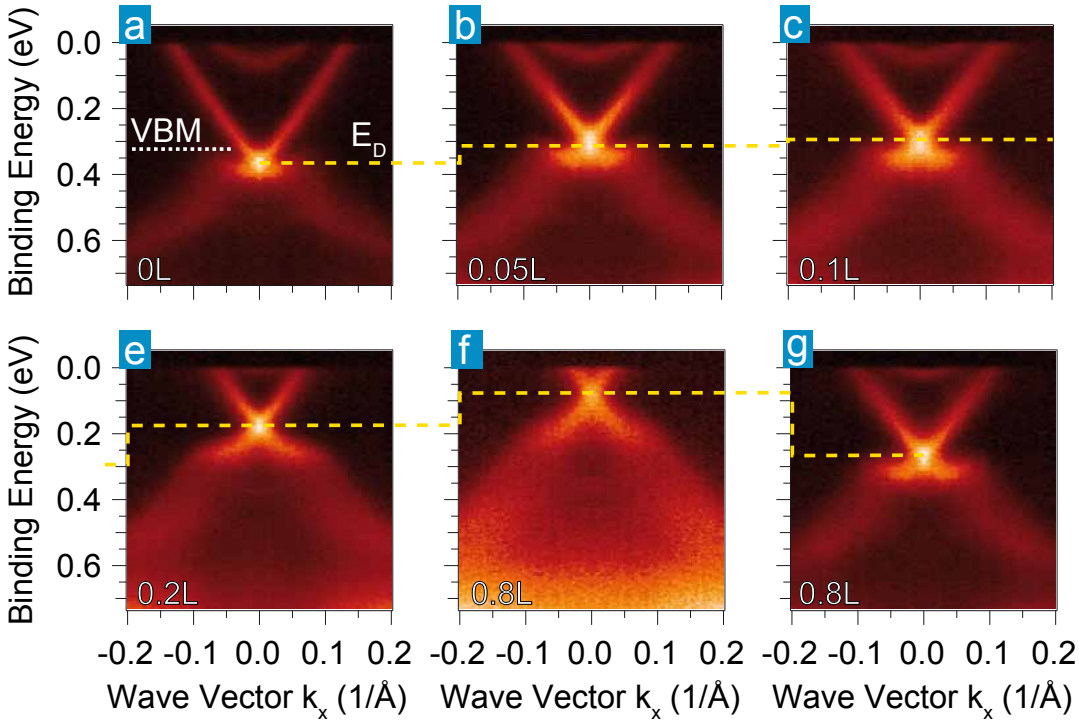

Figure 5.1: Monitoring the effect of exposing Bi_2Te_3 to oxygen with 50 eV photons. The temperature was set to 50 K during measurement and exposure. The dose is increased from 0 Langmuir (L) in a) to ∼0.8 L in f). A strong hole doping is observed but the band structure shifts non-rigidly. The yellow dashed line marks the shift of the Dirac point. The white dashed line marks the valence band maximum (VBM) in a). An over night warm up to 280 K releases most of the oxygen and the Dirac point appears at a similar position as for 0.1 L (g).

In Fig. 5.1 the surface state of Bi_2Te_3 is after cleavage exposed to an increasing dose of oxygen. The photon energy was set to 50 eV and the measurement as well as the deposition temperature was set to 50 K. Dispersions are taken along the $\overline{\Gamma K}$ direction. The dose is given in Langmuir (L), where 1 L$\sim 1.33\times10^{-6}$ mbar·s. In the clean sample (a) the Dirac point is observed at $\sim$365 meV binding energy. The bottom of the bulk conduction band is clearly visible at this photon energy, stage of intrinsic doping and temperature. After 10 s at a partial O_2 pressure of 5×10^{-9} mbar corresponding to $\sim$0.05 L the Dirac point has shifted to a slightly *lower* binding energy of $\sim$310 meV. Also, a small shift of the bulk conduction band is obvious. But if quantified, its shift is with less than 30 meV only about half the value of the Dirac point. Doubling the dose further shifts the Dirac point but less clearly. But at 0.2 L (e) there is again a very pronounced shift in the low binding energy direction of $\sim$120 meV. At this dose, the difference in the shift between surface and bulk bands is undeniable. Now the Dirac point lies above the top of the bulk valence band while in a clean sample, the Dirac point is fringed by the top of the valence band in all $k_{||}$-directions as indicated by the white dashed line in panel a) that marks the valence band maximum (VBM) along the $\overline{\Gamma K}$ direction. The binding energy of the Dirac point is now $\sim$175 meV and the total shift amounts to 190 meV. Directly at the Fermi level, between the two branches of the topological surface state a very faint trace of the bulk conduction band is still visible. Considering that the binding energy of the conduction band in the clean sample is about 60 meV (a) we can quantify the shift to be about 50 meV. In f) the dose is increased to 0.8 L and causes a further shift of the Dirac point of $\sim$100 meV and the binding energy is 75 meV. Assuming that the conduction band shifts by a similar amount than it did between 0 and 0.2 L it should now lie above the Fermi level and the band structure of Bi_2Te_3 would resemble that of a bulk insulator. But for the following reasons one is not allowed to draw such a conclusion from the presented photoemission results. First the absolute value of the Fermi vector k_F of the surface state is now $\sim$0.02 Å^{-1} and the half width at half maximum of the momentum distribution curve peaks is of similar size. Thus, there is an overlap of the peaks in the photoemission signal and it is impossible to decide whether there is spectral weight of the conduction band left or not. Second, assuming that the conduction band does not contribute to the photoemission signal anymore at 50 eV photon energy it is necessary to scan the full k_z range by varying the photon energy (compare Chapter 2) in order to decide if the conduction band is really above the Fermi level and does not disperse back in at a different k_z. And third, one should not forget that we probe only a few atomic layers in photoemission and we can thus not conclude on the bulk properties at all. To clarify the conductance of the bulk, transport measurements would be necessary for oxidized samples. An effect on the properties deep in the bulk can, however, only be expected if the adsorbate moves into the bulk.

We have remeasured the sample after one night keeping it on the manipulator in ultra high vacuum with the cooling switched off. The sample temperature reached about 280 K over night and the result after cooling back to 50 K is presented in panel g). The Dirac point has shifted back to the position where it was found for $\sim$0.1L. The bulk conduction band is visible at the Fermi level but at a binding energy comparable to a dose of 0.2L. It can be concluded that the oxygen is mainly physisorbed on the sample, in contrast to the case of Ag or Fe discussed below. The observed reversibility indicates that O_2 does not dissociate and that the binding energy shifts are more likely caused by a change in the surface potential instead of a transfer from charge carriers between substrate and added molecules.

A similar shift of the band structure on O_2 dosage has been observed for Bi_2Se_3 but the question of reversibility of the effect has not been addressed [111].

5.1.2 Ag on Bi_2Se_3

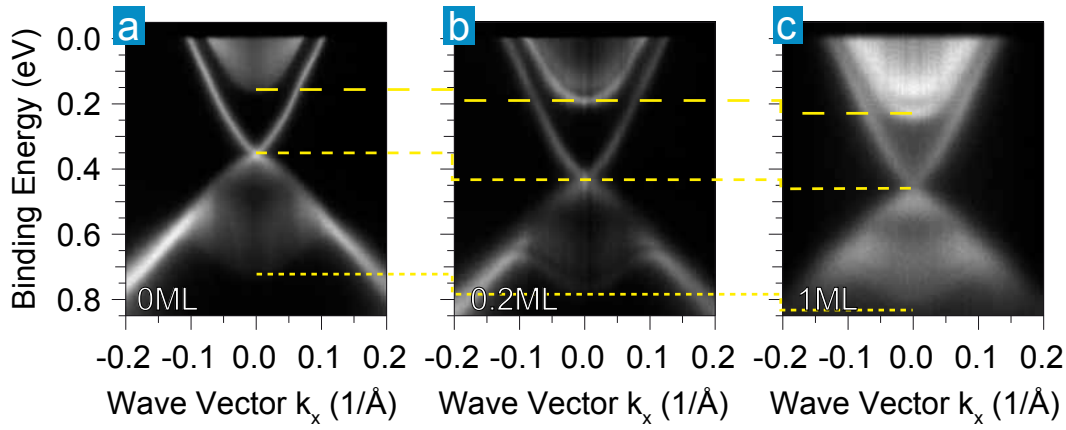

Figure 5.2: Room temperature deposition of Ag on Bi_2Se_3 leads to a strong electron doping as obvious from the two subsequent deposition steps of 0.2 ML and 1ML. As indicated by the yellow dashed lines all features get shifted to higher binding energies. The surface state shifts stronger than bulk conduction and valence band. Additional states appear in the valence and conduction band. The measurement temperature is 10 K and the photon energy was set to 18 eV.

Beyond the proof of concept, namely the robustness of the surface state, it is interesting for future applications to investigate the effect of metals deposited on the surface of a topological insulator. A successful integration in electronic circuits will necessitate a contact between a metal and the topological insulator surface. As an example we study Ag deposited on the surface of Bi_2Se_3.

The sample has been cleaved at ∼10 K. The dispersion of the clean surface is measured with 18 eV photons along the $\overline{\Gamma K}$ direction as shown in Fig. 5.2 a). We observe a very sharp topological surface state and the Dirac point, marked by a yellow dashed line with medium distances, is observed at a binding energy of ∼350 meV. As before, the sample shows a high intrinsic n-doping and the bottom of the conduction band at $\overline{\Gamma}$ is found at a binding energy of ∼150 meV for the given excitation energy and is marked by the dashed line with the largest distance between the dashes. As a third fix point we mark the bottom of the valence band, where the photoemission intensity vanishes at $\overline{\Gamma}$ with the smallest distance dashed line at ∼720 meV.

For the Ag deposition, the sample has been removed from the cooled manipulator and has been allowed to warm up for 10 minutes on a wobble stick before exposing it to the Ag atom beam. We estimate the temperature to be above 150 K during the deposition. Ag has been evaporated from a Ag rod heated by an electron beam. A high voltage of 2.5 kV has been applied between the Ag rod and a tungsten filament and for an emission current of 3.0 mA we found a rate of ∼ 0.1 monolayer (ML) per minute on a quartz microbalance placed at the same position as the sample during deposition.

After 2 minutes of deposition, corresponding to 0.2 ML, the surface state has shifted to higher binding energy and the Dirac point appears at ∼430 meV corresponding to a shift of ∼80 meV (Fig. 5.2 b)). The bulk valence and conduction bands appear to be shifted less than the surface state. On the one hand, one may expect such a result, as a surface deposition should effect the surface located states much more than the bulk states. On the other hand, the bulk bands have changed in a peculiar way. While the parabolic outline of the conduction band in a) is *filled* with intensity up to the Fermi level, we observe two sharper states in b). A similar effect is seen for the valence band, where a single broad feature is divided into two sharper features which mimic the shape of an M as they merge with the surface state away from $\overline{\Gamma}$. As we increase the amount of Ag to the mass equivalent of a full monolayer, the chemical potential further shifts in the same direction and the Dirac point is seen at ∼460 meV. Since a much higher amount of Ag added in the second deposition step shifts the band structure much less than the first deposition step, we assume that the shift of the chemical potential is saturated at some point. This assumption will turn out to be justified during the discussion of Fe impurities on Bi_2X_3 in the following sections.

Interestingly, the newly formed bands in the conduction and valence band have shifted by a similar amount in the second deposition step as compared to the first step and even more than the surface state. As the quality of the overall signal is reduced for the full monolayer, with all states appearing much broader than for 0.2 ML the M-shaped bands are not anymore clearly observed. Another remarkable result is the change of the relative intensities of the two nested parabolas in the conduction band. While for 0.2 ML the band at higher binding energy is more pronounced, for the full monolayer the lower binding energy one is more intense. In both cases we do not observe a splitting of the bands in k-space, i.e., a Rashba splitting as has been reported for many electron doping surface impurities, like e.g. CO [92], H_2O [112], Rb, Cs, and Gd [113], and K [114].

These findings have been confirmed in a related study [115]. In addition to photoemission results the authors show in STM that the Ag intercalates into the van der Waals gap[1] of the crystal structure. From this the authors conclude that the elevated topmost quintuple layer with the Ag underneath leads to the formation of the two dimensional extra states at the Fermi level which we have discussed above as being derived from the bulk conduction band. This is in contrast to the explanation given by Bianchi *et al.* who have explained the two dimensional states as quantum well states due to band bending effects [92]. In addition, the authors of Ref. [115] report that the topological surface state becomes trivial at least in the topmost quintuple layer as they find it becoming parabolic in the second derivative plot of the intensity map. An intercalation appears reasonable also in our case. The main supporting argument is that there is no obvious increase in the background intensity. However, we do not observe a change in the dispersion of the surface state. As can be seen in Fig. 5.2 a) the surface state of the pristine sample does not disperse linearly through the Kramers degeneracy but has a finite effective mass. This could be misinterpreted as a parabolic band without a Dirac point. In addition it is very important to align the sample exactly to normal emission as a small misalignment can even appear as a gap in the dispersion as discussed in Chapter 4.

Still, the described scenario with the Ag intercalating into the van der Waals gap is not unlikely to cause the observed changes in the band structure. Assuming that the

[1]The region between two quintuple layers is only weakly bond by van der Waals forces, therefore the name van der Waals gap.

intercalated Ag further decouples the top most quintuple layer from the rest of the sample we expect the decoupled layer to develop the dispersion of an isolated quintuple layer. The crossover from two to three dimensions has been nicely demonstrated for samples grown *in situ* by molecular beam epitaxy [116]. Indeed, for 1 quintuple layer, instead of the well known band structure of a bulk sample, only one parabolic band has been observed in photoemission close to the Fermi level at $\overline{\Gamma}$. In principle it is possible that the photoemission signal shows a superposition of the three and the two dimensional band structure, i.e., of a bulk and a one or few quintuple layer sample. In DFT calculations Eremeev *et al.* where able to show, that an expansion of the size of the van der Waals gap leads to the emergence of parabolic bands below the conduction band [117]. Moreover, these bands get energetically more separated from the conduction band states as the quintuple layer distance increases. Also the Rashba splitting was considered. The Rashba parameter α_R which gives the size of the splitting was found to be a function of the quintuple layer distance but it was found to increase up to an expansion of the van der Waals gap of 30% and beyond this value decrease again. The expansion is mainly determined by the type of intercalated species, i.e., their size. It could thus be an explanation why no splitting is observed with Ag, while larger atoms such as Rb, Cs, Gd [113] and K [114] produce a splitting.

5.2 Magnetic Impurities

In the previous section we have shown that the topological surface state, in contrast to its counterpart in trivial insulators is really robust against impurities. We have seen that the electronic structure can be tailored and that we can remove the bulk density of states of the conduction band in our photoemission spectra.

Qualitatively, this confirms the expectation for an ideal topological insulator. Next, we will show the effect of magnetic Fe deposited on the surface of Bi_2Te_3 and Bi_2Se_3 after discussing why such systems are important.

The interest in interfaces between topological insulators and ferromagnets is mainly motivated by the idea that a magnetic field will break time reversal symmetry and the lifting of the Kramers degeneracy $E(k,\uparrow) = E(-k,\downarrow)$ causes a gap in the topological surface state at zero momentum (wave vector $k = 0$). A very convincing probe of this characteristic point was already given in the first experimental study on the two dimensional topological insulator phase of HgTe/CdTe quantum wells in 2007 [48]. For a magnetic field oriented perpendicular to the quantum well plane a breakdown of the four-terminal conductance has been reported. The observed cusplike signature of the magnetoconductance has a full width at half maximum (FWHM) of 28 mT, thus already a small magnetic field ($\sim$14 mT) opens a band gap in the edge channels. Tilting the angle of the magnetic field with respect to the quantum well plane continuously increases the FWHM of the magnetoconductance peak and for the magnetic field within the quantum well plane a value of $\sim$0.7 T was reported for the FWHM. Furthermore, the authors pointed out that the gaps for the in-plane and out-of-plane magnetic fields differ from one another and the relative size was estimated with $E_{gap\perp}/E_{gap\parallel} \sim 10^2$.

Despite the fact that an external magnetic field would distort the photoelectrons in our experiment, it is much more efficient to deposit a ferromagnetic overlayer or ferromagnetic impurities. If the impurities really stay on the surface of the three dimensional topological insulator one may assume – appropriate magnetization provided – that the time reversal

symmetry is broken only at the surface and not in the bulk which is a precondition for observing the topological magnetoelectric effect. A magnetoelectric effect is defined as a magnetization induced by an electric field, or alternatively, a charge polarization induced by a magnetic field [118]. As the topological surface state resembles a two dimensional electron system, the breaking of time reversal symmetry by a magnetic field will lead to a quantum Hall state which is anomalous because of the fact that there is a single, i.e., an odd number of fermionic states on the surface. Consequently, this leads to a quantized Hall conductance of $\sigma_H = (2n+1)\frac{e^2}{2h}$, whereas e is the electron charge, h is Planck's constant and n is an integer. Thus, the conductance is fractional and not integral as in the conventional quantum Hall effect described in Chapter 3. Such a half-quantum Hall effect has been proposed in other systems, but in trivial systems there are always at least four degrees of freedom, left and right movers with a spin up *and* a spin down channel. The doubling of the channels will always lead to a total Hall conductance which takes an integral value. This doubling does of course not take place in a topological insulator with its odd number of fermions. In a dc transport experiment the half-quantum Hall effect cannot be observed since the whole surface is gapped as it is a closed manifold without any edges and thus no edge states can exist. However, the observation of unconventional Landau quantization in an external magnetic field, observed by means of scanning tunneling microscopy in Bi_2Se_3 is a strong indication for the realization of a quantum Hall effect in topological insulators [96, 97].

If magnetic impurities on the surface form a domain wall in a ferromagnetic phase then the Hall conductance has a jump across the wall and a chiral gapless edge state propagates along the domain wall [118]. The jump of the Hall conductance across the domain wall is, however, $\Delta\sigma_H = e^2/h$ and this will be the conductance measured in a dc transport experiment with the leads attached to the domain wall in the same manner as for a common Hall bar. Considering a cylindrical topological insulator with the side surfaces covered by a magnetic film magnetized radially, Qi, Hughes, and Zhang where able to show theoretically that an electric field $\mathbf{E}$ applied perpendicular to the top and bottom surface induces a Hall current $\mathbf{j}$ circling around the side surface, thus perpendicular to the electric field. This current, given by $\mathbf{j} = \frac{m}{|m|}\frac{e^2}{2h}\mathbf{n}\times\mathbf{E}$ induces a magnetic field parallel or antiparallel to $\mathbf{E}$. The unit vector $\mathbf{n}$ is normal to the side surface of the cylinder and the sign of the mass $\frac{m}{|m|}$ is determined by the direction of the magnetization on the side surface. The induced magnetization is then proportional to the electric field

$$\mathbf{M_H} = -\frac{m}{|m|}\frac{e^2}{2hc}\mathbf{E}. \tag{5.1}$$

There is no dependence on any material parameter and the magnetization can thus be viewed as a *topological response* of the system to the electric field. In addition, it contains the half-quantum Hall conductance and the topological magnetoelectric effect can thus be viewed as a measure of the *half-quantum Hall* or *quantum anomalous Hall effect*.

Another proposal, closely connected to the magnetoelectric effect is that a point charge placed closely above the ferromagnet-topological insulator interface will not solely induce an electric field inside the bulk which can be described by a mirror charge but also a magnetic field that would resemble an image magnetic monopole inside the topological insulator bulk [119]. More effects with a close connection to the magnetoelectric effect have been given in the literature and they have been reviewed by Qi and Zhang in Ref. [118].

While these effects appear more or less academic many other proposals already aim at applications by considering the magnetotransport. For example the inverse spin-galvanic

effect at the ferromagnet-topological insulator interface uses the coupling between the magnetic moment and the surface electric current to flip the magnetization of the ferromagnetic overlayer with the surface current by 180° dissipationless, i.e., without the generation of Joule heating [120].

Also the magnetoresistance has been considered and theoretically high values are expected for periodic magnetic modulations [121], for a ferromagnet/ferromagnet junction [122], and even for a single ferromagnetic barrier [123]. The magnetoresistance for ferromagnets on topological insulators is special as it is observable also for a magnetization which is parallel to the surface but canted with respect to the direction of current flow with the maximum effect for a perpendicular configuration. If we consider a coordinate system with the x direction along the current density and together with the y direction within the surface plane and the z direction perpendicular to both, then a magnetization oriented along the y direction shifts the two dimensional Fermi surface of the topological surface state along the k_y direction in momentum space. Hence, the overlap of Fermi surfaces between the regions inside and outside of the ferromagnet is suppressed and leads to a large magnetoresistance which is not observed in common systems [122].

Several experimental studies have investigated the effect of magnetic moments on the topological surface state. When Bi_2Se_3 is p-doped (hole doped) in the bulk by Mn, it is possible to move the Fermi level into the bulk band gap [111]. Bulk Mn doping of Bi_2Te_3 has led to ferromagnetic order below temperatures of 12 K [124]. Unfortunately, photoemission of the Dirac point region remained inconclusive for these systems, due to the strong p-doping and unclear position of the Dirac point [124]. For Bi_2Se_3, doped with Fe in the bulk, a band gap in the surface state dispersion at Fe concentrations in the melt composition and relative to Bi reaching from 5% to 25% [111] have been reported. This gap appears to be tunable with the amount of Fe which confirms the assumption that the gap is caused by the magnetic field as a higher amount of Fe means more magnetic moments and thus a higher field-strength. But the magnetic characterization showed that for Fe concentrations below 16%, like e.g. 12% where the observed size of the energy gap amounts to 45 meV, the system remains paramagnetic down to T=2 K which is below the temperature of the ARPES measurements of 10 K [111]. As the characterization technique used lacks surface sensitivity the authors speculate in the supporting online material[2] of Ref. [111] that impurities on the surface may have been ferromagnetically aligned via a Ruderman-Kittel-Kasuya-Yosida (RKKY) interaction with the surface state as it was suggested by Liu *et al.* [125]. Only recently mean-field calculations showed that a finite temperature window may exist in magnetically doped topological insulators in which the surface is ferromagnetic while the bulk stays paramagnetic [126].

According to Liu *et al.*, the RKKY interaction will lead to a magnetization which is always ferromagnetic when the Dirac point energy (E_D) lies at or very close to the Fermi level. The RKKY interaction oscillates between ferromagnetic and antiferromagnetic action and the period is given by the Fermi wavelength ($\lambda_F = 2\pi/k_F$) of the carriers that support the mediation. Consequently, the mediated action is always ferromagnetic when $E_D = E_F$ as k_F equals zero then and λ_F points towards the infinite. If $E_D \neq E_F$ than the average impurity distance must be smaller than the according Fermi wavelength. Gao *et al.* pointed out that for the *two dimensional* topological insulator the RKKY interaction mediated by the helical edge states leads to a noncollinear exchange coupling between two spins on the system which is in plane [127]. Furthermore, the angle between the spins can

[2] URL:www.sciencemag.org/cgi/content/full/329/5992/659/DC1

be controlled by adjusting the Fermi level. Randomly distributed ferromagnetic impurities on the surface of a three dimensional topological insulator have been investigated by Abanin and Pesin [128]. They found, that the *in plane* component of the spin will get frustrated due to a coexistence of ferromagnetic and antiferromagnetic exchange in orthogonal directions, independent of the microscopic details. Thus, the out-of-plane ferromagnetic configuration is always favored below a critical, but finite, temperature T_c which was estimated to be 30 K for Bi_2Se_3[3]. Furthermore, it has been argued that potential scattering will suppress the magnetic ordering process [128]. In contrast, Biswas and Balatsky argued that the magnetic impurities induce nontrivial spin textures and that the RKKY interaction, therefore, becomes anisotropic and the sign of the interaction, i.e., ferro or antiferromagnetic coupling depends on the induced spin texture. Only a high impurity density favors the out-of-plane ordering when the Dirac point is *at* the Fermi level [129].

Experimentally, Wray *et al.* report a band gap opening at the Dirac point – thus, lifting it – observed in angle resolved photoemission for Fe impurities deposited directly and *in situ* on the surface of Bi_2Se_3 [130]. The size of the gap amounts to ∼100 meV for a mass equivalent of 0.2 ML (monolayer) of Fe. No external field was applied for the magnetization and the authors speculate that the appearance of a band gap indicates a magnetization mediated by the surface electrons as predicted by Liu *et al.* and that the magnetization points out-of plane since an in-plane magnetization would simply shift the Dirac cone in k-space but not open a band gap [130]. Please note that such a shift in k also breaks time reversal symmetry. On the other hand, Fu found that an in-plane magnetic field may introduce a gap if hexagonal warping is present [19]. The latter leads to an out-of-plane rotation of the spin away from $\overline{\Gamma M}$ as discussed in detail in Chapter 4, and Zeeman splitting induced by an external field introduces a mass term which lifts the Kramers degeneracy of the topological surface state shifted in k-space.

Despite the fact that the conclusion of an out-of-plane magnetization is speculative for both, Fe in the bulk of Bi_2Se_3 [111] and on the surface [130] the shape of the gaps reported is very different. While the former resembles the simple expectation and the Dirac-cone is deformed into two parabolic bands with opposite signs of the effective mass, in the latter the lower half of the previous Dirac bands appears with the shape of the letter M and has a local minimum at $\overline{\Gamma}$. Thus, the band masses have the same sign at $\overline{\Gamma}$ for the upper and lower half. If the gaps in the two studies were caused for the same physical reason, i.e., a surface Fe layer magnetization, one would expect the gaps to have a similar shape. Naturally, one may ask the question whether both gaps are really due to a magnatization of the Fe impurities? We will address and answer this question to some extent with the help of our own results.

5.2.1 Fe on Bi_2Te_3

That the Dirac point in Bi_2Te_3 is somewhat hidden under the spectral weight of the bulk valence band makes it more challenging to investigate *gap opening phenomena* in this system as compared to Bi_2Se_3. This could be a reason why a larger amount of work has been done on Bi_2Se_3. When we started to investigate the effects of Fe on Bi_2Te_3 no related studies where published neither for Bi_2Te_3, nor for Bi_2Se_3. For the first batch of samples available to us, we found that the quality of the Bi_2Te_3 samples was better than that of Bi_2Se_3 and we decided to start out with the former. Therefore, we have studied Fe on

[3] Above a critical value of the relative ratio between in- plane and out-of-plane exchange coupling ($\delta = \mathbf{J}_{||}/\mathbf{J}_{\perp}$) the system stays paramagnetic for finite temperatures and turns into a *spin glass* at T=0 K [128].

Bi_2Te_3 up to much higher coverages than Bi_2Se_3 and the doping effects of the adatoms can be discussed more precisely with respect to Bi_2Te_3 than for Bi_2Se_3.

The *burried* Dirac cone makes it necessary to select a suitable photon energy, where the interplay of matrix element effects, atomic photoionization cross sections, and, for the bulk states, the k_z dispersion, are giving the best contrast for the Dirac point. We found that 55 eV pretty much enhances the intensity of the surface state over the bulk states and we thus favored this energy over lower photon energies despite a small loss of resolution which has to be paid at higher photon energies.

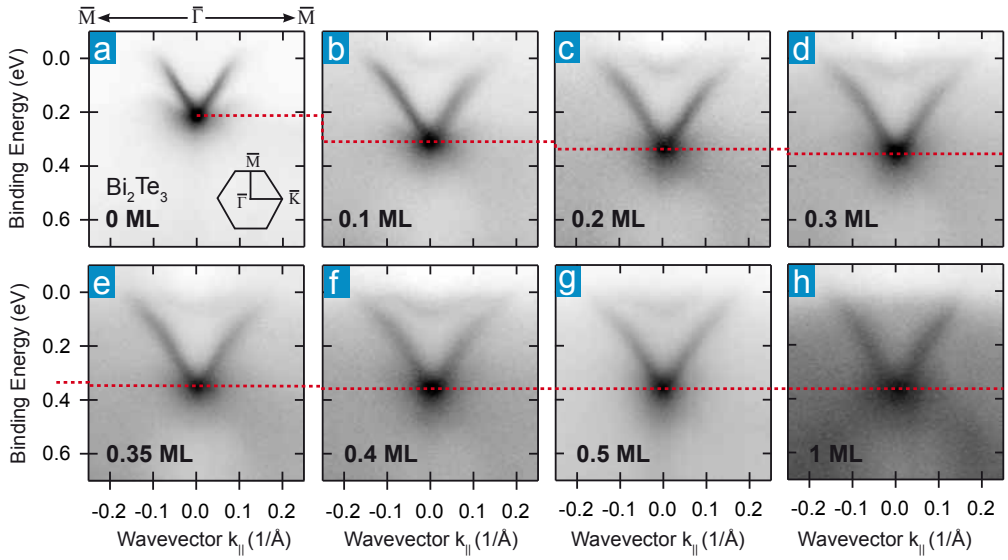

Figure 5.3: Effect of Fe impurities on the topological surface state of Bi_2Te_3.
a) Dispersion of the topological surface state of pristine Bi_2Te_3 measured at room temperature along the $\overline{\Gamma M}$ direction with 55 eV excitation energy. The inset shows the surface Brillouin zone and the red dashed line marks the energy position of the Dirac point E_D. b-h) Incremental increase of the deposited Fe mass from 0-1 monolayer (ML). A strong rigid-like shift of the dispersion is observed (b-f) together with the emergence of extra states at the Fermi level. The shift saturates at mass equivalents of 0.3-0.5 ML Fe (d-g). Even for thicknesses as high as 1 ML the topological surface state appears intact (h).

Doping effect of Fe on Bi_2Te_3

Fe impurities were evaporated directly from an Fe rod heated by an electron beam. Typical values of operation are 3.0 kV voltage between rod and filament and 4-5 mA emission current. Calibration of the evaporator was done by use of a quartz microbalance and rates were set to ∼0.05-0.1 monolayers (ML) per minute. The calibration was repeatedly confirmed during a set of subsequent deposition steps. To reduce the amount of evaporated contaminants, the evaporator was carefully degassed until total pressures during evaporation below 2×10^{-9} mbar were reached. This appears sufficient as we did not observe any additional contaminations besides the designated Fe in core level spectroscopy.

We have evaporated Fe in subsequent steps of 0.1 ML with the sample kept at room temperature from the moment of cleavage on. The effect on the topological surface state is shown in Fig. 5.3. For the pristine sample the Dirac point (E_D) is found at ~210 meV binding energy (a). Here we show angle resolved photoemission data collected along the $\overline{\Gamma M}$ direction. The warping related decrease of the group velocity, discussed in Chapter 4.1.2, is not yet pronounced for the given intrinsic doping. The bulk conduction band is not visible due to the k_z dispersion of the three dimensional states. The deposition of Fe shifts the electronic structure of the surface state rigidly towards higher binding energy reflecting an electron doping effect of the Fe (n-type). The effect can be traced best by following the Dirac point in panels a) through f) which is marked by the red dashed line and by comparing the energy distribution curves at zero momentum, i.e. $\overline{\Gamma}$, plotted in Fig. 5.4 a). The shift saturates between 0.4 and 0.5 ML which could be confirmed in different samples

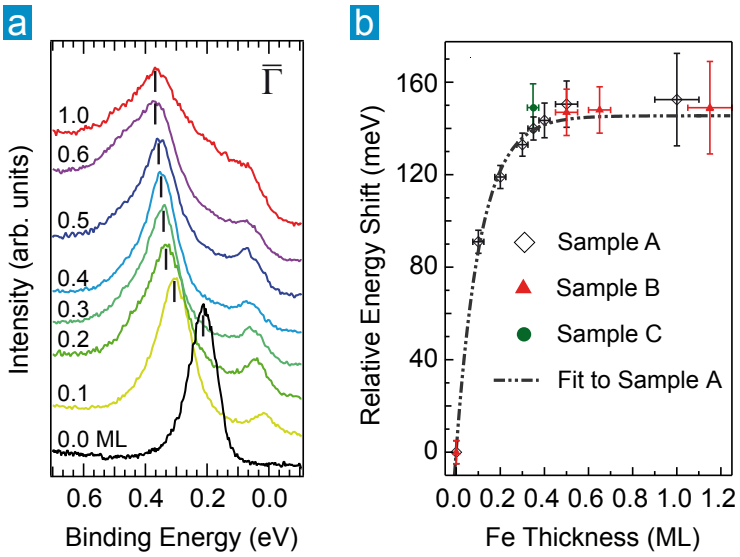

Figure 5.4: Binding energy shift of the Dirac point with increasing Fe deposition on Bi_2Te_3 at room temperature. a) Energy distribution curves at zero momentum ($\overline{\Gamma}$) for different Fe amounts. Black vertical ticks mark the position of the Dirac point. b) Relative energy shifts as a function of the Fe deposited mass in units of monolayer equivalents from three different Bi_2Te_3 samples. The shift undergoes a saturation and can be fitted by an exponential function (black dashed line). Within the error the n-type shift was reproduced in all samples.

as shown in panel b) of Fig. 5.4. Here, the relative shift of the Dirac point with respect to its initial position in the pristine sample is plotted against the deposited Fe mass in monolayer equivalents. All three data sets follow the exponential curve which has been fitted to the set of Sample A.

We have further increased the amount of Fe to mass equivalents in the full monolayer range as shown in panel h) of Fig. 5.3. Apart from the n-type shift of the band structure the most remarkable result is that the topological surface state is still visible in all stages of Fe deposition, even for the full monolayer. Neglecting the magnetic moment of Fe, this can be simply viewed as another example of the unique robustness of the surface state. Furthermore, the opening of a gap is not resolved for these room temperature

measurements. One may ask the question whether a gap is expected to open just by depositing magnetic adatoms. On a local scale, time reversal symmetry is broken whenever a magnetic impurity is present and a gap would open. However, the electronic band structure is not defined on a local scale but globally. The periodic lattice of a solid leads to the formation of energy bands but experience shows that this is the case even in an imperfect crystal with distortions, impurities and defects. Globally, we find a periodic system, but locally there are aberrations from the highly symmetric system. Thus, in the vicinity of a defect symmetries are broken. Nevertheless, band theory is based on the symmetries of the lattice. From this argument, one shall conclude that time reversal symmetry has to be broken globally and not just locally. At room temperature, Fe films in the submonolayer regime are not expected to be magnetized as the typical Curie temperatures are much lower. Even for a full *uncoated*[4] Fe(110) monolayer on W(110), neglecting the fact that it is not granted that Fe grows layerwise on Bi_2Te_3, the Curie temperature is with T_c=210 K still below room temperature [131] and T_c is found to decrease significantly as the coverage enters the submonolayer regime [132]. We can therefore expect that the magnetic moments of the Fe impurities are oriented arbitrarily and that time reversal symmetry is not broken on a global scale. Conversely, the fact that we do not see a gap in the surface state may be interpreted as a confirmation of our statement that a magnetic film has to be magnetized in order to open a gap. In a more general context of the expected enhanced scattering rates from ferromagnetic impurities due to spin flip processes, which will be the topic of Chapter 6, it means that such enhancement does not not lead to a localization of surface electrons.

Core Level Spectroscopy

As betoken above, an important aspect, is the growth of the Fe on Bi_2Te_3 and how it alters the chemical environment of adjacent crystal atoms. Some insight can be gained from photoemission of core levels. As most of our photoemission measurements where done at the UE112 beamline of BESSY II, which is a low energy beamline designed for ultimate resolution, we only investigate the low energy core levels of Bi_2Te_3, i.e., the Bi5d and Te4d states, as well as the Fe3p peak. Additionally, we need to relate the valence band dispersions at low photon energies directly to the core levels from the same sample. Reasonable light intensities can only be reached in the energy range up to $h\nu$ ∼200 eV and thus oxygen and carbon peaks are out of reach. This means also that about the purity of our sample and sample preparation can only be concluded from valence band spectra and from the lineshape of available core levels of Bi, Te and later Se.

The Bi5d state of a pristine sample gives spin-orbit split peaks with the $5d_{3/2}$ peak split-off by 3.05 eV to larger binding energy. The Te4d state produces a similar spectrum but with a two times smaller splitting of ∼1.5 eV. All peaks appear rather symmetric as can be seen in the upper inset of Fig. 5.5 a) for Bi5d and in the lower inset for Te4d (black line) or in Fig. 4.9 of Chapter 4.1.3. From all spectra a Shirley background has been removed and they have been normalized to the same area under each curve for clarity. This normalization will be justified later.

When Fe is evaporated on the sample three obvious changes occur in the spectra. First, we observe an overall shift of the peaks towards higher binding energy in agreement with

[4] If the samples are additionally coated by an Ag overlayer the Curie temperature is close to room temperature with T_c = 296 K [131]

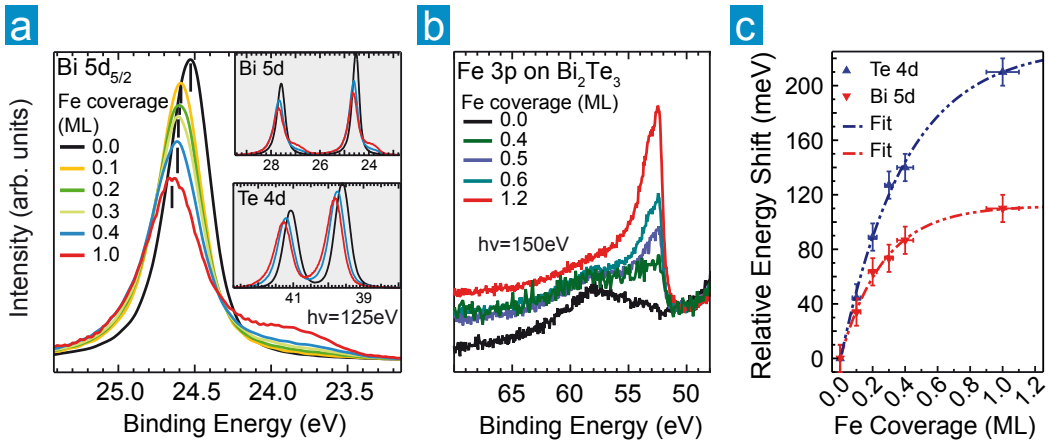

Figure 5.5: Effect of Fe deposition on the core level spectrum of Bi_2Te_3. a) The $Bi5d_{5/2}$ peak undergoes a shift to higher binding energies with increasing Fe coverage. In addition a pronounced and growing shoulder appears on the lower binding energy side. The $5d_{3/2}$ peak shows an analogous behavior as seen in the upper inset for three different Fe coverages. Te4d peaks also shift to higher binding energies while no shoulders seem to grow (lower inset). b) The increasing Fe3p peak at 52.5 eV binding energy confirms the increasing Fe coverage and that the described changes in the other core levels are really due to Fe. c) The relative energy shifts of the Te4d and Bi5d peaks (averaged over the multiplet peaks) as a function of Fe thickness shows that the core levels of Bi and Te exhibit different shifts. While the Bi5d peak seems to saturate at a similar Fe amount as the Dirac point (compare Fig. 5.4b)) the maximum shift is lower. The Te4d peaks experience a much stronger shift than Bi5d and the Dirac point and have not saturated for the available data.

the n-type shift seen for the surface state. This behavior is also seen for the Te4d states in the lower inset of panel a). However, as quantified in panel c) the Te4d peaks appear to shift more than twice as much as the Bi5d states. Even though the trend of the Te4d states (blue downwards triangles and dashed line) also follows an exponential curve, approaching an asymptotic value, it seems that the shift is not in a fully saturated regime for the highest thickness investigated by us. The shift of the Bi5d states saturates at around 1 ML which is also a higher value than observed for the Dirac cone (Fig. 5.4 b). In principle such a shift is expected as it reflects the change of the chemical potential due to electron doping. But the difference in the shifting is somewhat unexpected as one would expect a rigid shift of the complete band structure.

Second, with increasing Fe mass, we find the evolution of pronounced shoulders at the lower binding energy sides of the two Bi5d peaks as can be seen in the upper inset for both, and exemplified in the main panel of Fig. 5.5 a) for the $5d_{5/2}$ peak. The shoulders can unambiguously be assigned to a chemical shift due to a reduced oxidation state. This means that more electrons can be attributed to the Bi sites after Fe deposition. In the photoemission process the positively charged core is screened better with a higher electron density in the atom and thus the 5d electrons appear at lower binding energy.

Third, while no shoulder grows on the lower binding energy side of the Te4d peak we observe an asymmetry on the higher binding energy side of each multiplet peak. As this asymmetry deforms the peak to a lineshape which looks similar to a Doniach-Sunjic profile two explanations might be possible. On the one hand, the increased metallicity of the sample which is evident from the near Fermi edge photoemission may open a way for intrinsic plasmon excitations in connection with the photoemission process. On the other hand, a chemical shift stemming from an increased oxidation state is also reasonable. Which of these possibilities is more likely can be determined from a standard fitting procedure, which will be discussed further below.

That these changes are really caused by Fe is manifested by the growth of the Fe 3p peak which we have controlled with 150 eV excitation energy after each deposition step and put together in panel b). The broad bump visible already in the pristine sample (black line) cannot be specified in detail. One possibility would be a contamination of the sample with foreign species. The high purity materials which where used for the crystal growth may typically contain for example a very small amount of Ag and the Ag4p peak is expected at a similar binding energy. However, it is unlikely that for such a small amount of Ag (<2 ppm) a photoemission peak would be visible. Excited with different photon energies the structure appears always ∼5 eV away from the $Te4d_{3/2}$ peak. Thus an Auger peak, as it would always appear at the same *kinetic* energies, can be excluded as well as an excitation of core levels with photons from a higher diffraction order of the beamline monochromator. Most likely, the peak must be ascribed to a satellite structure of unknown origin.

Next we want to analyze the Bi5d and Te4d core levels more quantitatively. As mentioned already, the Bi5d peak develops pronounced shoulders which reflect a transfer of spectral weight from the peak ascribed to the Bi5d peak with oxidation state 3+ to a lowered oxidation state. However, already in the pristine sample the lineshape necessitates the presence of a second peak to achieve an accurate result in the fit. This is exemplified for the $5d_{5/2}$ state in the lowest panel of Fig. 5.6 a). To the experimental data, represented by black dots, two Voigt profiles have been adapted. A fit with a single Doniach-Sunjic-type asymmetric Lorentzian gave less accurate results. A similar asymmetry has been reported for the Bi4f states in $Bi_2(Sr,Ca)_3Cu_2O_y$ [133]. By comparing with electron energy loss

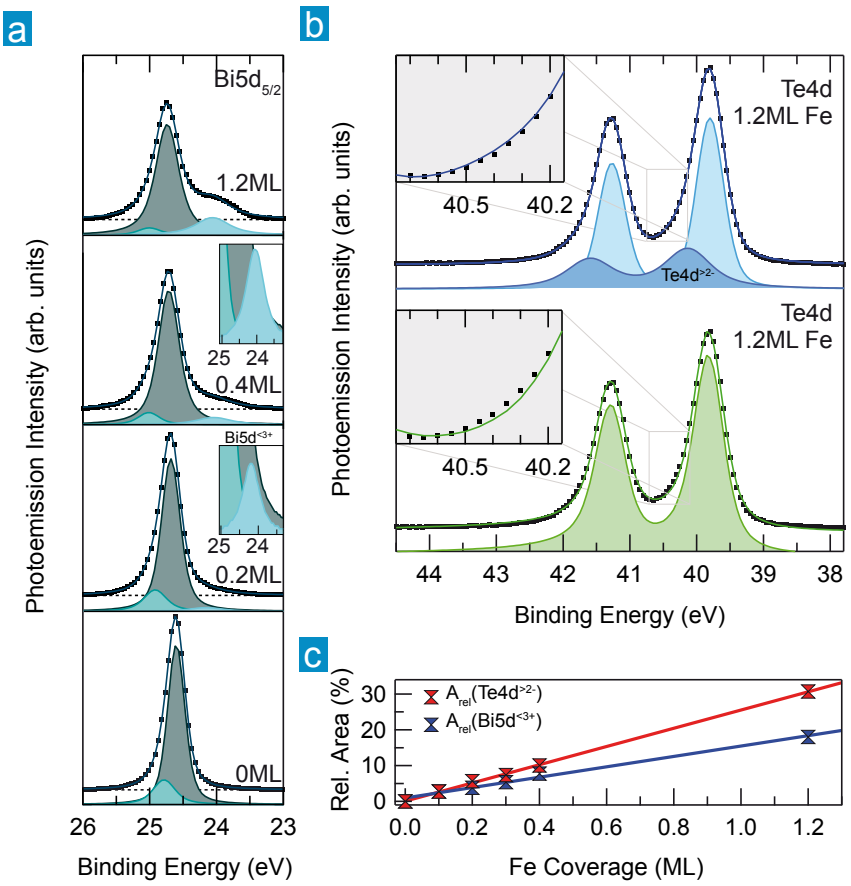

Figure 5.6: Core level analysis of Fe on Bi_2Te_3 deposited at room temperature. a) The $Bi5d_{5/2}$ of pristine (0 ML) Bi_2Te_3 requires fitting with two Voigt profiles (bottom). With increasing Fe coverage a third Voigt peak develops split off by -0.75 eV from the main peak. Simultaneously, the original peaks lose spectral weight. The insets show an enlargement of the range of the new peak for 0.2 and 0.4 ML Fe. b) Te4d develops an increasing asymmetry on the higher binding energy side. Compared is a fit with Doniach-Sunjic lineshape (bottom) to one with two pairs of spin-orbit split Voigt profiles (top). The Voigt fit is more accurate in the range of the asymmetry as shown in the insets. c) The relative area of the newly developed peaks increases linearly with the deposited mass. The area of the extra peak in Te4d increases by a factor of 1.8 faster than that of the shoulder in Bi5d.

spectroscopy data the authors attributed the asymmetry to energy loss satellites. This appears reasonable also in our case.

As the Fe coverage increases a third Voigt profile is added to the model to account for the growing shoulder on the low binding energy side. For the fit, we have started with the highest Fe coverage, i.e., 1.2 ML which is shown in the upper panel of Fig. 5.6 a). The parameters for the best fit as the Gaussian linewidth and the splitting from the main peak have been kept constant over all other Fe coverages, while the Lorentzian width has been restricted not to alter too much from the result for the highest Fe coverage. Even though this procedure does not result in the best fit possible it is the most reasonable from a physical point of view. The Gaussian broadening of the photoemission peak is caused by the finite temperature (room temperature throughout all core levels shown) and the experimental resolution, i.e., the monochromator and analyzer resolution, and is therefore assumed to be constant in all measurements. That the splitting from the main peak has to stay constant is implied in the model as the chemical shift between two oxidation states is a constant. The Lorentzian width on the other side is a measure of the lifetime of the created photohole. Impurities and disorder of course influence the decay of a photohole and the Lorentzian width may thus change with increasing Fe coverage. The fit results for 0.2 and 0.4 ML are shown in the lower and upper center panels, respectively. The insets show an enlargement of the third Voigt profile for clarity since the amplitude of the peaks is quite small for these coverages. Obviously, the fit confirms the increasing spectral weight with increasing Fe coverage. The transfer of spectral weight from the initial oxidation state (A^{3+}) to the reduced one ($A^{<3+}$) is a linear function of the Fe coverage. This is seen in panel c) where the blue double triangles represent the relative area ($A_{rel} = A^{<3+}/(A^{<3+} + A^{3+})$) of the reduced oxidation state peak. The rate by which the spectral weight increases can be quantified to ∼15%/ML. It should be emphasized that even though the best fit was achieved by reducing the area of the high binding energy component, the transfered spectral weight should be assigned to the main peak as one would not expect a reduced energy loss satellite with increasing disorder. We have accounted for this fact by combining the spectral weight of the main peak and the satellite to A^{3+} in the denominator of A_{rel}.

It was already mentioned that the Te4d state also develops an asymmetric shape on the high binding energy side upon Fe deposition. This is very well seen for a coverage of 1.2 ML Fe as highlighted in panel b), where black dots represent the experimental data. An accurate fit to the data can be achieved with two different models. In the lower part a spin-orbit split pair of Doniach-Sunjic profiles has been used while in the upper part two pairs of Voigt profiles have been fitted to the same data. The Doniach-Sunjic lineshape would reflect an increased metallicity and the excitation of intrinsic plasmons at the Fermi level causes the asymmetric shape. But as seen in the two insets, which enlarge the marked region of the high binding energy side of the $Te4d_{5/2}$ peak, there is a significantly larger deviation from the experimental data for the case of the Doniach-Sunjic lineshape. The Voigt profiles give a better result and two explanations for the growth of extra peaks can be given. As in the case of Bi5d, the asymmetry could be due to an energy loss satellite and with increasing disorder this satellite grows. But considering the crystal structure discussed in Chapter 4.1.1 one may ask the question why the Fe should have an effect on the oxidation state of the Bi atoms and not on the Te atoms. Let us assume that the Fe stays on the surface, then it will find only Te atoms as reaction partners, since Te forms the topmost layer after cleavage (see Fig. 4.1 c)). We expect that Fe forms a certain kind of chemical bond as opposed to a simple transfer of its electrons to the substrate. The

latter is often assumed for doping with alkalines (e.g. Ref. [134]) but note that these show a strong trend for ionic bonds which justifies such assumption. For the 3d transition metal Fe such an assumption would oversimplify the problem. The Te atoms are already in their minimum oxidation state of 2−. This means, that any newly formed bond to Fe has to be paid for by weakening an *inter*layer bond with the first Bi layer. Since the third layer is again made up of Te atoms, which are also in their minimum oxidation state, no new *inter*layer bonds can be formed. The only possibility is thus the formation of *intra*layer bonds between different Bi atoms. This means that more electrons can be attributed to Bi sites and the oxidation state of those atoms appears reduced.

If the appearance of an asymmetry on the high binding energy side in Te4d is also due to such a chemical shift than their oxidation state is enhanced, meaning less electrons reside on Te atoms. When a similar fitting procedure as for Bi5d is applied to the Te4d peak, i.e., a decreasing main peak and an increasing side peak then the area of the side peak also increases linearly. However, the overall increase is by a factor of 1.8 faster than that of the Bi5d side peak and one should expect that the sample experiences an effective net p-doping which is not the case as seen in the overall shift of the electronic structure. It can thus be concluded that the increasing asymmetry in Te4d is at least not entirely due to a chemical shift.

On the other side, the growth of shoulders or asymmetries in both peaks appears to be decoupled from the doping trends. While we clearly observe a saturation of the doping for the Dirac point position as well as in the shifts of the Te4d and Bi5d core levels, we observe an ongoing transfer of spectral weight between the different peaks in our model. It should thus be noted, that we cannot directly conclude from the transfer of spectral weight to neither amount nor sign of the doping.

The behavior of different growth rates of the Te4d and Bi5d adjacent peak areas could be confirmed in different samples as shown in panel a) of Fig. 5.7. When the sample is kept at room temperature during deposition then the Te4d peak transfers its spectral weight always faster to its adjacent peak, which we specify as $\mathrm{Te4d}^{>2-}$, as compared to the transfer between $\mathrm{Bi5d}^{3+}$ to $\mathrm{Bi5d}^{<3+}$. The given errors have been estimated from the accuracy of the evaporator calibration (±0.1 ML) and from the accuracy of the area determination in our fitting routine (±0.05%).

The situation is altered drastically if we cool the Bi_2Te_3 samples down to temperatures between 10 and 50 K prior to the Fe deposition, as seen in panel b). Now the transfer of spectral weight in Te (left) and Bi (right) is rather similar with ∼0.65%/ML. This gives a first hint that the deposition temperature has a strong influence in this experiment. A second hint is found by analyzing the energetic position of the shoulders of the Bi5d peaks. Averaging over all samples we determine the chemical shift for deposition at room temperature to (0.77±0.04) eV and for the deposition at low temperature to (0.63±0.03) eV. Thus the shoulder is placed by more than 100 meV closer to the main peak for low temperature deposition. This unambiguously indicates different chemical environments of the Fe on Bi_2Te_3 for the different deposition conditions. Moreover, comparing again the growth rates of the extra peaks shown in Fig. 5.7 we see that for both core levels the influence of Fe appears much stronger when deposited at low temperature. While we assume the sticking coefficient of Fe to be always close to unity, a possible explanation can be found in the different mobility of the adatoms for the different temperatures. On a cold sample we expect much lower mobility and the adatoms stay where they land on the sample. At room temperature the adatoms have a higher mobility and perform a random walk on the

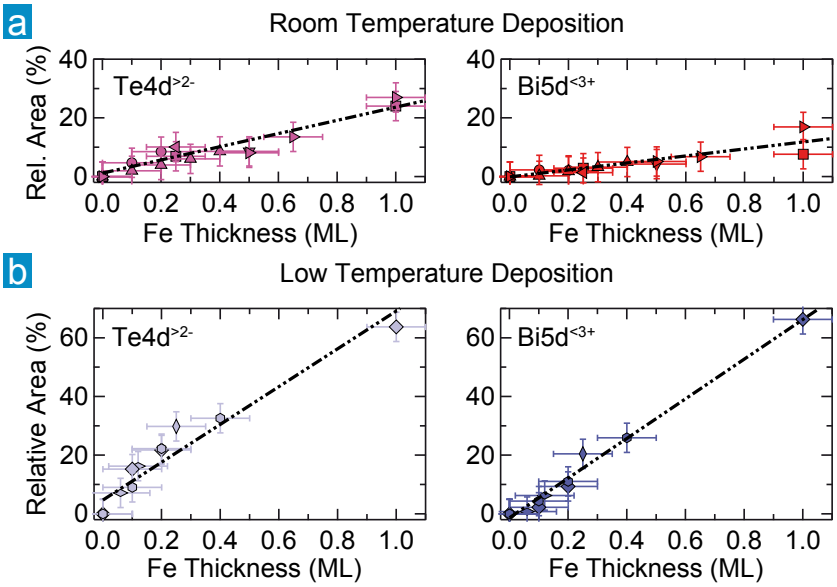

Figure 5.7: Core levels of Bi_2Te_3 upon Fe deposition. Dependence on Fe thickness and transfered spectral weight for different deposition temperatures. Different symbols represent different samples. The deposition has taken place at room temperature in (a). Over all samples we find a stronger increase of the extra states for the Te4d (left) than for the Bi5d (right). If the samples are cooled down to temperatures between 10 and 50 K prior to Fe deposition (b), then the slopes of the linear regressions to the data points are similar for Te4d (left) and Bi5d (right).

sample or even intercalate deeper into the bulk. The former may favor the formation of islands and only the Te atoms close to the islands would be influenced by the adatoms as well as those Bi atoms bond to the influenced Te atoms. Naturally this explains why the transfer of spectral weight is slowed down.

For the second case (intercalation) the slower transfer of spectral weight is owed to the escape depth of photoelectrons. The influence of deeply intercalated Fe atoms (e.g. in the first van der Waals gap from the surface; compare Chapter 4.1.1) is not visible in the data because only electrons excited within the first few atomic layers escape from the crystal (compare also Chapter 2.1.2). Unfortunately, the photoemission data obtained from the valence band of the samples cooled prior to Fe deposition remained inconclusive for Bi_2Te_3 because strong noise was introduced upon Fe deposition and the band structure was not resolved anymore. Therefore, the results are not presented in this thesis. The strong disruption of the photoemission signal may, however, be interpreted as an indication that Fe indeed stays on top if deposited at low temperature. In the next subsection we will see for Bi_2Se_3 that the deposition temperature plays a major role also for the behavior of the topological surface state and the interpretation of core level spectra will be continued therein.

Robustness at Low Temperatures

For now we again concentrate on data where Fe has been deposited on Bi_2Te_3 at room temperature. We have cooled the samples after deposition of Fe down to T=50 K and

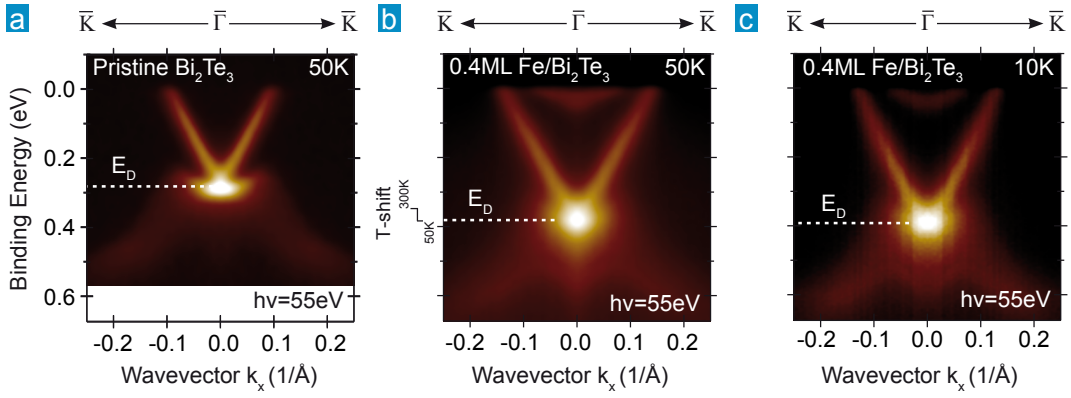

Figure 5.8: Low temperature measurements of Fe on Bi_2Te_3 at T=50 K and with 55 eV excitation energy along $\overline{\Gamma K}$. The topological surface state of a pristine sample (a) is compared to the one of a sample covered with 0.4 ML Fe deposited at room temperature (b). Upon cooling the dispersion shifts to slightly higher binding energies as described in Chapter 4.1.3. In both cases the Dirac point is very pronounced suggesting that no gap has opened in the topological surface state. c) Even at a sample temperature of 10 K no magnetization is obvious as the Dirac point still remains intact.

remeasured the dispersion of the topological surface state. For comparison we have plotted the dispersion of a clean sample[5] at the same temperature in Fig. 5.8 a) and with 0.4 ML Fe on top in b). Similarly to the behavior of a clean sample the Dirac point has shifted by 35 meV to higher binding energy upon cooling, as indicated on the energy axis of Fig. 5.3 b). However, the crossing of the two branches of the surface state at $\overline{\Gamma}$ is still very bright in intensity. This already indicates that no gap has opened as one would not expect such an intense spot at $\overline{\Gamma}$ for a single band without Kramers degeneracy. This observation is confirmed at a sample temperature of 10 K shown in panel c). In Fig. 5.9 a) the second derivative along the energy axis of the intensity plot of Fig. 5.8 b) is shown. For higher binding energy than 0.5 eV a band having the shape of an *M*, which was hardly visible in the intensity plot, is now clearly seen. This band is not an artifact of the data processing as becomes obvious by comparing with the plot of stacked energy distribution curves in panel b). The *M*-shaped band, marked with a black dashed line, is also seen in here and gives rise to a small bump on the high binding energy side of the intense Dirac point peak at $\overline{\Gamma}$, highlighted with blue color in the *waterfall* plot. Fitting this central energy distribution curve with three Voigt profiles after removal of a reasonable background, as shown in panel c), gives a very accurate result. Please note, that the data in panel c) is from a different sample with a similar amount of Fe to demonstrate the reproducibility of our results.

It is important to distinguish the described features very well, as one may tend to the conclusion that a gap has opened in the topological surface state by looking at the features best visible in the second derivative plot. The *M*-shaped band is not derived from the surface state but most likely from the bulk valence band[6]. It matches in energetic position and shape, as the valence band was predicted to have exactly this shape *after* taking into

[5]Please note that, since the deposition of Fe has been performed at room temperature, no low temperature data for the *same* sample has been acquired. We, therefore, show the data of a different sample which showed a similar intrinsic doping at room temperature as the one on which Fe was deposited

[6]This is very similar to the situation in Bi_2Se_3 [108]

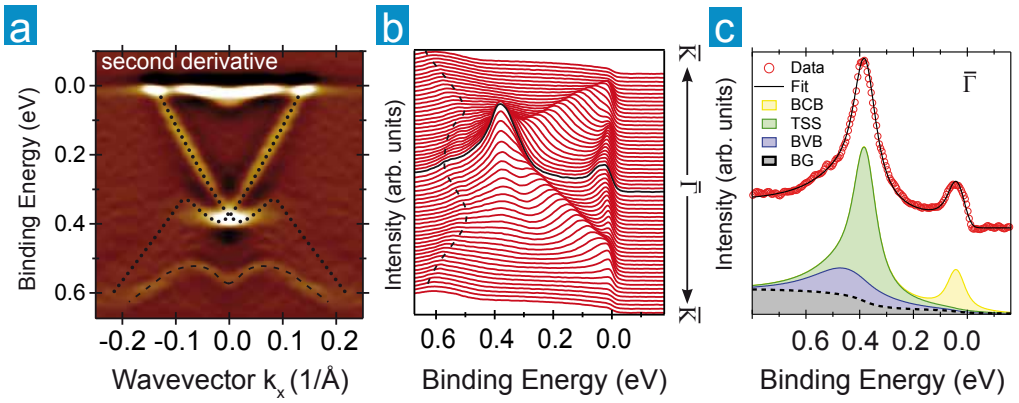

Figure 5.9: Detailed analysis of the sample covered with 0.4 ML Fe shown in Fig. 5.8 b). The second derivative (a) as well as the waterfall plot of energy distribution curves (EDC) (b) reveal an M-shaped band dispersing around 0.5 to 0.6 eV binding energy which is hardly seen in the intensity plot. The Dirac point is present and the topological surface state retains a similar dispersion as in the pristine sample. (c) EDC through the the $\overline{\Gamma}$-point (different sample) fitted with three Lorentzian peaks (bulk conduction band (BCB) topological surface state (TSS) and bulk valence including the lower half of the surface state (BVB)) added to a Shirley background (dashed line).

account the band inversion through spin orbit coupling (Fig. 4.4 a) [79]). Moreover, as indicated with a black dotted line in the second derivative plot, the topological surface state still follows more or less its initial dispersion. The pretty linear bands between E_F and E_D bend upright after crossing at the Dirac point and down again at $\sim$0.09 Å^{-1}. We can thus exclude the opening of a band gap at least within our energy resolution. This gives $\sim$20 meV as an upper limit of the gap size, if present.

It shall be mentioned once more that no magnetic field was applied and that we do not expect the Fe film to have ferromagnetic order. As explained in the preface of this section, this would mean that on a global scale, time reversal symmetry is preserved. From our point of view we do not expect a gap in this case, even of a size below our detection limit.

As a closing remark of this discussion we want to address the theoretical expectation about a magnetization of the Fe impurities *via* the topological surface state[125, 129, 128]. For such a mediation of the exchange coupling and the resulting out of plane spin orientation a transition temperature (T_c^{RKKY}) was estimated for the case of Bi_2Se_3 by the formula [128]:

$$T_c^{RKKY} \propto \frac{J_z^2}{v_F} n_m \cdot r, \tag{5.2}$$

where v_F is the Fermi velocity, n_m the impurity concentration and r is the inter-impurity distance. The size of the out-of-plane exchange coupling J_z was estimated to be proportional to the bulk band gap ΔE_{gap}:

$$J_z \propto \Delta E_{gap}, \tag{5.3}$$

For Bi_2Se_3 the gap is about 300 meV and T_c was estimated as $\sim$30 K [128]. This value is based on the assumption that the product $n_m \frac{v_F^2}{\Delta E_{gap}^2} \sim 1$. If we do the same assumption

for Bi_2Te_3 and estimate the bulk band gap to be ∼150 meV the transition temperature should be ∼15 K, thus within the range of the measurement shown in Fig. 5.8 c). It should be noted that the estimate of the transition temperature is based on the assumption, that the Fermi level intersects the Dirac point.

Recently, ferromagnetic transition temperatures for magnetic impurities on the surface of topological insulators have been estimated by Rosenberg and Franz [126]. For the surface of Bi_2Se_3 they found a value of T_c^{surf} ∼100 K for $E_D = E_F$[7]. This value was found to get strongly reduced for $E_D \neq E_F$ (∼ 0.15 K/meV) [126]. One should expect a similar dependence of the transition temperature for the *surface state mediated* magnetization, since strength and sign of the RKKY interaction also depends on the position of E_D, i.e., the size of the Fermi wave vector k_F. Thus it is likely, that the transition temperature is even below our estimate of 15 K.

In addition, disorder which is present for sure and the resulting potential scattering counteract the ordering process [128].

All this taken together justifies our assumption, that the Fe spins are not ferromagnetically aligned, that time reversal symmetry is preserved and that no gap has opened in the topological surface state.

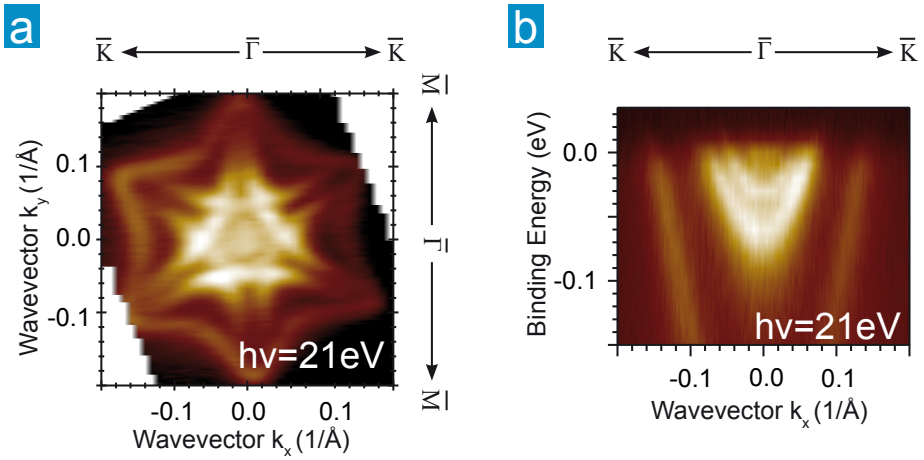

Figure 5.10: Fermi surface and low lying energy bands of Bi_2Te_3 with 0.4 ML Fe on top measured with 21 eV excitation energy at T=50K. a) The conduction band states, showing a complex structure at the Fermi level, are surrounded by the topological surface state which is strongly hexagonally warped. b) A cut along the $\overline{\Gamma K}$ direction shows a highly linear dispersion of the topological surface state towards the Fermi level. At this photon energy the bands in the center of the Brillouin zone are resolved as two parabolas shifted in energy against each other.

[7] Note that this transition temperature is distinct from the one considered by Abanin and Pesin [128]. The latter describes the temperature below which the surface state mediates an out-of-plane magnetization, while Rosenberg and Franz [126] consider the temperature below which a remanent magnetization might be observed at all.

Quantization at the Fermi Level

Before moving over to Bi_2Se_3 we have a closer look at the states in the vicinity of the Fermi level. As described already above, due to the intrinsic doping the bottom of the bulk conduction band at the Γ-point lies below the Fermi level, i.e., it is occupied with electrons, even in an as cleaved sample. The doping effect of the Fe adatoms not only moves the Fermi level even more into the conduction band but also leads to an effect which is currently understood as a quantization of the bands due to band bending and has been observed for a variety of impurities on Bi_2Se_3 [108, 109, 92]. If a crystal gets doped by the deposition of surface impurities the Fermi level in the near-surface region of the sample differs from that in the bulk. In order to level the potential difference the bands get bended around the junction between the doped and the undoped regions, i.e., between the surface and the bulk. A potential well is thus present and, depending on the strength of the potential difference, one or more quantized states may develop. At 55 eV photon energy, such states are not clearly resolved for Fe on Bi_2Te_3. However, if we lower the photon energy to 21 eV, as shown in Fig. 5.10 b) we observe two nested parabolas in the region of the bulk conduction band along the $\overline{\Gamma K}$-direction and another faint trace which could be the bottom of a third parabola is visible at the Fermi level. But as can be seen in panel a), where we show a constant energy cut close to E_F, these states do not mimic the circular shape expected for a simple free electron-like parabola but are altered in a peculiar way when moving around the Fermi arc of the topological surface state (compare Fig. 4.6). The outermost of the three described states seems to follow the threefold symmetry as it should, since these states are derived from the bulk conduction band. A Rashba-type spin orbit splitting, as reported for Bi_2Se_3 (see, e.g., [109, 92, 113, 112] is not observed for Fe on Bi_2Te_3.

5.2.2 Fe on Bi_2Se_3

The complications described for the Dirac point in Bi_2Te_3 are not present in Bi_2Se_3 which makes studying the effects of the magnetic impurities a bit easier. The Dirac point is well separated from all bulk bands and lies within the energy gap. We can thus choose a lower photon energy of 18 eV where the topological surface state is intense and we benefit from a higher energy and momentum resolution.

Room temperature deposition

We first describe the effects of Fe when deposited at room temperature. Fe has been evaporated as described before for Bi_2Te_3 and we show the changes in the near Fermi edge dispersion along the $\overline{\Gamma K}$ direction in Fig. 5.11 a-d). Panel a) shows the topological surface state of Bi_2Se_3 approximately 15 minutes after cleavage with the sample kept at room temperature throughout. The Dirac-point energy is marked by a red dashed line and is situated at ∼290 meV binding. The bulk conduction band, in between the two time reversal symmetric branches of the topological surface state appears as a filled electron pocket with its bottom at ∼160 meV. Between ∼440 and ∼600 meV we identify the bulk valence band which appears to merge, i.e., hybridize with the surface state as indicated by an enhanced intensity in the energy and momentum range where the two states match. As described in Chapter 4, pristine Bi_2Se_3 shows a sensitivity to photons at room temperature.

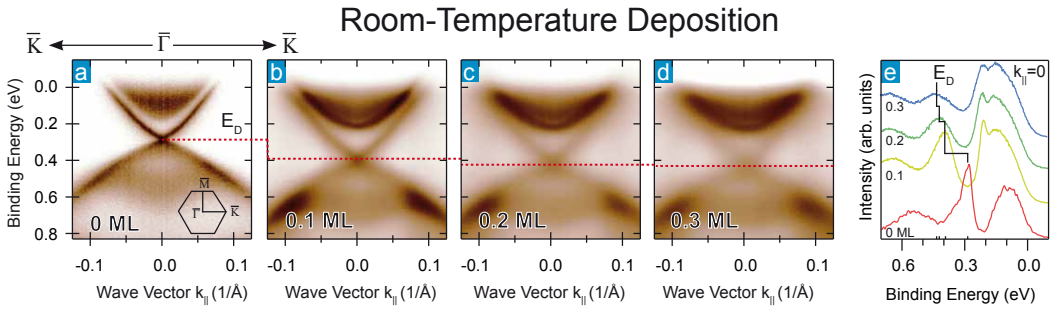

Figure 5.11: Effect of Fe impurities on the surface state of Bi_2Se_3 deposited at room temperature. a) Pristine sample measured with 18 eV excitation energy at room temperature along the $\overline{\Gamma K}$ direction. The surface Brillouin zone is shown as an inset. The Dirac point resides at ∼300 meV binding energy (E_D). b-d) Upon Fe deposition the surface state shifts to higher binding energies and in the bulk conduction band two clearly distinguishable bands appear. The red dashed line marks the shift for E_D. For 0.3 ML Fe on top (d) the n-type shift is close to saturation which is nicely seen in the stacked energy distribution curves through the $\overline{\Gamma}$ point ($k_{||}$=0) plotted in panel e).

We, therefore, kept the measurement time as short as possible, to achieve a sharp picture of the surface state, which explains the poor statistics of the measurement in panel a).

When Fe is deposited in subsequent steps of 0.1 ML (b-d), the general observations made for Bi_2Te_3 are reproduced. The band structure shifts to higher binding energies. At a deposited mass equivalent of 0.3 ML (d) this shift is close to saturation and amounts to less than 150 meV, i.e., the Dirac point is found at ∼430 meV binding energy. In a previous study, the authors reported an ongoing shift of the Dirac point up to twice the value that we observe [130]. The loss of intensity of the surface state makes it hard to follow the changes accurately in the intensity plots and we therefore show the respective energy distribution curves in panel d). The amount of Fe is indicated below each curve. One can easily follow the shift of the Dirac point as marked by the black lines. That the Dirac point of the clean sample shows a shoulder on its high binding energy side is attributed to a small misalignment. To exactly hit the angles which correspond to the $\overline{\Gamma}$ point is challenging and time consuming especially due to the clean sample's sensitivity to photons. But that the surface state in clean Bi_2Se_3 is gapless is beyond controversy.

In contrast to Bi_2Te_3 already at room temperature the quantization of the states assigned to the bulk conduction band is obvious. The bottom of the conduction band becomes, after the first deposition step shown in panel (b), surrounded by a sharp rim, parabolic in shape and constituting the most intense feature. Also a second band, shifted to lower binding energy is already visible. While these features follow the overall shift of the band structure to higher binding energies, no additional states are introduced with increasing Fe coverage. For 0.3 ML the energy distribution curve seems to show a shift of the quantized states to *lower* binding energy. But this is again possibly the artifact of a small misalignment mentioned above. Despite the energy shift no changes are identified in the valence band at room temperature.

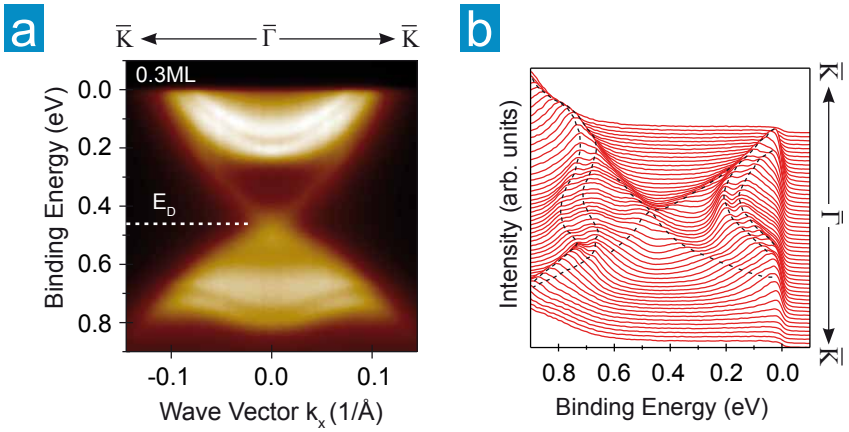

Figure 5.12: Low temperature measurements of Fe on Bi_2Se_3 at T=8 K and 18 eV excitation energy. The Fe was deposited at room temperature. a) Upon cooling the Dirac point shifts to a slightly higher binding energy as compared to the room temperature measurement shown in Fig. 5.11 d). No gap is seen in the surface state dispersion. The single features can be very well traced in the stacked energy distribution curves at different k_x shown in b). Despite the two nested parabolas dispersing between ∼0.2 eV and the chemical potential (0 eV) two M-shaped bands are seen at 650 meV and higher binding energy. The dispersion of the topological surface state is similar as for the pristine sample.

Low temperature measurements

In Fig. 5.12 the dispersion along the $\overline{\Gamma K}$ direction is shown after cooling the sample with 0.3 ML Fe on top to ∼10 K. The Dirac point is now found at ∼460 meV and has shifted by ∼30 meV upon cooling. Interestingly, the two parabolas, which appear more pronounced, sharper and very well distinguishable from each other, do not experience an obvious energy shift like the surface state does. As a consequence the Dirac point and the bottom of the larger parabola are separated by ∼30 meV more as compared to room temperature. Changes in the energetic position of the valence band are somewhat harder to figure out, as the data shown in panel a) and more clearly in the waterfall plot of panel b) suggest that a quantization has taken place in connection with the cooling process. Two M-shaped bands are now present, situated above ∼650 meV binding energy, as indicated by the black dashed lines in panel b). These bands are very similar to those reported for CO [92], Cs, Rb [113] and Ag (Chapter 5.1.2). A reasonable explanation for the formation of these bands was given by Bianchi *et al.* who claim that they are also due to the formation of quantum wells [92]. The lowest lying valence band states are followed by a gapped region and a mismatch of Fermi levels has to be leveled.

In the first study of Fe deposited on the surface of Bi_2Se_3 by Wray *et al.* such features have also been reported [130]. But instead of attributing them as valence band derived they have assigned the upper M-shaped band to be the lower half of the topological surface state after the opening of a band gap [130]. Consequently the size of the band gap at $\overline{\Gamma}$ was defined between the local minimum of the upper M-shaped band and the bottom of the upper half of the topological surface state, which appears parabolic in shape in their data. However, as unambiguously seen in our data both M-shaped bands coexist with the topological surface state. Furthermore, the topological surface state is ungapped and

shows in principle the same dispersion relation as it does in a pristine sample. This means that both branches of the surface state still connect the positive momentum space of the conduction band with the negative momentum space of the valence band, and *vice versa*.

The coexistence of topological surface state and M-shaped bands practically rules out the possibility that the reported gaplike feature for Fe on Bi_2Se_3 is a gap in the surface state due to an Fe film magnetized out of plane. Wray and co workers speculated that they had observed the mediation of the out of plane magnetization by the topological surface state for Fe on Bi_2Se_3 [125, 128, 130]. As an evidence they gave the gap itself; since an unmagnetized Fe film would not open a gap and an in-plane magnetization would simply shift the surface state in k-space they interpreted the formation of a gap as an out-of-plane magnetization [130]. As a second indication Wray *et al.* describe a regime in which the band structure gets sharper upon iron deposition. This regime approximately falls together with the formation of the gap and they thus interpret the sharpening being due to the magnetic ordering. According to their result, the ordering takes place at a mass equivalent of 0.2 ML, therefore a bit less than what we show in Fig. 5.12. One may of course argue that the calibration of evaporators is a source of error and that it is therefore possible that the amount of Fe differs much more than the calibration tells us. But, as we have shown, we are already in a saturated regime concerning the energy shifts in our deposition experiment, which means that even by putting more Fe we would not be able to reproduce the results in Ref. [130] where much stronger n-doping has been reported. This fact makes us confident, that the results reported by Wray *et al.* are most likely not caused by pure Fe but possibly by unwanted cross-contaminations. This assumption is supported by reports, where very similar results, with comparably strong n-doping have been obtained under bad vacuum conditions [109] and exposure of CO [92], a typical residual gas in ultra high vacuum systems.

An additional argument for this assumption can be derived from the extra states at the Fermi level. As is clearly seen in Fig. 5.12 the two parabolas are shifted against each other in energy but not in momentum space. Wray *et al.* report a pronounced Rashba-type splitting for the extra states in their system [130]. Again, similar features have been observed with non-magnetic contaminations [109, 92, 113].

The existence of the Rashba-split states in Ref. [130] can on the other hand be taken as evidence, that no magnetization is present. The Rashba effect gives a time reversal symmetric band structure, very similar to a topological surface state with a Kramers degeneracy at time reversal symmetric momenta. However, they are topologically trivial and thus cross the Fermi level an even number of times (compare Chapter 3). Nonetheless, for broken time reversal symmetry the Kramers degeneracy is lifted for Rashba-states as well as for topological surface states if the magnetic field is perpendicular to the surface plane. This lifted Kramers degeneracy is clearly not the case in Ref. [130]. Also an in-plane magnetization is ruled out, because for such a configuration one would expect the coexistence of Rashba and exchange splitting and the parabolic states would be shifted in momentum and energy simultaneously as was shown a few years ago for Gd [135].

Last but not least we want to reconsider the theoretical basis for an exchange interaction mediated by the surface state. This effect is unanimously based on the assumption, that the Dirac point is close to the Fermi level. The Ruderman-Kittel-Kasuya-Yosida (RKKY) interaction, responsible for a possible magnetization, is oscillating between ferromagnetic and antiferromagnetic interaction. The period of oscillation is determined by the Fermi

wavelength

$$\lambda_F = \frac{2\pi}{k_F}. \tag{5.4}$$

Thus the oscillation period goes to infinity when the Dirac point is at the Fermi level in Bi_2Se_3, as the Fermi momentum $k_F \to 0$ [125]. In that case the interaction is always out of plane. In our case and even more so in the data of Ref. [130] the Dirac point is far off the Fermi level and an oscillation is present. However, for an estimated k_F of $0.1\,\text{Å}^{-1}$ λ_F is with $\sim$60 Å still very large. The average impurity distance has only to be much smaller than λ_F for a ferromagnetic sign of the interaction, and from this point of view the theoretical prediction seems to be realizable. Nevertheless, the theoretical model cannot be applied since it is based on a single Dirac cone on the surface. The two dimensional states at the Fermi level are, however, confined to the near surface area as well and can thus be expected to contribute to the RKKY interaction as well and this makes a coherent interaction between surface electrons and surface impurities unlikely.

5.2.3 Doping Control in Bi_2Se_3

For Bi_2Te_3 it has been shown above that the shoulders developing next to the Bi5d peaks have a different binding energy when Fe is deposited at low temperature instead of room temperature. This shall now be investigated also for Bi_2Se_3 for core levels and the valence band.

Core Level Spectroscopy

Fig. 5.13 compares the Se3d (a,c) and Bi5d (b,d) core level spectra when Fe is deposited at room temperature (a,b) and at 10 K (c,d). First we want to prove that Fe has been deposited on the samples. In the case of Bi_2Se_3 this is not simply made evident from the growth of the Fe3p peak because it matches in binding energy with the Se3d peak and is thus hidden under the spectral weight of the latter. In a) the sample was cleaved and measured at room temperature and we observe around 54 eV binding energy two relatively broad peaks separated by $\sim$0.8 eV according to the $3d_{3/2}$ and $3d_{5/2}$ multiplet as shown in the lower inset. The upper inset repeats the Fe3p peak as measured (black circles) on Bi_2Te_3, and it has been fitted by two Voigt profiles after removing a background signal (green shaded area). The main image shows the Se3d multiplet after the deposition of 0.2 ML Fe where a Shirley background has been removed from the measurement signal (black open circles). No additional peak or deformations are obvious for the naked eye. However, by analyzing the intensity ratio $I_{rel} = I(3d_{5/2})/I(3d_{3/2})$ we find that it changes from $I_{rel} = 0.63$ to $I_{rel} = 0.74$ after deposition. In Bi_2Te_3 we have not observed a change in the relative intensities of the Te4d peaks and we conclude that it is not due to the growth of a chemically shifted Se3d multiplet. In that case one would not expect a change in the relative intensities, at least not without the development of a pronounced shoulder. Assume a small chemical shift, then the shoulders would reside close to their main peaks such that one could not distinguish them in the raw data. In this scenario the relative intensity would not change as the chemically shifted multiplet is expected to have the same intensity ratio. If, on the other hand the chemical shift would be of the size of the multiplet splitting, i.e., $\sim$0.8 eV then the intensity ratio would indeed change, but simultaneously a pronounced shoulder would appear next to the $3d_{3/2}$ peak, which is not the case. The only reasonable

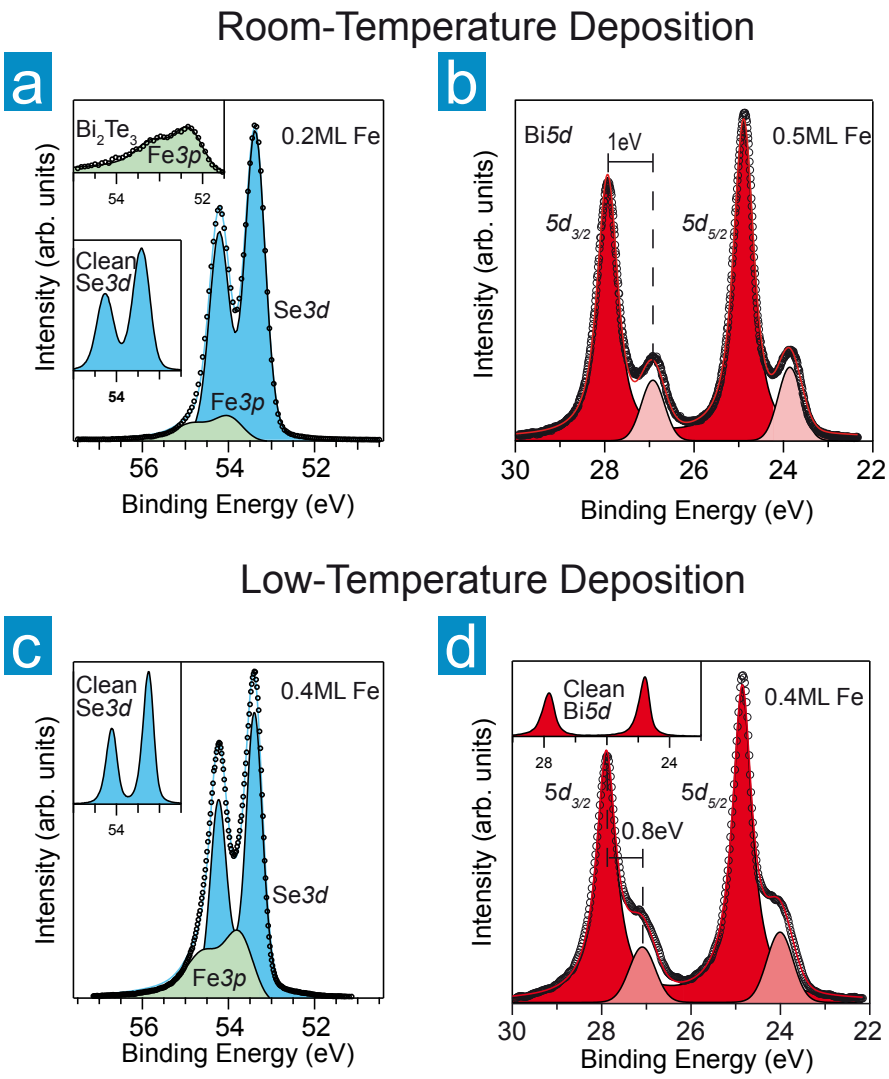

Figure 5.13: Fe on Bi_2Se_3. Core level spectroscopy distinguishes the different deposition methods. (a,c) The Se3d core levels cover the Fe3p emission. Se3d shifts to higher binding energy only for low-temperature (8 K) deposition of the Fe. (b,d) Bi5d develops shoulders with the core-level shifts having different values for room-temperature and low-temperature preparation. The photon energy is 125 eV and the sample temperature during measurement is according to the one at preparation, 300 K and 8K, respectively.

explanation for the change in the intensity ratio is thus the growth of an additional peak underneath, i.e., Fe3p.

This is confirmed by a fit, where we have used the lineshape of Fe3p from the deposition on Bi_2Te_3 and where we have fixed the intensity ratio of the Se3d peak to that of the clean sample. The result is shown as blue shaded (Se3d) and as green shaded (Fe3p) areas in the plot. The sum of the two features is shown as a blue straight line and it reproduces the experimental data quite accurately.

Similar results are obtained for the low temperature deposition of Fe as shown in panel c). The major difference is that the Se3d peaks appear sharper if measured at low temperature. For an Fe mass equivalent of 0.4 ML the Fe3p peak revealed by the same fitting procedure as for room temperature appears more pronounced. While the overall fit is again accurate, there is an obvious deviation at the high binding energy side of the $3d_{3/2}$ peak. It is likely, that the Se3d peak develops a similar chemical shift as the Te4d peak. However, for simplicity it has not been included in the fit as the major aim of the procedure is to qualitatively show the growth of the Fe3p peak and not to describe the experimental data in detail.

Second, we analyze the chemically shifted shoulders of the Bi5d peaks for 0.5 ML Fe deposited at room temperature and for 0.4 ML Fe deposited at 10 K. In both cases pronounced shoulders are observed. But as obvious already in the raw data the shoulders reside much closer to the main peak for the low temperature measurements. A fit quantifies this difference to as much as ∼200 meV. At low temperature the shoulders are split off by ∼0.8 eV while the splitting amounts to ∼1 eV for the deposition at room temperature. Thus, the result obtained in Bi_2Te_3 is confirmed also in Bi_2Se_3 and should be due to differences in the growth mechanism as described above.

Effects on the Band Structure

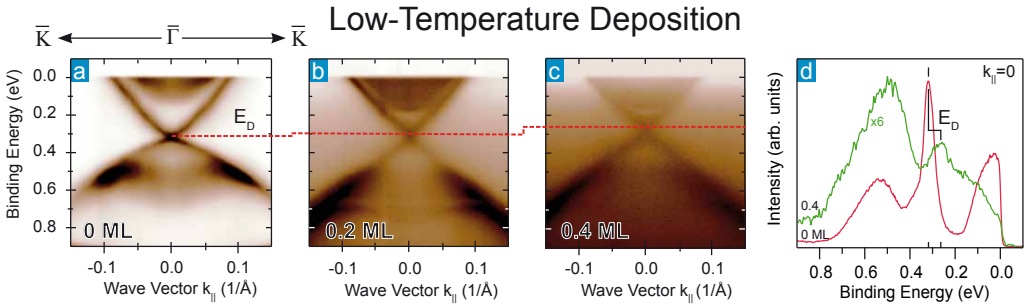

Figure 5.14: Effect of Fe on Bi_2Se_3 deposited at low temperature (T=8 K). a) Pristine sample at T=8 K measured with 18 eV photon energy. The Dirac point (E_D) appears at 310 meV and the bulk conduction band states appear less pronounced compared to Fig. 5.11 a). b-c) The deposition of 0.2 and 0.4 monolayer (ML) Fe at cryogenic temperatures leads to an shift of the surface state to lower binding energies. The topological surface state appears more linear now. The bulk conduction band appears as a completely filled electron pocket with a parabolic boundary. The shift of E_D can be quantified as 55 meV in the energy distribution curves at zero momentum ($k_{||}$=0) shown in d). For clarity a Shirley-background has been removed from the 0.4 ML spectra (green line) and it was multiplied by a factor 6. The photon energy in b) and c) and for the green curve in d) is 21.5 eV (see text).

We now analyze the evolution of the band structure, i.e., bulk conduction band, valence band and topological surface state when Fe is deposited with the sample cooled to 10 K. In Fig. 5.14 a) the angle resolved photoemission picture of a clean sample at the deposition temperature is shown. For excitation of photoelectrons, 18 eV photons have been used. The Dirac point is seen at ∼315 meV binding energy. In b) and c) two subsequent deposition steps of Fe are shown with mass equivalents of 0.2 and 0.4 ML, respectively. It should be noted, that after deposition we found a change in the photoemission cross sections, such that the surface state was hardly visible at 18 eV. Thus the photon energy has been changed to 21.5 eV in b) and c). The red dashed line marks the position of the Dirac point. In contrast to the deposition at room temperature, we find the Dirac point moving to lower binding energies as the Fe coverage is growing. This trend is observed for both deposition steps. A photon energy induced gating effect, as one may expect because of the change of photon energy between a) and b) [136], is therefore not responsible for this observation. This means that Fe acts as a donor or acceptor on Bi_2Se_3 depending on the deposition temperature. The hole-like doping has been confirmed also at T=50K, but at 70 K already n-doping is found [137]. The achieved hole-doping can be quantified to 55 meV for the sample with 0.4 ML Fe on the surface, which is clearly seen by comparing the energy distribution curve with that of a clean sample in d).

We can expect that at cryogenic temperatures the Fe has a much lower mobility on the surface. The adatoms get *freezed* on the surface and stay more or less where they land. This freeze-out also avoids an intercalation and the adatoms tend to stay on the surface. This naturally explains why we see a stronger influence on the core levels compared to room temperature deposition, as explained above. The penetration of Fe into the crystal matrix at room temperature would also explain the different doping. For Cu doped Bi_2Se_3 it is known that it may act as donor or acceptor depending on whether it resides on interstitial places, where it is singly ionized, or as substitutes for Bi atoms with a double negative charge, respectively [138, 136]. Similar effects may be expected for Fe. However, to carry these statements beyond speculation, a more profound experimental investigation of the structural changes by, e.g., photoelectron diffraction is necessary. So far, there is only microscopic data at low temperatures available. Honolka *et al.* showed by means of STM, that at least low Fe concentrations (∼0.01 ML) tend to stay on the surface if deposited on Bi_2Se_3 at low temperature [139]. Their analysis of the tunneling spectra revealed a tendency for strong electron doping which contrasts our findings. However, while it is questionable whether the much lower Fe concentrations deposited in Ref. [139] can be compared directly to the massive Fe amount in our case it should be noted, that angle resolved photoemission is much more reliable probe of the electronic structure. The tunneling spectra in STM only reflect the angle averaged local density of states which makes the impurity induced changes much harder to follow. In addition, a tip induced band bending is possibly capable to mask the real sign of the doping [140].

We repeat in Fig. 5.15 the dispersion observed for 0.2 ML Fe deposited at 10 K but with different color scale in a) and as stacked energy distribution curves in b). Two pronounced M-shaped bands above 0.6 eV are visible also in this case which has been emphasized in b) by black dashed lines. For the conduction band a quantization is hard to figure out. Only faintly, it appears that the filled parabola gets surrounded by a rim. This effect looks similar to what has been found for Bi_2Se_3 after some time in bad vacuum conditions [108]. The quantization observed in the valence band can be explained by band bending effects like in the case of n-doping. However, in the conduction band, for p-doping it is not

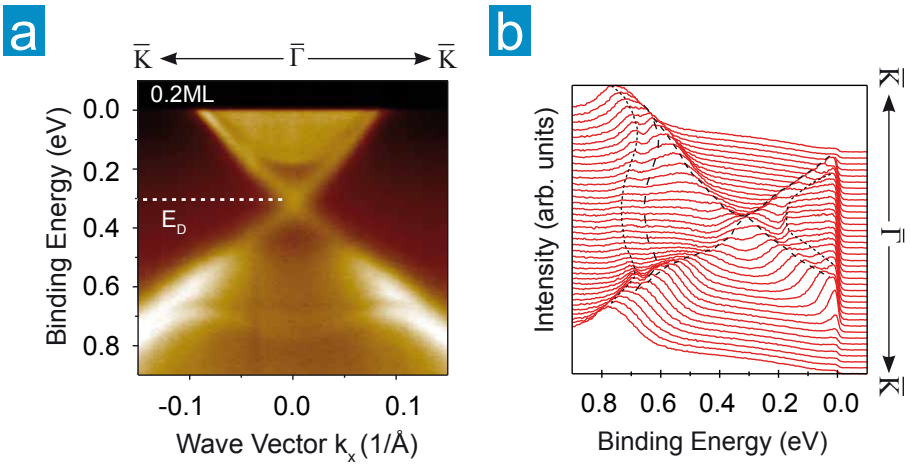

Figure 5.15: Enlarged view of the dispersion of Fig. 5.14 b) with 0.2 monolayer Fe on top measured with 21.5 eV photon energy (a) and corresponding stacked energy distribution curves for different momenta (b). Dashed lines mark the different observed features. The bulk conduction band is enclosed by a parabolic rim. The topological surface state is intact and no gap appears. Besides, it appears more linear compared to the pristine sample. One M-shaped band is resolved again above 650 meV binding energy. A second one is only allusively visible at a slightly lower binding energy.

expected to observe quantized bands since the bands get bended in the range above the Fermi-level and are not accessed by photoemission. This observation thus puts at least a question-mark behind the current believe about the origin of the two dimensional electron gas on the surface of Bi_2Se_3.

But the most striking result, that is seen in Fig. 5.15 is the intact topological surface state. No gap has opened by the deposition of Fe and this excludes the possibility that the sample has to be below the predicted transition temperature of 30 K [128] during the deposition in order to get a ferromagnetic out of plane alignment. However, an in plane ferromagnetic alignment can not be excluded since no gap is expected for such a configuration [130]. Indeed, x-ray magnetic dichroism has revealed that the easy axis for Fe impurities on Bi_2Se_3 is within the surface plane [139]. Though, it is not yet clear if the easy axis stays inside the plane for the much higher Fe concentrations deposited by us.

By comparing the clean and and the sample with 0.2 ML of Fig. 5.14 once again, we find that the dispersion of the topological surface state looks more linear *after* the deposition. This will be quantified in the next chapter where we analyze the quasiparticle scattering in Bi_2Te_3 and Bi_2Se_3.

Summary of Conclusions

To summarize the present chapter, we have seen that the topological surface state in Bi_2Te_3 and Bi_2Se_3 is indeed pretty much robust against perturbations. The expected robustness against non-magnetic impurities was confirmed with O_2 and Ag. Moreover, we have proven an unexpected robustness against magnetic impurities, i.e., Fe. For the Bi_2X_3 family of materials, the robustness has a very interesting side-effect: One can, in principle, overcome the intrinsic doping and drive the materials into an insulating state without destroying the

surface states by surface doping.

Furthermore, it has been shown that the sign of the impurity induced doping can be controlled via the sample temperature during the deposition. In core level spectroscopy it has been revealed that the chemical surrounding of Bi and Te/Se atoms gets modified differently if Fe is deposited at low temperature as compared to room temperature deposition. For Bi_2Se_3 it has been shown, that for both deposition conditions the topological surface state remains robust and ungapped. The presented results may be interpreted as a first step towards functional devices of interfaces between topological insulators and ferromagnets.

Chapter 6

Quasiparticle Scattering in Topological Insulators

The transport properties of topological insulators are a topic of very high interest. The spin filtered surface states promise dissipationless currents with large spin relaxation lengths, at least theoretically. In a three dimensional topological insulator, however, only 180° backscattering is strictly forbidden for the surface electrons, while small angle scattering is allowed and may reduce the mobilities of surface carriers drastically.

Experimentally, revealing the properties of the surface state of Bi_2X_3 in transport turns out to be challenging. In single crystalline Bi_2Se_3 samples Butch and co workers found in four-probe measurements in an external magnetic field only bulk contributions to the Shubnikov-de Haas oscillations and, therefore, concluded on rather strong surface state scattering [95]. However, in much higher and furthermore pulsed magnetic fields Analytis *et al.* where able to observe Shubnikov-de Haas oscillations of the surface state which in addition showed features at *fractionalized* values of the integer Landau indices [98]. Only recently, in Bi_2Se_3 thin films doped with Ca, to overcome the intrinsic doping, Checkelsky and colleagues could successfully identify a high mobility metallic channel as the topological surface state by gating the sample in a field effect transistor setup [141]. However, this channel turns out to be relevant only at low temperatures (T<100K) [141], while the large band gap of Bi_2Se_3 is promising room temperature applications.

A similar situation holds for Bi_2Te_3 where the only indication for a two dimensional conduction channel is so far found from Shubnikov-de Hass oscillations by Qu *et al.* [142].

Other systems appear to be more promising from a transport point of view. Recently, bulk HgTe grown under strain on CdTe develops a band gap and turns out to be a *three dimensional* topological insulator. A quantum Hall effect was observed, and the analysis of the Hall current showed that it is caused by two parallel two dimensional states. However, temperatures below 1 K are needed to overcome the residual bulk contributions to the conductivity [143].

6.1 Decay of Photoholes and its Connection to Scattering Rates

In this chapter we will investigate the scattering properties of the topological surface state by angle resolved photoemission. Photoemission is not at all a direct probe for the investigation of transport phenomena. But since electronic transport is intimately connected to

the scattering of electron or hole states we can in turn draw conclusions on the transport properties by investigating the scattering properties.

The emission of electrons leaves the system in an excited state and the peak that we measure in a spectrum contains information about the time scale the system needs to relax back into the ground state. The excited state is typically described in a one-particle approximation, where the photohole is obscured by a cloud of manybody-interactions which together behave like a single particle and this particle is thus named a *quasiparticle*. The Heisenberg uncertainty principle connects the width of a photoemission peak on the energy scale with the time the system needs to relax by $\Delta E \Delta t \gtrsim \hbar$. An ideal system, isolated from any other perturbation would last in the excited state forever and the peak would thus be infinitely narrow. In a real system there exist a couple of scattering mechanisms which lead to the relaxation of the system and thus to a broadening of the peak in photoelectron spectroscopy. As a basis for the interpretation of the following data we will at first review the most important mechanisms for the decay of photoholes before we turn to a deeper investigation of the connection between a photoemission spectrum and the quasiparticle lifetimes.

6.1.1 Photohole Decay in Topological Surface States

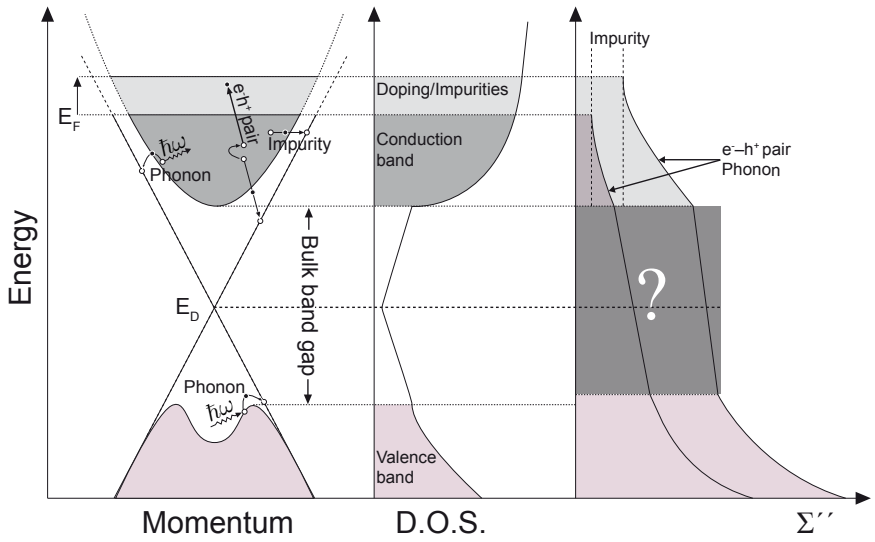

Figure 6.1: Decay of surface state photoholes into bulk states. Left: Sketch of the near-Fermi-edge electronic structure of Bi_2Se_3 with an *ideal* Dirac cone. A photohole created in the surface state may decay into bulk states by creation or annihilation of a phonon ($\hbar\omega$), creation of an electron-hole pair, or by scattering at an impurity. The probability for the decay is intimately connected to the density of states (D.O.S., center) and the imaginary part of the electron self energy Σ'' is a measure for the scattering probability which can be accessed by photoemission (right). In the presence of bulk states the probability for scattering is high and increases with the number of states available for scattering. Inside the gap the D.O.S. decreases from the bottom of the bulk conduction band to the Dirac point and increases again towards the valence band. The region of interest is marked by a question-mark, since the exact behavior of Σ'' is unknown and will be analyzed experimentally in this chapter.

Taking a sketch of the band structure of Bi_2Se_3 as an example, as shown on the left hand side of Fig. 6.1, we can at first distinguish two main groups of decay channels for the photoholes. The first group is characterized by a filling of the photoholes with electrons which stem from the surface state and we thus label these events with the term intra-band. This group is restricted by spin selection rules and will be discussed later on. The second group is built by processes in which bulk electrons are involved in the relaxation process and are thus called inter-band scattering processes.

Inter-band Scattering

In the sketch (Fig. 6.1), we find a parabolic band close to E_F which represents the bulk conduction band and the M-shaped band at higher binding energy is the valence band. Both are well separated by an energy gap in which the two straight lines, which represent the surface state, cross in the middle and form the Dirac point. An electron excited by a photon leaves back a photohole which is represented by white circles in the sketch. All mechanisms have to respect the principles of momentum and energy conservation and thus at least one more particle is always involved in the decay process.

At finite temperatures there are phonon modes present and a decay of a photohole can happen by annihilation of a phonon which gives, or by creation of a phonon which takes, energy ($\hbar\omega$) and momentum (Δk) necessary to scatter the photohole into a bulk state. Both processes allow scattering from valence band and conduction band electrons into the surface state holes. Due to the temperature dependence of the phonon occupancy, it is possible to discuss the influence of phonons on the scattering rates by analyzing the temperature dependence of the imaginary part of the electron self energy. This will be the topic of Section 6.3.

Of special importance is the scattering at impurities. This process is typically assumed not to transfer any energy but the scattering may be inelastic and thus the absolute value of the electron momentum may change. This allows a scattering of the photohole into a bulk state. Impurity scattering is expected to be the dominant contribution close to the Fermi level and, furthermore, to be constant in energy.

A last scattering mechanism is given by the possibility of a spontaneous decay of photoholes into the conduction band, whereas energy and momentum are conserved by the excitation of an additional electron-hole (e^-–h^+) pair. This process depends solely on the bulk density of states.

For impurity scattering no transfer of energy between the impurity and the electron is expected and thus the probability for such an event is proportional to the impurity density and to the density of bulk states at the electron (or hole) energy. As sketched in the center of Fig. 6.1 the density of states for the conduction band is decreasing with increasing binding energy and thus the contribution of this process to the imaginary part of the electron self energy (Σ'') should also decrease with increasing binding energy. In contrast, the phase space for e^-–h^+ pair processes for a hole created at a binding energy ϵ is assembled from all states with energy in the interval reaching from E_F to ϵ. Therefore, it gives an increasing contribution to Σ'' with increasing binding energy, which in the Fermi liquid theory is proportional to E^2.

Within the bulk energy gap, the density of states decreases linearly down to the Dirac point energy and afterwards increases again as the only states present are formed by the Dirac cone with its linear dispersion relation. Impurities may only contribute to surface state-surface state scattering in this range and these processes will be discussed below.

However, a scattering of holes within the bulk gap into bulk states is in principle possible by exciting e^-–h^+ pairs over the Fermi level and the available phase space is given by the density of states of the occupied conduction band, integrated over all energies. Assuming for simplicity, that the probability for an e^-–h^+ pair creation does not depend on the binding energy of the created hole, we expect that the scattering into bulk states has a more or less constant contribution to Σ'' within the gap. In a finite energy range, defined by the energy of available phonon modes and the top of the valence band, i.e., bottom of the conduction band, in-gap surface state holes may also be scattered into valence, i.e., conduction band states by electron-phonon interaction. This would lead to an increasing contribution to Σ'' with increasing binding energy close to the top of the valence band and to an decreasing contribution close to the bottom of the conduction band.

Ideally, one would like to have the Fermi level within the bulk band gap, where a surface state hole may only be filled by a surface state electron. According to the argumentation in the previous paragraph, any strong changes of Σ'' in the range marked by a question mark in Fig. 6.1 are likely to be connected to intra-surface state scattering. These processes, especially the restrictions connected to them, will be discussed next.

Intra-band Scattering

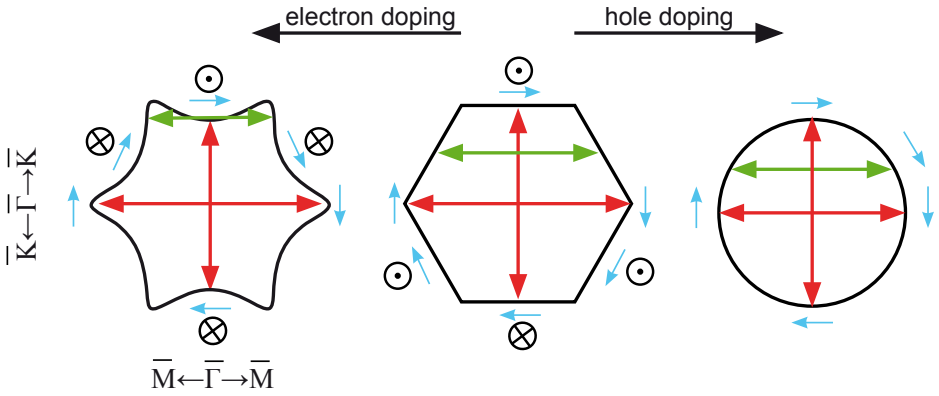

Figure 6.2: Spin dependent scattering and warping of the Fermi surface. 180° backscattering is prohibited (red arrows) independently of warping and spin rotation (blue arrows; ⊙ and ⊗ mark the direction of the out of plane spin components). Scattering under different angles has a finite probability, exemplified by green arrows. Warping is controllable by the doping of the sample. For strong warping (left), like in Bi_2Te_3, the shown green arrow fulfills a (near) nesting condition.

The most interesting question concerning the (three dimensional) topological insulator is, whether the scattering is really suppressed due to the helical spin structure, or not. In a two dimensional system, like the HgTe/CdTe quantum wells [48, 44] with its one dimensional edge states, backscattering is strictly forbidden as the scattering angle is always 180° and the spins of forward and backward movers are opposite. But in a three dimensional system, the surface state is two dimensional and electrons are allowed to move in any surface direction. In an ideal Dirac cone, as depicted in Fig. 6.1 the shape of the Fermi surface is circular as shown to the right of Fig. 6.2. The spin is helical in the sense that it is always perpendicular to the in plane momentum vector and is represented by blue arrows

in Fig. 6.2. Thus, 180° backscattering is also forbidden for a two dimensional surface state. However, scattering under any other angle is only suppressed and the probability that an electron with spin $\mathbf{S}(\mathbf{k})$ is scattered into a final state with spin $\mathbf{S}(\mathbf{k}+\mathbf{q})$ is given by [84]

$$\Phi(\mathbf{q}) = \int D(\mathbf{k})T(\mathbf{k},\mathbf{q})D(\mathbf{k}+\mathbf{q})d^2\mathbf{k}, \tag{6.1}$$

with the density of states $D(\mathbf{k})$ and the matrix element $T(\mathbf{k},\mathbf{q})$ which calculates the overlap of the spin eigenstates:

$$T(\mathbf{k},\mathbf{q}) = \left|\langle \mathbf{S}(\mathbf{k})|\ \mathbf{S}(\mathbf{k}+\mathbf{q})\rangle\right|^2. \tag{6.2}$$

This means that, the higher the overlap of spin eigenstates in initial and final states, the higher the scattering probability is. Small angle scattering has a high probability, while scattering angles close to 180° are unlikely but possible [144].

As already pointed out in Chapter 4.1.2 the warping of the Fermi surface [19] is influencing its spin texture quite strongly. As a consequence, the spin is predicted not to be perpendicular to the momentum in every point of the surface Fermi surface [20] and even to have a finite canting out of the surface plane [19, 20]. The latter was experimentally observed for Bi_2Te_3 by Souma *et al.* [94].

The spin rotation is exemplified in Fig. 6.2 for two more shapes which have been observed in Bi_2Te_3 [2] and in Bi_2Se_3[85, 145, 113]. Along the $\overline{\Gamma M}$ direction, the spin is fully inside the surface plane, independent of the detailed warping, since the mirror plane of the crystal is along this axis [20]. The out of plane rotation follows a sixfold symmetry and points alternately inside and outside the crystal and takes a maximum along the $\overline{\Gamma K}$ direction. Instead of being perpendicular to the momentum, the in plane component is predicted to be tangential to the Fermi surface. Still, and thus independent of the warping and spin rotation, 180° backscattering is forbidden as the spin is always opposite (in three dimensions) on opposite sides of the Fermi surface.

Another important aspect concerning the shape of the surface Fermi surface is nesting. Especially the hexagonally shaped contour (center) leads to strong nesting, as opposite parts of the Fermi surface are nearly straight lines and can be translated upon each other by wave vectors $\mathbf{Q} = 2\mathbf{k}_F^{\overline{\Gamma K}}$ where $\mathbf{k}_F^{\overline{\Gamma K}}$ is the Fermi momentum along the $\overline{\Gamma K}$ direction. The nesting may lead to the formation of a spin density wave, as a charge density wave is forbidden by time reversal symmetry [19].

Another consequence of the warping is that Friedel oscillations of the local density of states, which should be absent for non-concave and non-degenerate Fermi surfaces (e.g. right and center picture of Fig. 6.2) are present for the concavely warped case (left in Fig. 6.2). Such oscillations are caused by scattering between states at "stationary" points on the Fermi surface, where the Fermi velocity is parallel to the direction in which the oscillations occur [19, 146]. Indeed, Friedel oscillations have been observed in Bi_2Te_3 by STM in the range where the surface Fermi surface mimics a hexagram [147] but not for the convex cases. Two examples of stationary points are given by the end points of the green arrow in the left picture of Fig. 6.2.

Doping Effects

For the following analysis and discussion, the doping which is caused by impurities will play a major role. As can be seen in Fig. 6.1, electron doping will move the Fermi level

into the unoccupied states, which then get occupied, and therefore the density of occupied states increases. The offset in the imaginary part of the self energy is caused mainly by impurity scattering, since for the electron hole pair creation, occupied density of states with lower binding energy must be available which is not the case for electrons scattered at the Fermi level. For a parabolic three dimensional band, the density of states increases proportionally to $\sqrt{E}$ which leads to a higher offset for a more n-doped sample. As a second contribution the impurity density should play a role which also increases as the electron doping in our case is caused by surface impurities. Overall a strong increase in the offset at E_F is expected.

The increase in the bulk density of states also expands the available phase space for electron-electron interactions and the creation of electron-hole pairs, which should be visible in Σ'' such that the slope in the energy range of the conduction band increases more up to the bottom of the conduction band, but with a similar slope as for the undoped case.

The doping also affects the warping of the Fermi surface such that hole doping decreases the warping and electron doping increases the warping as indicated by the arrows above the three shapes in Fig. 6.2. This makes the influence of the warping on the scattering rates accessible to ARPES and it has been argued by Valla *et al.* that the warping is the main reason for increased scattering rates by comparing different donor impurities [113]. Especially for the comparison of magnetic and non-magnetic impurities no general difference was found and thus the authors concluded that magnetic impurities do not open any other scattering channels by breaking of time reversal symmetry which appears to agree with the results presented in the previous chapter. In a similar study, comparing freshly cleaved and aged surfaces of Bi_2Se_3, Park and co-workers concluded that a decay of photoholes is only possible by bulk electrons and that intra-surface-state scattering is indeed strongly suppressed [148]. This contradicts the findings in Ref. [113], as the increase of scattering due to warping implies a surface state surface state scattering. The conclusion by Park *et al.* was drawn from the observation that Σ'' only increases with energy in the presences of the bulk states, and strongly decreases within the bulk gap [148]. In contrast Valla and colleagues report a monotonic increase of Σ'' in agreement with the E^2 dependence in Fermi liquid theory [113]. We will return to this discussion with respect to our own results in Section 6.4.

6.1.2 Determination of Quasiparticle Lifetimes in Photoemission

An important aspect in order to provide reliable information on the scattering rates is the proper analysis of the ARPES data. Thus it shall first be reviewed –in short– how electron correlations, i.e., electron interaction with other particles which is nothing else than scattering, enters the ARPES data. This part will follow the very nice introduction given by Damascelli *et al.* [16].

The probability that an electron added to (or removed from) a Bloch state in a solid at momentum $\mathbf{k}$ is still there (or is still missing) after a time interval $(t - t')$ is given by the time ordered one-electron Greens function $\mathcal{G}(t - t')$. A Fourier transform allows to express $\mathcal{G}(t - t')$ in terms of energy (ω) and momentum $(\mathbf{k})$:

$$\mathcal{G}(\mathbf{k}, \omega) = G^+(\mathbf{k}, \omega) + G^-(\mathbf{k}, \omega). \tag{6.3}$$

Here G^+ and G^- are the one-electron addition and removal Greens functions, respectively[1]. The retarded Greens function $G(\mathbf{k}, \omega) = G^+(\mathbf{k}, \omega) + [G^-(\mathbf{k}, \omega)]^*$ and its imaginary part is

[1] see Ref. [16] for the explicit expressions.

proportional to the spectral function $A(\mathbf{k},\omega) = A^+(\mathbf{k},\omega) + A^-(\mathbf{k},\omega)$. A^+ and A^- are the spectral functions which are probed by inverse and direct photoemission, respectively. A^- is proportional to the ARPES measured intensity $I(\mathbf{k},\omega)$. Since ARPES does not probe the ground state, but an excited state of a many body system, many body interactions are encoded in the spectral function. The corrections to the latter can be expressed in terms of the electron self energy

$$\Sigma(\mathbf{k},\omega) = \Sigma'(\mathbf{k},\omega) + i\Sigma''(\mathbf{k},\omega), \tag{6.4}$$

where Σ' and Σ'' are the real and imaginary parts of the electron self energy. For the spectral function one obtains:

$$A(\mathbf{k},\omega) = -\frac{1}{\pi}\frac{\Sigma''(\mathbf{k},\omega)}{\left[\omega - \epsilon_{\mathbf{k}} - \Sigma'(\mathbf{k},\omega)\right]^2 + \left[\Sigma''(\mathbf{k},\omega)\right]^2}. \tag{6.5}$$

The excitation of the electron in the photoemission process from an initial into a final state is broadened with contributions from the finite lifetime of the photohole and the momentum broadening of the photoelectron [149, 150], and the total line broadening Γ_{exp} is in general given by [9, 151]

$$\Gamma_{exp} = \frac{\frac{\Gamma_h}{|v_{h\perp}|} + \frac{\Gamma_e}{|v_{e\perp}|}}{\left|\frac{1}{v_{h\perp}}\left[1 - \frac{mv_{h||}}{\hbar k_{||}} sin^2\theta\right] - \frac{1}{v_{e\perp}}\left[1 - \frac{mv_{e||}}{\hbar k_{||}} sin^2\theta\right]\right|}, \tag{6.6}$$

with the hole (Γ_h) and electron (Γ_e) contributions, the group velocities of electrons (e) and holes (h) parallel ($||$) and perpendicular ($\perp$) to the surface ($v_{i,j}$), and the angle between surface normal and electron detection direction θ. For a normal emission experiment the expression gets simplified to

$$\Gamma_{exp}(\theta = 0) = \frac{\Gamma_h + \frac{v_{h\perp}}{v_{e\perp}}\Gamma_e}{|1 - \frac{v_{h\perp}}{v_{e\perp}}|}. \tag{6.7}$$

In the case of a two dimensional state, like the topological surface state, the dispersion of the hole state is perfectly flat in the perpendicular direction and thus the group velocity equals zero. One can thus write

$$\Gamma_{exp} = \Gamma_h, \tag{6.8}$$

which is the imaginary part of the electron self energy according to Eq. 6.5.

The real part of the electron self energy is given by the deviation of the peak positions measured in photoemission from an uncorrelated band structure. For the latter, calculations or at least assumptions are necessary, but such methods have been successfully used to determine the full electron self energy as far as it is accessible by angle resolved photoemission (see Ref. [16] and references within).

According to the above argumentation, the most direct way to extract the imaginary part of the self energy is, and on this part we are going to focus from now on, to determine the full width at half maximum (FWHM) of the peaks of energy distribution curves (ΔE) which relates to Σ'' as:

$$\Delta E = \frac{\hbar}{\tau} = 2|\Sigma''|, \tag{6.9}$$

with the lifetime of the created photohole τ. The relation is only at normal emission exactly valid, but we can assume that deviations are not too strong in the small angle range examined here ($\sim \pm 7°$) and that the proportionality is still given. Much greater problems arise from the fact, that the peaks from energy distribution curves typically have complex line form, as the spectral function is varying with energy and also the electron background from inelastically scattered photoelectrons is not straightforward to be taken into account. Also the energy cutoff at the Fermi level, as photoemission probes only the occupied states, makes data analysis more complicated and assumptions like particle-hole symmetry [152] have to be made if one is interested in the states close to E_F, which typically is the case.

Much more easy to analyze are momentum distribution curve (MDC) peaks. Usually momentum distribution curves show only a simple constant background and the peaks are Lorentzians which show only slight asymmetries at higher binding energies due to the binding energy dependence of the self energy. Similar to the energy distribution curve (EDC) peak width, the width of peaks from MDCs (Δk) are related to the inelastic mean free path l such that [153]

$$l = \frac{1}{\Delta k}. \tag{6.10}$$

The excitation's velocity (v_k) gives a connection to the lifetime and one can relate the momentum broadening in good approximation to the imaginary part of the self energy:

$$\hbar v_k \Delta k = \frac{\hbar v_k}{l} \approx |2\Sigma''(\mathbf{k}, \omega)|. \tag{6.11}$$

The obvious question is now which group velocity to use. What one determines in angle resolved photoemission from the peak positions is in general a *retarded* band dispersion. Thus, if one calculates the group velocity v_g^{exp} via

$$v_g^{exp} = \frac{\partial \omega}{\partial k} \tag{6.12}$$

one gets only a retarded group velocity which is related to the bare or non-interacting group velocity (v_g^0) by the real part of the self energy [150]:

$$v_g^{exp} = v_g^0 \left(1 - \frac{\partial \Sigma'}{\partial \omega}\right)^{-1}. \tag{6.13}$$

For an ideal Dirac cone with a linear band dispersion the multiplication with v_g^{exp} or v_g^0 will only change the absolute value but not the qualitative behavior of Σ'' over the energy range. But if kinks are introduced in the band structure by correlations or for strong hexagonal warping like in Bi_2X_3, there are strong deviations from linearity along the energy range and the multiplication will also change the qualitative behavior of Σ'' which complicates the drawing of conclusions. Strictly speaking, the real part of the self energy Σ' has to approach zero in order to allow to use the renormalized, i.e., experimental, group velocity instead of the bare group velocity [87]. For this case, Σ'' is nearly energy independent. The importance of a proper data analysis of the momentum distribution curves will be exemplified in the following section.

6.2 Anisotropic Broadening in Bi_2Te_3

The observation of strong hexagonal warping effects in the band dispersion of Bi_2Te_3 [2] and Bi_2Se_3 [85, 145] and its theoretical description [19, 154, 20] has led to a manifold of interesting predictions and observations. The influence on the spin texture with a finite out of plane rotation has been theoretically predicted [19] and in spin resolved photoemission experimentally observed [94]. That the spin is not anymore locked perpendicularly to the momentum has also been predicted [20]. However, so far there is no direct proof for the lifting of the perpendicular locking since the only experimental report, making use of circular dichroism in the angle distribution (CDAD) of photoelectrons [155] appears questionable as will be discussed in detail in Chapter 7. Also by CDAD the observation of an influence of the warping on the orbital angular momentum has been reported [156] which will also be discussed in Chapter 7.

The influence of the warping on the spin orientation also alters the possible channels for quasiparticle scattering, as described above, and this has been the topic of two theoretical investigations considering spin-orbit scattering [82] and the scattering at magnetic point defects [83]. The quasiparticle interference has been extensively studied by means of scanning tunneling microscopy (STM) and spectroscopy (STS) and anisotropies in the interference patterns have been ascribed to the hexagonal warping [157, 158, 159, 160, 161]. In addition the possibility of a spin density wave and Friedel-like oscillations of the local density of states have been predicted [19] and the latter has been experimentally observed in STM [147].

A current induced spin polarization has been predicted theoretically and it has been shown that a current may enhance the out of plane spin component when hexagonal warping is present [162, 163].

Also by angle resolved photoemission a strong influence of the warping on the scattering rates has been reported [113, 160].

A detailed discussion of all of these findings is beyond the scope of this thesis, but as the warping influences the spin orientation of the surface state [19, 20, 94] and the spin orientation influences the scattering properties of surface electrons [82, 83] we investigate in the following part whether the surface state of Bi_2Te_3 shows an anisotropy in its scattering properties due to the hexagonal warping.

The differences in the electron dispersions for the two high symmetry directions $\overline{\Gamma M}$ and $\overline{\Gamma K}$ of the surface Brillouin zone of Bi_2Te_3 have been discussed in Chapter 4.1.2 and the measured angle resolved photoemission band structure is shown in Fig. 4.5.

By varying the polar angle φ of the manipulator and measuring the photoelectron angle distribution along the vertical direction for each φ we obtain a volumetric dataset containing the dispersion along all in plane momenta $k_{||}$. The sample temperature is set to 50 K and the photon energy is 21 eV. This gives a k-resolution of about $0.003\,\text{Å}^{-1}$. From this set we extract the dispersions along the two high symmetry directions and we analyze MDCs by fitting a Lorentzian line to the surface state peak (see also Fig. 6.6 c) and d) for fit examples of MDCs). Due to the binding energy dependence of Σ'' [153] the peaks show a slight asymmetry at higher binding energies but by fitting with a simple Lorentzian we have nevertheless obtained very accurate results. From the peak positions one obtains the surface state dispersions $k_x(E)$ for the $\overline{\Gamma M}$ and the $\overline{\Gamma K}$ direction, represented in Fig. 6.3 a) by red and blue hexagons, respectively. Along the $\overline{\Gamma K}$ direction the dispersion differs only slightly from the linear behavior. For this specific sample the Dirac point is found at a binding energy of ∼330 meV and accurate fits were obtained from the Fermi level up to

binding energies of ∼220 meV for the $\overline{\Gamma M}$ direction and ∼270 meV for the $\overline{\Gamma K}$ direction. At higher binding energies the intensity of the bulk valence band prevents accurate fitting. The anisotropic dispersion along the two different directions is obvious and consistent with the hexagonal warping. However, the experimental results clearly deviate from the expectations from $k \cdot p$ theory which predicts a deviation from the linear dispersion with increased group velocity along the $\overline{\Gamma K}$ direction [19]. In reality we observe a deviation to reduced group velocities along the $\overline{\Gamma M}$ direction as already pointed out in Chapter 4.5.

The anisotropy is also reflected in the half width at half maximum (HWHM) of the Lorentzian fits as shown in Fig. 6.3 b). In the energy range where the dispersion of the $\overline{\Gamma M}$ direction deviates from the linear behavior, i.e., between ∼180 meV and ∼50 meV binding energy in the present case, the HWHM increases from ∼0.011 Å^{-1} to a maximum value of ∼0.014 Å^{-1} at a binding energy of ∼80 meV and decreases towards the Fermi energy to approach the value of ∼0.007 Å^{-1} which matches the one of the $\overline{\Gamma K}$ direction. Assuming a constant and isotropic *bare* group velocity for both directions, this would mean enhanced scattering for electrons moving along the $\overline{\Gamma M}$ direction when compared with the $\overline{\Gamma K}$ direction. The experimental group velocities are, however, anisotropic and not constant as shown Fig. 6.3 c). It should be noted, that the definition of the group velocity as $\frac{1}{\hbar}\frac{\partial E}{\partial k}$ implies that it has to be determined from the $E(k)$ dispersion and not by differentiating the $k(E)$ dispersion and taking the reciprocal value of the result. Such is only valid for a linear dispersion where the group velocity is independent of E. In the case of Bi_2Te_3 one has either to approximate the group velocities linearly over small energy intervals, taking into account artificial steps in the imaginary part of the self energy, or determine the $E(k)$ dispersion. For the results shown in panel c) we have chosen the latter method and have mapped the function $v_g(k)$ to $v_g(E)$ using the $E(k)$ dispersion. To avoid the introduction of strong noise we have fitted the $E(k)$ dispersions with polynomials before differentiating the functions. Along the $\overline{\Gamma K}$ direction the group velocities vary only slowly with energy and the increase towards lower binding energies shows a linear dependence, consistent with a slight parabolic shape of the dispersion between E_D and E_F. Towards the $\overline{M}$ point, however, we find a strong binding energy dependence of the group velocity between ∼3.5 eVÅ and the minimum value of ∼1.4 eVÅ around ∼80 meV binding energy. The Fermi velocity v_F is ∼2.5 eVÅ for the $\overline{\Gamma M}$ direction and ∼3.5 eVÅ for the $\overline{\Gamma K}$ direction.

If we multiply the HWHM from the MDC fits with the experimental group velocities to determine the imaginary part of the self energy Σ'', we qualitatively get the reversed result of panel b) as it is shown in panel d) of Fig. 6.3. Now we find scattering rates which are almost constant in energy for the $\overline{\Gamma K}$ direction with a slight decrease while approaching the Fermi level. In contrast, the scattering rates for electrons moving along the $\overline{\Gamma M}$ direction get reduced as the dispersion experiences the hexagonal deformation. Below 100 meV binding energy the decrease saturates and we find an almost constant Σ'' down to E_F. This analysis shows the importance of a proper group velocity determination as pointed out above. Therefore, before discussing the results, we want to justify the usage of the experimental group velocities by a second method, the results of which are shown in Fig. 6.4. In principle we perform an analysis of EDCs but we want to avoid an artificial broadening caused by the angle between the band dispersion and the cut direction. Assume a parabolic band with a constant energy width over the whole energy range. If the band is now cut into EDCs along the energy axis the peaks will appear broader away from the band minimum. We refer to this extra broadening as geometrical broadening. Only the cut through the minimum will show the real width as one is able to cut through

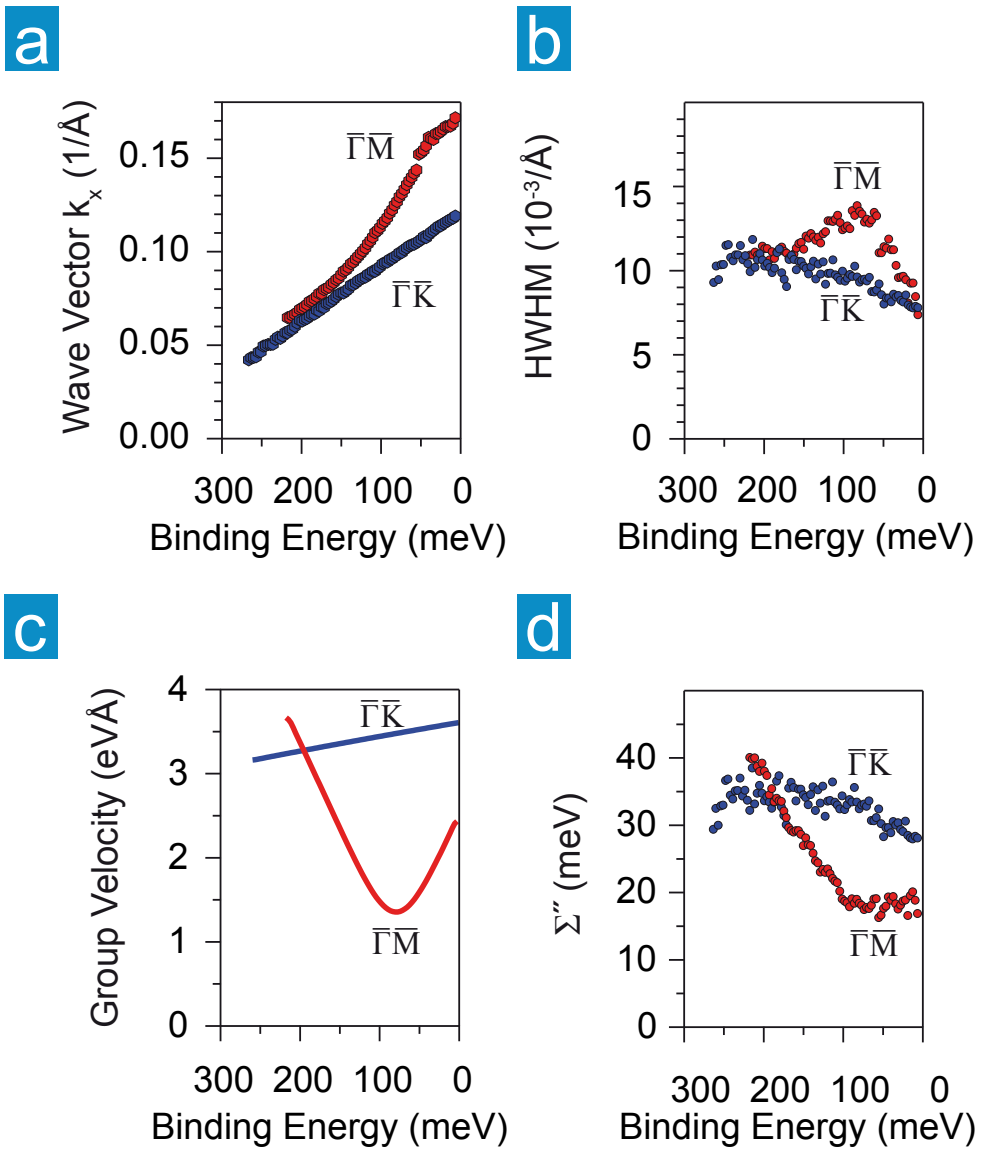

Figure 6.3: Analysis of momentum distribution curves of the surface state of Bi_2Te_3. a) The $k(E)$ dispersion of the surface state shows an anisotropic behavior which is also reflected in the half widths at half maximum (HWHM) of the peaks shown in b). c) The group velocity, obtained from the derivative of a polynomial fit to the dispersion ($E(k)$) to avoid extra noise, is strongly altered over the analyzed binding energy range along the $\overline{\Gamma M}$ direction (eVÅ$\equiv \hbar$m/s). d) Multiplication of the HWHM with the group velocity at each binding energy gives the imaginary part of the electron self energy Σ'' and reflects scattering rates that are anisotropic in k-space.

it perpendicularly without mixing energy and momentum space. But making use of the volumetric data set, it is possible to measure the energy width of a certain band and always cut perpendicularly through it. The method we have used is illustrated in Fig. 6.4 a). At

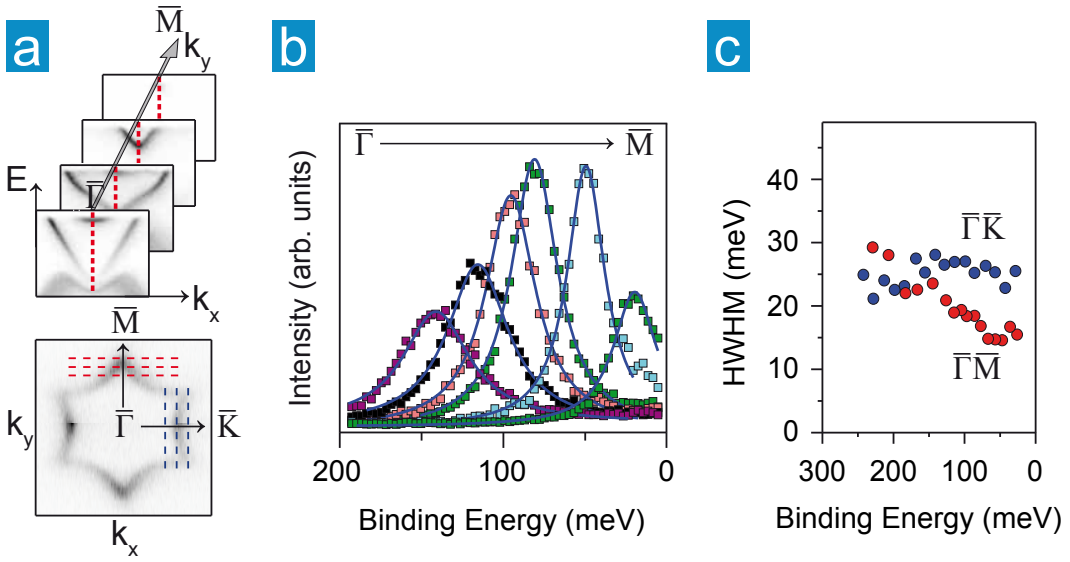

Figure 6.4: Extraction of undistorted bands from the constant energy surface mapping. a) From cuts perpendicular to the high symmetry directions (dashed lines in the lower plot) a sequence of $E(k_x)$ ($E(k_y)$) dispersions at different constant k_y (k_x) values is obtained. Parts of a sequence are shown in the upper plot. b) Energy distribution curves extracted from the sequence at $k_x = 0$ for the $\overline{\Gamma M}$ direction cut through a flat band and show rather symmetric peaks for the surface state represented by colored squares. Solid lines show the result of a Lorentzian fitted to the data points. c) The half widths at half maxima (HWHM) represent Σ'' and show the same qualitative behavior as Σ'' gained from momentum distribution curves in Fig. 6.3 d). Please note the difference between panel c) and Fig. 6.3 b) and d).

the bottom we show a constant energy surface at ∼80 meV. If we want to analyze the widths of the energy band along the $\overline{\Gamma M}$ direction we have to extract a sequence of $E(k)$ plots from the volumetric data set which cut perpendicularly to the $\overline{\Gamma M}$ direction, as indicated by the red dashed lines along the k_x direction. Above the constant energy surface, we show the results of these cuts. In each of these plots the minimum of the band is a point on the dispersion along $\overline{\Gamma M}$ and by extracting energy distribution curves at each of these points we get the full dispersion and the peaks do not suffer from the described geometrical broadening. Some of the extracted EDCs are shown as colored squares in panel b), where each color represents a different cut. Now the peaks are described by simple Lorentzian profiles as we have minimized asymmetries caused by the binding energy dependence of Σ'' with the described procedure, as well. Of course, other problems connected to the EDC analysis may still exist like the secondary electron background and the cutoff at the Fermi level. However, in our case no background correction is necessary and we simply assume that the peaks are symmetric across the Fermi level (see e.g. Ref. [164]).

The half widths at half maximum gained by the fitting of the EDCs are shown in panel c) and directly represent Σ'' for the two different directions $\overline{\Gamma K}$ (blue circles) and $\overline{\Gamma M}$ (red circles). By comparing with panel d) of Fig. 6.3 we find qualitative agreement.

While the absolute values are a bit smaller in the second analysis, the reduced scattering rates for the $\overline{\Gamma M}$ direction as compared to the $\overline{\Gamma K}$ direction in the range of the warping are confirmed. Furthermore, we also find an increase of the widths from approximately 100 meV on for the $\overline{\Gamma M}$ direction. Around 200 meV binding energy, the scattering rates match for both directions as one would expect for an isotropic dispersion like it is found in this energy range (compare for example the constant energy cuts of Fig. 4.6). Finally, we can conclude that the multiplication of the width of momentum distribution curves with the experimental group velocity to get the scattering rates, i.e., Σ'', is well justified for the topological surface state in Bi_2Te_3 at least to examine the qualitative behavior over a certain binding energy range.

The anisotropy of Σ'' in Bi_2Te_3 for the two high symmetry directions is thus in agreement with a related analysis of Cu intercalated Bi_2Te_3 by van Heumen and co-workers [160] who performed a standard analysis of the width of momentum distribution curves. However, Ref. [160] lacks a detailed description of their analysis and it does not address the question whether the use of the experimental group velocities influences the qualitative behavior of Σ''.

There are three possibilities which can explain the anisotropy in the scattering rates which are all related to the warping and to some degree connected to each other, which we will discuss in the following. A first explanation of the anisotropic behavior of the scat-

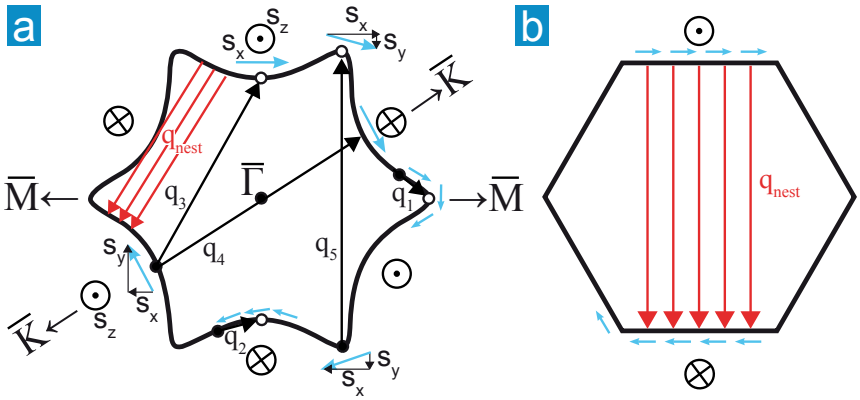

Figure 6.5: Schematics of different scattering channels. a) For a snowflake shaped constant energy surface the in plane spin direction (components s_x and s_y, indicated by blue arrows) varies stronger in the vicinity of the $\overline{\Gamma M}$ direction as compared to the $\overline{\Gamma K}$ direction, leading to a reduced probability of small angle scattering events, e.g. q_1 as compared to events exemplified by q_2. The out of plane rotation for k vectors away from the $\overline{\Gamma M}$ direction is sixfold symmetric, as indicated by the symbols $\odot$ (s_z points out of the paper plane) and $\otimes$ (s_z points into the paper plane). The scattering probability is, hence, increased for scattering under q_3, whereas backscattering (e.g. q_4) is still forbidden. The almost flat pieces of the constant energy surfaces, connected by red scattering vectors (q_{nest}) fulfill a near nesting condition. b) Even stronger nesting is expected for a hexagonal shape, however, for this case time reversal symmetry strongly suppresses scattering. Thus a spin density wave would be favored over a charge density wave [19].

tering rates lies in the spin dependent scattering, i.e., spin dependent decay of photoholes in our case. As pointed out above, for a two dimensional non-degenerated time reversal symmetric surface state, backscattering is forbidden and the strong warping does not affect

this prohibition. However, the prohibition is valid only for 180° backscattering and scattering under different angles is not completely suppressed. The probability for a scattering event is given by Eq. 6.1. In a theoretical work it has been shown that the warping affects the spin such that it is not anymore perpendicular to the momentum but tangential to the constant energy surface [20], as indicated by blue arrows in Fig. 6.5. This spin rotation was claimed to be found experimentally in Bi_2Se_3 as well [155], but the method used, i.e., circular dichroism, appears questionable as it is discussed in Chapter 7 of this thesis. Nevertheless, the spin rotation nicely explains the observed anisotropy of the scattering rates in Bi_2Te_3. Assume that an electron has been removed from the tip of a snowflake-shaped constant energy surface (Fig. 6.5 a), i.e., along the $\overline{\Gamma M}$ direction. Its spin is fully in plane ($s_x \neq 0$ and/or $s_y \neq 0$, $s_z = 0$) consistent with the mirror symmetry of the crystal [20]. As mentioned above, scattering under small angles is allowed, but it is less likely for the $\overline{\Gamma M}$ direction (e.g. q_1 of Fig. 6.5 a)), since the spin varies strongly while following the constant energy surface (blue arrows in Fig. 6.5). In contrast, a hole caused by removing an electron from the same binding energy but with the momentum pointing along the $\overline{\Gamma K}$ direction can be filled with electrons from adjacent sites in k-space since the in plane components are nearly parallel (e.g. q_2 of Fig. 6.5 a)).

Furthermore, for the $\overline{\Gamma K}$ direction the electron spin exhibits a finite out of plane component (s_z, indicated by $\odot$- and $\otimes$-symbols), which can reach as much as 60% [19], reverses its sign with an angular periodicity of $\frac{\pi}{6}$ and vanishes along the $\overline{\Gamma M}$ direction due to mirror symmetry [20]. This does not alter the first explanation, since the out of plane component varies only smoothly along a constant energy surface. Hence, adjacent places on a constant energy surface may have a different absolute values of the out of plane component but the same sign. In addition, a second explanation for the increased scattering rates along $\overline{\Gamma K}$ can be derived from the finite out of plane spin along this direction. Consider a scattering vector as exemplified by q_3 in Fig. 6.5 a). The initial state (marked by the black dot at the beginning of q_3) has finite components s_x and s_y, but there is no overlap between these components in the final state, which has s_y=0 and s_x pointing antiparallel as compared to s_x of the initial state. However, s_z is pointing out of the paper plane for initial and final state leading to a relatively strong contribution in the overlap integral (Eq. 6.2). A comparable scattering event for electrons moving along the $\overline{\Gamma M}$ direction, e.g., q_5 has only a small overlap of the in plane component (s_y in the example) between initial and final state.

A third aspect, that may play a role in the anisotropy of the scattering rates, was pointed out by Fu [19]. In contrast to an ideal Dirac cone, or for example a two dimensional free electron gas, the warped constant energy surfaces in the vicinity of the $\overline{\Gamma K}$ direction fulfill a nesting condition especially for those constant energy surfaces which imitate a hexagonal shape, as shown in Fig. 6.5 b), but also for a snowflake-like shape [165] at least a near-nesting condition is fulfilled as indicated by the red arrows in a) and b). Nesting means that parts of the constant energy surface can be mapped onto each other by a single scattering vector q_{nest}. Such nesting conditions may enhance scattering and lead to instabilities, like, for example, a charge density wave [166]. However, time reversal symmetry disfavors the formation of a charge density wave, since, independently of the warping, states at opposite k have opposite spin (Fig. 6.5 b), but Fu suggested that a spin density wave could be a possible instability in Bi_2Te_3 introduced by the warping [19]. While no signs of a spin density wave are seen in the band dispersion, i.e., a band gap at the Fermi level, it is still possible that such nesting vectors contribute to an enhanced scattering. But since the

nesting vector q_{nest} given in Fig. 6.5 b) is strongly suppressed by time reversal symmetry and the one in Fig. 6.5 a) does not favor a scattering of electrons along the $\overline{\Gamma K}$ direction, it is likely that the nesting plays a minor role for the observed anisotropy.

It is often stated that the ideal Dirac cone prevents the electrons from backscattering [165]. However, we observe an increase of the scattering rates along the $\overline{\Gamma M}$ direction as with increasing binding energy the constant energy surfaces get more and more circular. One may think of two possible explanations for this increase. First, one may expect a higher possibility for small angle scattering events since the variation of the spin direction is smaller along a circle than in the tips of the snowflake shaped constant energy surfaces. Second and more important may be the influence of the bulk valence band. Considering again the electronic structure of Bi_2Te_3 discussed in Chapter 4.1.2, parts of the topological surface state are surrounded by the valence band and photoholes can be scattered off easily into the bulk continuum. This has also been given as an explanation for the superposition of standing waves with different wavelength observed in STM for the energy range close to the Dirac point [157]. It should be noted, that a similar increase of Σ'' with increasing binding energy is observed for the $\overline{\Gamma K}$ direction as will be shown in Section 6.4. The reason why the increase is not seen in the data shown in Fig. 6.3 d) is simply that we have not analyzed the line width broadening in the full energy range up to E_D and the increase starts at higher binding energy than for the $\overline{\Gamma M}$ direction.

In contrast, we find that Σ'' increases away from the Fermi level for the $\overline{\Gamma K}$ direction, while it is almost constant along $\overline{\Gamma M}$. But the reliability of the data close to E_F for the $\overline{\Gamma M}$ direction suffers from an intermixture of surface state and bulk conduction band which is also seen in the dispersion shown in Fig. 4.5.

In an analysis of the scattering rates of the surface electrons of Bi_2Se_3, for which the warping is much less pronounced than in Bi_2Te_3 [85], conducted by Park and colleagues [148], an increase of Σ'' was found from the Fermi level to the bottom of the bulk conduction band along the $\overline{\Gamma K}$ direction. This is in agreement with our data for Bi_2Te_3 along $\overline{\Gamma K}$. The lifetime of the states is given by $\tau = \frac{\hbar}{2|\Sigma''|}$ and close to E_F we find τ=10 fs and τ=18 fs for the $\overline{\Gamma K}$ and the $\overline{\Gamma M}$ direction, respectively. This seems to be substantially less than the 40 fs reported for Bi_2Se_3 by Park *et al.* but it appears that the authors have overestimated the lifetime by a factor of 2π and thus the lifetime for photoholes in Bi_2Se_3 is with 6 fs in a similar range as in Bi_2Te_3. For our own Bi_2Se_3 samples we find lifetimes of 16 fs along the $\overline{\Gamma K}$ direction (see Section 6.4). Interestingly, this value is more close to the one of Bi_2Te_3 along the $\overline{\Gamma M}$ direction. The fact that the warping in Bi_2Se_3 is less pronounced and in the present case almost absent at E_F (circular Fermi surface) supports our argumentation that scattering is *enhanced* in the concave parts of the Fermi surface like for the $\overline{\Gamma K}$ direction in Bi_2Te_3.

To place the observed quasiparticle lifetimes in a wider context we compare to those of photoholes created in the prominent Dirac cone of graphene on SiC. From the MDC peak widths given by Bostwick *et al.* [167] we estimate τ to be similar to 5 fs at E_F which is a similar order of magnitude. This appears remarkable since the Dirac cone of graphene is spin degenerate and shows no resolvable spin orbit splitting on SiC [168] and thus the spin is not expected to extend the lifetime like in a topological surface state. However, in graphene a 180° backscattering is prohibited by the pseudospin in a similar way as for the topological surface state [49].

6.3 Electron-Phonon Coupling in Bi_2Te_3

As mentioned in the beginning of this chapter the coupling to phonons is an important decay mechanism of photoholes created in a topological surface state. For any future application the phononic contribution to the surface electron scattering will be a dominant process since its influence on pure samples can only be reduced by lowering the temperature which is not desirable for, e.g., electronic applications. In the literature there is some controversy on the influence of phononic modes on the electron self energy and statements vary from superlatives like *exceptionally weak* [87] to *surprisingly high* [144] for the strength of the electron-phonon coupling in Bi_2Se_3. We have analyzed the coupling strength λ in Bi_2Te_3 and find a value for λ in between the ones reported for Bi_2Se_3 which agrees reasonably well with a theoretical investigation by Giraud and Egger [169].

To obtain the coupling strength from an angular resolved photoemission experiment one has to analyze the temperature dependence of the imaginary part of the electron self energy. This method has also been used in the studies concerning Bi_2Se_3, but the different groups have analyzed different parts of the surface state. While Pan *et al.* [87] analyze an energy range of 30 meV below the Fermi level, Hatch and co workers [144] average Σ'' between 50 meV and 100 meV above the Dirac point. We follow the first approach as summarized in Fig. 6.6. We fit momentum distribution curves, like the examples for 0 eV binding energy given in panels c) and d), in the same way as described in the previous section and gain width and dispersion in that way for temperatures around 50 K and at room temperature for four different samples. The photon energy is 55 eV for Sample 1 and 50 eV for Sample 2, 3, and 4. The corresponding k-resolution is about 0.005 $Å^{-1}$. The group velocity in a binding energy range of 35 meV is approximated linearly as shown in panel a), where the dispersion of Sample 4 at room temperature, shown in red color scale, is compared directly to the one at 35 K in blue color scale. Clearly seen is an increase of the Fermi wave vector k_F from $\sim$0.07 $Å^{-1}$ to $\sim$0.11 $Å^{-1}$ when cooling from room to low temperature, in agreement with the temperature induced shift of the chemical potential reported in Chapter 4.1.3. Since the group velocity varies with binding energy, as seen in the previous section, the Fermi velocity also varies with temperature and between the samples due to the different intrinsic doping (Tab. 6.1).

Sample	1	2	3	4
v_F(RT) / eVÅ	3.19	2.88	3.06	2.76
v_F(LT) / eVÅ	3.26	3.48	3.35	3.48
$\Delta E_D(T_{ind.})$/ meV	100	30	140	90
$\Delta k_F(T_{ind.})/Å^{-1}$	0.03	<0.01	0.04	0.03
λ	0.17	0.21	0.21	0.14
λ_{avg}	0.18±0.03			

Table 6.1: Fermi velocities (v_F) for the different Bi_2Te_3 samples at room temperature and low temperature (between 40 K and 50 K) as well as the temperature induced energy shifts of E_D and the increase of k_F along the analyzed $\overline{\Gamma K}$ direction. Also given are the individual electron-phonon coupling constants λ extracted from the temperature dependence of Σ'' and the averaged coupling constant λ_{avg}

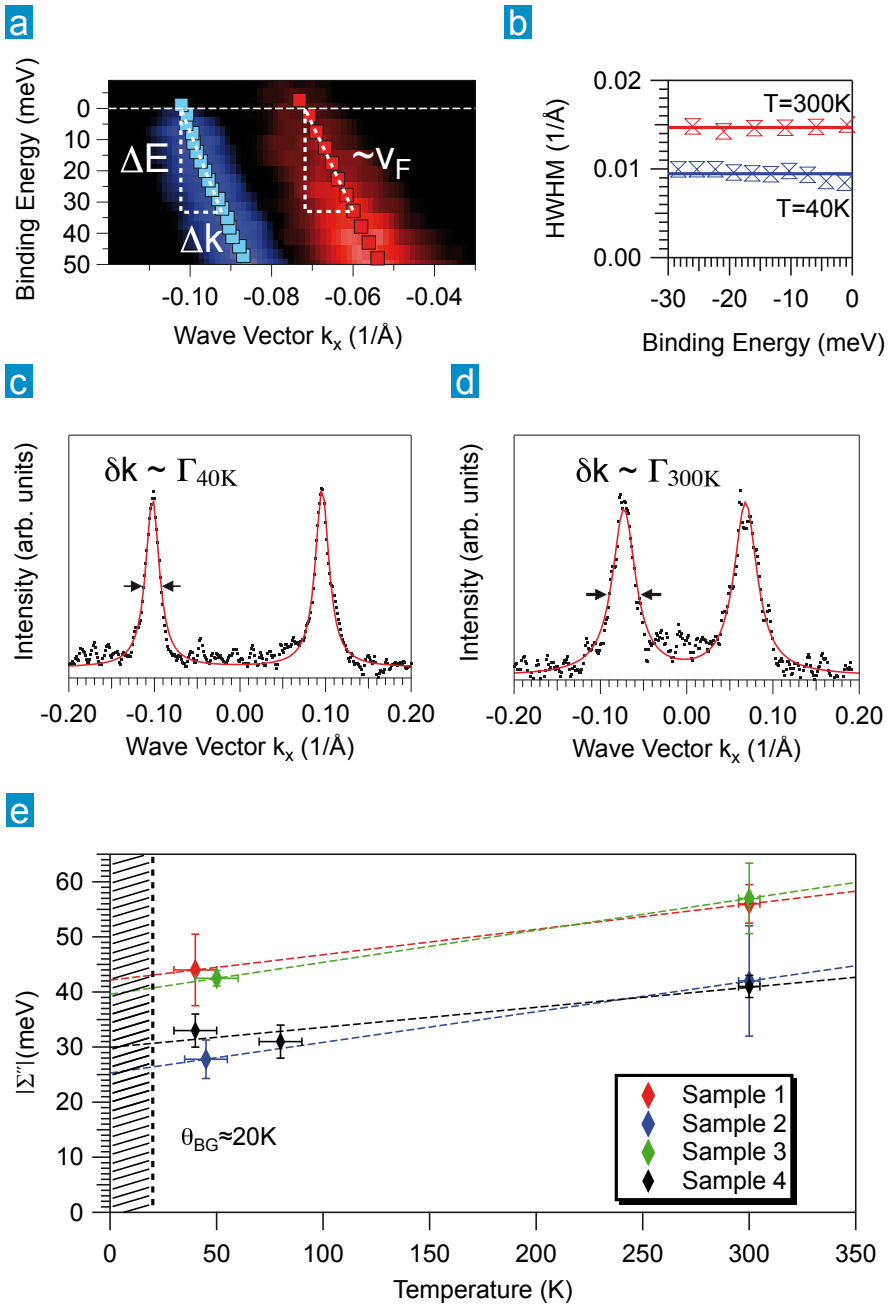

Figure 6.6: Electron-phonon coupling in Bi_2Te_3. a) Superimposed are the near Fermi edge dispersions of the surface state of Sample 4 along the $\overline{\Gamma K}$ direction at 300 K (red color scale) and at 40 K (blue color scale). The large difference in k_F is a result of the temperature induced shift of the Fermi level. The Fermi velocity v_F is determined by the slope of a linear approximation in an energy range between 0 and 35 meV binding energy. b) Half widths at half maximum (HWHM) obtained from momentum distribution curves (MDC) fitted by Lorentzian profiles (red solid line in c) and d)) at 40 K (blue double-triangles; MDC at 0 meV binding energy in c) and at 300 K (red double-triangles; MDC in d)). The full width at half maximum δk is proportional to the scattering rate Γ. Red and blue solid lines mark the average HWHM. e) The electron-phonon coupling constant λ is determined from the slope of the temperature dependence of $\Sigma'' = \text{HWHM} \times v_F$ for four different samples. The hatched area marks the temperature range below the Bloch-Grüneisen-temperature θ_{BG}.

The HWHM of the momentum distribution curves is averaged over the same energy range as indicated by the straight horizontal lines in panel b). The increase of the HWHM with the temperature is nicely seen in the MDC examples shown in panel c) and d) and fitting a Lorentzian profile gives accurate results. Panel e) summarizes the temperature dependence of Σ'' and the differently colored symbols represent the investigated individual samples. The given error bars for the temperature are estimated and are larger for low temperature since it was not possible in our setup to determine the temperature on the sample but only on the sample holder of the manipulator. The error of Σ'' is obtained through error propagation from the standard deviations of v_F and HWHM obtained by the linear regression and averaging, respectively.

For high enough temperatures the electron-phonon contribution to the imaginary part of the self energy can be approximated linearly and is given by

$$|\Sigma''(E,T)| \approx \lambda \pi k_B T, \tag{6.14}$$

with the electron phonon coupling constant λ and the Boltzmann constant k_B. Thus, from the slope $\Delta|\Sigma''|/\Delta T$ of a linear fit to the data in panel e) one obtains λ for the different samples which are given in Tab. 6.1. Except for Sample 4 we have measured only at two temperatures and thus the uncertainty of the linear regression is quite large. To minimize the error we average over all obtained values and get a mean value $\lambda_{avg} = 0.18 \pm 0.03$. The variation in the absolute values of Σ'' over the 4 samples can be ascribed to imperfections of the sample surface due to sample cleavage. Such defects contribute similarly to impurities with a constant offset to the scattering rate. It goes without saying that different densities of impurities may also contribute to the variation.

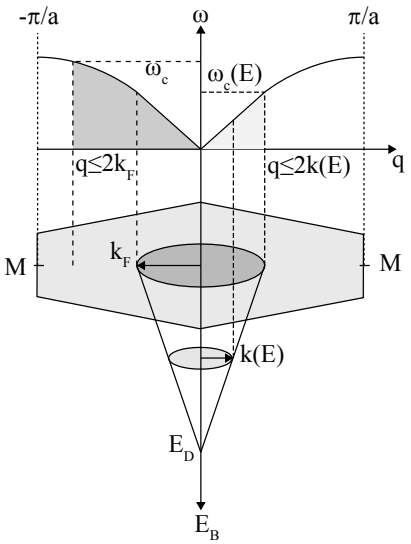

Figure 6.7: Sketch to visualize the contributing phonon modes to electron-phonon scattering for an ideal Dirac cone. All related phonon momenta (q) are described by their dispersion relation $\omega(q)$ within the first Brillouin zone ($\pm\pi/a$). Electrons at E_F can only be scattered elastically by phonons with momentum $q \leq 2k_F$. The contributing phonon modes are reduced further at higher binding energies E_B of the electrons, as the radius $k(E)$ of the constant energy surface gets reduced ($q \leq 2k(E)$).

Concerning the temperature one has to keep in mind that not at all temperatures Σ'' depends linearly on T. For bulk metals the Debye temperature θ_D is the critical temperature, and only for $T \gg \theta_D$ the linearity is a good approach. The Debye temperature is a measure for the energy of the highest phonons involved. Below this temperature the phonon spectrum is not fully occupied since the high energy modes cannot be excited. This results in a stronger temperature dependence of the resistivity or scattering rates of the electrons. Since electron-phonon scattering events are quasielastic, the maximum phonon momentum involved is limited to $2\hbar k_F$ [170] which corresponds to a 180° backscattering event. In many metals k_F is of the same order as the size of the Brillouin zone and thus all populated phonons can scatter off electrons [170]. However, in low dimensional metallic systems this is not the case since, like for Bi_2Se_3 and Bi_2Te_3 the Fermi surface is much smaller than the Brillouin zone and thus only a small part of the acoustic phonons with energies $\hbar c_s \mathbf{q} \leq 2\hbar c_s k_F$ may contribute to the electron-phonon coupling, where $\mathbf{q}$ is the phonon wavevector and c_s is the sound velocity. This is illustrated in Fig. 6.7 for an ideal Dirac cone situated in a hexagonal surface Brioullin zone. For simplicity it is assumed that only acoustic phonons described in the surface Brillouin zone contribute to the scattering. The limited number of phonon modes that contribute to the scattering are the modes that have the lowest energies ω which can be understood from the qualitative dispersion relation $\omega(\mathbf{q})$ in Fig. 6.7. Thus, the phonon modes involved start to *freeze out* at temperatures far below θ_D and, therefore, a linear behavior is observed down to much lower temperatures. Hence, for low dimensional systems one defines the Bloch-Grüneisen temperature θ_{BG} as a function of the Fermi momentum k_F [169]

$$\theta_{BG} \equiv \frac{2\hbar k_F c_s}{k_B}. \tag{6.15}$$

This dependence has been successfully probed experimentally in graphene, where the size of the Fermi wave vector can be tuned by a gate voltage and by this the onset of the linear temperature dependence of the resistivity has been shifted [170].
For our Bi_2Te_3 samples we can estimate θ_{BG} to be in the range of 20 K, which is almost an order of magnitude less than the bulk Debye temperature of Bi_2Te_3, $\theta_D \approx 160\,K$ [171] and well below our measurement temperature of ∼50 K. Thus, the assumption of a linear behavior appears justified. Moreover, in Bi_2Se_3 a linear temperature dependence of Σ'' was observed down to 18 K [87] and the size of the Fermi surface is comparable in both systems.

However, as obvious from Fig. 6.6 a) and from Chapter 4.1.3 the size of k_F increases upon cooling. As a consequence the maximum energy of phonons that may contribute to the scattering of electrons is reduced at room temperature. In addition, the available electron density of states in which photoholes could scatter is reduced at room temperature since the bulk conduction band is depopulated according to the rigid band shift reported in Chapter 4.1.3. Both effects could lead to an underestimation of the phonon coupling constant, since Σ'' would appear reduced at room temperature and thus the slope of the temperature dependence is smaller. But by comparing the coupling constants of the individual samples with the temperature induced changes of E_D and the changes in k_F no obvious correlation is found. Moreover, for Sample 2, where the temperature induced changes are negligible as compared to the others, λ is as high as for Sample 3 where the largest changes are observed. Another aspect which may increase Σ'' at low temperature is the impurity scattering. While there is no significant temperature dependence for the scattering itself, the impurity density is likely to increase upon cooling due to condensation of residual gases in the vacuum system. This assumption is supported by the observation

that the pressure in the vacuum system is typically decreased by almost an order of magnitude when cooling the manipulator. An increase of Σ'' caused by impurities on the cold sample will decrease the slope and thus λ. Different impurity densities on the sample should lead to different offsets of Σ'' at E_F and indeed Fig. 6.6 e) shows such differences as samples 1 and 3 show a $\sim$1.3 times higher Σ'' value at low temperature. But this difference seems to be constant over the whole temperature range and should thus not influence the results. Moreover, following the argumentation in Chapter 4.1.3 more impurities should be present in samples with a higher energy shift of the band structure. But since no correlation between the strength of temperature induced shifts and the absolute value of λ is found from Tab. 6.1 we can conclude that the influence of condensated impurities on the analysis is negligible. Indeed we find a relatively small effect on the scattering rates with non magnetic impurities in the following section and we can expect any residual gases in the vacuum system to have negligible magnetic moments.

The reliability of our analysis is further supported by the excellent agreement with a recent theoretical investigation where the electron-phonon coupling in Bi_2Te_3 was found to be $\lambda_{th} \approx 0.13$ [169]. Also, the extracted λ is of the order of magnitude reported by Hatch and coworkers for Bi_2Se_3 ($\lambda_{Bi_2Se_3} \approx 0.25$) [144]. As mentioned above they analyzed the width of momentum distribution curves in an energy window relative to E_D and their analysis does therefore not suffer from a change in k_F. As pointed out in Ref. [144] the strength of the phonon coupling is thus higher than expected for a topological surface state with the expectation based on the fact that the available phase space is reduced due to the spin texture and the electron spin is conserved during electron-phonon scattering [172].

On the other side there is the very low value of $\lambda_{Bi_2Se_3} \approx 0.08$ reported by Pan *et al.* [87] and the absence of a characteristic *kink* in the surface state dispersion like it is known from metals [164] or high-T_c superconductors [173]. But the latter is visible at a characteristic energy given by the Debye temperature or, as in our case by the Bloch-Grüneisen temperature. This energy scale is as low as $\theta_{BG}/k_B \approx$2 meV, and thus below the detection limit of our experiment given by the energy resolution of $\sim$20 meV. Even if the full phonon spectrum up to the maximum energy ($\approx$ 20 meV [174]) would contribute, a *kink* would hardly be observed in our experiment. This was also pointed out by Pan and colleagues [87]. From inelastic helium-atom scattering, thus looking at the coupling of surface state electrons to phonons, an even higher coupling strength was reported only recently [175]. But while we cannot distinguish the coupling to a specific phonon mode in angle resolved photoemission, the experiment by Zhu *et al.* [175] may mix up bulk and surface electronic contributions which might explain the high value of λ=0.43. However, it may still be interpreted as a confirmation of the higher coupling measured by us and Hatch *et al.* as compared to Pan *et al.*

Nevertheless, the fact that the low coupling constant observed by Pan *et al.* was confirmed in three different samples and, moreover, that Σ'' has been measured at many more temperatures than in our case and in that of Hatch *et al.* leaves also doubts about the validity of the high coupling constants and calls for a more profound investigation including other methods to finally conclude about the strength of the phonon coupling to the Dirac fermions in Bi_2X_3.

6.4 Impurity Induced Scattering

In the last section of this chapter the influence of magnetic and non-magnetic impurities on the quasiparticle lifetimes will be analyzed. The influences on the band structure have been addressed already in Chapter 5 and are assumed to be known by the reader. However, the most important result of that chapter shall be repeated once more, namely that the topological surface state shows its predicted and unique robustness against surface impurities for both investigated types of impurities, magnetic and non-magnetic ones. This statement concerns the existence of the surface state and the absence of an energy gap in its dispersion at the Dirac point.

However, in this section it will be shown that there *is* interaction between impurities and the surface state electrons, which is not surprising keeping in mind the results from the two previous sections, and that there *is* a difference between magnetic and non-magnetic impurities. The latter was indeed doubted in a recent photoemission experiment by Valla and colleagues [113] in contrast to theoretical investigations of the quasiparticle interference patterns where new scattering channels arise which are explained by a spin flip caused by a magnetic point defect [83].

6.4.1 Non-Magnetic Impurities

First, we analyze the quasiparticle scattering rates for Bi_2Se_3 prior to and after deposition of 0.2 monolayer (ML) and 1 ML of *non-magnetic* silver impurities. We apply the same procedure described in the previous sections, namely extraction of the half widths at half maximum (HWHM) of the peaks and its dispersion from momentum distribution curves (MDCs) and calculate the imaginary part of the self energy Σ'' by multiplication of the HWHM with the experimental group velocities v_g. The results are shown in Fig. 6.8. For the clean sample we show the positive k_x values of the surface state above and slightly below the Dirac point (E_D) in the top part of the figure as a function of binding energy. Overlaid is the result of the position of the peak maxima as obtained by the fitting procedure as black dots. The characteristic energy points of the band structure, E_D and the bottom of the bulk conduction band are marked by white dashed lines. The photon energy is 18 eV and the measurement temperature ∼8 K. The data is taken along the $\overline{\Gamma K}$ direction. The lower half of the top figure shows the dispersion after 0.2 ML of Ag have been deposited at room temperature (detailed discussion in Chapter 5.2). Photon energy and measurement temperature are the same as for the clean sample.

For the clean sample we find a rather flat behavior of Σ'' as a function of binding energy represented by red dots in the lower panel of Fig. 6.8. We observe only a slight increase from E_F to approximately the bottom of the bulk conduction band at ∼140 meV binding energy. For higher binding energies a slight decrease is seen in the energy dependence up to E_D. At even higher binding energies the fit gets more and more inconclusive as an intermixture of the surface state with the bulk valence band takes place. While being much less pronounced in our case, the observed increase and decrease are in agreement with the results reported by Park *et al.* [148]. In a perfect sample one would expect Σ'' to increase with increasing binding energy from 0 meV at E_F, thus the relatively high offset can be interpreted as impurity scattering due to the defects and vacancies that cause the intrinsic doping (see Chapter 4 for details) as well as step edges and imperfections caused by the sample cleavage. Also adsorbed residual gases may already play a role.

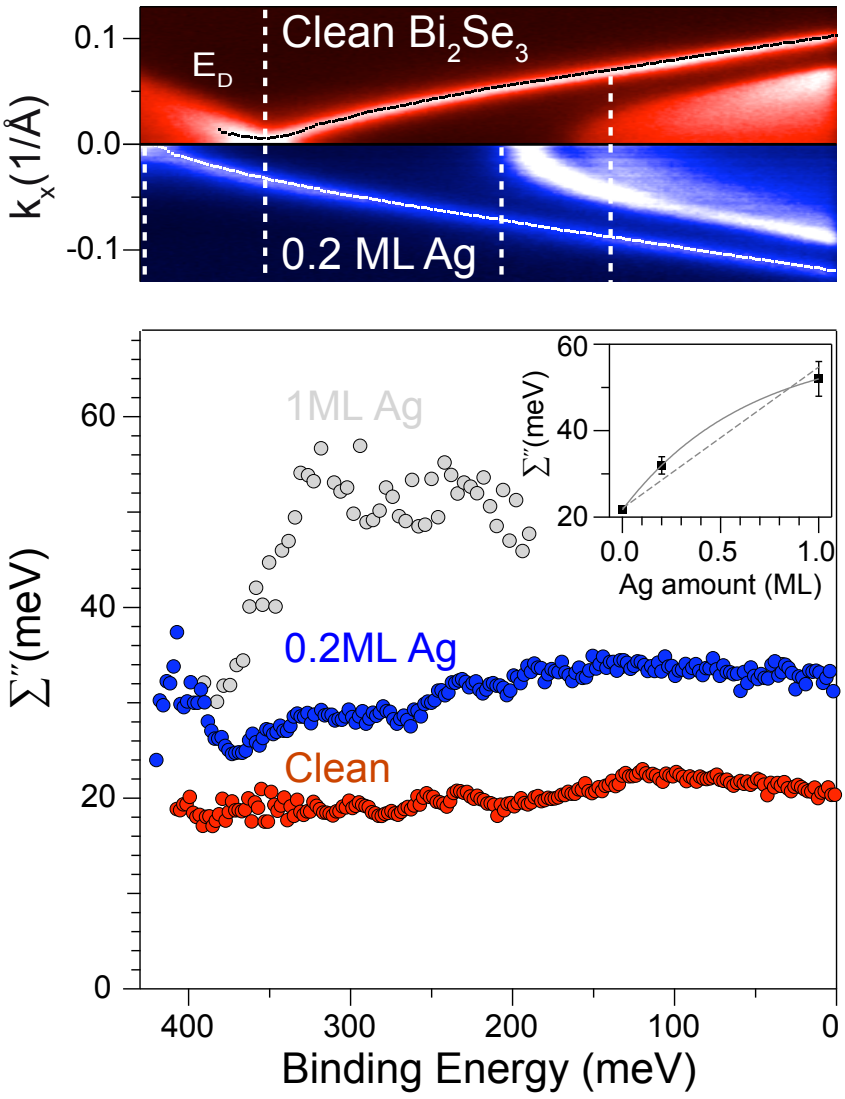

Figure 6.8: Ag deposition on Bi_2Se_3. Top: Direct comparison of the dispersions of clean Bi_2Se_3 (red color scale) and after deposition of 0.2 ML Ag (blue color scale). Dots represent the peak maxima of the MDC fits. Dashed lines mark the energy of the Dirac point (E_D) and the bulk conduction band bottom, i.e., after Ag deposition the bottom of the additional bands. The photon energy is 18 eV and the measurement temperature is 8 K. Bottom: The imaginary part of the electron self energy gets increased upon Ag depostion (blue dots) as compared to the clean sample (red dots). For 1 ML of Ag on top (grey dots) Σ'' is even higher, indicating some proportionality of the scattering rates to the impurity density as shown in the inset. The dashed line shows a linear regression to the data points while the solid line assumes an exponential behavior.

The scattering by impurities is typically assumed to be constant over the whole binding energy range, since one assumes that the impurities stay unaffected and experience no excitations by the scattered electrons, which means that the electrons are scattered elastically. For the topological surface state, however, the degenerate bulk bands increase the available phase space and thus scattering should show a proportionality to the bulk density of states [148]. This is a reasonable explanation for the decrease of Σ'' observed within the bulk energy gap. Naively, one may expect a sharp drop of Σ'' rather then a slender decrease but the two other processes that scatter off electrons, electron-phonon and electron-electron interaction are connected to energy transfers which can excite in-gap surface electrons into the bulk continuum. For the impurity scattering the available phase space gets reduced but stays finite since small angle scattering is allowed and only the exact 180° backscattering event is forbidden. Considering the arguments concerning the Bloch-Grüneisen temperature given in the previous section, another explanation for the decrease at binding energies above the conduction band bottom is that with decreasing diameter of the constant energy cuts less and less modes may contribute to the electron-phonon scattering (compare Fig. 6.7). Assuming that only the surface located phonons scatter off surface located electrons, a simple linear decrease is straightforward to derive. The wave vectors of the phonons ($\mathbf{q}$) which contribute to the scattering are given by $2k(E)$, where $k(E)$ is the surface electron wave vector at a given binding energy E. Assuming further a perfect Dirac cone with a linear dispersion it is easy to see that $k(E)$ reduces linearly with increasing binding energy E. Linearity is also a good approximation for the phonon dispersion $\omega(\mathbf{q})$ if $\mathbf{q}$ is small enough. Thus the phonon density of states $D(\omega)$, where ω is the phonon energy, is constant and the number of contributing phonons is proportional to the cutoff energy ω_C given through the diameter of the Dirac cone at energy E. It follows that the number of contributing phonons decreases proportional as the binding energy increases up to E_D and this proportionality naturally explains the decrease of Σ''.

While the described trends appear quite obvious and explainable, it should be noted that Σ'' varies only between 18 meV and 23 meV over the whole analyzed binding energy range and the variation is thus within the error of the analysis. On the other hand, a simple increase over the whole binding energy range, from E_F to ∼250 meV, as reported by Valla *et al.* [113] cannot be confirmed by our data.

The obvious effect of Ag deposition, despite the n-doping and the formation of parabolic bands in the bulk conduction band range as described in Chapter 5.2, is an increased offset of Σ'' from the Fermi level on (blue dots). This increase can be easily explained by an increase of the impurity density. The energy region of increase observed in the clean sample extends now to a slightly higher binding energy of ∼160 meV which is followed by a small dip. This dip is seen in the energy range of the *gap* between the two parabolic features that form upon Ag deposition. A small bump can be observed and falls energetically together with the bottom of the second parabolic feature. However, the described variation is again very small and the correlations with the parabolic features could be by chance or an artifact of the fit. In total one could identify the range of the parabolic features as increasing and the range below as decreasing if one takes into account the error of the analysis. This means that the only change of Σ'' is an increased offset and a shift of the characteristic variations of Σ'' already observed in the clean sample consistent with the n-doping.

When Ag is deposited on Bi_2Te_3, than quasiparticle interference fringes are observed in STM along the $\overline{\Gamma M}$ direction in an energy range where bulk conduction band and surface state coincide, thus outside the gap [157]. Inside of the gap the fringes and the

related standing wave patterns are smeared out. A similar behavior was observed for Bi_2Se_3 in the vicinity of the Dirac node and at higher binding energies [159]. This has also been attributed to a scattering between surface state and bulk valence band states as the observed scattering vectors were too large and too broad to be explained by surface state scattering. Both results agree well with the observed behavior of decreasing scattering rates between conduction band bottom and Dirac point for pristine and Ag impured Bi_2Se_3. We also observe increasing HWHM at binding energies above E_D but due to the intermixture with bulk bands the surface state can not be well distinguished and we do not present the results here.

In a second deposition step we have increased the Ag mass equivalent to 1 ML (grey dots) which results only in a slight additional doping (see Fig. 5.2 for the resulting dispersion). Since the fitting gets rather inconclusive due to a strong overlap of the peaks derived from the topological surface state and from the Ag induced parabolic features we show only the results for the energy range where the features could well be distinguished. We observe again a strong increase in Σ'' and the behavior observed for 0.2 ML makes the assumption reasonable that this is caused by a higher offset from the Fermi level on. The sharp decrease is likely to be an artifact of the analysis caused by a slight missalignment of the photoemission experiment such that we do not cut the Dirac point exactly which gives a parabolic instead of a gapless surface state. This gives a strong *virtual* reduction of v_g which in turn produces the drop off of Σ''.

The important result is the increase of Σ'' with increasing impurity density rather than with increased warping as suggested by Valla and co-workers [113]. This can be understood by the fact that the 1 ML Ag has hardly shifted the band structure to higher binding energy and thus does not increase the warping much more than the first deposition step already did. We therefore show in the inset of Fig. 6.8 Σ'' averaged over the whole binding energy range as a function of the Ag amount. Since we can not analyze the whole dispersion for 1 ML Ag there is some uncertainty about the accurate dependence. However, assuming that the surface electrons interact only with impurities residing directly on the sample surface, a saturating behavior (solid line) appears more likely than a linear increase (dashed line).

6.4.2 Magnetic Impurities

Next we turn to magnetic impurities. In Fig. 6.9 b) we present the linewidth analysis for Fe deposited on Bi_2Se_3. Since the changes are more drastic than in the case of Ag impurities we also present the *raw* fitting parameters in panel a) where all data has been shifted relative to the energy of the Dirac point E_D. Throughout Fig. 6.9, red color represents the sample prior to Fe deposition, green color has been chosen for the low temperature deposition of Fe (T$\sim$8 K) and blue color for the room temperature deposition (T$\sim$300 K). The measurement temperature is $\sim$8 K for all three samples and the photon energy is 18 eV for the clean and room temperature deposition and 21.5 eV for the low temperature deposition. The Bi_2Se_3 sample is the same for both deposition conditions, but the surface has been recleaved prior to the low temperature deposition. Since the cleavage goes along with the formation of new step edges and other defects, the data for the clean sample are strictly only to be taken as the basis of the low temperature deposition; for the room temperature deposition no data of the clean sample exists at T$\sim$8 K since the sample has been cooled only after deposition of Fe. In detail, Σ'' varies between different cleavages depending on the quality of the surface, as obvious from comparing the result of the clean

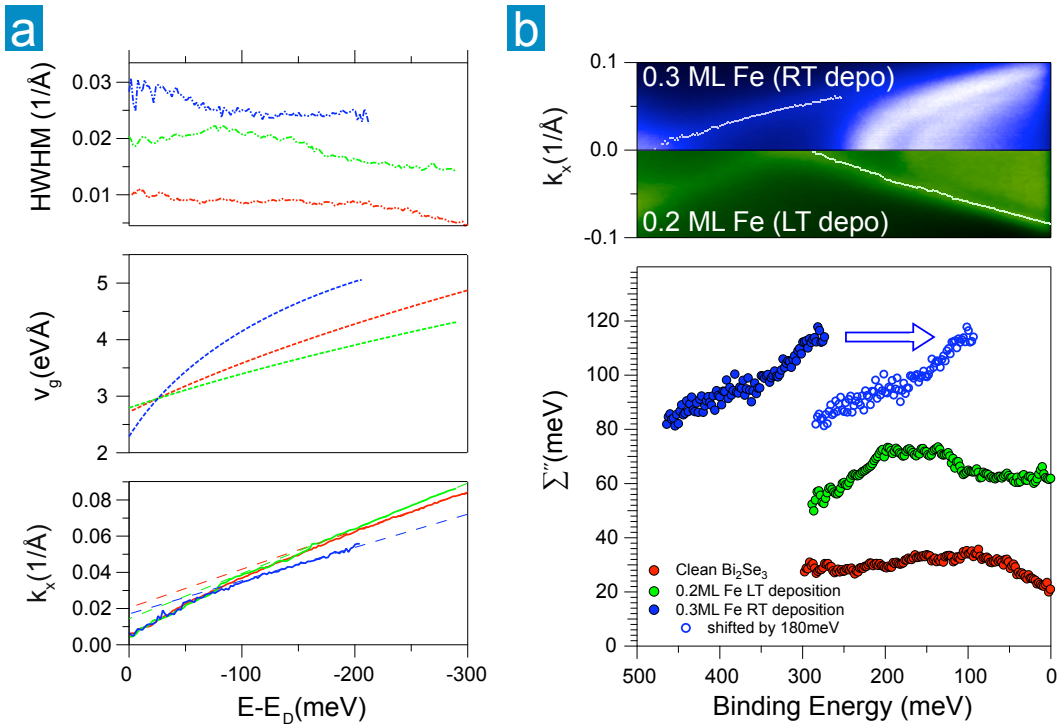

Figure 6.9: Fe deposition on Bi_2Se_3. a) Dispersion $k(E)$ (bottom), group velocities $v_g(E)$ (center) and half width at half maximum (HWHM) (top) as a function of the energy relative to the Dirac point before deposition (red) and after deposition of 0.2 ML Fe at T=8 K (green) and 0.3 ML Fe at T=300 K. The photon energy is 18 eV for the clean sample and room temperature deposition and 21.5 eV for low temperature deposition. The measurement temperature is 8 K throughout. Fe reduces v_g slightly when deposited at low temperature and increases the HWHM while the dispersion appears more linear. For room temperature deposition we observe an enhanced v_g while the HWHM is increased even more and the dispersion is more parabolic. b) Direct comparison (top) of room (blue color scale) and low temperature (green) deposition of Fe. White dots mark the peak maxima obtained from the fits. The imaginary part of the electron self energy Σ'' (bottom) is increased independent of the sign of the doping and deposition condition indicating enhanced scattering rates. The enhancement is stronger than for non-magnetic impurities (Ag) in Fig. 6.8.

sample in Fig. 6.9 b) with that of Fig. 6.8.

The direct comparison of the dispersion obtained from the peak maxima of the MDCs is shown in the bottom panel of Fig. 6.9 a) (and overlaid on the intensity plot in the upper panel of b). Following the red line of the clean sample we already find a rather strong deviation from the linear dispersion expected for a Dirac fermion. This has been emphasized by plotting a straight red dashed line that matches the measured dispersion well above E_D. This behavior is even more pronounced when Fe is deposited at T$\sim$300 K. Please note that a fit is possible only in a limited energy range for this case since the strong intensity of the extra states introduced by the Fe in the range of the bulk conduction band hides the intensity of the surface state completely. In contrast, the green dashed curve follows the experimental dispersion of Bi_2Se_3 when Fe is deposited at low temperature over a longer energy range indicating an enhanced linearity. This is also reflected in the behavior of the group velocities v_g as a function of energy plotted in the center of panel a). Accordingly, the enhanced linearity is achieved by a reduction of v_g at binding energies below E_D. This is again in contrast to the case of room temperature deposition where v_g gets increased well below E_D and strongly decreases towards the Dirac point. The HWHM as a function of energy are shown in the upper panel and after multiplication with v_g we obtain Σ'' as shown in the bottom panel of Fig. 6.9 b).

Despite the steeper increase in the energy range of the bulk conduction band we observe a very similar behavior for the clean sample as described for the clean sample before the Ag deposition above. The offset at E_F is within the error of the analysis the same for both and amounts to $\Sigma''(E_F)$ $\sim$20 meV indicating a comparable amount of impurities. But the increase amounts to $\sim$35 meV at a binding energy of 80 meV, whereas only $\sim$23 meV are observed at $\sim$140 meV in Fig. 6.8. The sample temperature is similar, thus a similar amount of phonon modes may contribute to the scattering. According to Ref. [148] the only explanation would be an enhancement of electron-hole pair creation, which would mean a stronger increase of the bulk density of states for the case presented in Fig. 6.9. However, the obviously stronger n-doping in the previous case would mean a higher integrated value of the bulk density of states. One possible explanation could be that the strong n-doping has led already to the formation of a two-dimensional electron gas in the region of the bulk conduction band [108] which would have a constant density of states. However, while we do observe a difference in the intensity distribution in this energy range for samples prior to Fe and Ag deposition (compare Fig. 5.2 a) and Fig. 5.14) clear fingerprints of a two-dimensional electron gas are missing. A second explanation could be an anisotropy similar to the case of Bi_2Te_3. On the one hand the warping is much less pronounced in Bi_2Se_3 and a one to one matching of the sample positions examined with low energy electron diffraction and photoemission is almost impossible and thus the $\overline{\Gamma K}$ and $\overline{\Gamma M}$ directions could get confused by viewing the dispersions only. But on the other hand the anisotropy should be much weaker with reduced warping. Thus, the observed differences remain puzzling at the moment.

After deposition of 0.3 ML Fe at room temperature Σ'' gets increased by more than a factor of 2 to 3, depending on the considered energy. In the figure we have shifted the result by a constant energy offset given by the amount of extra n-doping of $\sim$180 meV (blue open circles). Even though we are not able to analyze the topological surface state in the vicinity of the Fermi level because of the strong intensity of the extra parabolic states, we ascribe the strong increase of Σ'' as mainly being due to an increased offset at E_F caused by the Fe impurities. Moreover, the Dirac point is now at a similar binding energy as in

the case of 0.2 ML Ag, due to the higher *intrinsic* n-doping observed for the Ag/Bi_2Se_3 sample prior to the Ag deposition. This also means a similar amount of warping of the constant energy cuts. This already gives a hint that the warping, while being undoubtedly important for the scattering rates, plays only a minor role for increased scattering rates upon impurity deposition. It has been suggested instead as the main reason by Valla *et al.* [113].

Our argument is reinforced even more by looking at the result for 0.2 ML Fe deposited at T$\sim$8 K. Σ'' is increased less than for the case of room temperature deposition, but still obviously increased showing a by a factor of $\sim$3 higher offset at the Fermi level than the clean sample. It goes without saying, that the slight p-doping observed for that case is equivalent to a reduction of warping. Nevertheless, the scattering rate at E_F is still a factor two higher than for the case of 0.2 ML Ag. This is already a strong indication, that there is a difference between ferromagnetic and non-magnetic impurities, another contradiction to the results of Ref. [113]. It appears therefore likely, that spin flip processes occur by scattering at magnetic impurities, in agreement with theoretical predictions [83], and STM results for $Bi_{2-x}Fe_xTe_{3+d}$ [158], where new, by time reversal symmetry strictly forbidden, scattering vectors show up in the quasiparticle interference patterns. For Co impurities deposited on the surface of Bi_2Se_3, where X-ray magnetic dichroism revealed the absence of magnetic order [176], the observed quasiparticle interference patterns in STM appear more isotropic in all k-directions [176] as compared to the case of $Bi_{2-x}Fe_xTe_{3+d}$ [158]. This is in contrast to the absence of quasiparticle interference along the $\overline{\Gamma K}$ direction observed with STM in Ref. [159] for clean Bi_2Se_3 and in Ref. [157] for Ag on Bi_2Te_3.

Also the binding energy dependence of Σ'' indicates strong differences between magnetic and non-magnetic impurities. In stark contrast to all other cases, the low temperature deposition of Fe leads to an almost constant Σ'' between 0 meV and $\sim$100 meV. At 100 meV binding energy we observe a kink followed by an increase up to $\sim$140 meV where a second kink is observed. Up to $\sim$200 meV binding energy Σ'' is again constant before it decreases strongly towards E_D initialized by a third kink. Such kind of kinks are not seen for Fe deposited at room temperature, but comparable regions have not been analyzed due to the described problems of lacking distinguishability from the other states at lower binding energy. Similar features can thus at least not be excluded.

Kinks in the imaginary part of the self energy are manifestations of quasiparticle interactions but are typically escorted by kinks in the electron dispersion which are hardly seen by the naked eye, if not absent at all in the case shown here. More insight can in principle be obtained from the real part of the electron self energy which can be gained by subtracting the bare band dispersion from the renormalized one. Unfortunately, the bare band dispersion for Fe on Bi_2Se_3 is unknown at the present state, and the assumption of a straight line [164] does not seem to be valid in our case keeping in mind that the dispersion of the pristine sample is not linear at all. Therefore the presented results give only a slight hint that new quasiparticle interactions might be introduced by the deposition of Fe and call for a deeper theoretical investigation which is beyond the scope of this thesis.

Similar results are gained for Bi_2Te_3 as shown in Fig. 6.10 where we compare dispersions and Σ'' prior and after deposition of 0.4 ML Fe at room temperature. The measurement shown is along the $\overline{\Gamma K}$ direction at a temperature of $\sim$50 K and the photon energy is 55 eV. In the clean sample we now observe a similar behavior as in Bi_2Se_3, i.e., an increase of Σ'' from the Fermi level to approximately 50 meV binding energy. This is followed by a slight decrease to 240 meV. In contrast to Bi_2Se_3 we observe a strong increase from here

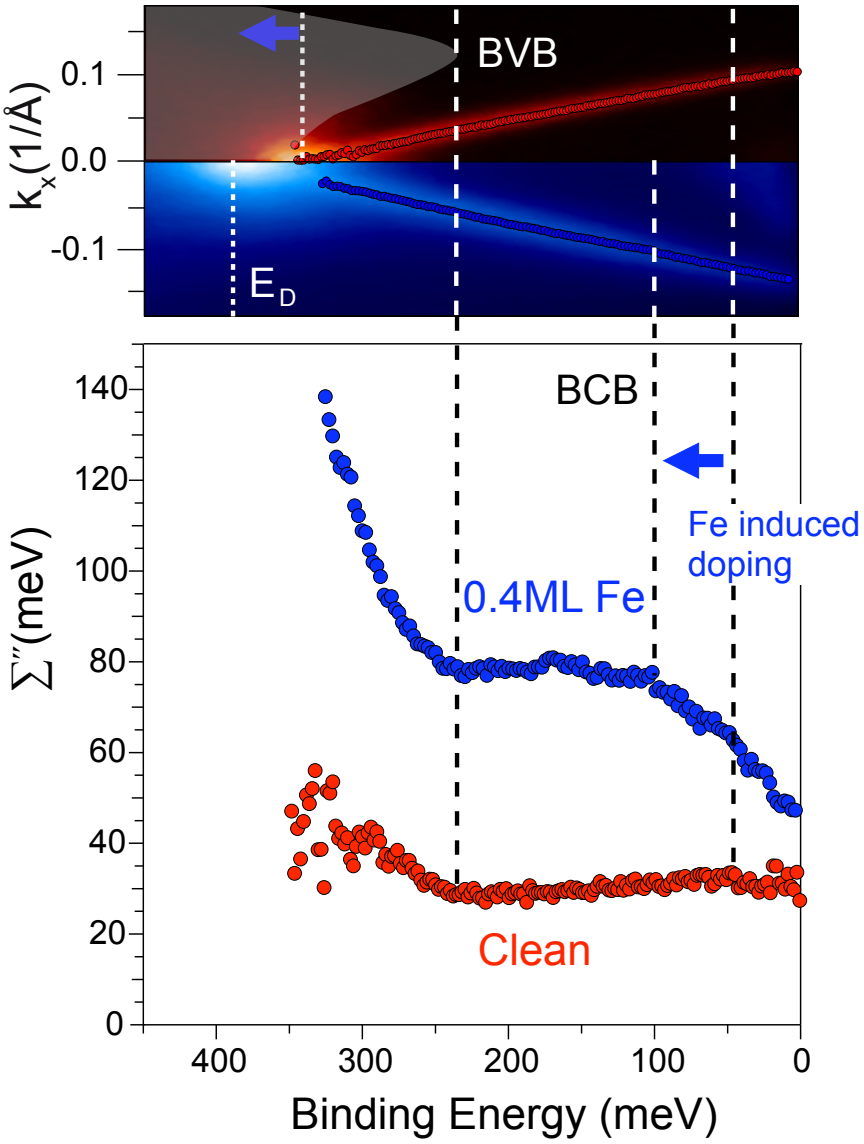

Figure 6.10: Fe deposition on Bi_2Te_3. Top: Direct comparison of the dispersions prior to (red color scale) and after Fe deposition (blue color scale). Red and blue dots mark the peak maxima of the Lorentzian fits. White dashed lines indicate the energetic of Dirac point E_D, bottom of the bulk conduction band (BCB), and top of the bulk valence band (BVB) which is emphasized for the clean sample by the grey shaded area. The photon energy is 55 eV and the measurement temperature is 50 K. Bottom: Prior to Fe deposition the imaginary part of the electron self energy Σ'' is almost constant between BCB and BVB (red dots). Σ'' gets enhanced after Fe deposition (blue dots). Strong increases are observed in the regions where bulk bands are present at the same binding energy.

up to the limit of our analysis. This increase is well below the Dirac point binding energy ($E_D \approx$340 meV) marked by a white dashed line in the dispersion shown in the upper panel of Fig. 6.10. Again, the red color scale represents the clean sample whereas the blue color scale has been chosen for the sample after Fe deposition. The reason for the sudden increase of Σ'' is simply the presence of the bulk valence band at higher k values as sketched by a grey shaded area in Fig. 6.10. The valence band maximum (BVB) is again marked by a white dashed line. Please note, that electrons might be scattered off under any angle which means, that one has to take into account the absolute band maximum rather than the maximum of the projection along $\overline{\Gamma K}$.

After the deposition of Fe, with the outcome discussed in Chapter 5, Σ'' has changed drastically as can be seen by following the blue dots in the lower panel of Fig. 6.10. First of all the offset at the Fermi level was measured from ∼30 meV to ∼50 meV. The following increase is much more pronounced and goes to higher binding energies. The latter is in agreement with the shift of the Fermi level due to the filling of unoccupied states with electrons donated by Fe adatoms. Since the bulk conduction band is hardly resolved at this photon energy due to a low cross section and furthermore we are away from the minimum energy of the k_z dispersion, we have estimated the shift to be similar to the one of the Dirac point and it fits quite well with the energy where the increase is terminated. Inside of the bulk energy gap we observe, in contrast to the clean sample, a plateau, similar to the case of 0.2 ML Fe on Bi_2Se_3 deposited at low temperature. Afterwards, now again in agreement with the clean sample, a strong increase is observed. The increase appears even stronger than for the clean sample but the onset is seen at a similar binding energy. This is an interesting observation. One would expect the onset at a higher binding energy, if one assumes that the valence band shifts by the same amount as conduction band and surface state. All these observations taking together give a strong indication, that new scattering mechanisms are introduced or that restrictions due to the time reversal symmetry get obsolete after Fe has been deposited. Moreover, since the warping is already very pronounced in the clean sample it can not be given as a possible explanation for the strong changes. Strong changes are only expected as soon as new scattering vectors, especially such that fulfill a nesting or near nesting condition get introduced. This is the case when the shape of the constant energy cuts changes from a circle to a convex hexagon or from the convex hexagon to a concave shape [158].

Summary of Conclusions

To conclude this chapter, it has been shown, that the strong hexagonal warping in Bi_2X_3 leads to a strong anisotropy of the scattering rates for quasiparticles traveling along the two distinct high symmetry directions of the surface Brillouin zone. The electron-phonon coupling is found to be relatively strong in Bi_2Te_3 in agreement with theory [169] and ARPES results for Bi_2Se_3 [144]. However, it has been argued that the number of phonon modes contributing to the scattering process is limited by the diameter of the surface Brillouin zone in agreement with results for the Dirac fermions in graphene [170]. We find that the effect of surface impurities on the scattering rates differs between magnetic and non-magnetic impurities thus contrasting the results of Ref. [113] where an increase of warping was given as the main reason for increased scattering rates and no difference was found between magnets and non-magnets. Our results suggest that new scattering mechanisms get introduced with magnetic impurities in agreement with theoretical considerations[83] as well as STM results [158, 176].

Chapter 7

Circular Dichroism in the Angle Distribution: A New Spin Sensitive Method?

From the discussion in the previous chapters, especially regarding the spin-resolved results given in Chapter 4.2, two important aspects should have become evident. First, there is great interest in the detailed *spin texture* of the topological surface states in Bi_2X_3. For example the question, if the hexagonal warping is lifting the in-plane locking of the spin and tilts it out-of-plane [19], or if the spin is then still locked perpendicular to the momentum [20], how the spin behaves in the subsurface region [177] or during hybridization with bulk states[101]. Some of these questions are of course not limited to the topological surface states but extend to *trivial* systems, like for example the Au induced $(\sqrt{3} \times \sqrt{3})$-reconstruction of Ge(111) where a complex spin texture has been observed recently [178], in surface alloys of Bi or Pb on Ag(111) [179], or in Tl/Si(111)-(1×1) [180]. Even such basic questions like how high the absolute value of the spin polarization in Bi_2X_3 is are still under heavy debate [81, 80, 103, 99] as discussed in detail in Chapter 4.2.

The second aspect that should have become clear is the difficulties that arise due to the rather demanding experimental technique of spin-resolved photoemission. The figure of merit for state of the art Mott type spin detectors is typically in the range of 10^{-4}, making it thus several orders of magnitude less efficient than spin-integrated photoemission. While in some cases it is possible to overcome the low efficiency by just measuring for a longer time, this approach is not feasible if the surface or the states under investigation are sensitive and exhibit modifications over time like it has been observed for Bi_2Se_3 (see for example Chapter 4.2.2 and Ref. [109]).

A second approach to overcome the low efficiency is to increase the intensity of the signal. This can be done by either increasing the intensity of the light source or by increasing the number of electrons that enter the detector. At a synchrotron, the former can be easily achieved by increasing the width of the beamline exit slit. This, however, is attended by a loss of energy resolution of the incoming photons and as a consequence of the excited electrons. If for example the spin texture of a system is expected to vary strongly as a function of binding energy the loss of energy resolution translates to the spin polarization: an admixture of differently oriented spins reduces the measured spin polarization. The same holds if one tries to increase the number of electrons entering the detector. Increasing the analyzer pass energy increases the number of electrons but decreases the energy

resolution. Increasing the entrance slit also increases the intensity, but decreases the angle, i.e., momentum resolution with similar consequences.

The importance of new techniques to gain the desired informations is thus evident. The development of new *spin sensitive* detectors has made great progress in recent years. For example, by reflecting the photoelectrons at a W(100) *spinfilter crystal* and detecting the (0,0) reflex with a state of the art two dimensional electron detector it is possible to increase the figure of merit by orders of magnitude since it is possible to measure a wide angle range simultaneously, just like in spin integrated photoemission [181].

7.1 Circular Dichroism in Photoemission

As pointed out above, there is great demand for new spin sensitive techniques which allow for a more efficient detection with higher resolution. In photoemission of core-levels, the spin resolution is largely complementary to circular dichroism. The so called X-ray magnetic circular dichroism (XMCD) is able to detect a splitting of core levels caused by a magnetization of the sample and has first been observed for the Fe2p states [182]. In a paramagnetic sample the excitation of core electrons with circularly polarized light leads to photocurrents which are highly spin polarized. Electrons which stem from, e.g., a $2p_{1/2}$ state have +100% polarization if excited with photons of positive helicity while electrons occupying the $2p_{3/2}$ have -50% polarization [182]. If the light helicity is reversed, the sign of the polarization is reversed as well, but the intensities are the same and the asymmetry as a function of binding energy, defined as

$$A(E) = \frac{I^+(E) - I^-(E)}{I^+(E) + I^-(E)} \tag{7.1}$$

equals zero for all energies E. Here I^+ and I^- are the photoemission intensities with positive and negative light helicity, respectively. If the sample is a ferromagnet with a defined magnetization then the core level multiplets exhibit an additional splitting into majority and minority electrons. If the same experiment is repeated then the asymmetry $A(E)$ will be nonzero as the photons select preferably minority or majority electrons depending on the sign of their helicity, the magnetization direction and the multiplet from which the electrons originate. Thus, photoemission from core levels is sensitive to the sample magnetization if one makes use of circularly polarized light. Two things should, however, be noted: First, the experimental geometry has to be such that the helicity of the incoming light is oriented along the magnetization direction. And second, the photon energy has to be much higher than the binding energy of the electrons to ensure the excitation into a free electron like final state [182]. In this case the atomic model is a very good approximation and subsequently the results have been explained theoretically within the framework of local-spin-density-functional theory as an initial state effect [183] simply by analyzing the polarization dependence of x-ray *absorption* based on a formalism developed by Ebert *et al.* [184]. Consequently, the method has been used to investigate for example the magnetic properties of rare-earth elements [185] and the results have been confirmed by Mott-polarimetry as well [186].

It is not straightforward to apply the described method to band electrons. The obvious reason is that the atomic model is not a good approximation since the electron orbitals are not unperturbed, like it is the case for core levels. Another aspect is the fact that in valence band photoemission, especially with angle resolution, typically much lower photon

energies in the uv-regime are used and a free-electron-like final state is not guaranteed *ad hoc*. However, it is the final state that may be viewed as an *intrinsic spin detector* in terms of spin dependent matrix elements. In general, the electric field of the dipole operator that excites the electron from its initial into a final state does not couple to the spin but only to the spatial part of the electron wavefunction. This is still true for the case of spin-orbit coupling, but the two distinct spin settings $|\uparrow\rangle$ and $|\downarrow\rangle$ couple to wavefunctions of different spatial symmetry, $|\phi_a\rangle$ and $|\phi_b\rangle$, respectively [12]. This leads to the so called *relativistic* selection rules which allow the excitation of electrons that are spin polarized in their *final* state [187] by making use of circularly polarized light[1] in a suitable experimental geometry as will be described below. This implies also a dependence on the excitation energy, since it determines the final state into which electrons get excited. It is important to realize, that a different spatial symmetry of the wavefunctions does in general not lead to a lifting of the degeneracy of states with opposite spin. Thus, if one conducts a photoemission experiment with opposite photon helicity (also: *photon spin*) with the intensity of the incoming beam kept constant then the energy distribution curves will be the same for both photon spins. But, if in addition the spin polarization is determined the state can appear polarized but with opposite polarization for the two helicities.

Before effects of the initial state come into play, it should be mentioned, that also the third step in the three-step model of photoemission, the transmission through the surface, may cause a circular dichroism in the angle distribution (CDAD) of the photoelectrons. If the crystal is terminated by elements of a high atomic number Z, which is tantamount to a strong spin-orbit coupling, then the transmission through the surface might be spin dependent in terms of Mott scattering. Electrons with a specific spin are more likely to be scattered in one direction while electrons with opposite spins get scattered into the opposite direction. Thus, it is the same principle that works in a Mott detector in spin resolved photoemission where in fact heavy elements (e.g. Au (Z=79), W (Z=74), Th (Z=90)) are used as scattering targets. This effect has first been observed and explained in photoemission from Pt(111) [189, 190, 191] (Z=78) and was given as a possible explanation for a strong dichroic effect in the high-T_c superconductor Bi2212, a layered compound terminated by Bi-O layers (Bi Z=83) after cleavage [192].

Another effect worth mentioning, which is based on the broken inversion symmetry at a crystal surface was reported by Zabolotnyy *et al.* [193]. In the theoretical description of photoemission in Chapter 2 it has been argued that the vector potential $\mathbf{A}$ of the photon field is assumed to be constant inside the crystal because of the translational symmetry of the solid [9]. However, at the surface $\mathbf{A}$ has to smoothly evolve between its crystal and vacuum value. Thus, $\nabla\mathbf{A}$ is nonzero in the component perpendicular to the surface and enters the matrix elements. It follows that surface localized states show a strong dichroic effect when excited with circularly polarized light, while bulk states do not and it is therefore possible to distinguish the contributions [193].

The up to date most prominent and applicable effect of circular dichroism of valence and conduction band states is, however, observed in ferromagnetic systems. In addition to the spin-orbit coupling which – once again – is essential for any spin dependent dichroism, the states get split by the exchange coupling into majority $|\uparrow\rangle$ and minority $|\downarrow\rangle$ spin states, where the former gain binding energy and the latter loose binding energy as compared to the unsplit states. This in turn leads to the eponymous imbalance of $|\uparrow\rangle$ and $|\downarrow\rangle$ states

[1] Please note that also linearly polarized light may, in principle, cause a spin polarization in the final state. See for example Ref. [188].

since the latter get (for itinerant ferromagnets partially) lifted above the Fermi level, i.e., depopulated, while the former are shifted (partially) below the Fermi level and previously unoccupied states become populated. The lifting of the degeneracy provides ground states that are spin polarized and since the spin is conserved in the optical excitation process the dichroic signal generated by the photoelectrons can be traced back to the polarization of the initial states. This effect was first observed in the 3d states of ferromagnetic fcc Co thin films on Cu(001) [194] and independently in the 3d states of Fe(100) [195]. For a more detailed introduction the reader is referred to the review article by Kuch and Schneider [12].

But this method entails a significant drawback. As mentioned above, the final states cannot assumed to be free electron like. While the selection rules between initial and final states are essential for the *observation* of the effect, a detailed knowledge of the initial and final states is essential for the *interpretation* of the effect. For a definite answer, only a comparison to fully relativistic band structure calculations and or fully relativistic one-step photoemission calculations is necessary, which will in general not be available. The variety of effects that may cause a circular dichroism as described above, may superimpose each other and further complicate the interpretation of the obtained data.

Nevertheless, the obvious advantage, namely the high efficiency and resolving power of conventional (spin-integrated) electron analyzers over the Mott detection, has and will overcome these disadvantages in specific cases, especially when a detailed knowledge of the spin-dependence of a band structure is needed and thus the effort of fully relativistic band structure calculations seems worthwhile.

To summarize, with the combination of spin-orbit coupling and *initial* state spin polarization it is possible to conduct spin-resolved measurements without explicit spin detection. For topological insulators, spin-orbit coupling is essential and the surface states are spin polarized and naturally the question arises whether or not one can make use of circular dichroism to determine the spin texture of the surface states.

7.2 Circular Dichroism in Bi_2Te_3

As has been discussed in detail in Ref. [12] the experimental geometry is crucial for the observation of a dichroic effect. The examples given there cover the reversal of the sample magnetization, light polarization (linear and circular) and light incidence angle. In our case only the reversal of the circular light polarization is of importance, since the samples are nonmagnetic and the light incidence is not variable.

When can we expect a dichroism to occur in a specific sample? Let us assume that a spectrum is measured with right circularly polarized light in a setup as sketched in Fig. 7.1 a). The incoming light hits the sample under an angle $\phi = 45°$ with respect to the surface normal[2] n which is along the z-axis. Electrons with wave vector $\mathbf{k} = (k_x, k_y, k_z)$ are emitted under angles θ and η according to the rules of in-plane momentum conservation described in Chapter 2. Let us further assume that the crystal is oriented such, that the $x - z$ plane, rimmed with a green line, is a mirror plane of the crystal. Now we change to left circularly polarized light. Since the polarization vector for circularly polarized light is *axial*, we can reverse the polarization by reflection at the $x - z$ plane. A dichroism may now occur, if and only if, the experimental geometry is non-equivalent to the one before the reflection. For example, an electron with momentum inside the mirror plane, i.e., $k_y = 0$,

[2]Please note that the light incidence in our setup is additionally tilted above the $x - z$ plane by 6°.

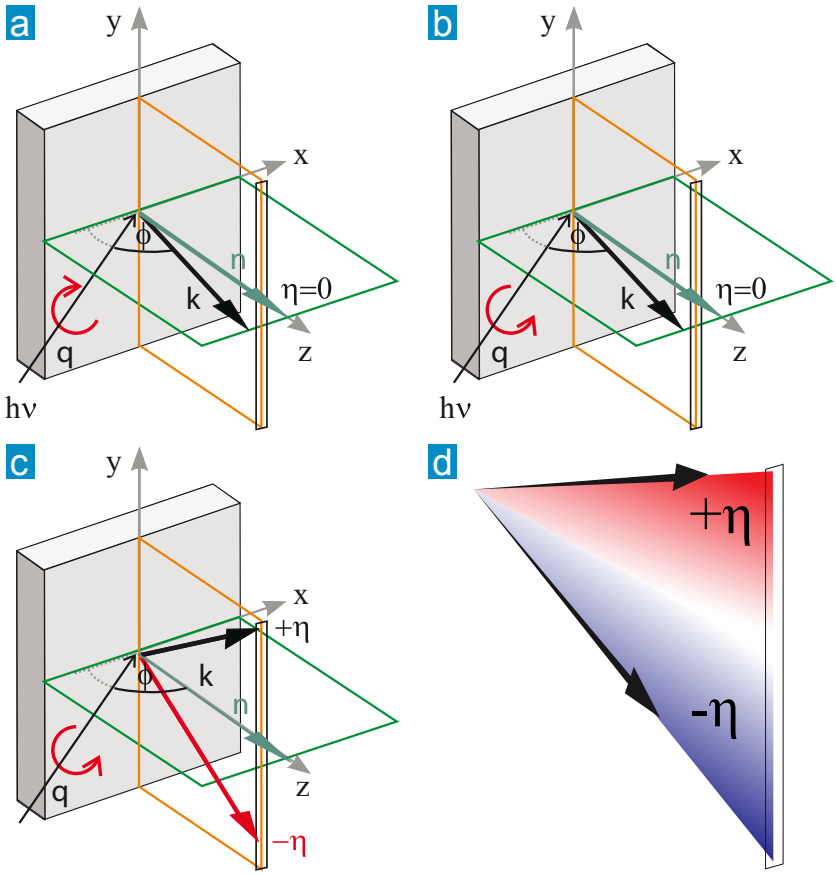

Figure 7.1: Geometric origin for the observation of circular dichroism in the angle distribution. The green plane is the mirror plane which transforms the incoming light from right circular (a) into left circular (b) polarization. The k-vector of the photoelectron lies within the mirror plane, stays unaffected by the mirror operation and no dichroism can occur. In contrast, the k-vector in (c) has a finite component pointing out of the mirror plane which gets reversed by the mirror operation. Dichroism is expected for electrons inside the red plane which is the detection plane of our analyzer as indicated in (d).

$\eta = 0$ is unaffected by the mirror operation as shown in panel b) and thus the geometry is equivalent to the one before the reflection. No dichroism occurs, and the plane is a nodal plane [196]. In contrast, an electron with $k_y \neq 0$ emitted under an angle $\eta \neq 0$ is mirrored at the plane ($k_y \rightarrow -k_y$, $\eta \rightarrow -\eta$) and thus a dichroism may occur. This kind of dichroism has a purely geometrical origin and may thus be viewed as trivial. As indicated by the narrow rectangle in Fig.7.1, which represents the entrance slit of the analyzer, this is the geometry used in our experiment, and thus the occurrence of a trivial dichroism is expected, whereas the sign of the dichroism should be opposite for positive and negative emission angles η as shown in panel d).

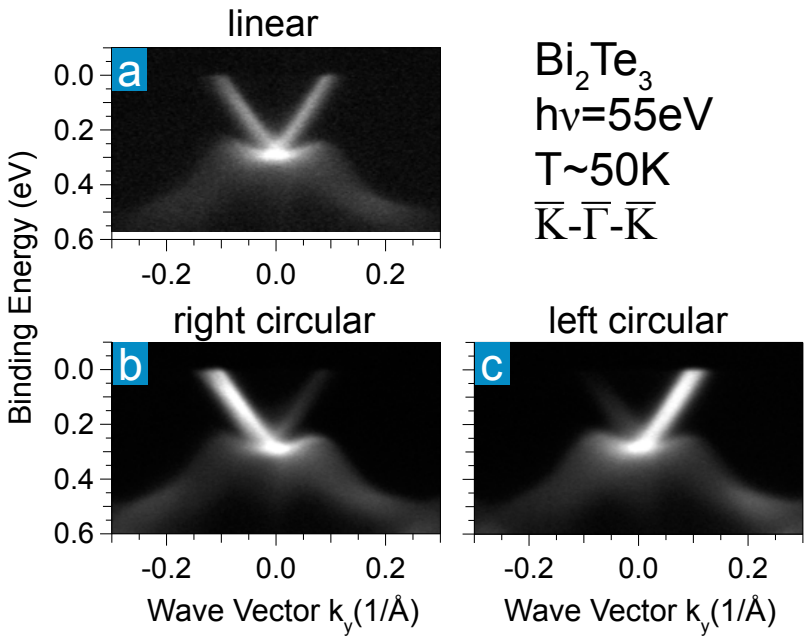

Figure 7.2: Bi_2Te_3 raw data along the $\overline{\Gamma K}$ direction excited by a) linearly and b) right and c) left circularly polarized light of $h\nu = 55\,\text{eV}$ and at $T \sim 50\,\text{K}$. The effect of the light polarization is visible without need for difference spectra and is strongest for the topological surface state within the bulk band gap (see Chapter 4.1.2 for details on the electronic structure).

In Fig. 7.2 we show data obtained for the topological surface state of Bi_2Te_3 obtained with linearly (a), right circularly (b), and left circularly (c) polarized light. While the intensity is highly symmetric for linearly (p or, in the present case, horizontally) polarized light with respect to k_y=0, in the case of right circularly polarized light the intensity distribution is strongly asymmetric. Below[3] the Dirac point energy (E_D), i.e., at binding energies smaller than E_D, the branch at negative k_y shows a much higher intensity than the branch at opposite k_y. Moreover, this branch has relatively gained intensity as compared to linear polarization. For the latter the intensity is highest at E_D just as if the intensities of the two branches add up[4]. In contrast, in panel b) the negative branch has a similar

[3]Please note that *below* and *above* are referred to the binding energy scale and thus *below* is closer to the upper edge of the figure as compared to E_D and *vice versa*.

[4]In fact, the high intensity at E_D is quite anomalous. Similar effects have been observed in Bi_2Se_3 and

intensity as the Dirac point. In panel c) the same picture is obtained but mirrored with respect to k_y=0, thus the positive branch is a lot more intense than the negative one. Up to this point, our observation fits well with a trivial effect based on the experimental geometry.

Above the Dirac point energy the situation is more complicated. Despite the intermixture of surface and bulk states the effect is less well visible in the raw data. Differences in the intensity distribution are hard to recognize even more so, as another small asymmetry constitutes as well. That one is already visible with linearly polarized light and can definitely be ascribed to the not highly symmetric experimental setup[5] and is thus observed also with circularly polarized light.

A better understanding can be gained if the normalized difference spectrum between right and left circularly polarized light is produced, according to Eq. 7.1. This is shown in panel c) of Fig. 7.3. As expected, the dichroism is very strong for the topological surface state below the Dirac point reaching asymmetry values of more than 80% and changes sign when going from positive to negative emission angles. At the Dirac point we find zero dichroism, in agreement with our geometrical consideration from above, since electrons with zero momentum lie inside the mirror plane and stay unaffected by the mirror operation. At higher binding energies and away from normal emission the difference plot shows again dichroism which is still very pronounced even though much weaker than within the bulk energy gap. The most important observation is, however, that the sign is reversed for positive and negative emission but opposite as compared to the situation before the crossing at E_D. Please note, that *before* and *after* the crossing of the states at E_D is referred to the case that one follows the dispersion from the Fermi level to higher binding energies. *After* the crossing at E_D the topological surface state disperses first back to *lower* binding energy and, hence, takes on binding energy values smaller than E_D. The colors encoding the sign of the dichroism are consistent with this peculiarity of the dispersion, i.e., red-blue before the crossing and blue-red after the crossing of the topological surface state. These observations already disqualify two possible explanations of the observed dichroism: First, a dichroism which is caused by geometrical reasons only, would have the same sign independently of the electrons binding energy as indicated in Fig. 7.1 d). In principal, a final state effect could reverse the sign of the dichroism even in such a trivial geometric case. But that the reversal of the sign even holds at binding energies below E_D after the crossing rules out a final state effect in this case.

Recently, Ishida *et al.* have reported a circular dichroism for Bi_2Se_3 in a similar geometry as ours [198]. Their analysis is focussed on the nodal planes, i.e. planes of zero dichroism, that show up in their results for the $x-z$ plane in Fig. 7.1 a)-c) and additionally for the $y-z$ plane where we observe the strong dichroism. The Bi_2Se_3 sample in their case was aligned with the mirror plane of the crystal, i.e., the $\overline{\Gamma M}$-z plane perpendicular to the light incidence, in contrast to our setup where the mirror plane is perpendicular to the detection plane. Ishida *et al.* argued that the additional nodal plane, which they observe only for the surface state at binding energies close to E_D occurs due to the two dimensional confinement of the surface state. At binding energies close to E_F dichroism was observed, and has been explained as a geometrical effect which does not vanish due to

were discussed as a final state interference effect [197].

[5] A highly symmetric setup, for which such effects are not expected is for example given when the light incidence is normal to the crystal surface as well as the analyzer axis. In our case, the light enters under 45° with respect to the surface normal in the $x-z$ plane of Fig. 7.1 a)-c) and is tilted by 6° above the $x-z$ plane.

a surface-state-surface-resonance transition at higher k-values which is accomplished by a higher penetration depth of the electron wave function into the bulk, so that the surface state loses its surface confinement [198, 199, 79]. It should be stressed that the disappearance of the dichroism in Bi_2Se_3 is not compellingly in contradiction to our findings of strong circular dichroism in Bi_2Te_3 since two preconditions given by Ishida and co workers for the observation of the null effect do not exactly match with our setup. First, the mirror plane should be perpendicular to the light incidence. In our case, the light incidence is approximately within the mirror plane. The second precondition is that the de Broglie wavelength λ_{dB} of the electron in the *final* state has to be larger than the width of the confinement layer [198]. Theoretically, for the case of Bi_2Se_3 it has been shown that the surface state penetrates up to 2 quintuple layers deep into the bulk where it is isolated from bulk states [79]. Assuming that a similar penetration can be expected for Bi_2Te_3, it is straightforward to show, that the de Broglie wavelength for the final state energy of photoelectrons in our case ($\sim$1 to 3 Å) is smaller than the penetration depth of the surface state. Interestingly, Zabolotnyy *et al.* report a circular dichroism in $YBa_2Cu_3O_{7-\delta}$ *due* to the two dimensional confinement of electronic states and the non-vanishing term $\nabla\mathbf{A}$ in the matrix element for the same geometry as we use and at $h\nu$=55 eV [193]. But the pattern of the sign change at the Dirac point observed for Bi_2Te_3 is again not consistent with the explanation given in Ref. [193] and it is thus the second explanation that can be ruled out for our system.

In Chapter 4.2 it has been shown in terms of spin and angle resolved photoemission that the topological surface state of Bi_2Te_3 is highly spin polarized and that it shows the reversal of the spin polarization in an energy distribution curve cutting through the state before and after the crossing. Furthermore, in Ref. [81] it has been shown, that the sign of the polarization gets reversed for a momentum distribution curve close to E_F when going from positive to negative emission angles. Together, while neglecting the warping effects to the spin orientation [19, 20] for a moment as well as possible finite polarization effects [80], we can conclude that the surface state shows exactly the polarization pattern expected for a topological surface state and that the pattern observed in the circular dichroism resembles the polarization pattern as well. In addition, Bi_2Te_3 entails similar preconditions as in the case of ferromagnets, namely spin-orbit coupling, which is rather strong as compared to the 3d-transition metals, and spin polarization. The latter is, however, quite different as it exists only in k-space, while the spin polarization in ferromagnets leads to the observation of magnetism in real space. As a consequence, the symmetry properties of the system get reduced which in some sense simplifies the interpretation of dichroism [12]. Hence, the comparison of dichroic behavior with spin resolved photoemission lets the conclusion that it is due to the spin polarization appear reasonable. However, it should be stressed again that the dipole operator couples to the spatial part of the electron wavefunction only and that therefore the interpretation of the results is not straightforward. In an ideal Dirac cone, where the spin is locked perpendicularly to the momentum the interpretation might be straightforward. But as soon as the influences of spin-orbit coupling [80] and warping [19, 20], which we neglected above come into play, which by the way were named as a motivation for the development of new, highly efficient spin sensitive techniques, an interpretation might get complicated; even more so when final state effects become important an aspect which will be discussed in the following section.

7.3 Photon Energy Dependence of the Circular Dichroism

Recently, Wang *et al.* conducted circular dichroism measurements at a photon energy of $h\nu = 6$ eV using a pulsed laser source and a time-of-flight detector [155]. The dichroism effect is interpreted tacitly assuming transitions into a spin-degenerate continuum of final states and, therefore, is sensitive only to the spin in the initial state of the photoemission process. By measuring one spin component in the surface plane before and after rotating the sample by 60° and applying symmetry arguments, the two in-plane spin components $\langle S_x \rangle$, $\langle S_y \rangle$ and the perpendicular component $\langle S_z \rangle$ are determined [155]. Another measurement on Bi_2Se_3 at photon energies of 10 and 13 eV, using a conventional hemispherical electron analyzer, led to similar results and a circular dichroism effect of 30% [200]. Park *et al.* concluded that for these photon energies a free-electron final state can be assumed and for left- and right-circularly polarized light final states of different orbital angular momentum character are reached. The orbital angular momentum was found to be locked to the momentum in a similar way as the spin, and the orbital and spin angular momenta were determined to be antiparallel to each other [200]. Jung *et al.* reached a similar conclusion for Bi_2Te_3 [156] with an excitation anergy of 8 eV. But in addition they found a strong binding energy modulation of the dichroism with a reversal of its sign for the surface state within the bulk energy gap and *before* the crossing at E_D which they assigned to a modulation of the orbital angular momentum due to the strong warping in Bi_2Te_3.

All of these studies (Refs. [155, 200, 156] aim at a determination of the spin texture of the topological surface state to a greater or lesser indirect degree[6]. It should be noted, that the two interpretations are not in contradiction to each other if the spin and orbital momentum are locked perpendicular to each other.

In Fig. 7.3 we show selected difference spectra of the dispersion of the topological surface state of Bi_2Te_3 obtained with right and left circularly polarized light at photon energies of $h\nu$=21 eV (a), 25 eV (b), 55 eV (c) and 100 eV (d). All data have been obtained from the same crystal and cleavage and it has been oriented with the $\overline{\Gamma K}$ direction along the analyzer entrance slit thus the crystal's mirror axis is perpendicular to the detection plane, as described above. The temperature is set to $\sim$ 40 K. Small deviations in the binding energy of the Dirac point are likely due to a small surface doping by residual gases in the vacuum system and not due to a photon energy induced gating as observed for Cu intercalated Bi_2Se_3 which would have opposite sign [136].

At every photon energy a strong dichroism is observed for the topological surface state within the bulk gap, whereas modulations are restricted to the strength, i.e., no sign reversal is observed at energies below the Dirac point E_D along each branch, in contrast to the observations made in Ref. [156]. Except for 21 eV, the sign of the dichroism *is* reversed after the crossing of the two branches at E_D, i.e., k_y=0 Å^{-1}, and in all cases the sign reverses when going from k_y to $-k_y$. Generally, the strength of the effect is stronger at low binding energies, where the surface state is isolated from bulk contributions. The higher binding energy range has to some extent bulk-like contributions as well, which however seem to show a similar dichroism. The deviations observed in panel a), i.e., the lack of a clear sign reversal between positive and negative emission after the Dirac point crossings are likely due to reduced data quality as the light spot might have entered a sample region where differently oriented facets are present resulting in a distortion of the obtained pattern.

[6] Since the dipole operator that provides the optical excitation does not couple to the electron spin itself, a direct probe by circular dichroism is *a priori* excluded.

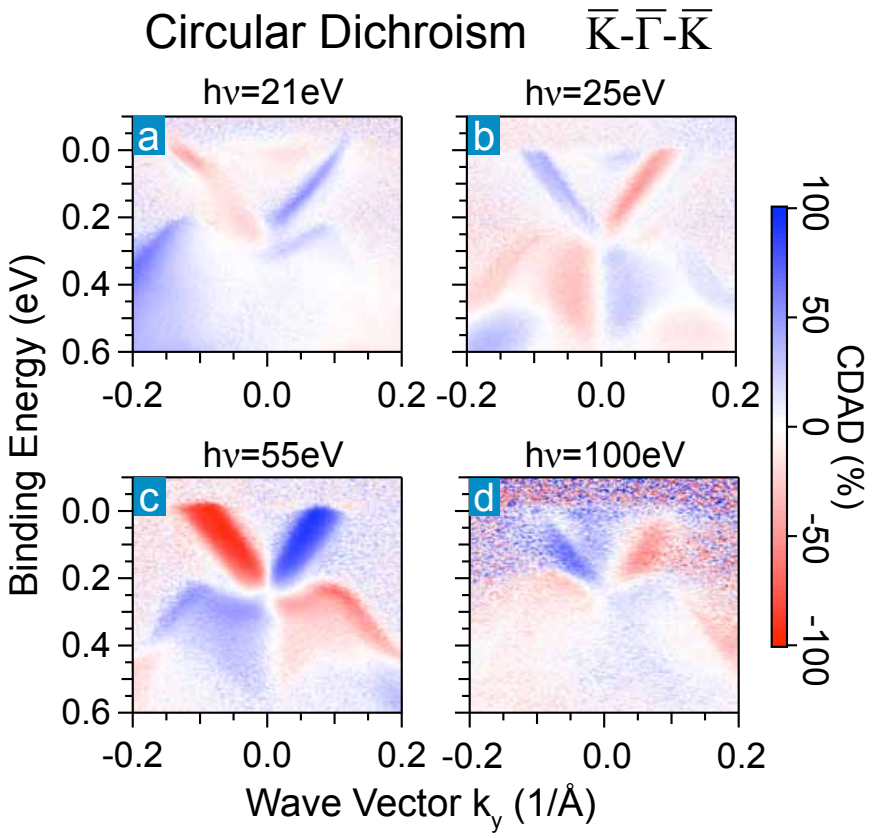

Figure 7.3: Difference spectra for excitation energies of $h\nu$ =21 eV (a), 25 eV (b), 55 eV (c) and 100 eV (d) along the $\overline{\Gamma K}$ direction. Obviously, sign and strength of the effect are functions of the excitation energy.

Yet, the whole color pattern gets inverted at 25 eV and 100 eV as compared to 55 eV and for 21 eV at least for the in-gap region. Fig. 7.4 shows for $h\nu$ <70 meV the detailed behavior of the dichroism strength for the positive (blue line and symbols) and the negative (red line and symbols) branch with smaller photon energy steps extracted at three different binding energies inside the bulk band gap, i.e., 70 meV in a), 120 meV in b) and 170 meV in c). The values have been averaged over the full width at half maximum of the respective momentum distribution curves. Obviously, the strength of the effect is strongly varying with the excitation energy while the binding energy dependence is less pronounced. The strongest effect is observed at 55 eV where the dichroism amounts to ∼80% which is more than an order of magnitude higher than the effects reported for ferromagnets (typically 3-5% [195, 194, 12]). A similarly strong effect is observed at 27 and 30 eV, hence close to the sign reversal at 25 eV and we can conclude that the sign change appears rather abrupt. However, at 26 eV the overall dichroism strength is comparably small with values of less than 20%. At 70 meV binding energy, shown in panel a), it is even close to zero and both branches appear to have the same sign. Thus the sign reversal takes place in a relatively small energy window and appears as a smooth rather than a discontinuous transition. At 45 eV we again observe a change in the sign along the branches indicating that even more

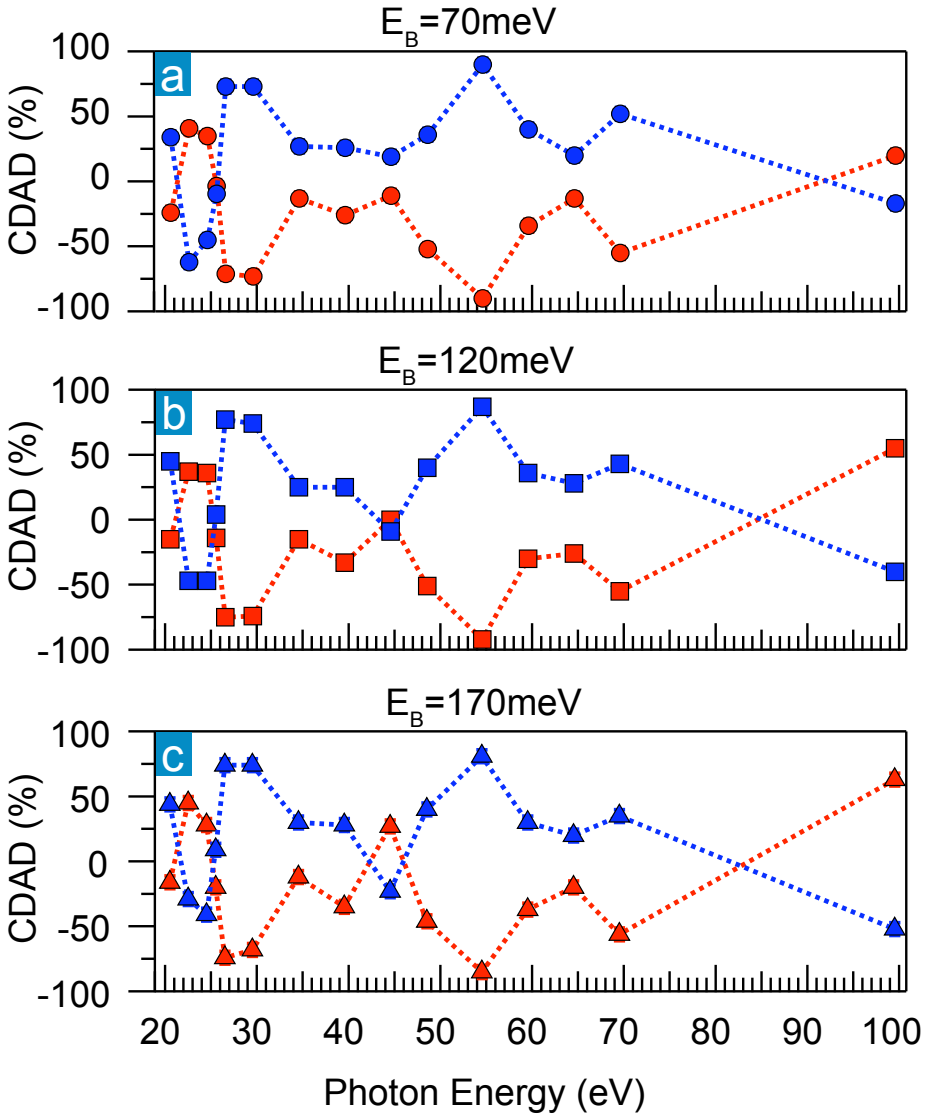

Figure 7.4: Strength of the dichroism of the topological surface state extracted at binding energies of 70 meV (a), 120 meV (b), and 170 meV (c) for excitation energies between $h\nu$=21 eV and 100 eV. The effect is strongest at $h\nu$ =55 eV. At 45 eV the effect is rather weak at 120 meV but the sign changes between 70 meV and 170 meV. A similar but less pronounced behavior is observed at 26 eV.

sign changes could be present that have not been recognized during the measurements. From the described observations three statements are already obvious:

First, the conclusion by Jung *et al.* that the warping influences the orbital angular momentum from the reversal of the dichroism sign along one branch [156] is highly misleading as this sign change vanishes as a function of excitation energy. Even though they have measured at a photon energy of 8 eV, hence below our minimum of 21 eV, our data strongly suggests that by chance they were measuring close to a full sign reversal. It should however be noted that effects of the orbital angular momentum are not excluded by our results, only the derivation from a sign change in dichroism is wrong.

Second, the inversion of the color pattern is in clear contradiction to the initial-state model for the spin given in Ref. [155] because it would be tantamount to a reversal of the initial spin during the photon energy scan. This is not possible, not even under the assumption of a layered spin texture, which has been predicted to reverse in the first atomic layers [177], because the photocurrent from the topmost atomic layer dominates in the photoemission signal from the topological surface state. Thus it may cause a variation of the strength, as the attenuation length varies with the excitation energy, but a complete sign reversal is out of question.

And third, a similar problem arises with the initial-state orbital angular momentum model given by Park *et al.*. Again, it is unclear how the probed initial state can depend on the photon energy of the probing radiation.

7.4 Comparison to One-Step Photoemission Calculations

In order to further underpin these statements, we compare our experimental results with fully relativistic one-step photoemission calculations coupled to *ab initio* theory which have been carried out by our collaborators J. Braun, J. Minár and H. Ebert from the *Ludwig-Maximilians-Universität München*.

The bulk electronic structure of Bi_2Te_3 has been obtained by performing first-principles calculations within the framework of the density functional theory using the generalized gradient approximation to model exchange-correlation effects. The spin-orbit coupling is included in the self-consistent cycles of the electronic structure calculations. The results of these calculations serve as a basic input for the one-step photoemission calculations, according to the model described by Hopkinson, Pendry and Titterington [201], from which the angle resolved photoemission intensity is obtained. A fully relativistic formalism, allowing to consider in a natural way effects in the photocurrent calculation induced by spin-orbit coupling has been used because the practical calculation is based on the Dirac formalism [202, 203]. The photoemission calculation itself is based on multiple-scattering theory, using explicitly the low-energy electron diffraction (LEED) method to calculate the initial and final states for a semi-infinite atomic half-space. In this way the final state is calculated by the best available single-particle approach as a so-called time-reversed LEED state [204]. In line with this, the initial state is represented by the retarded one-electron Green function for the same semi-infinite half-space. The photoemission calculations include matrix-element effects, multiple scattering effects in the initial and final states, the effect of the photon momentum vector, and the escape depth of the photoelectrons via an imaginary part in the inner potential. These lifetime effects in the final states have been included in the analysis in a phenomenological way using a parameterized complex inner potential $V_o(E) = V_{or}(E) + iV_f(E)$. Herein, the real part serves as a reference energy

inside the crystal with respect to the vacuum level. To account for impurity scattering, a small constant imaginary value of $V_i = 0.004$ eV was used for the initial state. A realistic description of the surface potential is given through a Rundgren-Malmström barrier [205] which connects the asymptotic regime $z < z_A$ to the bulk muffin-tin zero V_{or} by a third order polynomial in z, spanning the range $z_A < z < z_E$. In other words z_A defines the point where the polynomial region starts whereas z_E defines the point where the surface region ends and the bulk region starts with the first atomic layer. The effective z-dependent surface barrier V is scaled with respect to the vacuum level $E_{vac} = 0.0$ eV utilizing the value of the work function $\phi = 5.0$ eV. The zero of the z scale lies in the uppermost layer of atoms.

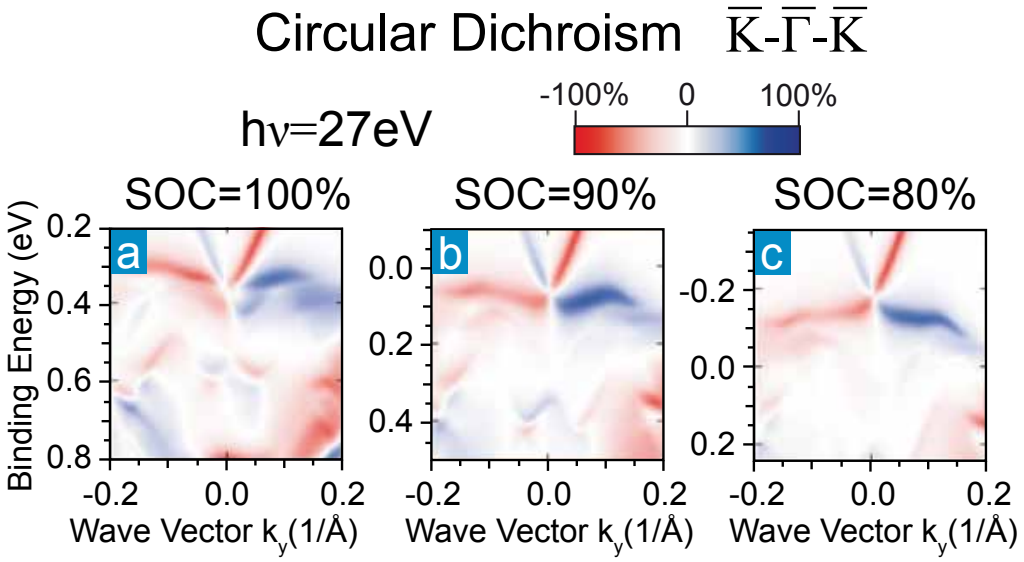

Figure 7.5: Calculations for a reduced spin-orbit interaction for the example of $h\nu = 27$ eV. The spin-orbit coupling (SOC) is reduced from (a) 100% to (b) 90% and (c) 80%. This modifies the inverted bulk band gap and moves the topological surface state in energy. The circular dichroism remains very similar indicating a minor role of the electron spin polarization for the circular dichroism.

The experimental geometry resembles the one from our experimental setup. The resulting dichroism in angle resolved photoemission for $h\nu$=27 eV for the $\overline{\Gamma K}$ direction is depicted in Fig. 7.5 a) using the same representation and, hence, compares very well to the experimental results in Fig. 7.3: angle and binding energy dependences are very similar[7]. We first investigate the influence of the spin-orbit-coupling strength on the resulting dichroism. This can be done in calculations by simply *increasing* the speed of light in the Hamiltonian of the one-step-photoemission calculations, which in turn decouples the spin and orbital momenta of the electrons in their final state. The idea behind this is that the decoupling will reduce the effect that the spin polarization can have on the circular dichroism. To understand this one has to keep in mind that the dipole operator only cou-

[7]Please note that different binding energy ranges are shown in the experimental as compared to the theoretical results.

ples to the spin in an indirect manner through spin-orbit coupling. The results for 90% and 80% of the full spin-orbit coupling that was used in Fig. 7.4 a) are shown in panels b) and c). The first impact that one notes is a change in the binding energy of the Dirac point, and to allow for a better comparison, we have chosen the binding energy range such that E_D is at the same height in all three panels of Fig. 7.4. The shift can be understood simply by the fact that the spin-orbit coupling is the driving force for the band inversion in the bulk electronic structure as has been discussed in detail in Chapter 4. As the band gets narrower, the surface state shifts in energy. It should be stressed at this point that if the spin-orbit coupling would be reduced further the band inversion and with it also the topological surface state would disappear [64]. Interestingly, the strength of the dichroism appears rather unaffected by the reduced spin-orbit coupling as can be seen clearly by comparing panels a)-c) to each other. This gives an additional hint that the contribution of the spin to the circular dichroism is a minor one.

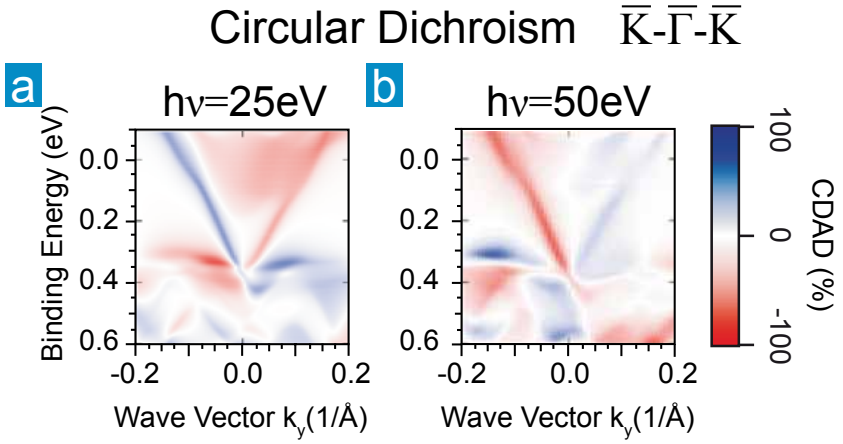

Figure 7.6: Results from the one-step photoemission calculation. The calculated circular dichroism changes sign between photon energies of a) 25 eV and b) 50 eV in qualitative agreement with the experiment.

Next, we focus on the photon energy dependence. For this purpose one-step-photoemission calculations for excitation energies between 21 eV and 50 eV have been carried out. At the photon energies where the experiment shows the reversal of the sign, i.e., between 25 eV and 27 eV the calculations do not reproduce the experimental results as can be seen by comparing Fig. 7.5 a) with Fig. 7.6 a). However, since the photoemission calculations are based on band structure calculations, in general, the final states obtained for higher photon energies often deviate from the experimental situation depending on the excitation energy. In this sense, the results have to be viewed in a qualitative way. And, as depicted in Fig. 7.6, there is a clear sign reversal observed at an excitation energy of 50 eV (b) as compared to 25 eV in panel a). While being qualitative, this is, nevertheless, an important confirmation of the experimental results shown in Fig. 7.3 and allows for the conclusion that the sign change can be ascribed to the final states.

Similar results have been obtained recently for the L-gap surface state of Cu(111) [206]. In that case, the dichroism also depends strongly on the excitation energy. By analyzing the final states a interrelation between strong circular dichroism and *d*-type final states

was found [206]. We can conclude that the same mechanism underlies the results presented here, i.e., a transition from a p-type initial state to d-type final states. However, a detailed analysis of the final states is far more complicated in the case of Bi_2Te_3 as compared to fcc Cu, due to frequent backfolding; a result of the relatively small Brillouin zone along the k_z-direction, i.e., perpendicular to the (111) surface. An analysis of the initial state obtained from the *ab initio* calculations shows that all three p-orbitals, i.e. p_x, p_y, and p_z contribute and this explains the stronger dependence on the final states concerning the sign changes as compared to the p_z-orbital that contributes to the sp-type surface state of Cu(111). It should be noted, that the spin-orbit coupling is much weaker in Cu than in Bi_2Te_3 but nevertheless the observed dichroism is comparably strong [206]. In fact, strong spin-orbit coupling is not in every case a precondition for the observation of a strong circular dichroism in the angle distribution. This has been demonstrated also early on: In graphite, transitions from the π-band into d final states lead to dichroism asymmetries of up to 60%, while the spin-orbit coupling is negligibly weak [207].

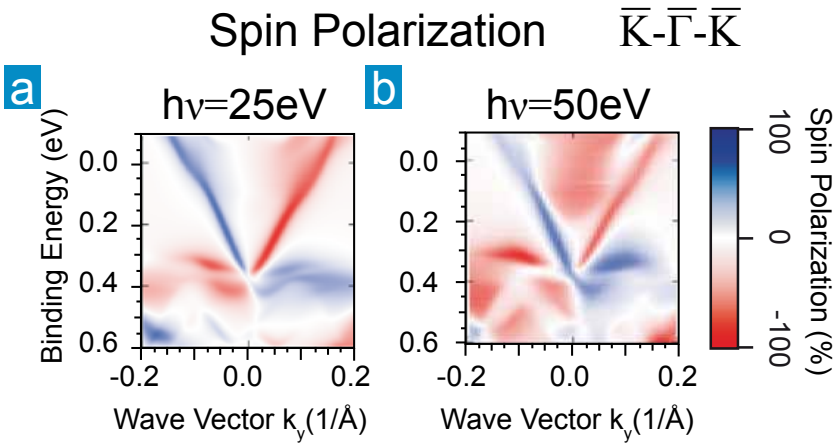

Figure 7.7: The calculated spin polarization P of the photoemission from the topological surface state is unaffected by the photon energy. It reaches $P \sim 80\,\%$ at 25 eV in a) and 75 % at 50 eV in b).

Remembering the results from spin-resolved photoemission of Chapter 4, where it has been shown that the spin polarization appears reduced compared to the theoretical expectation of 100%, the question may arise whether final state effects may also influence the measured spin polarization in Mott polarimetry. This question can be negated by one-step photoemission calculations as well if one plots the spin polarization instead of the circular dichroism as it is shown in Fig. 7.7 for the same photon energies of 25 eV (a) and 50 eV (b). Clearly, the sign of the spin polarization is not reversed and it is overall much less influenced by the photon energy. At a binding energy of 100 meV below the Dirac point the polarization amounts to P=80% at 25 eV and P=75% at 50 eV. Hence, spin-resolved photoemission is much less affected by final-state effects than the circular dichroism, and is, therefore, a much more reliable method to deduce the electron spin in the initial state. Furthermore, this result demonstrates that the experimentally measured spin polarization of $P_{exp.}$ =70% presented in Chapter 4 for Bi_2Te_3 with 50 eV is pretty close to the maximum value expected from photoemission theory.

Summary of Conclusions

In summary, our analysis of the circular dichroism in Bi_2Te_3 shows a strong dependence of the sign and strength of the effect on the excitation energy. In photoemission it is typically assumed that for final state energies larger than ∼10 eV the final states are free electron like, and this assumption has been shown to describe photoemission intensities from metal surfaces like Cu(001) [208] or semiconductors like GaAs(001) [209] reasonably well. However, our analysis shows that effects from non-free electron like final states may arise even for excitation energies that are 10 times higher than those considered to reach free-electron like final states, at least for excitation with circularly polarized light. Further, it has been shown that the various initial-state models favoring the spin [155] or the orbital angular momentum [200, 156] cannot be applied and the same holds for pure geometric effects. The circular dichroism has clearly been identified as a final-state effect experimentally and our observations withstand a comparison to one-step photoemission calculations. While we are not able to rule out the suggestion by Ishida *et al.* [198] that an additional nodal plane in the observed dichroism occurs due to the two dimensionality of the surface state, our results show that this nodal plane does not persist at all photon energies and that, therefore, the nodal plane could be a final state effect as well.

Finally, we can answer the question raised in the title of this chapter: The circular dichroism in the angle distribution of photoemission from topological surface state is not capable of measuring the initial state spin polarization.

Chapter 8

Summary

This thesis is focussed on the electronic properties of the new material class named topological insulators. Spin and angle resolved photoelectron spectroscopy have been applied to reveal several unique properties of the surface state of these materials. The first part of this thesis introduces the methodical background of these quite established experimental techniques.

In the following chapter, the theoretical concept of topological insulators is introduced. Starting from the prominent example of the quantum Hall effect, the application of topological invariants to classify material systems is illuminated. It is explained how, in presence of time reversal symmetry, which is broken in the quantum Hall phase, strong spin orbit coupling can drive a system into a topologically non trivial phase. The prediction of the spin quantum Hall effect in two dimensional insulators an the generalization to the three dimensional case of topological insulators is reviewed together with the first experimental realization of a three dimensional topological insulator in the $Bi_{1-x}Sb_x$ alloys given in the literature.

The experimental part starts with the introduction of the Bi_2X_3 (X=Se, Te) family of materials. Recent theoretical predictions and experimental findings on the bulk and surface electronic structure of these materials are introduced in close discussion to our own experimental results. Furthermore, it is revealed, that the topological surface state of Bi_2Te_3 shares its orbital symmetry with the bulk valence band and the observation of a temperature induced shift of the chemical potential is to a high probability unmasked as a doping effect due to residual gas adsorption.

The surface state of Bi_2Te_3 is found to be highly spin polarized with a polarization value of about 70% in a *macroscopic* area, while in Bi_2Se_3 the polarization appears reduced, not exceeding 50%. We, however, argue that the polarization is most likely only extrinsically limited in terms of the finite angular resolution and the lacking detectability of the out of plane component of the electron spin. A further argument is based on the reduced surface quality of the single crystals after cleavage and, for Bi_2Se_3 a sensitivity of the electronic structure to photon exposure.

We probe the robustness of the topological surface state in Bi_2X_3 against surface impurities in Chapter 5. This robustness is provided through the protection by the time reversal symmetry. Silver, deposited on the (111) surface of Bi_2Se_3 leads to a strong electron doping but the surface state is observed up to a deposited Ag mass equivalent to one atomic monolayer. The opposite sign of doping, i.e., hole-like, is observed by exposing oxygen to Bi_2Te_3. But while the n-type shift of Ag on Bi_2Se_3 appears to be more or less rigid, O_2

is lifting the Dirac point of the topological surface state in Bi_2Te_3 out of the valence band minimum at $\overline{\Gamma}$. After increasing the oxygen dose further, it is possible to shift the Dirac point to the Fermi level, while the valence band stays well beyond. The effect is found reversible, by warming up the samples which is interpreted in terms of physisorption of O_2.

For magnetic impurities, i.e., Fe, we find a similar behavior as for the case of Ag in both Bi_2Se_3 and Bi_2Te_3. However, in that case the robustness is unexpected, since magnetic impurities are capable to break time reversal symmetry which should introduce a gap in the surface state at the Dirac point which in turn removes the protection. We argue, that the fact that the surface state shows no gap must be attributed to a missing magnetization of the Fe overlayer. In Bi_2Te_3 we are able to observe the surface state for deposited iron mass equivalents in the monolayer regime. Furthermore, we gain control over the sign of doping through the sample temperature during deposition.

Chapter 6 is devoted to the lifetime broadening of the photoemission signal from the topological surface states of Bi_2Se_3 and Bi_2Te_3. It is revealed that the hexagonal warping of the surface state in Bi_2Te_3 introduces an anisotropy for electrons traveling along the two distinct high symmetry directions of the surface Brillouin zone, i.e., $\overline{\Gamma K}$ and $\overline{\Gamma M}$. We show that the phonon coupling strength to the surface electrons in Bi_2Te_3 is in nice agreement with the theoretical prediction but, nevertheless, higher than one may expect. We argue that the electron-phonon coupling is one of the main contributions to the decay of photoholes but the relatively small size of the Fermi surface limits the number of phonon modes that may scatter off electrons. This effect is manifested in the energy dependence of the imaginary part of the electron self energy of the surface state which shows a decay to higher binding energies in contrast to the monotonic increase proportional to E^2 in the Fermi liquid theory due to electron-electron interaction.

Furthermore, the effect of the surface impurities of Chapter 5 on the quasiparticle lifetimes is investigated. We find that Fe impurities have a much stronger influence on the lifetimes as compared to Ag. Moreover, we find that the influence is stronger independently of the sign of the doping. We argue that this observation suggests a minor contribution of the warping on increased scattering rates in contrast to current belief. This is additionally confirmed by the observation that the scattering rates increase further with increasing silver amount while the doping stays constant and by the fact that clean Bi_2Se_3 and Bi_2Te_3 show very similar scattering rates regardless of the much stronger warping in Bi_2Te_3.

In the last chapter we report on a strong circular dichroism in the angle distribution of the photoemission signal of the surface state of Bi_2Te_3. We show that the color pattern obtained by calculating the difference between photoemission intensities measured with opposite photon helicity reflects the pattern expected for the spin polarization. However, we find a strong influence on strength and even sign of the effect when varying the photon energy. The sign change is qualitatively confirmed by means of one-step photoemission calculations conducted by our collaborators from the LMU München, while the calculated spin polarization is found to be independent of the excitation energy. Experiment and theory together unambiguously uncover the dichroism in these systems as a final state effect and the question in the title of the chapter has to be negated: Circular dichroism in the angle distribution is *not* a new spin sensitive technique.

Bibliography

[1] D. Hsieh *et al.*, Nature **452**, 970 (2008).

[2] Y. L. Chen *et al.*, Science **325**, 178 (2009).

[3] Y. Xia *et al.*, Nature Physics **5**, 398 (2009).

[4] K. Siegbahn *et al.*, Nova acta Regiae Soc. Sci. Upsaliensis **20** (1967).

[5] H. Hertz, Annalen der Physik **267**, 983 (1887).

[6] A. Einstein, Annalen der Physik **322**, 132 (1905).

[7] A. Einstein, Annalen der Physik **325**, 199 (1906).

[8] A. Einstein, Physikalische Gesellschaft Zürich (1916).

[9] S. Hüfner, *Photoelectron Spectroscopy: Principles and Applications*, Third ed. (Springer Verlag, Berlin, 2003).

[10] P. D. Johnson, Reports on Progress in Physics **60**, 1217 (1997).

[11] T. Feuchtwang, P. Cutler, and J. Schmit, Surf Sci **75**, 490 (1978).

[12] W. Kuch and C. M. Schneider, Reports on Progress in Physics **64**, 147 (2001).

[13] M. P. Seah and W. A. Dench, Surface and Interface Analysis **1**, 2 (1979).

[14] *User Manual for the Hemispherical Energy Analyzer Series PHOIBOS 100/150* (SPECS GmbH, Berlin, 2008).

[15] E. Plummer and R. Gomer, (1975).

[16] A. Damascelli, Z. Hussain, and Z. Shen, Reviews of Modern Physics **75**, 473 (2003).

[17] J. H. Dil, Journal of Physics: Condensed Matter **21**, 3001 (2009).

[18] N. F. Mott, Proceedings of the Royal Society of London. Series A **124**, 425 (1929).

[19] L. Fu, Phys. Rev. Lett. **103**, 266801 (2009).

[20] S. Basak *et al.*, Physical Review B **84**, 121401 (2011).

[21] http://www.helmholtz-berlin.de, 2012.

[22] J. Sánchez-Barriga, Dissertation, Universität Potsdam (2010).

[23] G. C. Burnett, T. J. Monroe, and F. B. Dunning, Review of Scientific Instruments **65**, 1893 (1994).

[24] M. Z. Hasan and C. L. Kane, Reviews of Modern Physics **82**, 3045 (2010).

[25] M. Z. Hasan and J. E. Moore, Annual Review of Condensed Matter Physics **2**, 55 (2011).

[26] X.-L. Qi and S.-C. Zhang, Physics Today **63**, 33 (2010).

[27] K. von Klitzing, G. Dorda, and M. Pepper, Physical Review Letters **45**, 494 (1980).

[28] C. Kittel, *Introduction to Solid State Physics*, Seventh ed. (John Wiley & Sons. Inc, New York, 1996).

[29] R. Laughlin, Physical Review B **23**, 5632 (1981).

[30] J. E. Avron, D. Osadchy, and R. Seiler, Physics Today **56**, 38 (2003).

[31] D. J. Thouless, World Scientific Singapore , 426 (1998).

[32] Y. Aharonov and D. Bohm, Physical Review **115**, 485 (1959).

[33] B. I. Halperin, Physical Review B **25**, 2185 (1982).

[34] D. J. Thouless, M. Kohmoto, M. P. Nightingale, and M. den Nijs, Physical Review Letters **49**, 405 (1982).

[35] R. Kubo, Reports on Progress in Physics **29**, 255 (1966).

[36] J. E. Avron, R. Seiler, and B. Simon, Physical Review Letters **51**, 51 (1983).

[37] M. V. Berry, Proceedings of the Royal Society of London. Series A **392**, 45 (1984).

[38] M. Chang, Spintronics- From GMR to Quantum Information, Lecture Notes of the 40th IFF Springschool 2009 **10**, A7.1 (2009).

[39] C. L. Kane, Nature Physics **4**, 348 (2008).

[40] Y. Hatsugai, Physical Review Letters **71**, 3697 (1993).

[41] Y. Hatsugai, Physical Review B **48**, 71761 (1993).

[42] C. L. Kane and E. Mele, Physical Review Letters **95**, 146802 (2005).

[43] C. L. Kane and E. J. Mele, Physical Review Letters **95**, 226801 (2005).

[44] B. A. Bernevig, T. L. Hughes, and S.-C. Zhang, Science **314**, 1757 (2006).

[45] J. E. Moore and L. Balents, Physical Review B **75**, 121306 (2007).

[46] L. Fu, C. L. Kane, and E. J. Mele, Physical Review Letters **98**, 106803 (2007).

[47] R. Roy, Physical Review B **79**, 195322 (2009).

[48] M. Koenig *et al.*, Science **318**, 766 (2007).

[49] A. H. C. Neto, F. Guinea, N. M. R. Peres, K. S. Novoselov, and A. K. Geim, Reviews of Modern Physics **81**, 109 (2009).

[50] R. Roy, Physical Review B **79**, 195321 (2009).

[51] L. Fu and C. L. Kane, Physical Review B **74**, 195312 (2006).

[52] L. Fu and C. L. Kane, Physical Review B **76**, 45302 (2007).

[53] X.-L. Qi, T. L. Hughes, and S.-C. Zhang, Physical Review B **78**, 195424 (2008).

[54] J. C. Y. Teo, L. Fu, and C. L. Kane, Physical Review B **78**, 45426 (2008).

[55] D. Hsieh *et al.*, Science **323**, 919 (2009).

[56] Y. Liu and R. E. Allen, Physical Review B **52**, 1566 (1995).

[57] B. Lenoir, M. Cassart, J. Michenaud, H. Scherrer, and S.Scherrer, J Phys Chem Solids **57**, 89 (1996).

[58] S. Murakami, New Journal of Physics **9**, 356 (2007).

[59] E. I. Rashba, Sov. Phys. Solid State **2**, 1109 (1960).

[60] S. Lashell, B. A. McDougall, and E. Jensen, Physical Review Letters **77**, 3419 (1996).

[61] F. Reinert, G. Nicolay, S. Schmidt, D. Ehm, and S. Hüfner, Physical Review B **63**, 115415 (2001).

[62] M. Hoesch *et al.*, Physical Review B **69**, 241401 (2004).

[63] A. Nishide *et al.*, New Journal of Physics **12**, 5011 (2010).

[64] H. Zhang *et al.*, Nature Physics **5**, 438 (2009).

[65] A. F. Ioffe, *Semiconductor Thermoelements and Thermoelectric Cooling* (Infosearch, London, 1957).

[66] H. J. Goldsmid, *Thermoelectric Refrigeration* (Plenum, New York, 1964).

[67] S. K. Mishra, S. Satpathy, and O. Jepsen, Journal of Physics: Condensed Matter **9**, 461 (1997).

[68] J. P. Fleurial, L. Gailliard, R. Triboulet, H. Scherrer, and S. Scherrer, J Phys Chem Solids **49**, 1249 (1988).

[69] M. Imamuddin and A. Dupre, Physica Status Solidi (a) **10**, 415 (1972).

[70] H. Cui *et al.*, Journal of Solid State Chemistry **177**, 4001 (2004).

[71] J. Zhou, C. Jin, J. H. Seol, X. Li, and L. Shi, Appl Phys Lett **87**, 3109 (2005).

[72] X. B. Zhao *et al.*, Appl Phys Lett **86**, 2111 (2005).

[73] K. Kadel, L. Kumari, W. Li, J. Y. Huang, and P. P. Provencio, Nanoscale Research Letters **6**, 57 (2010).

[74] L. Shelimova *et al.*, Inorganic Materials **40**, 451 (2004).

[75] T. Debies and J. W. Rabalais, Chem Phys **20**, 277 (1977).

[76] C.-X. Liu *et al.*, Physical Review B **82**, 045122 (2010).

[77] H. Weng *et al.*, Physical Review B **84**, 60408 (2011).

[78] G. A. Thomas *et al.*, Physical Review B **46**, 1553 (1992).

[79] W. Zhang, R. Yu, H.-J. Zhang, X. Dai, and Z. Fang, New Journal of Physics **12**, 5013 (2010).

[80] O. V. Yazyev, J. E. Moore, and S. G. Louie, Physical Review Letters **105**, 266806 (2010).

[81] D. Hsieh *et al.*, Nature **460**, 1101 (2009).

[82] W.-C. Lee, C. Wu, D. P. Arovas, and S.-C. Zhang, Physical Review B **80**, 245439 (2009).

[83] X. Zhou, C. Fang, W.-F. Tsai, and J. Hu, Physical Review B **80**, 245317 (2009).

[84] P. Roushan *et al.*, Nature **460**, 1106 (2009).

[85] K. Kuroda *et al.*, Physical Review Letters **105**, 76802 (2010).

[86] H.-J. Noh *et al.*, Europhysics Letters **81**, 57006 (2008).

[87] Z.-H. Pan *et al.*, Physical Review Letters **108**, 187001 (2012).

[88] R. Paniago, R. Matzdorf, G. Meister, and A. Goldmann, Surf Sci **336**, 113 (1995).

[89] N. Ashcroft and D. Mermin, *Solid State Physics* (Thomson Learning, Inc., London, 1976).

[90] D. M. Riffe, W. Hale, B. Kim, and J. L. Erskine, Physical Review B **54**, 94488 (1996).

[91] J. A. Knapp, F. J. Himpsel, A. R. Williams, and D. E. Eastman, Physical Review B **19**, 2844 (1979).

[92] M. Bianchi, R. C. Hatch, J. Mi, B. B. Iversen, and P. Hofmann, Physical Review Letters **107**, 86802 (2011).

[93] C. Pauly *et al.*, arXiv **1201.4323v1** (2012).

[94] S. Souma *et al.*, Physical Review Letters **106**, 216803 (2011).

[95] N. P. Butch *et al.*, Physical Review B **81**, 241301 (2010).

[96] P. Cheng *et al.*, Physical Review Letters **105**, 76801 (2010).

[97] T. Hanaguri, K. Igarashi, M. Kawamura, H. Takagi, and T. Sasagawa, Physical Review B **82**, 81305 (2010).

[98] J. G. Analytis *et al.*, Nature Physics **6**, 960 (2010).

[99] C. Jozwiak *et al.*, Physical Review B **84**, 165113 (2011).

[100] J. G. Checkelsky *et al.*, Physical Review Letters **103**, 246601 (2009).

[101] S. V. Eremeev *et al.*, Nature Communications **3**, 635 (2012).

[102] P. G. Silvestrov, P. W. Brouwer, and E. G. Mishchenko, arXiv **1111.3650v1** (2011).

[103] Z.-H. Pan *et al.*, Physical Review Letters **106**, 257004 (2011).

[104] T. Hirahara *et al.*, Physical Review B **76**, 153305 (2007).

[105] A. Varykhalov *et al.*, Physical Review Letters **101**, 256601 (2008).

[106] E. E. Krasovskii and E. V. Chulkov, Physical Review B **83**, 155401 (2011).

[107] A. Kimura *et al.*, Physical Review Letters **105**, 76804 (2010).

[108] M. Bianchi *et al.*, Nature Communications **1**, 128 (2010).

[109] P. D. C. King *et al.*, Physical Review Letters **107**, 96802 (2011).

[110] S. Murakami, S. Iso, Y. Avishai, M. Onoda, and N. Nagaosa, Physical Review B **76**, 205304 (2007).

[111] Y. L. Chen *et al.*, Science **329**, 659 (2010).

[112] H. M. Benia, C. Lin, K. Kern, and C. R. Ast, Physical Review Letters **107**, 177602 (2011).

[113] T. Valla, Z.-H. Pan, D. Gardner, Y. S. Lee, and S. Chu, Physical Review Letters **108**, 117601 (2012).

[114] Z.-H. Zhu *et al.*, Physical Review Letters **107**, 186405 (2011).

[115] M. Ye *et al.*, arXiv **1112.5869v1** (2011).

[116] Y. Zhang *et al.*, Nature Physics **6**, 712 (2010).

[117] S. V. Eremeev, T. V. Menshchikova, M. G. Vergniory, and E. V. Chulkov, arXiv **1107.3208v1** (2011).

[118] X.-L. Qi and S.-C. Zhang, Reviews of Modern Physics **83**, 1057 (2011).

[119] X.-L. Qi, R. Li, J. Zang, and S.-C. Zhang, Science **323**, 1184 (2009).

[120] I. Garate and M. Franz, Physical Review Letters **104**, 146802 (2010).

[121] Y. Zhang and F. Zhai, Appl Phys Lett **96**, 2109 (2010).

[122] T. Yokoyama, Y. Tanaka, and N. Nagaosa, Physical Review B **81**, 1 (2010).

[123] B. D. Kong, Y. G. Semenov, C. M. Krowne, and K. W. Kim, Appl Phys Lett **98**, 3112 (2011).

[124] Y. S. Hor *et al.*, Physical Review B **81**, 195203 (2010).

[125] Q. Liu, C.-X. Liu, C. Xu, X.-L. Qi, and S.-C. Zhang, Physical Review Letters **102**, 156603 (2009).

[126] G. Rosenberg and M. Franz, Physical Review B **85**, 195119 (2012).

[127] J. Gao, W. Chen, X. C. Xie, and F.-C. Zhang, Physical Review B **80**, 241302 (2009).

[128] D. Abanin and D. Pesin, Physical Review Letters **106**, 136802 (2011).

[129] R. R. Biswas and A. V. Balatsky, Physical Review B **81**, 233405 (2010).

[130] L. Wray *et al.*, Nature Physics **7**, 32 (2010).

[131] M. Przybylski and U. Gradmann, Physical Review Letters **59**, 1152 (1987).

[132] H. J. Elmers *et al.*, Physical Review Letters **73**, 898 (1994).

[133] A. Fujimori *et al.*, Physical Review B **39**, 2255 (1989).

[134] M. Sing *et al.*, Physical Review Letters **106**, 56403 (2011).

[135] O. Krupin *et al.*, Physical Review B **71**, 201403 (2005).

[136] A. Kordyuk *et al.*, Phys. Rev. B **83**, 081303 (2011).

[137] M. Bianchi, Private communication.

[138] A. Vaško, L. Tichý, J. Horák, and J. Weissenstein, Applied Physics **5**, 217 (1974).

[139] J. Honolka *et al.*, Physical Review Letters **108**, 256811 (2012).

[140] M. Morgenstern *et al.*, Journal of Electron Spectroscopy and Related Phenomena **109**, 127 (2000).

[141] J. G. Checkelsky, Y. S. Hor, R. J. Cava, and N. P. Ong, Physical Review Letters **106**, 196801 (2011).

[142] D.-X. Qu, Y. S. Hor, J. Xiong, R. J. Cava, and N. P. Ong, Science **329**, 821 (2010).

[143] C. Brüne *et al.*, Physical Review Letters **106**, 126803 (2011).

[144] R. C. Hatch *et al.*, Physical Review B **83**, 241303 (2011).

[145] T. Hirahara *et al.*, Physical Review B **82**, 155309 (2010).

[146] L. M. Roth, H. J. Zeiger, and T. A. Kaplan, Physical Review **149**, 519 (1966).

[147] Z. Alpichshev *et al.*, Physical Review Letters **104**, 16401 (2010).

[148] S. R. Park *et al.*, Physical Review B **81**, 41405 (2010).

[149] J. Inglesfield and E. Plummer, *The Physics of Photoemission in Angle Resolved Photoemission edited by S.D. Kevan* (Elsevier, Amsterdam, 1992).

[150] P. Johnson, A. V. Federov, and T. Valla, Journal of Electron Spectroscopy and Related Phenomena **117-118**, 153 (2001).

[151] N. V. Smith, P. Thiry, and Y. Petroff, Physical Review B **47**, 87158 (1993).

[152] M. Norman, H. Ding, H. Fretwell, M. Randeria, and J. Campuzano, Physical Review B **60**, 7585 (1999).

[153] T. Valla *et al.*, Science **285**, 2110 (1999).

[154] E. Frantzeskakis and M. Grioni, Physical Review B **84**, 155453 (2011).

[155] Y. H. Wang *et al.*, Physical Review Letters **107**, 207602 (2011).

[156] W. Jung *et al.*, Physical Review B **84**, 245435 (2011).

[157] T. Zhang *et al.*, Phys. Rev. Lett. **103**, 266803 (2009).

[158] Y. Okada *et al.*, Physical Review Letters **106**, 206805 (2011).

[159] S. Kim *et al.*, Physical Review Letters **107**, 56803 (2011).

[160] E. van Heumen *et al.*, arXiv **1110.4406v1** (2011).

[161] J. Wang *et al.*, Physical Review B **84**, 235447 (2011).

[162] T. Misawa, T. Yokoyama, and S. Murakami, Physical Review B **84**, 165407 (2011).

[163] C. Wang and F. Yu, Physical Review B **84**, 155440 (2011).

[164] T. Valla, A. V. Fedorov, P. D. Johnson, and S. L. Hulbert, Physical Review Letters **83**, 2085 (1999).

[165] M. Z. Hasan, H. Lin, and A. Bansil, Physics **2**, 108 (2009).

[166] R. Peierls, *Quantum Theory of Solids* (Oxford University Press, London, 1955).

[167] A. Bostwick, T. Ohta, T. Seyller, K. Horn, and E. Rotenberg, Nat Phys **3**, 36 (2007).

[168] D. Marchenko *et al.*, (2011), Unpublished.

[169] S. Giraud and R. Egger, Physical Review B **83**, 245322 (2011).

[170] D. K. Efetov and P. Kim, Physical Review Letters **105**, 256805 (2010).

[171] G. E. Shoemake, J. A. Rayne, and R. W. Ure, Physical Review **185**, 1046 (1969).

[172] P. Thalmeier, Physical Review B **83**, 125314 (2011).

[173] A. Lanzara *et al.*, Nature **412**, 510 (2001).

[174] W. Richter and C. R. Becker, Physica Status Solidi (B) **84**, 619 (1977).

[175] X. Zhu *et al.*, Physical Review Letters **108**, 185501 (2012).

[176] M. Ye *et al.*, Physical Review B **85**, 205317 (2012).

[177] J. Henk *et al.*, Physical Review Letters **108**, 206801 (2012).

[178] P. Höpfner *et al.*, Physical Review Letters **108**, 186801 (2012).

[179] F. Meier, H. Dil, J. Lobo-Checa, L. Patthey, and J. Osterwalder, Physical Review B **77**, 165431 (2008).

[180] K. Sakamoto *et al.*, Physical Review Letters **102**, 096805 (2009).

[181] M. Kolbe *et al.*, Physical Review Letters **107**, 207601 (2011).

[182] L. Baumgarten, C. M. Schneider, H. Petersen, F. Schäfers, and J. Kirschner, Physical Review Letters **65**, 492 (1990).

[183] H. Ebert, L. Baumgarten, C. M. Schneider, and J. Kirschner, Physical Review B **44**, 4406 (1991).

[184] H. Ebert, P. Strange, and B. L. Gyorffy, J Appl Phys **63**, 3055 (1988).

[185] E. Arenholz, E. Navas, K. Starke, L. Baumgarten, and G. Kaindl, Physical Review B **51**, 8211 (1995).

[186] E. Vescovo, O. Rader, G. van der Laan, and C. Carbone, Physical Review B **56**, 70659 (1997).

[187] M. Wöhlecke and G. Borstel, Physical Review B **23**, 980 (1981).

[188] B. Schmiedeskamp, B. Vogt, and U. Heinzmann, Physical Review Letters **60**, 651 (1988).

[189] H. Oepen, K. Hünlich, J. Kirschner, A. Eyers, and F. Schäfers, Solid State Communications **59**, 521 (1986).

[190] H. P. Oepen, K. Hünlich, and J. Kirschner, Physical Review Letters **56**, 496 (1986).

[191] J. Garbe and J. Kirschner, Physical Review B **39**, 9859 (1989).

[192] S. V. Borisenko *et al.*, Physical Review B **69**, 224509 (2004).

[193] V. Zabolotnyy *et al.*, Physical Review B **76**, 1 (2007).

[194] C. M. Schneider *et al.*, Physical Review B **44**, 73830 (1991).

[195] J. Bansmann, M. Getzlaff, C. Westphal, F. Fegel, and G. Schönhense, Surf Sci **269/270**, 622 (1992).

[196] G. Schönhense, Physica Scripta **31**, 255 (1990).

[197] A. A. Kordyuk *et al.*, Physical Review B **85**, 75414 (2012).

[198] Y. Ishida *et al.*, Physical Review Letters **107**, 77601 (2011).

[199] P. Gartland, Solid State Communications **25**, 489 (1978).

[200] S. R. Park *et al.*, Physical Review Letters **108**, 46805 (2012).

[201] J. F. L. Hopkinson, J. B. Pendry, and D. J. Titterington, Computer Physics Communications **19**, 69 (1980).

[202] J. Braun, Reports on Progress in Physics **59**, 1267 (1996).

[203] J. Minár, J. Braun, S. Mankovsky, and H. Ebert, Journal of Electron Spectroscopy and Related Phenomena **184**, 91 (2011).

[204] A. X. Gray *et al.*, Nature Materials **10**, 759 (2011).

[205] G. Malmström and J. Rundgren, Computer Physics Communications **19**, 263 (1980).

[206] M. Mulazzi *et al.*, Physical Review B **79**, 165421 (2009).

[207] G. Schönhense, C. Westphal, J. Bansmann, and M. Getzlaff, Europhysics Letters **17**, 727 (1992).

[208] A. Baalmann *et al.*, Journal of Physics C: Solid State Physics **19**, 3039 (1986).

[209] J. Olde *et al.*, Physical Review B **41**, 9958 (1990).

Publication List

Refereed Publications

1. T. Sünner, M. Gellner, **M. Scholz**, A. Löffler, M. Kamp, A. Forchel
Dispersive properties of photonic crystal waveguide resonators. Physica Status Solidi (a) **204**, 11, 37273738 **(2007)**

2. S. Glawion, **M. R. Scholz**, Y.-Z. Zhang, R. Valentí, T. Saha-Dasgupta, M. Klemm, J. Hemberger, S. Horn, M. Sing and R. Claessen
Electronic structure of the two-dimensional Heisenberg antiferromagnet VOCl: A multiorbital Mott insulator. Physical Review B **80**, 155119 **(2009)**

3. A. Varykhalov, **M. R. Scholz**, Timur K. Kim and O. Rader
Effect of noble-metal contacts on doping and band gap of graphene. Physical Review B **82**, 121101(R) **(2010)**

4. J. Sánchez-Barriga, A. Varykhalov, **M. R. Scholz**, O. Rader, D. E. Marchenko, A. G. Rybkin, A. M. Shikin, E. Vescovo
Chemical vapour deposition of graphene on Ni(111) and Co(0001) and intercalation with Au to study Dirac-cone formation and Rashba splitting. Diamond and Related Materials **19**, 734-741 **(2010)**

5. M. Sing, S. Glawion, M. Schlachter, **M. R. Scholz**, K. Goss, J. Heidler, G. Berner and R. Claessen
Photoemission of a Doped Mott Insulator: Spectral Weight Transfer and a Qualitative Mott-Hubbard Description. Physical Review Letters **106**, 056403 **(2011)**

6. **M. R. Scholz**, J. Sánchez-Barriga, D. Marchenko, A. Varykhalov, A. Volykhov, L. V. Yashina and O. Rader
Tolerance of Topological Surface States towards Magnetic Moments: Fe on Bi_2Se_3. Physical Review Letters **108**, 256810 **(2012)**

7. A. Varykhalov, D. Marchenko, **M. R. Scholz**, E. D. L. Rienks, T. K. Kim, G. Bihlmayer, J. Sánchez-Barriga and O. Rader
Ir(111) Surface State with Giant Rashba Splitting Persists under Graphene in Air. Physical Review Letters **108**, 66804 **(2012)**

8. J. Sánchez-Barriga, A. Varykhalov, D. Marchenko, **M. R. Scholz** and O. Rader
Minigap isotropy and broken chirality in graphene with periodic corrugation enhanced by cluster superlattices. Physical Review B **85**, 201413 **(2012)**

9. A. Varykhalov, D. Marchenko, J. Sánchez-Barriga, **M. R. Scholz**, B. Verbeck, B. Trauzettel, T. O. Wehling, C. Carbone and O. Rader
Intact Dirac cones at broken sublattice symmetry: Photoemission study of graphene on Ni and Co. Physical Review X **2**, 041017 **(2012)**

10. D. Marchenko, A. Varykhalov, **M. R. Scholz**, G. Bihlmayer, E. I. Rashba, A. Rybkin, A. M. Shikin and O. Rader
Graphene for spintronics: giant Rashba splitting due to hybridization with Au. Nature Communications **3**, 1232 **(2012)**

11. C. Pauly, G. Bihlmayer, M. Liebmann, M. Grob, A. Georgi, D. Subramaniam, **M. R. Scholz**, J. Sánchez-Barriga, A. Varykhalov, S. Blügel, O. Rader and M. Morgenstern
Probing two topological surface bands of Sb_2Te_3 by spin-polarized photoemission spectroscopy. Physical Review B **86**, 235106 **(2012)**

12. **M. R. Scholz**, J. Sánchez-Barriga, J. Braun, D. Marchenko, A. Varykhalov, M. Lindroos, Y. J. Wang, H. Lin, A. Bansil, J. Minár, H. Ebert, A. Volykhov, L. V. Yashina and O.Rader
Reversal of the circular dichroism in angle-resolved photoemission from Bi_2Te_3. Physical Review Letters **110**, 216801 **(2013)**

13. **M. R. Scholz**, J. Sánchez-Barriga, D. Marchenko, A. Varykhalov, A. Volykhov, L. V. Yashina and O. Rader
Intact Dirac cone of Bi_2Te_3 covered with a monolayer Fe physica status solidi - Rapid Research Letters **7**, 139-141 **(2013)**

14. D. Marchenko, J. Snchez-Barriga, **M. R. Scholz**, O. Rader, and A. Varykhalov
Spin splitting of Dirac fermions in aligned and rotated graphene on Ir(111). Physical Review B **87**, 115426 **(2013)**

15. L. V. Yashina, J. Snchez-Barriga, **M. R. Scholz**, A. A. Volykhov, A. P. Sirotina, V. S. Neudachina, M. E. Tamm, A. Varykhalov, D. Marchenko, G. Springholz, G. Bauer, A. Knop-Gericke and O. Rader
Negligible Surface Reactivity of Topological Insulators Bi_2Se_3 and Bi_2Te_3 towards Oxygen and Water. ACS Nano **7**, 5181 **(2013)**

16. A. M. Shikin, A. G. Rybkin, D. Marchenko, A. A. Rybkina, **M. R Scholz**, O. Rader, and A. Varykhalov
Induced spinorbit splitting in graphene: the role of atomic number of the intercalated metal and pid hybridization. New Journal of Physics **15**, 013016 **(2013)**

17. D. Marchenko, A. Varykhalov, **M. R. Scholz**, J. Sánchez-Barriga, O. Rader, A. Rybkina, A. M. Shikin, Th. Seyller and G. Bihlmayer
Spin-resolved photoemission and ab initio theory of graphene/SiC. Physical Review B **88**, 075422 **(2013)**

18. A. Barfuss, L. Dudy, **M. R. Scholz**, H. Roth, P. Höpfner, C. Blumenstein, G. Landolt, J. H. Dil, N.C. Plumb, M. Radovic, A. Bostwick, E. Rotenberg, A. Fleszar, G. Bihlmayer, D. Wortmann, G. Li, W. Hanke, R. Claessen, J. Shäfer
Elemental topological insulator with a tunable Fermi level: Strained α-Sn on InSb(001). arXiv:1308.0826v2, *accepted for publication in Physical Review Letters* **(2013)**

Non-refereed Publications

1. **M. R. Scholz**, J. Sánchez-Barriga, D. Marchenko, A. Varykhalov, A. Volykhov, L. V. Yashina and O. Rader
High spin polarization and circular dichroism of topological surface states on Bi_2Te_3. arXiv:1108.1053v2 **(2011)**

2. **M. R. Scholz**, J. Sánchez-Barriga, D. Marchenko, A. Varykhalov, A. Volykhov, L. V. Yashina and O. Rader
Tolerance of topological surface states towards magnetic moments: Fe on Bi_2Te_3 and Bi_2Se_3. arXiv:1108.1037v1 **(2011)**

Conferences

1. **M. R. Scholz**, D. Marchenko, A. Varykhalov, O. Rader, A. Volykhov and L. V. Yashina
Spin-resolved photoemission and circular dichroism of topological insulators Bi_2Te_3 and Bi_2Se_3. Poster presentation, 449. Wilhelm and Else Heraeus Seminar: "Rashba and related spin-orbit effects in metals", Bad Honnef, Germany **(2010)**

2. **M. R. Scholz**, D. Marchenko, A. Varykhalov, O. Rader, A. Volykhov and L. V. Yashina
Spin-polarized topological surface states of topological insulators Bi_2Te_3 and Bi_2Se_3. Oral presentation, DPG Frühjahrstagung, Regensburg, Germany **(2010)**

3. **M. R. Scholz**, D. Marchenko, J. Sánchez-Barriga, A. Varykhalov, O. Rader, A. Volykhov and L. V. Yashina
Tolerance of topological surface state towards adsorbed magnetic moments: Fe on Bi_2Te_3. Poster presentation, 2nd HZB Joint BERII and BESSYII Users Meeting, Berlin, Germany **(2010)**

4. **M. R. Scholz**, D. Marchenko, J. Sánchez-Barriga, A. Varykhalov, A. Volykhov, L. V. Yashina and O. Rader
Tolerance of topological surface state towards adsorbed magnetic moments: Fe on Bi_2Te_3. Oral presentation given on behalf by Oliver Rader, DPG Frühjahrstagung, Dresden, Germany **(2011)**

5. **M. R. Scholz**, D. Marchenko, A. Varykhalov, J. Sánchez-Barriga, A. Volykhov, L. V. Yashina and O. Rader
Stability of the topological surface state of Bi_2Te_3 against magnetic moments up to 1 monolayer Fe. Oral presentation, EMRS Fall Meeting, Warsaw, Poland **(2011)**

6. **M. R. Scholz**, J. Sánchez-Barriga, D. Marchenko, A. Varykhalov, A. Volykhov, L. V. Yashina and O. Rader
Control of doping and stability of topological surface states towards magnetic moments: Fe on Bi_2Se_3. Poster presentation, 3rd HZB Joint BERII and BESSYII Users Meeting, Berlin, Germany **(2011)**

7. **M. R. Scholz**, J. Sánchez-Barriga, D. Marchenko, A. Varykhalov, A. Volykhov, L. V. Yashina and O. Rader
Influence of magnetic impurities on the scattering properties of topological surface states: Fe on Bi_2X_3 (X=Te,Se) Poster presentation, 3rd HZB Joint BERII and BESSYII Users Meeting, Berlin, Germany **(2011)**

8. **M. R. Scholz**, J. Sánchez-Barriga, D. Marchenko, E. Rienks, A. Varykhalov, A. Volykhov, L. V. Yashina and O. Rader
Influence of magnetic impurities on doping and scattering properties of topological surface states: Fe on Bi_2Se_3. Poster presentation, POF Midterm-Begutachtung, Berlin, Germany **(2012)**

9. **M. R. Scholz**, J. Sánchez-Barriga, D. Marchenko, A. Varykhalov, E. Rienks A. Volykhov, L. V. Yashina and O. Rader
Influence of magnetic impurities on doping and scattering properties of topological surface states: Fe on Bi_2X_3 (X=Te, Se). Oral presentation, DPG Frühjahrstagung, Berlin, Germany **(2012)**

10. **M. R. Scholz**, J. Sánchez-Barriga, D. Marchenko, A. Varykhalov, A. Volykhov, L. V. Yashina, J. Braun, J. Minár and O. Rader
Strong Circular Dichroism and Robustness of Topological Insulators Against Magnetic Moments. Oral presentation given on behalf by Oliver Rader, MRS Spring Meeting, San Francisco, USA **(2012)**

11. **M. R. Scholz**, J. Sánchez-Barriga, D. Marchenko, A. Varykhalov, E. Rienks A. Volykhov, L. V. Yashina and O. Rader
Influence of magnetic impurities on doping and scattering properties of topological surface states: Fe on Bi_2X_3 (X=Te, Se). Oral presentation, CMD-24, Edinburgh, Great Britain **(2012)**

Invited Talks

1. **M. R. Scholz**, J. Sánchez-Barriga, D. Marchenko, A. Varykhalov, E. Rienks A. Volykhov, L. V. Yashina and O. Rader
Robustness of Topological Protection: Impurities on Bi_2Te_3., MI-1 Seminar Helmholtz-Zentrum Berlin, Berlin, Germany **(2011)**

2. **M. R. Scholz**, J. Sánchez-Barriga, D. Marchenko, A. Varykhalov, E. Rienks A. Volykhov, L. V. Yashina, J. Braun, J. Minär, H. Ebert and O. Rader
Strong Circular Dichroism and Robustness of Topological Insulators Against Magnetic Moments., Quantum many-body phenomena in the solid state Seminar, Universität Würzburg, Würzburg, Germany **(2012)**